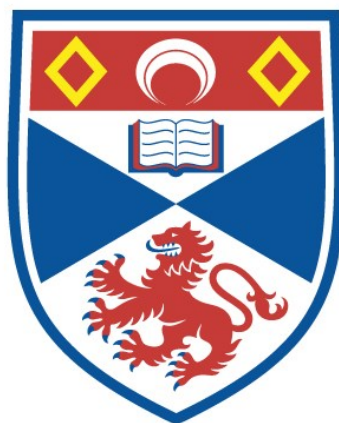


MAGNETIC FIELD INDUCED SUM FREQUENCY MIXING IN  
SODIUM VAPOUR.

Alistair J. Poustie

A Thesis Submitted for the Degree of PhD  
at the  
University of St Andrews



1990

Full metadata for this item is available in  
St Andrews Research Repository  
at:  
<http://research-repository.st-andrews.ac.uk/>

Please use this identifier to cite or link to this item:  
<http://hdl.handle.net/10023/13765>

This item is protected by original copyright

**MAGNETIC FIELD INDUCED SUM FREQUENCY MIXING  
IN SODIUM VAPOUR**

**A thesis presented by**

**Alistair J. Poustie, B.Sc.**

**to the**

**University of St. Andrews  
in application for the degree of  
Doctor of Philosophy**

**April 1990**



ProQuest Number: 10166253

All rights reserved

INFORMATION TO ALL USERS

The quality of this reproduction is dependent upon the quality of the copy submitted.

In the unlikely event that the author did not send a complete manuscript and there are missing pages, these will be noted. Also, if material had to be removed, a note will indicate the deletion.



ProQuest 10166253

Published by ProQuest LLC (2017). Copyright of the Dissertation is held by the Author.

All rights reserved.

This work is protected against unauthorized copying under Title 17, United States Code  
Microform Edition © ProQuest LLC.

ProQuest LLC.  
789 East Eisenhower Parkway  
P.O. Box 1346  
Ann Arbor, MI 48106 – 1346

TH A1207

## DECLARATIONS

I hereby certify that this thesis has been composed by myself, that it is a record of my own work, and that it has not been presented for partial or complete fulfilment of any other higher degree.

This research was carried out in the Department of Physics and Astronomy, University of St. Andrews under the supervision of Dr. M.H. Dunn.

A.J. POUSTIE  
April 1990

I hereby certify that Alistair James Poustie has fulfilled the conditions of the Resolution and Regulations appropriate to the degree of Doctor of Philosophy.

M.H. DUNN  
Research Supervisor  
April 1990

## ABSTRACT

A study of magnetic field induced sum frequency mixing (SFM) in sodium vapour was carried out using continuous-wave lasers as the sources of the fundamental radiation. The three-wave mixing nonlinear optical process was resonantly enhanced by tuning the laser frequencies close to single and two-photon resonances in the sodium atoms. The coherent ultraviolet radiation at the sum frequency of the two input laser frequencies was emitted by the coherently driven 3S-4D electric-quadrupole, which was rotated by the transverse magnetic field to allow collinear generation of the sum frequency wave.

Two single-frequency dye lasers were used to examine in detail the role of the intermediate 3P atomic states in the coherent two-photon absorption. Resonant single photon transitions were investigated for the first time in a nonlinear optical process in an atomic vapour. High resolution SFM line profiles were obtained which illustrated the complicating contributions of hole-burning, velocity selection, optical pumping, saturation and frequency dependent phase mismatching to the three-wave mixing effect. The use of additional single photon resonant enhancement and control over the refractive index of the sodium vapour showed that large effective nonlinear  $\chi^{(2)}$  susceptibilities were possible in atomic vapours which could exceed those of nonlinear crystals.

The variation of SFM power with atomic particle density due to bulk phase mismatching reflected the wavelength dependence of the sodium dispersion with the 3P intermediate state off-resonance. Phase shifts of the focused Gaussian laser beams led to an asymmetric behaviour of the phase matching with respect to the sign of the phase mismatch  $\Delta k$ .

Saturation spectroscopy was utilised for the first time to examine the Zeeman spectra of the sodium 3S-3P D line resonances in a transverse magnetic field. A novel experimental method was used to restrict the detrimental effects of velocity changing collisions on the resolution of the nonlinear laser spectroscopic technique.

The possibility of using optical pumping with a transversal, resonant light beam to induce the second-order nonlinearity necessary for second harmonic generation in sodium vapour was experimentally investigated.

## ACKNOWLEDGEMENTS

I would like to thank my research supervisor, Dr. Malcolm Dunn, for his guidance and help throughout the course of this work. I am also especially grateful to Dr. Bruce Sinclair for his assistance. I wish to thank all my fellow researchers for their friendship and help over the last three years. I am grateful to the technical staff of the Department of Physics and Astronomy for their assistance and to Karen Lumsden who expertly word-processed this thesis. My thanks go to the Carnegie Trust for the Universities of Scotland who awarded my scholarship to carry out this research work.

I would also like to thank Dr. Bill MacGillivray for his help with some of the theoretical aspects of this project and Mr. Grahame Rogers, the University of Manchester and British Aerospace, Filton for the loan of equipment. I am grateful to the managers at British Telecom who allowed me time to finish this thesis.

Finally, I thank all my family for their love and support during my studies in St. Andrews and especially my wife Alison for her love, encouragement and patience.

# CONTENTS

Page

DECLARATIONS

ABSTRACT

ACKNOWLEDGEMENTS

<b><u>CHAPTER 1 : INTRODUCTION</u></b>	<b>1</b>
1.1 LINEAR OPTICS	1
1.2 NONLINEAR OPTICS	2
1.3 NONLINEAR MEDIUM	3
1.4 PHASE MATCHING	6
1.5 SYMMETRY BREAKING TECHNIQUES TO INDUCE $\chi^{(2)}$ NONLINEAR OPTICAL PROCESSES IN ATOMIC VAPOURS	7
1.5.1 <i>Transverse DC Electric Field</i>	8
1.5.2 <i>High Power Laser Pulses</i>	10
1.5.3 <i>Non-Collinear Beam Excitation</i>	11
1.5.4 <i>Transverse DC Magnetic Field</i>	12
1.6 RELATED AREAS OF STUDY	16
<b><u>CHAPTER 2 : THEORY</u></b>	<b>18</b>
2.1 EIGENSTATES AND EIGENENERGIES OF THE SODIUM ATOM IN AN EXTERNAL MAGNETIC FIELD	18
2.1.1 <i>3S States</i>	18
2.1.2 <i>3P States</i>	20
2.1.3 <i>4D States</i>	23
2.2 MICROSCOPIC THEORY OF SHG	25
2.3 THREE-LEVEL ATOM	27
2.3.1 <i>Semiclassical Model</i>	28
2.3.2 <i>Quantum Electrodynamical (QED) Model</i>	31
2.3.3 <i>Discussion of the Semiclassical Model</i>	32
2.3.4 <i>Theoretical Results</i>	33
<b><u>CHAPTER 3 : EXPERIMENTAL APPARATUS</u></b>	<b>46</b>
3.1 DYE LASER SYSTEMS	46
3.1.1 <i>Spectra Physics 380D dye laser</i>	46
3.1.2 <i>Spectra Physics 380A dye laser (V)</i>	48
3.1.3 <i>Coherent 699-21 dye laser (VI)</i>	48
3.1.4 <i>Standing-wave dye laser (V, VII)</i>	49

<b>3.2</b>	<b>MONITORING AND DETECTION DEVICES</b>	<b>51</b>
3.2.1	<i>Laser Parameters</i>	51
3.2.2	<i>Signal detection apparatus</i>	53
<b>3.3</b>	<b>METAL VAPOUR</b>	<b>53</b>
<b>3.4</b>	<b>TRANSVERSE MAGNETIC FIELD</b>	<b>56</b>
<b>3.5</b>	<b>OPTICS</b>	<b>57</b>
 <b><u>CHAPTER 4 : MEASUREMENT OF THE ZEEMAN SPLITTING OF THE SODIUM 3S and 3P ATOMIC STATES BY SATURATED ABSORPTION SPECTROSCOPY</u></b>		<b>58</b>
<b>4.1</b>	<b>SATURATED ABSORPTION SPECTROSCOPY</b>	<b>59</b>
4.1.1	<i>Basic Principles of Saturation Spectroscopy</i>	59
4.1.2	<i>Line Broadening Mechanisms</i>	62
4.1.3	<i>Crossover Resonances</i>	64
4.1.4	<i>Optical Pumping</i>	66
4.1.5	<i>Velocity Changing Collisions</i>	67
<b>4.2</b>	<b>EXPERIMENTAL ZEEMAN SPLITTINGS MEASURED BY SATURATION SPECTROSCOPY</b>	<b>69</b>
 <b><u>CHAPTER 5 : MAGNETIC FIELD INDUCED <math>\chi^{(2)}</math> SUM FREQUENCY MIXING</u></b>		<b>79</b>
<b>5.1</b>	<b>SFM : MICROSCOPIC EFFECTS</b>	<b>80</b>
5.1.1	<i>Combination of <math>\omega_1</math> and <math>\omega_2</math> for SFM</i>	80
5.1.2	<i>Magnetic Field Strength</i>	80
5.1.3	<i>Laser Intensity</i>	82
5.1.4	<i>Excitation of Quadrupole Moments</i>	82
<b>5.2</b>	<b>SFM : MACROSCOPIC EFFECTS</b>	<b>83</b>
5.2.1	<i>Phase-matching Techniques for Nonlinear Optical Processes in Atomic Vapours</i>	86
5.2.2	<i>Focusing Effects</i>	93
5.2.3	<i>Experimental Results for SFM Phase-matching</i>	96
 <b><u>CHAPTER 6 : SUM FREQUENCY MIXING WITH A RESONANT OR NEAR-RESONANT INTERMEDIATE STATE</u></b>		<b>107</b>
<b>6.1</b>	<b>TWO-PHOTON SPECTROSCOPY</b>	<b>109</b>
6.1.1	<i>Single and Two-Photon Resonant Enhancement</i>	109
6.1.2	<i>On Resonance Excitation</i>	113
<b>6.2</b>	<b>VELOCITY SELECTIVE EXCITATION</b>	<b>114</b>
<b>6.3</b>	<b>OPTICAL PUMPING</b>	<b>118</b>

<b>6.4 COLLISIONAL EFFECTS</b>	121
6.4.1 <i>Pressure Broadening</i>	121
6.4.2 <i>Pressure Shifts</i>	123
6.4.3 <i>Collisional Redistribution</i>	124
6.4.4 <i>Velocity Changing Collisions</i>	125
<b>6.5 LASER POWER EFFECTS</b>	125
6.5.1 <i>Single Photon Saturation</i>	126
6.5.2 <i>Two-Photon Saturation</i>	128
6.5.3 <i>Autler-Townes Effect</i>	128
6.5.4 <i>Light Shifts</i>	129
6.5.5 <i>Higher Order Nonlinear Effects</i>	130
<b>6.6 ABSORPTION AND REFRACTIVE INDEX</b>	132
6.6.1 <i>Linear Single-Photon Absorption</i>	132
6.6.2 <i>Two-Photon Absorption</i>	134
6.6.3 <i>Refractive Index</i>	135
6.6.4 <i>Phase Matching</i>	138
<b>6.7 EXPERIMENTAL RESULTS FOR ON-RESONANCE SUM FREQUENCY MIXING</b>	139
6.7.1 <i>Two-Photon Spectroscopy with a Resonant Intermediate State</i>	139
6.7.2 <i>SFM Line Profiles</i>	146
<b>6.8 SUM FREQUENCY MIXING WITH IMPROVED CONVERSION EFFICIENCY</b>	159
<b><u>CHAPTER 7 : <math>\chi^{(2)}</math> NONLINEARITY INDUCED IN AN ATOMIC VAPOUR BY OPTICAL PUMPING</u></b>	159
<b>7.1 PRINCIPLES OF OPTICAL PUMPING</b>	159
7.1.1 <i>Pumping Source</i>	162
<b>7.2 RELAXATION OF THE ATOMIC ORIENTATION</b>	163
7.2.1 <i>Relaxation on the Cell Walls</i>	163
7.2.2 <i>Diffusion to the Cell Walls</i>	164
7.2.3 <i>Spin Destroying Collisions</i>	165
7.2.4 <i>Radiation Trapping</i>	165
<b>7.3 EFFECT OF OPTICAL PUMPING ON SHG</b>	167
<b>7.4 EXPERIMENTAL RESULTS AND CONCLUSIONS</b>	169
<b>7.5 FUTURE WORK</b>	172
<b><u>CHAPTER 8 : SUMMARY AND FUTURE WORK</u></b>	173
<b>8.1 SUMMARY</b>	173
<b>8.2 FUTURE WORK</b>	175
<b><u>REFERENCES</u></b>	178

# CHAPTER 1

## INTRODUCTION

# Chapter 1

## INTRODUCTION

### 1.1 LINEAR OPTICS

The interaction of light with a medium can be described by the induced polarisation in the medium by the electric field of the electromagnetic light wave. The magnitude  $|E_0|$  of the oscillating electric field

$$E(\mathbf{r}, t) = E_0 \exp[i(\mathbf{k} \cdot \mathbf{r} - \omega t)] \quad (1.1.1)$$

associated with the light wave can be determined from the Poynting vector  $\mathbf{S} = \mathbf{E} \times \mathbf{H}$  which is the energy flux per unit time [1]. For a plane, sinusoidal wave,

$$|S|_{av} = \frac{1}{2} c \epsilon_0 |E_0|^2 \quad (1.1.2)$$

where  $|S|_{av}$  ( $\text{Wm}^{-2}$ ) is the average energy flux per unit time,  $c$  ( $\text{ms}^{-1}$ ) is the velocity of light,  $\epsilon_0$  is the permittivity of free space and  $|E_0|$  ( $\text{Vm}^{-1}$ ) is the electric field amplitude of the light wave at frequency  $\omega$ . When  $|E_0|$  is much smaller than the intra-atomic electric field responsible for binding the electron to the nucleus ( $E_{\text{atom}} \approx \text{binding energy} / \text{size of atom}$ ) then the interaction of the light field with the atom is perturbative. The induced polarisation in the atom is then expressed in the linear form

$$\mathbf{P} = \epsilon_0 \chi(\omega) \mathbf{E} \quad (1.1.3)$$

where  $\chi(\omega)$  is the complex frequency dependent electronic susceptibility of the atom. This induced polarisation acts as a source term in Maxwell's equation

$$\nabla^2 \mathbf{E} = \mu_0 \epsilon_0 \frac{\partial^2 \mathbf{E}}{\partial t^2} + \mu_0 \frac{\partial^2 \mathbf{P}}{\partial t^2} \quad (1.1.4)$$

and re-radiates a light wave, also at frequency  $\omega$ . The complex nature of  $\chi(\omega)$  takes account of the interaction of the original and the generated light fields. The real part of  $\chi(\omega)$  describes the change of phase of the fundamental light field as it propagates through the medium and is

interpreted as the refractive index  $n$  of the medium

$$n \sim 1 + \frac{1}{2} \operatorname{Re} \chi(\omega). \quad (1.1.5)$$

The imaginary part of  $\chi(\omega)$  is a damping term for the fundamental electric field  $\mathbf{E}$  and describes the absorption of the light in the medium. The absorption coefficient  $\alpha$  ( $\text{m}^{-1}$ ) is approximately given by

$$\alpha \sim \frac{k}{2n^2} \operatorname{Im} \chi(\omega) \quad (1.1.6)$$

where  $k$  ( $\text{m}^{-1}$ ) is the wave vector of the light field and  $n$  is the non-resonant refractive index of the medium.

The functional form of  $\chi(\omega)$  depends upon the composition of the medium but this interpretation of the light/atom interaction can generally be applied in linear optics by invoking the Kramers-Kronig relations [2].

## 1.2 NONLINEAR OPTICS

Whilst the linear model of the light/atom interaction holds in many experimental situations, it is no longer valid when the electric field of the light wave approaches the value of the intra-atomic electric field. The induced polarisation in the medium then has a nonlinear dependence on the electric field of the light wave. Many nonlinear optical effects can be phenomenologically described by expanding the polarisation as a power series in the incident optical electric field [3].

$$\mathbf{P} = \epsilon_0 \chi^{(1)} \mathbf{E} + \epsilon_0 \chi^{(2)} \mathbf{E}^2 + \epsilon_0 \chi^{(3)} \mathbf{E}^3 + \dots \quad (1.1.7)$$

The first term in the series is the linear response which was described in §1.1. The first order electric susceptibility has been relabeled  $\chi^{(1)}$  to distinguish it from the higher order terms. The second and third terms in the power series describe the nonlinear response of the medium to the incident optical field.

The second order susceptibility  $\chi^{(2)}$  describes the coupling of two incident waves  $\mathbf{E}_1(\omega_1)$  and  $\mathbf{E}_2(\omega_2)$  to form components of the induced polarisation oscillating at  $2\omega_1$ ,  $2\omega_2$ ,  $\omega_1 + \omega_2$  and  $\omega_1 - \omega_2$ . These are termed three-wave mixing nonlinear optical effects because

power is transferred from two fundamental optical fields to generate a new optical field at one of these sum or difference frequencies. This group of  $\chi^{(2)}$  nonlinear optical effects includes second harmonic generation (SHG), sum frequency mixing (SFM), difference frequency mixing (DFM), parametric amplification and optical rectification. Second order  $\chi^{(2)}$  processes are usually forbidden in isotropic media due to symmetry requirements on the potential energy of electrons in the atomic medium [2]. The work described in this thesis concentrates on  $\chi^{(2)}$  nonlinear optical effects using an atomic vapour as the nonlinear medium and a technique to break the symmetry of the vapour, specifically magnetic field induced SFM.

Third order  $\chi^{(3)}$  nonlinear optical effects are allowed in isotropic media and describe a variety of four-wave mixing processes. These include third harmonic generation (THG), two-photon absorption, intensity dependent refractive index and optical phase conjugation. Atomic and molecular vapours have often been used as nonlinear media to study  $\chi^{(3)}$  nonlinear optical processes [4] although they will generally not be considered here.

The observation of nonlinear optical mixing effects became possible with the demonstration of the first laser in 1960 [5]. Lasers can produce intense optical electric fields which are necessary to induce the high order components in the atomic polarisation. This is possible because of the intrinsic high laser powers and the ability to focus the coherent laser radiation to dimensions of the order of the wavelength of light. The first report of an experimental nonlinear optical effect came as soon as 1961 where the second harmonic of ruby laser light (694.2 nm) was generated using crystalline quartz as the nonlinear medium [6].

Over the last 30 years, the study of nonlinear optical effects has grown into a vast field in optical physics. There are many comprehensive reviews of nonlinear optics, see for example [2, 3, 4, 7, 8, 9].

### 1.3 NONLINEAR MEDIUM

Historically, noncentrosymmetric crystalline materials such as ammonium dihydrogen arsenate (ADA) have been used as nonlinear media for generating  $\chi^{(2)}$  nonlinear optical effects. These crystals have been developed to have the advantages of large second-order electronic susceptibilities (typically  $\sim 1 \text{ pm V}^{-1}$ ), transparency over reasonably wide ranges of the

electromagnetic spectrum, good resistance to optical damage (typically  $> \text{GW cm}^{-2}$ ) and are usually birefringent so that phase- matching of the nonlinear optical process can be achieved. Conversion from the fundamental to the second harmonic can be over 50% in these materials [10].

Although nonlinear crystalline materials have practical applications in many commercial devices, there is also interest in using vapours as nonlinear media. Most nonlinear crystals have an ultraviolet (UV) absorption edge at  $\sim 200 \text{ nm}$  and suffer irreversible damage at high optical field intensities whereas vapours are transparent down to the vacuum ultraviolet (VUV) region of the spectrum and do not suffer damage due to constant availability of the atomic or molecular species. Vapours can be prepared with high optical quality and with long interaction lengths over which the nonlinear optical conversion can take place. Due to the normal isotropy of a gaseous nonlinear medium, most studies of nonlinear optical effects in vapours have concentrated on  $\chi^{(3)}$  processes such as THG [11]. In order to study  $\chi^{(2)}$  nonlinear optical processes in a vapour, some method must be used to break the symmetry of the medium. This has been achieved by the application of static transverse electric or magnetic fields, by using high power pulses to induce photoionisation or by using a noncollinear beam geometry to impose the asymmetry. These methods are reviewed in §1.4. A novel alternative method of removing the atomic isotropy is to create a background transversal polarisation or orientation of the atoms by optical pumping [12]. This technique is discussed and experimentally evaluated in Chapter 7 of this thesis.

In an atomic vapour the energy levels of the medium are quantised and this allows a microscopic expression for the second order susceptibility to be derived. For SFM [13]

$$\chi^{(2)} \sim \frac{N \mu_{ik} \mu_{kj} \mu_{ji}}{2\hbar^2 \epsilon_0 (\omega_{ji} - \omega_1) (\omega_{ki} - \omega_2 - \omega_1)} \quad (1.3.1)$$

where  $N(\text{m}^{-3})$  is the particle density of the atoms in the atomic ground state,  $\mu_{\alpha\beta}$  is the electric dipole matrix element between levels  $\alpha$  and  $\beta$  and  $\omega_{\alpha\beta}$  is the atomic transition frequency as shown in Figure 1.1.

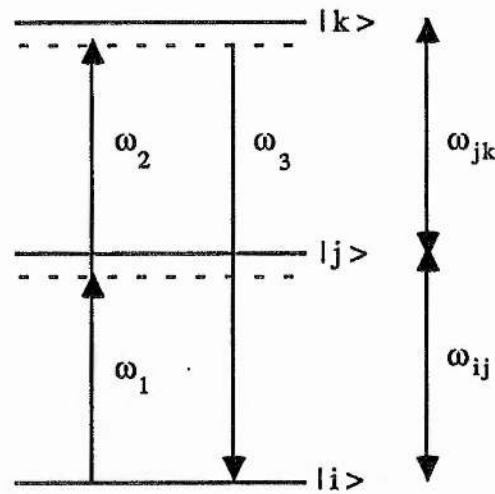


Figure 1.1 : Fundamental optical waves  $\omega_1$  and  $\omega_2$  interacting nonlinearly with atomic energy eigenstates  $|i\rangle$ ,  $|j\rangle$  and  $|k\rangle$  to produce a sum frequency wave at frequency  $\omega_3$ .

Atomic energy level wavefunctions have definite parity and so  $\chi^{(2)}$  is forbidden in the dipole approximation. Consider equation (1.3.1), if the atomic transitions  $|i\rangle \rightarrow |j\rangle$  and  $|j\rangle \rightarrow |k\rangle$  are dipole allowed then the matrix elements  $\mu_{ij}$  and  $\mu_{jk}$  are non-zero. However, since the selection rule for a dipole transition is  $\Delta l = \pm 1$ , this implies that atomic states  $|i\rangle$  and  $|k\rangle$  must have the same parity and so  $\mu_{ik} = 0$  which also makes  $\chi^{(2)}$  equal to zero. This is no longer necessarily true when electric quadrupole or other higher order radiation processes are considered. If one of the atomic transitions is electric quadrupole allowed with matrix element  $Q_{\alpha\beta}$  then the parity argument is satisfied and a  $\chi^{(2)}$  process may be possible in an atomic vapour if suitable asymmetry is introduced.

As in any parametric nonlinear optical interaction, the state of the atoms in the vapour must remain unchanged and this imposes conservation laws on the process. Energy conservation must apply so that

$$\omega_3 = \omega_1 + \omega_2 . \quad (1.3.2)$$

Momentum conservation implies that

$$\mathbf{k}_3 = \mathbf{k}_1 + \mathbf{k}_2 \quad (1.3.3)$$

where  $k_i = 2\pi n_i \hat{k} / \lambda_i$  is the wavevector of the light wave at frequency  $\omega_i$  and wavelength  $\lambda_i$ . In addition, photon angular momentum must be conserved in the parametric nonlinear optical process and this dictates why collinear three-wave mixing is not possible in an isotropic medium such as an atomic vapour. Since the electromagnetic waves are transverse, each photon carries  $\pm 1$  units of angular momentum along the quantisation axis  $\hat{z}$ , which may be chosen as the direction of collinear wave propagation in an isotropic medium. Therefore the angular momentum conservation law

$$M_z(\omega_3) = M_z(\omega_1) + M_z(\omega_2), \quad (1.3.4)$$

where  $M_z(\omega_i)$  is the component of angular momentum of wave  $\omega_i$  along  $\hat{z}$ , can never be satisfied for the three interacting waves in a  $\chi^{(2)}$  SFM nonlinear optical process with a collinear geometry. Application of a transverse external field imposes a preferred direction in the vapour and allows this conservation law to be satisfied, allowing collinear three-wave mixing in the atomic vapour.

The SFM nonlinear optical process can also be interpreted from a photon model, rather than interacting waves. This is shown in Figure 1.2 where two fundamental photons of energy  $\hbar\omega_1$  and  $\hbar\omega_2$  are combined by the nonlinear medium to create a single photon with an energy equal to the sum of the fundamental photon energies.

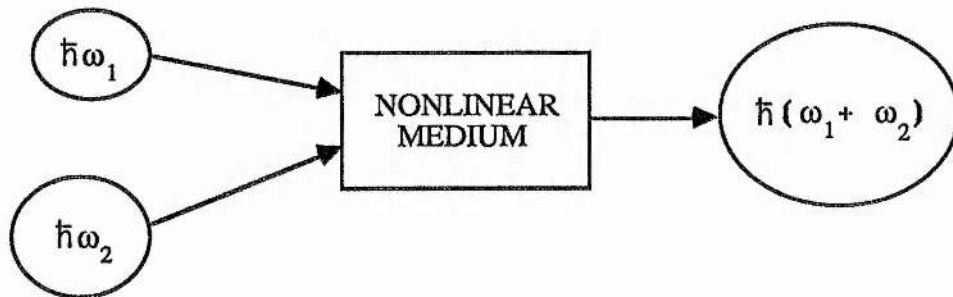


Figure 1.2 : Schematic photon picture of SFM.

#### 1.4 PHASE MATCHING

An important consideration in all nonlinear optical effects is the phase matching of the

fundamental and generated waves in the nonlinear medium [3]. Lack of phase matching leads to destructive interference between the different parts of the generated wave (originating from different parts of the induced nonlinear polarisation) as it propagates through the medium and less net nonlinear power is generated. For collinear plane waves, phase matching is perfectly satisfied when

$$\Delta k = k_3 - k_1 - k_2 = 0 . \quad (1.4.1)$$

The dependence of the power of the generated sum frequency wave on the phase mismatch  $\Delta k$  is discussed in §5.2.

In bulk nonlinear crystals, the birefringence of the material can be used to perfectly phase match the nonlinear optical process since different polarisations of the light waves can experience the same refractive index in the crystal to give  $\Delta k = 0$ . Angle or temperature tuning of the crystal refractive indices can be used to satisfy phase matching.

In an atomic vapour, the refractive index experienced by the interacting waves is determined by the frequency detuning of the waves from natural atomic resonances and the population distribution among the atomic energy levels. The effects of the fundamental wave frequency on the phase-matching behaviour of three-wave SFM is discussed in Chapter 5 where the nonlinear SFM process is two-photon but not single photon resonant. Focusing the fundamental laser beams into the nonlinear atomic medium is shown to affect the detailed nature of the phase-matching. In Chapter 6, the role of intermediate atomic state populations is considered and the high resolution SFM line profiles are shown to be modified by complicated frequency dependent refractive index and phase matching variations.

## 1.5 SYMMETRY BREAKING TECHNIQUES TO INDUCE $\chi^{(2)}$ NONLINEAR OPTICAL PROCESSES IN ATOMIC VAPOURS

Four techniques have been successfully demonstrated for inducing  $\chi^{(2)}$  nonlinear optical effects in otherwise isotropic media such as atomic vapours. These are briefly described below with emphasis on previous studies concerning SFM or DFM which are

relevant to the work presented here. A comprehensive review of symmetry breaking methods which have been used in  $\chi^{(2)}$  nonlinear optical studies up to 1987 can be found in reference 14.

### 1.5.1 Transverse DC Electric Field

Application of a static transverse electric field to the atomic vapour has two main effects on  $\chi^{(2)}$ . The first is that the electric field perturbs the eigenfunctions of the atom and mixes atomic states of opposite parity [15, 16]. If the electric field is weak then second order perturbation theory can be used to give

$$\varepsilon(\alpha JM) = \varepsilon_0(\alpha J) + |E_0|^2 \sum_{\alpha', J'} \frac{|\langle \alpha' J' m | er | \alpha J m \rangle|^2}{\varepsilon(\alpha J) - \varepsilon(\alpha' J')} \quad (1.5.1)$$

$$\Psi(\alpha JM) = \psi(\alpha JM) - |E_0| \sum_{\alpha', J'} \frac{\langle \alpha' J' m | er | \alpha J m \rangle}{\varepsilon(\alpha J) - \varepsilon(\alpha' J')} \psi(\alpha' J' m) \quad (1.5.2)$$

where  $\varepsilon(\varepsilon_0)$  is the energy level of the perturbed (unperturbed) atomic state  $|\alpha J M\rangle$ ,  $\Psi(\psi)$  is the perturbed (unperturbed) atomic wavefunction and  $E_0$  is the static transverse electric field. The wavefunction mixing by the electric field allows all three dipole matrix elements in equation (1.3.1) to be non-zero and thus  $\chi^{(2)}$  can be finite. The second effect of the electric field is to impose a transverse quantisation axis in the atomic vapour. Conservation of photon angular momentum is possible in this direction and so collinear three-wave mixing nonlinear optical effects become allowed.

The application of the external electric field can also be interpreted as inducing a  $\chi^{(3)}$  four wave mixing process where the two input optical waves couple with the zero frequency external field to generate an optical sum frequency wave through the nonlinear polarisation

$$P(\omega_3 = \omega_1 + \omega_2) \sim \varepsilon_0 \chi^{(3)}(\omega_1, \omega_2, 0) E_1(\omega_1) E_2(\omega_2) E_0. \quad (1.5.3)$$

Four wave mixing nonlinear optical effects are allowed in isotropic media. This  $\chi^{(3)}$  argument breaks down if the electric field dependence of the wavefunction mixing is complicated [17, 18] or if the mixing becomes independent of  $E_0$  at high electric field strengths [19].

Bethune et al [20] have studied the interference of electric field induced and

non-collinear (see §1.5.3) SFM to measure the quadrupole moment of the sodium 3S-4D atomic transition. The optical excitation frequencies  $\omega_1$  and  $\omega_2$  were chosen to be close to the Na 3S-3P and 3P-4D dipole transitions respectively to resonantly enhance  $\chi^{(2)}$ . The two input laser beams were crossed at a small angle between two electrodes in the Na oven to form a non-collinear geometry. The transverse electric field contribution to the induced polarisation in the atomic vapour was

$$\begin{aligned}
 P(\omega_3) \sim \frac{N}{\hbar^2} \left[ \sum_n \left\{ \frac{\langle 3S | er | nP \rangle \langle nP | er | 4D \rangle}{\hbar(\omega_{np} - \omega_3)} \right. \right. \\
 \left. \left. + \frac{\langle nP | er | 4D \rangle \langle 3S | er | nP \rangle}{\hbar\omega_{np}} \right\} E_0 \right] \frac{\langle 4D | er | 3P \rangle \langle 3P | er | 3S \rangle}{(\omega_1 - \omega_{3P})(\omega_3 - \omega_{4D} + i\Gamma)} E_1 E_2
 \end{aligned}
 \tag{1.5.4}$$

where  $E_1(\omega_1)$  and  $E_2(\omega_2)$  are the fundamental optical electric fields,  $E_0$  is the external field, and  $\Gamma$  is the relaxation rate of the Na 4D atomic state.

Abrams et al studied electric field induced DFM both theoretically [17] and experimentally [18] in the molecular gas  $\text{NH}_2\text{D}$ . A single frequency cw  $\text{CO}_2$  laser at  $\lambda = 10.6 \mu\text{m}$  was mixed with a 4 GHz microwave source to generate a single sideband at the difference frequency. In addition to allowing the DFM nonlinear process to occur, the static transverse electric field of  $\sim 350 \text{ V cm}^{-1}$  was used to Stark shift the molecular energy levels for additional resonant enhancement of the DFM.

The most detailed study to date of an electric field induced SFM nonlinear optical process has been carried out by Boyd and co-workers in Na vapour [19, 20, 21]. Their excitation scheme was similar to Figure 1.1 where the atomic state  $|i\rangle$  was the  $3S_{1/2}$  ground state,  $|j\rangle$  was the  $3P_{3/2}$  first excited state and  $|k\rangle$  was a high lying Rydberg level of the sodium atom. A theoretical calculation assumed that the Rydberg levels were hydrogenic with linear rather than quadratic Stark shifts. The calculation of the second order susceptibility  $\chi^{(2)}$  under these conditions showed that the expected value should be  $\sim 55.7 \text{ pm V}^{-1}$  which is several hundred times greater than the nonlinear susceptibility of a good nonlinear crystal such as potassium dihydrogen phosphate (KDP). A subsequent experimental investigation used two

excimer pumped pulsed dye lasers as the source of the fundamental radiation. The pulse energies were typically 0.5 mJ with linewidths of  $\sim 5$  GHz and durations of  $\sim 4$  ns. Laser frequency  $\omega_1$  was tuned close ( $\Delta\nu \sim 5$  GHz) to the sodium  $3S_{1/2} - 3P_{3/2}$  single photon transition at 590 nm for resonant enhancement of  $\chi^{(2)}$ . The second laser frequency  $\omega_2$  was tuned from  $\sim 420$ - $427$  nm to be on resonance with the 11P-14S Rydberg levels of Na. The measured value of  $\chi^{(2)}$  was only  $\sim 10$  times larger than that of KDP due to the relatively small applied electric field strength ( $\sim 1500$  V cm $^{-1}$ ) and the approximated hydrogenic behaviour of the sodium energy levels. Further study with higher transverse electric field strengths ( $\sim 2000$  V cm $^{-1}$ ) showed that the SFM became almost continuously tunable due to complete mixing of the Stark shifted Rydberg levels. Tuning  $\omega_1$  close to but not onto resonance with the 3S-3P D line single photon transition was shown to be crucial in obtaining a good conversion efficiency. The SFM process was not phase matched but a maximum energy conversion efficiency of  $\sim 3 \times 10^{-4}$  was obtained with  $\omega_1$  detuned by  $\sim 30$  GHz from the D line resonance and  $\omega_1 + \omega_2$  on resonance with the 13S Rydberg level.

### 1.5.2 High Power Laser Pulses

Even if no external fields are applied to the vapour to break the symmetry, three-wave mixing has been demonstrated many times in isotropic atomic media by using high power laser pulses as the source of the fundamental radiation [eg. 22, 23, 24, 25, 26]. Some controversy over the physical mechanism of this symmetry breaking technique exists. One fairly consistent explanation is that the  $\chi^{(2)}$  nonlinear optical process becomes allowed due to local radial electric fields at the focus of the fundamental laser beam [27, 38]. These electric fields are produced by photoelectrons which are generated by multiphoton ionisation and the electric field acts in a similar manner to the static field discussed in the previous section.

However, unexplained deviations from this argument have been observed [26, 29] which might be attributed to spatial variations in the atomic ground state density or collisional effects being of importance.

Most of these studies concerned SHG and two-photon resonant enhancement of the nonlinear optical process was utilised. With high power excitation, the classical selection rules

for atomic transitions are not longer valid, allowing SHG between atomic S states for which no multiple transition exists [30]. Other optical parametric processes can also be driven in the atomic vapour under high power excitation [31].

### 1.5.3 Non-Collinear Beam Excitation

The photon angular momentum conservation law prevents collinear three-wave mixing in an isotropic medium. By arranging the two fundamental beams to be non-collinear with wavevectors  $\mathbf{k}_1$  and  $\mathbf{k}_2$ , there is an angular momentum component along the quantisation direction  $\mathbf{k}_1 + \mathbf{k}_2$  which is zero and this allows conservation of angular momentum among the three interacting waves. This non-collinear geometry thus breaks the symmetry of an atomic vapour and forward generation of the sum frequency wave is possible [32].

Bethune et al [32, 33, 34, 20] have studied this symmetry breaking method in detail, using two pulsed dye lasers to generate SFM in sodium vapour. Resonant enhancement of  $\chi^{(2)}$  was obtained by tuning  $\omega_1$  close to the Na 3S-3P resonance and  $\omega_1 + \omega_2$  on resonance with the 3S-4D two-photon transition. The induced nonlinear optical polarisation for non-collinear excitation was

$$\begin{aligned}
 P(\omega_3 = \omega_1 + \omega_2) \sim & -i(\mathbf{k}_1 + \mathbf{k}_2) \frac{N}{\hbar^2} \sum_{3P} \frac{\langle 3S | \mathbf{err} | 4D \rangle \langle 4D | \mathbf{er} | 3P \rangle \langle 3P | \mathbf{er} | 3S \rangle}{(\omega_1 - \omega_{3P})(\omega_3 - \omega_{4D} + i\Gamma)} \\
 & \times E_1(\omega_1) E_2(\omega_2) \quad (1.5.5)
 \end{aligned}$$

SFM is a maximum when  $E_1$  is perpendicular to  $E_2$  and one of them lies in the plane of  $\mathbf{k}_1$  and  $\mathbf{k}_2$ . Phase matching of the nonlinear optical process was achieved by compensating the natural dispersion of the sodium vapour with the intersection angle of the two fundamental beams. This second order dipole-forbidden SFM was as strong as a third-order dipole allowed process such as THG.

Limiting effects on the generated SFM power were also considered [33]. At high atomic densities, the linear absorption of the laser beam at  $\omega_1$  reduced the SFM power, even for relatively large single photon detunings of  $\sim 50 \text{ cm}^{-1}$ . Saturation of the enhancing two-photon absorption limited the SFM power above a fundamental beam power product of

$\sim 10^9 \text{ W}^2 \text{ cm}^{-4}$ . The high pump power intensities also induced refractive index changes in the sodium vapour through saturation of the single and two-photon resonances. This broke the phase matching to make  $\Delta k \neq 0$  with a corresponding decrease in SFM power. Self-defocusing was also evident which decreased the optical intensities at the focus of the input laser beams. The multiphoton ionisation process was estimated to be insignificant with a fractional ionisation of only  $\sim 1\%$  with their highest available fundamental intensities of  $\sim 0.5 \text{ MW cm}^{-2}$ .

#### 1.5.4 *Transverse DC Magnetic Field*

The application of a static transverse magnetic field to an atomic vapour has a similar symmetry breaking effect to a static electric field. In this case the magnetic field perturbs and mixes the wavefunctions of the Zeeman sublevels within an atomic state but the parity of the states remains unchanged. A multipole transition moment, usually an electric quadrupole, must be used in the nonlinear optical process to complete the chain of matrix elements forming  $\chi^{(2)}$ . Photon angular momentum is conserved since the transverse magnetic field defines a quantisation axis in the atomic vapour which is perpendicular to the optical waves. This is the symmetry breaking technique considered in this thesis to induce three-wave SFM in sodium vapour.

Flusberg et al [35] were the first investigators to report a magnetic field induced, collinear three-wave mixing nonlinear optical process. DFM was studied in atomic thallium vapour where the two input pulsed laser beams at 378 nm and 535 nm were chosen to lie close to the  $6P_{1/2} - 7S_{1/2}$  and  $6P_{3/2} - 7S_{1/2}$  atomic dipole transitions for resonant enhancement of  $\chi^{(2)}$ . Parametric emission of the 1280 nm DFM radiation occurred on the  $6P_{3/2} - 6P_{1/2}$  magnetic dipole transition rather than via an electric quadrupole. The induced magnetisation in the vapour was

$$M = N [\alpha E_1 (E_2^* \cdot H) + \beta E_2^* (E_1 \cdot H) + \gamma H (E_1 \cdot E_2^*)] \quad (1.5.6)$$

where  $N$  is the atomic particle density,  $\alpha$ ,  $\beta$  and  $\gamma$  are related to the atomic matrix elements and laser detunings from atomic resonances,  $E_{1,2}$  are the electric fields of the fundamental optical

beams and  $\mathbf{H}$  is the transverse magnetic field. They confirmed experimentally that the DFM power varied as  $N^2 H^2 P_1 P_2$ , where  $P_1$  and  $P_2$  were the powers of the fundamental beams, and that no DFM was produced with a longitudinal magnetic field. In their analysis, they incorrectly proposed that the symmetry breaking effect of the magnetic field was due to the mixing of hyperfine levels. This was shown to be incorrect by Matsuoka et al [36] who demonstrated that magnetic field induced SHG was possible in calcium vapour. Calcium has no hyperfine atomic structure, it was the mixing of the magnetic sublevels by the transverse magnetic field which allowed SHG to take place.

Three-wave SFM was investigated in sodium vapour using both non-collinear beams and a transverse magnetic field to remove the isotropy of the atomic vapour [37, 38]. Destructive or constructive interference between the sum-frequency waves generated by each symmetry breaking method was observed, depending upon the relative direction of the transverse magnetic field to  $\mathbf{E}_1$  or  $\mathbf{E}_2$ . The sum frequency powers generated by each mechanism were comparable at magnetic field strengths of  $\sim 30$  G. Magnetic field induced SHG has also been reported in thallium vapour by the same authors [39].

The studies of magnetic-field induced, three-wave mixing nonlinear optical processes which are most relevant to the work presented here have been by Matsuoka et al [36, 40, 41], Dunn [42] and Sinclair and Dunn [43, 44] who all used sodium vapour as the nonlinear medium. Their studies of magnetic field induced SHG has led to a detailed understanding of the microscopic and macroscopic properties of the nonlinear optical process.

Matsuoka et al have established a microscopic model for the symmetry breaking action of the transverse magnetic field. In the absence of the applied field, the fundamental optical wave induces a two-photon absorption [45] between energy states of the atomic medium. This creates quadrupole moments which oscillate at twice the frequency of the original optical wave but which radiate transversely to the fundamental optical beam. When a transverse magnetic field is applied, the induced quadrupole moments are rotated by magnetic sublevel eigenfunction mixing and a component can now radiate in the propagation direction of the fundamental optical field. This allows a net, coherent second harmonic wave to be produced. The induced rotated quadrupole moments can be regarded as two "effective dipoles" which are

perpendicular to each other and to the fundamental beam as shown in Figure 1.3. The relative magnitude and phase of these dipoles determines the amplitude and polarisation of the second harmonic wave.

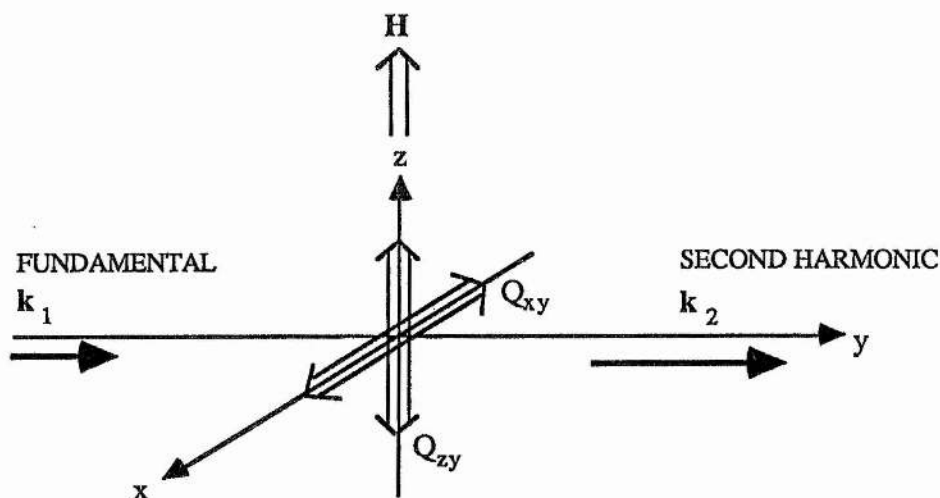


Figure 1.3 : Effective dipoles  $Q_{xy}$  and  $Q_{zy}$  which generate the second harmonic wave at frequency  $2\omega = k_2c$ .

Sinclair and Dunn have used a cw, single-mode laser to examine the microscopic behaviour of the effective dipoles  $Q_{xy}$  and  $Q_{zy}$  in detail. Excellent agreement was obtained between experimental results and theory which included homogeneous/ inhomogeneous broadening, laser polarisation/frequency and atomic transitions/ selection rules. This behaviour is discussed in the following chapter.

As an extension to this recent work on SHG, this thesis describes the study of cw, high resolution SFM in sodium vapour with the  $\chi^{(2)}$  nonlinearity induced with a transverse magnetic field.

Two fundamental cw laser beams of different frequency were used to excite the Na 3S-4D two-photon transition as shown in Figure 1.4. The laser systems and ancillary experimental equipment used in this study are described in Chapter 3.

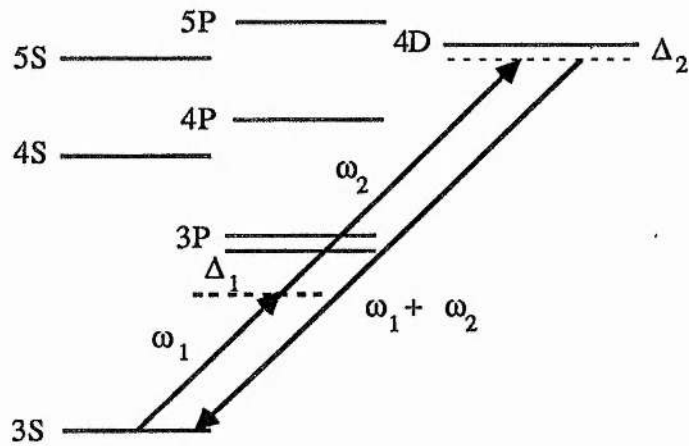


Figure 1.4 : Schematic diagram of the sodium energy levels and frequencies involved in the SFM effect.

The investigation of SFM is divided into two areas, depending upon the detuning of laser frequency  $\omega_1$  from the Na 3S-3P single photon D line resonances:

(i)  $\Delta\omega_1 > \Delta\omega_D$ , the 3S-3P Doppler width :- In this case, the SFM nonlinear optical effect is two-photon but not single photon resonant so that no atomic population is transferred to the intermediate P states. This situation is analogous to the previous SHG study. In Chapter 5, the microscopic behaviour of the SFM is shown to be identical to SHG as expected. However, the bulk macroscopic phase matching of the SFM differs from SHG because the wavelengths of the two fundamental waves can be varied. The refractive index of the sodium vapour is wavelength dependent and so the phase mismatch  $\Delta k$  can be changed. In particular the sign of  $\Delta k$  can be controlled to be positive or negative, depending on  $\Delta_1$ , so that the variation of SFM power with atomic density displays asymmetric effects due to the focusing parameters of the Gaussian laser beams [46]. Phase matching techniques for nonlinear optical effects in atomic vapours are reviewed and it is shown that SFM in sodium vapour can be optimally phase matched at all atomic particle densities by tuning  $\omega_1$  between the D<sub>1</sub> and D<sub>2</sub> line resonances.

(ii)  $\Delta\omega_1 < \Delta\omega_D$  :- When  $\omega_1$  is tuned within the 3S-3P single photon transition Doppler width, the SFM process becomes simultaneously single photon and two-photon resonant. The

microscopic and macroscopic behaviour of SFM under these conditions is quite different from the previous case and this is discussed in Chapter 6.

The influence of resonant single photon transitions on nonlinear optical processes in atomic vapours has not previously been studied. Tuning  $\omega_1$  close to or on single photon resonance has the benefit of increasing the probability of two-photon absorption by several orders of magnitude [47]. This has previously been considered in the context of two-photon spectroscopy [48] where excited state populations rather than induced atomic coherences are of interest. In Chapter 6, a detailed experimental study of magnetic field induced SFM with a resonant intermediate state is presented using two cw, narrow linewidth dye lasers as the sources of the fundamental radiation. The microscopic behaviour is shown to be complicated by several processes such as velocity selection, optical pumping and collisional effects. Moderate laser powers on resonance induce saturation of the single and two-photon resonances such that a perturbative theory of the simultaneously resonant SFM effect may not be always applicable. Chapter 2 discusses the theory of two coupled Doppler broadened atomic transitions from the viewpoint of inducing atomic coherences as well as reviewing the non-resonant SFM and SHG microscopic theory. Macroscopic effects due to phase matching became unavoidable with single photon resonance due to the optically induced movement of atomic population in the atomic levels and subsequent refractive index variations.

With appropriate control over single photon detunings and the atomic refractive index, significant SFM powers can be generated using the vapour as a nonlinear medium. The effective nonlinearity of the vapour can exceed that of a good bulk nonlinear crystal. This offers the possibility of using atomic vapours as true practical devices for UV and VUV generation.

## **1.6 RELATED AREAS OF STUDY**

The use of on-resonance single photon atomic transitions for the first time in magnetic field induced SFM required an accurate measurement of the Na 3P state Zeeman splittings to be made. The sodium 3S-3P hyperfine Zeeman spectrum was investigated using the nonlinear

laser spectroscopic technique of saturated absorption spectroscopy [49], which has not been previously applied to a study of Zeeman spectra. This is discussed in Chapter 4 where obtained spectra are presented using a novel experimental method which increased the obtainable resolution in a spectrum. Velocity changing collisions reduce the resolution which can be achieved in the spectrum. Limitations on interpreting the Zeeman spectrum are shown to arise due to the large number of non-degenerate atomic transitions and associated cross-over resonances.

A novel technique for breaking the symmetry of an atomic vapour and allowing a  $\chi^{(2)}$  nonlinear optical process to take place is considered in Chapter 7. A resonant, polarised light wave can be used to optically pump the ground state of an atomic vapour into an oriented rather than random spin direction [50]. If a large transverse background orientation of the atoms can be produced then this can act as a nonlinear medium for a three-wave nonlinear optical process [51], in a similar manner to an applied transverse magnetic field. A theoretical and experimental investigation of using optical pumping in sodium vapour to create a nonlinear medium for SHG is presented.

# **CHAPTER 2**

## **THEORY**

## Chapter 2

### THEORY

In this chapter, some aspects of the theory of magnetic field induced SFM are discussed. The perturbing effect of the external magnetic field on the atomic energy levels and wavefunctions of the sodium atoms is described in §2.1 and this serves as an introduction to the review of the microscopic theory of SFM/SHG with a non-resonant intermediate state in §2.2. A semiclassical model of a cascade three level atomic system interacting with two resonant light waves is developed in §2.3. Some new aspects of this theoretical model which are relevant to SFM with a resonant intermediate state, such as atomic coherences and refractive index, are illustrated.

#### 2.1 EIGENSTATES AND EIGENENERGIES OF THE SODIUM ATOM IN AN EXTERNAL MAGNETIC FIELD

##### 2.1.1 *3S States*

The  $3S_{1/2}$  ground state of sodium contains two non-degenerate sublevels, even in the absence of an applied magnetic field, due to the hyperfine interaction of the nuclear magnetic moment  $\mu_I = -g_I \mu_B I$  with the magnetic field produced at the nucleus by the orbiting electrons [51]. This atomic coupling is fully described in many texts on atomic physics [52].

The nuclear spin of sodium is  $I = 3/2$  and the nuclear g factor  $g_I = -0.0008$ . The electronic angular momentum  $J$  is coupled to the nuclear spin  $I$  and the total atomic angular momentum  $F$  is the sum of these two components. The hyperfine energy shifts of the  $F = 1$  and  $F = 2$  levels of the  $3S_{1/2}$  ground state produced by the interaction is

$$\Delta E_s(F) = \frac{A}{2} [ F(F+1) - I(I+1) - J(J+1) ]. \quad (2.1.1)$$

This frequency separation is 1771.6261288(10) MHz for the sodium ground state, the hyperfine constant  $A/h$  is half of this value.

The degeneracy of the hyperfine magnetic substates is lifted by the application of an external magnetic field  $B$ . This is the well known Zeeman effect. In low magnetic fields ( $\mu_B B \ll A/2$ ) the energies of the magnetic sublevels shift linearly in energy according to

$$\Delta E_s (F, m_F) = g_F \mu_B B m_F \quad (2.1.2)$$

where  $g_F$  is the effective hyperfine  $g$ -factor,  $\mu_B$  is the Bohr magneton,  $B$  is the magnetic field strength and  $m_F$  is the quantised projection of  $F$  on the magnetic field direction. In high magnetic fields ( $\mu_B B \gg A/2$ ) the coupling of  $I$  and  $J$  is broken and the hyperfine interaction is a small perturbation on the Zeeman effect. The absolute energy levels of the magnetic substates are then given by

$$E_s (I, J, m_I, m_J) = A m_I m_J - \frac{\mu_J B m_J}{J} - \frac{\mu_I B m_I}{I} \quad (2.1.3)$$

where  $m_I$  and  $m_J$  are the projections of  $I$  and  $J$  on  $B$  and  $\mu_J$  ( $\mu_I$ ) is the electronic (nuclear) magnetic moment. Since  $|\mu_J| \gg |\mu_I|$ , the energy levels approximately shift linearly with  $m_J$ . This is the Paschen-Back regime. With intermediate magnetic field strengths ( $\mu_B B \approx A/2$ ) neither the hyperfine or Zeeman interaction dominates and the eigenenergies are found from the solution of a secular equation. For  $J = \frac{1}{2}$  states, such as the  $3S_{1/2}$  ground state of sodium, the eigenenergies can be found from the Breit-Rabi formula [53].

$$\Delta E_s (F, m_F) = -\frac{A}{(2I+1)} - g_I \mu_B B m_F \pm A \left[ 1 + \frac{4 m_F}{2I+1} x + x^2 \right]^{\frac{1}{2}} \quad (2.1.4)$$

where

$$x = \frac{2 (g_J + g_I) \mu_B B}{A} \quad (2.1.5)$$

The electronic  $g$ -factor  $g_J$  is equal to 2.002 for the  $3S_{1/2}$  state. The upper sign in equation (2.1.4) corresponds to the magnetic substates belonging to the  $F = I + \frac{1}{2}$  hyperfine level and the lower sign to those of the  $F = I - \frac{1}{2}$  level.

A plot of the frequency (energy) of the hyperfine magnetic energy levels of the

sodium  $3S_{1/2}$  state against applied magnetic field strength is shown in Figure 2.1.

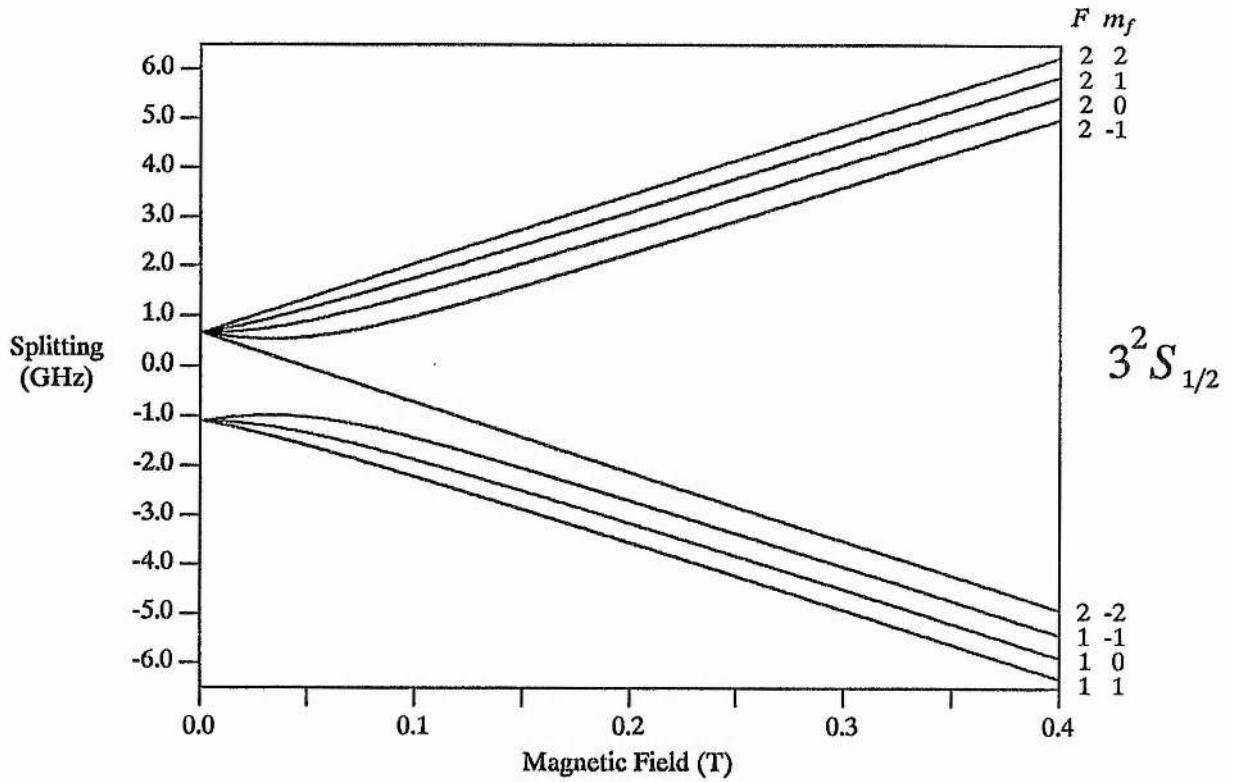


Figure 2.1 : Energy levels of the Na 3S states as a function of magnetic field strength.

The wavefunctions of the 3S states can be expressed in the  $|l s I m_l m_s m_I\rangle$  basis as

$$\begin{aligned}
 |S_F^{m_F}\rangle = & S_A(F, m_F, B) |0 \frac{1}{2} \frac{3}{2} 0 \frac{1}{2} m_F - \frac{1}{2}\rangle \\
 & + S_B(F, m_F, B) |0 \frac{1}{2} \frac{3}{2} 0 -\frac{1}{2} m_F + \frac{1}{2}\rangle .
 \end{aligned}
 \tag{2.1.6}$$

The coefficients  $S_A$  and  $S_B$  of the spin up and spin down states are dependent upon the atomic hyperfine state and the strength of the applied magnetic field. Explicit expressions for these coefficients have been given by Uchiki et al [41] and Sinclair [14].

### 2.1.1.2 3P States

The 3P states of atomic sodium are composed of two fine structure states of different J

value. The  $3^2P_{1/2}$  and the  $3^2P_{3/2}$  states are separated in zero external magnetic field by  $\sim 17.2 \text{ cm}^{-1}$  and the fine structure interaction energy is  $2/3$  of this value. Transitions between these excited sodium states and the  $3S_{1/2}$  ground state give rise to the well known sodium  $D_2$  and  $D_1$  lines of wavelength  $588.995 \text{ nm}$  and  $589.592 \text{ nm}$  respectively.

Normally in magnetic field induced SFM/SHG in sodium vapour, the detuning of laser frequency  $\omega_1$  or  $\omega_2$  from the  $3P$  states is much greater than either the  $3S$ - $3P$  Doppler width or the magnetic splittings of the  $3P$  states. In this case, the magnetic splittings of these states can be disregarded. However, when the SFM nonlinear optical process is single photon resonant as discussed in Chapter 6, the magnetic splittings of the  $3P$  states and the associated laser detunings became important. Chapter 4 is a study of the Zeeman spectrum of the sodium  $3S$ - $3P$  transition using saturated absorption spectroscopy.

The lower energy  $3P_{1/2}$  excited state is split into two hyperfine components in zero magnetic field in an analogous manner to the  $3S_{1/2}$  ground state. The hyperfine interaction energy is  $h \times 94.3 \pm 0.1 \text{ MHz}$  and the frequency separation of the  $F = 1$  and  $F = 2$  hyperfine levels is twice this value. The energy splittings of the hyperfine magnetic sublevels with an applied magnetic field can also be described by the analytic Breit-Rabi formula using the  $3P_{1/2}$  interaction constants and the  $g_j$  value of  $2/3$ . The magnetic splittings of the hyperfine sublevels of the  $3P_{1/2}$  state are shown in Figure 2.2.

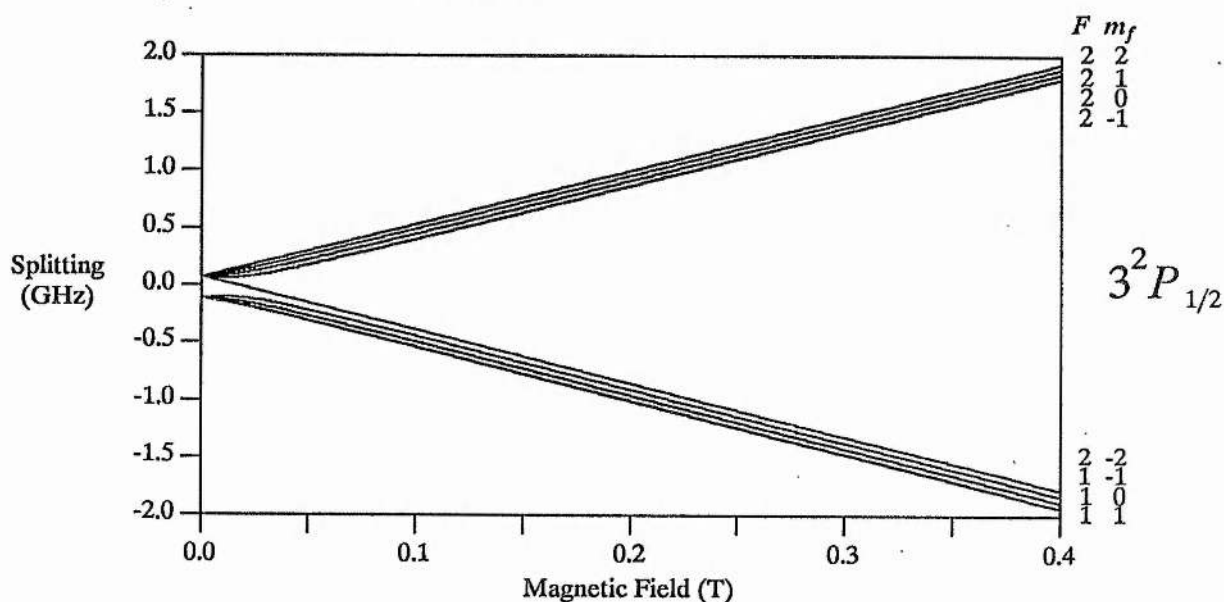


Figure 2.2 : Energy levels of the Na  $3P_{1/2}$  state as a function of magnetic field strength.

The higher energy  $3P_{3/2}$  sodium state is also influenced by the nuclear coupling and has a hyperfine structure. The  $J = 3/2$  state is not spherically symmetric and so the nuclear quadrupole moment must be included in a calculation of the energy eigenstates. With no applied magnetic field, the energies of the  $F = 0, 1, 2, 3$  hyperfine states are given by

$$E_P(F) = \frac{A'}{2} \kappa + \frac{B}{4} \frac{3/2 \kappa(\kappa+1) - 2I(I+1) J(J+1)}{I(2I-1) J(2J-1)} \quad (2.1.7)$$

where  $A'$  is the dipole constant ( $A' \equiv 18.69 \pm 0.09$  MHz),  $B$  is the quadrupole constant ( $B \equiv 2.90 \pm 0.21$  MHz) and  $\kappa = F(F+1) - I(I+1) - J(J+1)$ . The  $3P_{3/2}$  hyperfine structure in zero magnetic field is shown in Figure 2.3

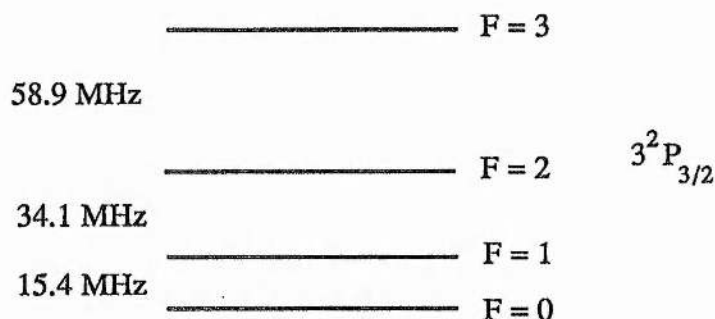


Figure 2.3 : Hyperfine structure of the Na  $3P_{3/2}$  state in zero magnetic field.

The influence of a transverse magnetic field on these hyperfine states is more complicated than for the  $3P_{3/2}$  states due to the additional quadrupolar contribution. In very low strength magnetic fields ( $\mu_B B \ll A', B$ ) the splitting of the hyperfine magnetic sublevels is linear and is given by equation (2.1.2). This approximation is not valid in sodium for magnetic field strengths of the order of  $\sim 15$  G. The energy eigenstates can be found at higher magnetic field strengths from a secular equation but no analytical solution is possible for a  $J = 3/2$  state. Since the hyperfine coupling is relatively weak, it can be neglected for magnetic field strengths above a few tens of Gauss. The magnetic energy levels of the  $3P_{3/2}$  state then split linearly in a magnetic field according to the value of  $m_J$  as shown in Figure 2.4. The splittings are given by

$$\Delta E_p(m_j) = g_J \mu_B B m_j \quad (2.1.8)$$

where the  $g_J$  value is  $4/3$  for the  $3P_{3/2}$  state.

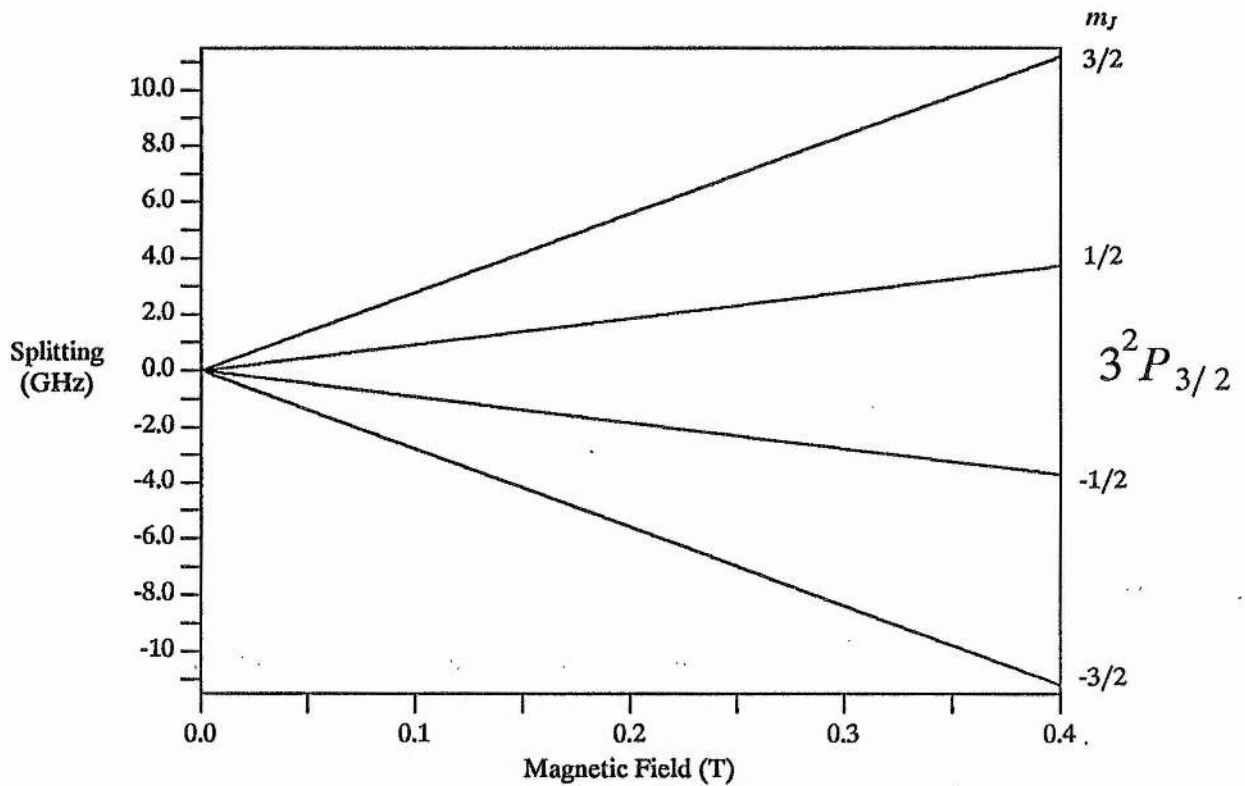


Figure 2.4 : Energy levels of the  $3P_{3/2}$  state as a function of magnetic field strength with the hyperfine interaction neglected.

### 2.1.3 4D States

The 4D state of atomic sodium contains the two non-degenerate  $4D_{3/2}$  and  $4D_{5/2}$  fine structure states. The position of these states is inverted so that the  $4D_{5/2}$  level has a lower energy than the  $4D_{3/2}$  level [54]. In the absence of a magnetic field, the frequency separation between the fine structure states has been measured as  $1028.3 \pm 0.6$  MHz by two-photon or level crossing spectroscopy [55, 56]. The fine structure constant  $\gamma$  is  $-411.3 \pm 0.2$  MHz which is  $2/5$  of this frequency separation. The hyperfine splitting of the 4D states is extremely small since the 4D wavefunctions do not interact significantly with the atomic nucleus. The hyperfine splitting of the  $4D_{3/2}$  level has been measured as  $0.507 \pm 0.068$  MHz using a

quantum beat method. This is significantly less than the natural homogeneous width of  $\sim 3.1$  MHz and therefore the hyperfine splitting is negligible.

The splitting of the spin sublevels of the 4D states in an external magnetic field is of a similar form to the description of the hyperfine splitting of the  $3S_{1/2}$  ground state. In low strength magnetic fields, the energy splitting is linear with magnetic field strength, as given in equation (2.1.7) with  $g_J$  values of  $4/5$  for the  $4D_{3/2}$  state and  $6/5$  for the  $4D_{5/2}$  state.

In high magnetic fields, the energy level splittings are proportional to  $m_\ell + 2m_s$  where  $m_\ell$  and  $m_s$  are the electron orbital spin quantum numbers. The description of the eigenenergies in intermediate magnetic field strengths is treated by Condon and Shortley [57], Uchiki et al [41] and Sinclair [14]. The eigenenergies are

$$E \left( D_{5/2}^{\pm 5/2} \right) = (1 \pm 3y) \gamma \quad (2.1.9)$$

$$E \left( D_{5/2}^{m_J} \right) (m_J \neq \pm 5/2) = \left( -\frac{1}{4} + m_J y + \frac{1}{4} \left[ 4 y^2 + 8 m_J y + 25 \right]^{\frac{1}{2}} \right) \gamma \quad (2.1.10)$$

$$E \left( D_{3/2}^{m_J} \right) = \left( -\frac{1}{4} + m_J y - \frac{1}{4} \left[ 4 y^2 + 8 m_J y + 25 \right]^{\frac{1}{2}} \right) \gamma \quad (2.1.11)$$

where  $y = \mu_B B/\gamma$ .

The magnetic splitting of the 4D  $m_J$  levels is shown in Figure 2.5.

The eigenfunctions of the 4D states can also be expressed in the  $|\ell s m_\ell m_s\rangle$  basis as

$$\begin{aligned} |D_J^{m_J}\rangle &= D_A(J, m_J, B) |2 \frac{1}{2} m_J - \frac{1}{2} \frac{1}{2}\rangle \\ &+ D_B(J, m_J, B) |2 \frac{1}{2} m_J + \frac{1}{2} - \frac{1}{2}\rangle \end{aligned} \quad (2.1.12)$$

the expressions for the expansion coefficients are again given in [14, 41].

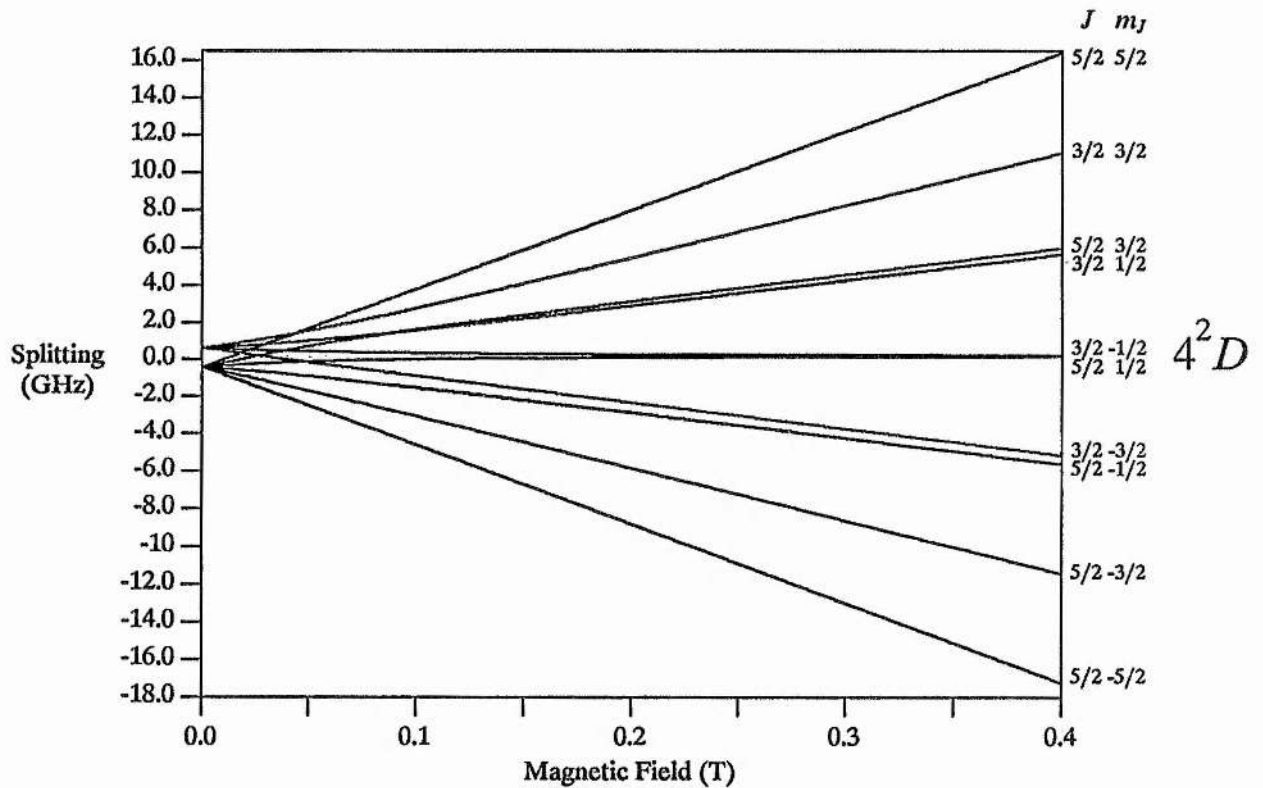


Figure 2.5 : Energy levels of the 4D states as a function of magnetic field strength.

## 2.2 MICROSCOPIC THEORY OF SHG

A detailed theoretical model of magnetic field induced SHG has been developed by Sinclair and Dunn [43] based on the treatment of Uchiki et al [41]. The model derives expressions for the microscopic quadrupole moments between the sodium 3S and 4D states coherently excited by cw two-photon absorption. A second-order perturbation calculation using the semiclassical density matrix approach was used. This calculation included all the details of the atomic parameters, the frequency and polarisation of the exciting laser field, the transverse magnetic field and the homogeneous and inhomogeneous damping of the induced coherence. As discussed in §1.5.4, the two induced quadrupole moments act as the effective dipoles

$$(P_x, P_z) = -\frac{i}{2} |k_2| (Q_{xy}, Q_{zy}) \quad (2.2.1)$$

to radiate the second harmonic wave. The cartesian geometry is defined for the magnetic field applied along the  $\hat{z}$  axis and the waves propagating collinearly along the  $\hat{y}$  axis. The calculated quadrupole moments are

$$\tilde{Q}_{xy} = -\frac{i e^2 r_{dp} r_{ps} Q_{sd} \rho_{ss} \epsilon_x^2}{20 \sqrt{3} \hbar^2 \Omega < \omega_{ps} - \omega - i\gamma_{ps} >} \sum_{J_d, m_d}^{F, m_F} (B_2 - B_{-2}) Z [(2\omega - \omega_{ds} + i\gamma_{ds}) / \Omega] \quad (2.2.2)$$

$$\tilde{Q}_{zy} = -\frac{i e^2 r_{dp} r_{ps} Q_{sd} \rho_{ss} \epsilon_x \epsilon_z}{20 \sqrt{3} \hbar^2 \Omega < \omega_{ps} - \omega - i\gamma_{ps} >} \sum_{J_d, m_d}^{F, m_F} 2 (B_1 - B_{-1}) Z [(2\omega - \omega_{ds} + i\gamma_{ds}) / \Omega] \quad (2.2.3)$$

and the intensity of the second harmonic (SH) radiation is given by

$$I_{SH} \propto \tilde{Q}_{xy} \tilde{Q}_{xy}^* + \tilde{Q}_{zy} \tilde{Q}_{zy}^* \quad (2.2.4)$$

The  $B_q$  spherical tensor elements contain the atomic selection rules and the mixing of the 3S and 4D state wavefunctions by the magnetic field B.

$$B_q = S_A^2 (F, m_F, B) D_A^2 (J_d, m_d, B) \delta (m_d - \frac{1}{2} + q) \\ + S_B^2 (F, m_F, B) D_B^2 (J_d, m_d, B) \delta (m_d + \frac{1}{2} + q) \quad (2.2.5)$$

where  $S_{A,B}$ ,  $D_{A,B}$  are the wavefunction expansion coefficients given in §2.1.1 and §2.1.3. The  $Q_{xy}$  quadrupole moment is driven by  $\Delta m_q = \pm 2$  transitions and the component of the laser polarisation perpendicular to the magnetic field direction. The  $Q_{zy}$  quadrupole moment is driven by  $\Delta m = \pm 1$  transitions and both the components of the laser polarisation perpendicular to and parallel to the magnetic field direction.

The terms  $r_{ij}$  and  $Q_{ij}$  are the reduced dipole and quadrupole matrix elements between the atomic states  $|i\rangle$  and  $|j\rangle$  [58]. The single photon resonance factor  $(\omega_{ps} - \omega - i\gamma_{ps})^{-1}$  is removed from the sum over 3S ( $F, m_F$ ) and 4D ( $J_d, m_d$ ) and replaced with an average value because the intermediate 3P states are well off resonance with the fundamental photon frequency and this term remains approximately constant with magnetic field and laser frequency.

Homogeneous damping of the induced S-D coherence due to collisions and spontaneous emission is accounted for by the relaxation rates  $\gamma_{ij}$ . Inhomogeneous broadening

due to the Doppler shifts of the atomic frequencies in the atomic vapour is expressed in the plasma dispersion function  $Z(a + ib)$  [59, 60] where

$$Z(a + ib) = \frac{1}{\sqrt{\pi}} \int_{-\infty}^{\infty} \frac{\exp(-t^2) dt}{t - (a + ib)} \quad (2.2.6)$$

With no applied magnetic field, the  $B_{2(1)}$  and  $B_{-2(-1)}$  tensor elements are equal when summed over the 3S and 4D substates and so no effective dipole exists to generate the SH radiation. A transverse magnetic field mixes the  $S_{A,B}$ ,  $D_{A,B}$  coefficients and changes the  $B_q$  elements to make the sum non-zero. This allows coherent SHG to take place. At low magnetic field strengths, both  $\tilde{Q}_{xy}$  and  $\tilde{Q}_{zy}$  are linearly proportional to  $B$  and so the second harmonic intensity increases as the square of the magnetic field strength. At higher magnetic fields of  $\sim 1$  kG, the mixing of the S and D wavefunctions saturates due to the decoupling of the atomic orbital and spin angular momentum, with a subsequent saturation in the SH intensity. The relative phasing of the two orthogonal effective dipoles generating the SH radiation also changes with magnetic field strength. The plane of polarisation of the SH light is rotated or becomes elliptically polarised depending upon the detuning of  $2\omega$  from the centre of the Doppler broadened two-photon absorption profile.

The resonant terms in  $\tilde{Q}_{xy}$  and  $\tilde{Q}_{zy}$ , which are encompassed in  $Z[(2\omega - \omega_{ds} + i\gamma_{ds}) / \Omega]$  are dependent on the magnetic field strength and the laser frequency. The contribution to the resonant enhancement of the SHG nonlinear optical process by any given atomic transition depends on the relative detuning of the SH frequency from the atomic resonance. The Zeeman shifting of the atomic transition frequencies can increase or decrease the degree of resonant enhancement for a fixed laser frequency.

### 2.3 THREE-LEVEL ATOM

In this section, a semiclassical model of a three-level atom interacting with two resonant light fields is discussed to illustrate some new features which are relevant to magnetic field induced SFM with a resonant intermediate state. The strong signal theory takes saturation into account, which has generally been neglected in previous theoretical treatments of coupled

Doppler broadened transitions [12, 49, 61, 62, 63, 64]. The saturation produces changes in the atomic populations and the refractive index experienced by the optical waves. The theory here evaluates the induced two-photon coherence, rather than the upper state population which is usually of interest in two-photon spectroscopy [65, 66, 67, 68, 69]. These studies have mainly concentrated on modelling the optically induced atomic populations rather than coherently coupled atomic states which are the driving terms for the nonlinear optical process of SFM. The importance of predicting such coherences in atomic systems has been shown by the interest in population trapping with a folded three-level atom configuration at two-photon resonance [70, 71, 72].

### 2.3.1 Semiclassical Model

Consider a cascade, three-level atomic system interacting with two light fields as shown in Figure 2.6.

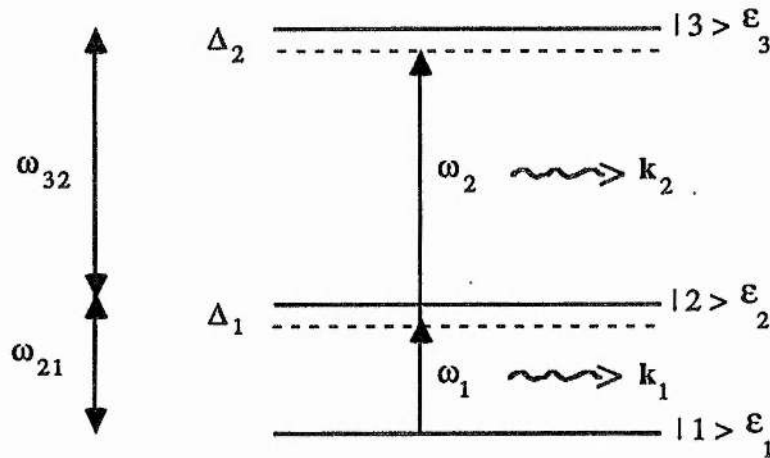


Figure 2.6 : Schematic three-level atom interacting with two coherent light fields of different frequency.

The three atomic states  $|1\rangle$ ,  $|2\rangle$  and  $|3\rangle$  have eigenenergies of  $\epsilon_1$ ,  $\epsilon_2$  and  $\epsilon_3$  ( $\epsilon_3 > \epsilon_2 > \epsilon_1$ ). The atomic resonant frequencies between these states when the atom is at rest are given by

$$\omega_{ij} = \frac{\epsilon_i - \epsilon_j}{\hbar} . \quad (2.3.1)$$

The inhomogeneously broadened atomic system interacts with two copropagating coherent light fields of frequency  $\omega_1$  and  $\omega_2$  ( $\omega_1 \neq \omega_2$ ) which have electric fields described by

$$E_i(z, t) = \frac{E_{i0}}{2} \exp [i (\omega_i t - k_i z)] + \text{c.c.} \quad i = 1, 2 \quad (2.3.2)$$

The laser frequencies  $\omega_1$  and  $\omega_2$  are close to the natural atomic resonances at frequencies  $\omega_{21}$  and  $\omega_{32}$  respectively, with the exact detunings of  $\omega_1$  from single photon resonance and  $\omega_1 + \omega_2$  from two-photon resonance as

$$\Delta_1 = \omega_{21} - \omega_1 + k_1 V_z \quad (2.3.3)$$

$$\Delta_2 = \omega_{31} - (\omega_1 + \omega_2) + (k_1 + k_2) V_z \quad (2.3.4)$$

where  $V_z$  is the velocity of a particular homogeneous atomic group viewed along the light propagation direction  $\hat{z}$ .

A density matrix treatment of this system can be used which is valid in all powers of the amplitudes of the two applied fields since each electromagnetic field can only induce transitions between one pair of atomic energy levels [67]. The time-dependent behaviour of the density matrix  $\rho$  is given by [2, 65]

$$i \hbar \dot{\rho} = [H, \rho] - \Gamma (\rho - \rho_0) \quad (2.3.5)$$

where  $\Gamma$  describes the relaxation of the density matrix and the Hamiltonian  $H$  is composed of the free atom Hamiltonian  $H_0$ ,

$$H_0 |i\rangle = \epsilon_i |i\rangle \quad (2.3.6)$$

and the electric dipole interaction Hamiltonian  $H_I$ ,

$$H_I = -\boldsymbol{\mu} \cdot \mathbf{E}(z, t) \quad (2.3.7)$$

where  $\boldsymbol{\mu}$  is the dipole moment of the atom. The electric dipole matrix elements between the three atomic states are defined as

$$\mu_{12} = \langle 1 | \boldsymbol{\mu} | 2 \rangle \neq 0, \quad (2.3.8a)$$

$$\mu_{23} = \langle 2 | \boldsymbol{\mu} | 3 \rangle \neq 0, \quad (2.3.8b)$$

$$\mu_{13} = \langle 1 | \boldsymbol{\mu} | 3 \rangle = 0. \quad (2.3.8c)$$

The Rabi frequencies [73] which describe the strength of the interaction of the light fields with

the atom are given by

$$\alpha = \frac{\mu_{12} E_1}{2\hbar} \quad (2.3.9)$$

and

$$\beta = \frac{\mu_{23} E_2}{2\hbar} . \quad (2.3.10)$$

The oscillations of the density matrix components at optical frequencies are removed by transforming the off-diagonal elements  $\rho_{ij}$  to the slowly varying operators  $\tilde{\rho}_{ij}$  where

$$\rho_{12} = \tilde{\rho}_{12} \exp [i (\omega_1 t + k_1 z)] , \quad (2.3.11)$$

$$\rho_{23} = \tilde{\rho}_{23} \exp [i (\omega_2 t + k_2 z)] , \quad (2.3.12)$$

$$\rho_{13} = \tilde{\rho}_{13} \exp [i (\omega_1 + \omega_2)t + (k_1 + k_2)z] . \quad (2.3.13)$$

Solving the time dependent equation (2.3.5) for the slowly varying operators  $\tilde{\rho}_{ij}$  and using the rotating wave approximation (RWA) to remove rapidly oscillating terms gives the system of equations

$$\dot{\rho}_{11} = i \alpha (\tilde{\rho}_{21} - \tilde{\rho}_{12}) - \Gamma_{11} (\rho_{11} - \rho_{11}^0) \quad (2.3.14a)$$

$$\dot{\rho}_{22} = i \alpha (\tilde{\rho}_{12} - \tilde{\rho}_{21}) + i \beta (\tilde{\rho}_{32} - \tilde{\rho}_{23}) - \Gamma_{22} (\rho_{22} - \rho_{22}^0) \quad (2.3.14b)$$

$$\dot{\rho}_{33} = i \beta (\tilde{\rho}_{12} - \tilde{\rho}_{32}) - \Gamma_{33} (\rho_{33} - \rho_{33}^0) \quad (2.3.14c)$$

$$\dot{\tilde{\rho}}_{12} = -i (\Delta_1 - i \Gamma_{12}) \tilde{\rho}_{12} + i \alpha (\rho_{22} - \rho_{11}) - i \beta \tilde{\rho}_{13} \quad (2.3.14d)$$

$$\dot{\tilde{\rho}}_{23} = -i (\Delta_2 - \Delta_1 - i \Gamma_{23}) \tilde{\rho}_{23} + i \beta (\rho_{33} - \rho_{22}) + i \alpha \tilde{\rho}_{13} \quad (2.3.14e)$$

$$\dot{\tilde{\rho}}_{13} = -i (\Delta_2 - i \Gamma_{13}) \tilde{\rho}_{13} - i \beta \tilde{\rho}_{12} + i \alpha \tilde{\rho}_{23} . \quad (2.3.14f)$$

The decay rates  $\Gamma_{ii}$  and  $\Gamma_{ij}$  describe the relaxation of the atomic populations (longitudinal) and the atomic coherences (transverse) respectively. The populations of the atomic levels under thermal equilibrium and in the absence of the applied light fields are given by  $\rho_{11}^0$ ,  $\rho_{22}^0$  and  $\rho_{33}^0$ . For moderate temperatures and optical transition frequencies, the thermal populations are

$$\rho_{11}^0 = 1, \quad \rho_{22}^0 = \rho_{33}^0 = 0 . \quad (2.3.15)$$

The set of complex equations (2.3.14 a-f) can be replaced by a real set by defining

$$\tilde{\rho}_{ij} = \text{Re } \tilde{\rho}_{ij} + i \text{Im } \tilde{\rho}_{ij} \quad (2.3.16)$$

$$\tilde{\rho}_{ij}^* = \tilde{\rho}_{ji} = \text{Re } \tilde{\rho}_{ij} - i \text{Im } \tilde{\rho}_{ij} . \quad (2.3.17)$$

The steady-state solution to the set of equations for  $\rho$ , which is desired for calculating the behaviour of the atom under cw laser excitation, can be found by setting all of the time derivatives equal to zero.

Analytical solutions to the steady-state equations have previously been derived [65] but the complexity of the solutions is such that little physical insight is gained from them. However, they should include all saturation effects due to both optical fields. A numerical solution to the set of equations is discussed in §2.3.3.

### 2.3.2 *Quantum Electrodynamical (QED) Model*

A QED model for the three-level atom under two-photon excitation is appropriate when the main relaxation mechanism of the atomic populations is by spontaneous/ stimulated emission [66]. This model is useful if the atoms under study are in an isolated system with no collisions, such as an atomic beam.

The QED model is formulated in terms of the Heisenberg equations of motion of the atomic operators  $\sigma$  [74] where

$$\sigma_{ij} = |i\rangle\langle j|. \quad (2.3.18)$$

The atomic operators are related to the density matrix elements by

$$\rho_{ji}(t) = \langle \sigma_{ij}(t) \rangle \quad (2.3.19)$$

where  $\langle \rangle$  denotes the expectation value. The optical fields are treated as quantised in the QED model with photon creation (destruction) operators  $a_\lambda^\dagger$  ( $a_\lambda$ ) of the field mode  $\lambda$ . This approach has the advantage that the generalised relaxation terms arise naturally from the calculations, rather than being added phenomenologically as in the semiclassical model [75]. In a multilevel atom, additional atomic state coherences can arise which would not be anticipated with a semiclassical model [74].

Interesting and unexpected results are predicted by a QED model of the three-level atom [66]. With the incident light intensity of the two optical fields several times above the saturation intensity, a steady-state population inversion can be generated between atomic states  $|2\rangle$  and  $|1\rangle$  or  $|3\rangle$  and  $|2\rangle$  in a homogenous atomic system [76], which could not be predicted from a rate equation analysis of the light/atom interaction.

### 2.3.3 Discussion of the Semiclassical Model

From a spectroscopic viewpoint, a calculation of the upper state population  $\rho_{33}$  is of interest since this determines the lineshape of the two-photon absorption signal as observed in fluorescence. This population term has been derived in several detailed analyses [48], but often with the situation of counter-propagating beams to reduce Doppler broadening or with equal frequency photons, neither of which is appropriate to SFM. In general, the population in the upper state of the three-level atomic system can be excited via two routes [77]:

$$\rho_{11} \xrightarrow{E_1} \rho_{12} \xrightarrow{E_1} \rho_{22} \xrightarrow{E_2} \rho_{23} \xrightarrow{E_2} \rho_{33} \quad (2.3.20)$$

$$\rho_{11} \xrightarrow{E_1} \rho_{12} \xrightarrow{E_2} \rho_{13} \xrightarrow{E_1} \rho_{23} \xrightarrow{E_2} \rho_{33} \quad (2.3.21)$$

The first of these routes passes through the intermediate state population  $\rho_{22}$  and can be regarded as a "two-step" or "stepwise" excitation of atomic population by the two light fields. The second route is the coherent two-photon excitation which does not involve any intermediate state population. Both of these excitation schemes contribute to the upper state population but in the absence of collisions, the two routes are indistinguishable. When the laser field at frequency  $\omega_1$  is detuned from single photon resonance, only the two-photon route can populate  $\rho_{33}$ .

Here, the interest is in the atomic coherence  $\rho_{13}$  between the upper and lower atomic states which drives the quadrupole moments in magnetic field induced SFM. It has previously been assumed that the  $\rho_{13}$  coherence vanishes in an inhomogeneously broadened three-level atom when both laser fields are resonant with the Doppler broadened atomic transitions and co-propagate along the same axis [12]. An integration over the velocity distributions of the atoms suggested that a folded level configuration was required to generate multipole radiation

via DFM and that SFM was not possible. In fact, the numerical calculation presented in §2.3.4 and the experimental results presented in Chapter 6 show that this assumption was incorrect.

To first order, the excitation of the two-photon atomic coherence only involves the optical fields  $E_1$  and  $E_2$  once:

$$\rho_{11} \xrightarrow{E_1} \rho_{12} \xrightarrow{E_2} \rho_{13} \quad (2.3.22)$$

The other higher order terms are dependent on the intermediate state or upper state populations and multiple orders of optical fields  $E_1$  or  $E_2$ . In magnetic field induced SFM, the expectation values of the quadrupole moments are found from  $\text{Tr}(\rho Q_{13})$  and are therefore proportional to  $|\rho_{13}|^2$ . This quantity is also numerically calculated in §2.3.4.

The other important factor of the three-level atomic model which is relevant to SFM is to calculate the refractive index experienced by the two fundamental optical waves. The dispersion of the generated wave on the  $|3\rangle \rightarrow |1\rangle$  quadrupole transition is assumed to be negligible. The refractive index changes for the optical waves modify the phase-matching behaviour of the nonlinear optical effect. The dispersion associated with a two-photon transition has only been studied once before, with the intermediate state off-resonance [78, 79]. The dispersion of the wave at frequency  $\omega_2$  occurs due to the induced absorption at  $\omega_{2\text{photon}} - \omega_1$  by the field at frequency  $\omega_1$ . The wave at frequency  $\omega_1$  also experiences a change in refractive index when  $\omega_1 + \omega_2$  is two-photon resonant due to movement of population through the three levels. In fact, the refractive index of the atomic vapour cannot be simply deconvoluted into two separate dipole transition contributions because of the strong two-photon coupling. These effects are illustrated in the numerical calculations in §2.3.4.

#### 2.3.4 Theoretical Results

Real solutions to the set of density matrix equations (2.3.14 a-f) were obtained for a variety of optical field strengths, detunings from atomic resonance and relaxation constants. A numerical computer model was used to solve the nine simultaneous linear equations in the steady state and numerically integrate over the atomic velocities to account for the Doppler shifts of the atoms in a vapour.

The solution terms which were of interest to the magnetic field induced SFM study were :  $|\rho_{13}|^2$ ,  $\text{Re } \rho_{12}$ ,  $\text{Re } \rho_{23}$  and  $\rho_{33}$ .

As mentioned in the previous section, the quadrupole moment which generates the sum-frequency wave is proportional to  $\rho_{13}$  and thus the intensity of the SFM wave is proportional to  $|\rho_{13}|^2$ . The real terms  $\text{Re } \rho_{12}$  and  $\text{Re } \rho_{23}$  give the refractive index experienced by the optical fields at frequency  $\omega_1$  and  $\omega_2$  respectively which is [2]

$$n_1 \sim 1 + \frac{\chi'(\omega_1)}{2} = 1 + \frac{\mu_{12}^2 N}{2 \epsilon_0 \hbar} \frac{\text{Re } \rho_{12}}{\alpha} \quad (2.3.23)$$

$$n_2 \sim 1 + \frac{\chi'(\omega_2)}{2} = 1 + \frac{\mu_{23}^2 N}{2 \epsilon_0 \hbar} \frac{\text{Re } \rho_{23}}{\beta} \quad (2.3.24)$$

where  $n_i$  is the refractive index for frequency  $\omega_i$ ,  $\chi'(\omega)$  is the real part of the linear electric susceptibility,  $N$  is the atomic density and  $\mu_{ij}$  is the electric dipole moment between the atomic states  $|i\rangle$  and  $|j\rangle$ .

The population term  $\rho_{33}$  of the upper atomic state describes the incoherent fluorescence signal which is observed at 330 nm due to cascade fluorescence from the sodium 4D state. This gives the spectroscopic lineshape of the two-photon resonance.

Population was conserved in the three-level model by defining

$$\rho_{11} + \rho_{22} + \rho_{33} = 1 \quad (2.3.25)$$

and the off-diagonal relaxation rates were given by

$$\Gamma_{ij} = \frac{1}{2} (\Gamma_{ii} + \Gamma_{jj}) \quad (2.3.26)$$

where  $\Gamma_{ii}$  and  $\Gamma_{jj}$  were the decay rates for the atomic population in states  $|i\rangle$  and  $|j\rangle$ . This assumed that there were no phase-disturbing collisions [68, 77]. The degree of single photon saturation produced by the optical fields through the Rabi frequency  $\Omega$  was [7]

$$\frac{I}{I_{\text{sat}}} = \frac{4 \Omega^2}{\Gamma_{ii} \Gamma_{ij}} \quad (2.3.27)$$

Using these definitions and the developed three level atom model, five examples are presented below to illustrate the various criteria which are relevant to magnetic field induced SFM.

(i) With  $\beta = 0$ , ie. no applied second optical field at frequency  $\omega_2$ , the atom behaves like a two-level system and only responds to the optical field at  $\omega_1$ . Figure 2.7 shows the calculated variation of  $\text{Re } \rho_{12} / \alpha$ , proportional to the refractive index change experienced by the wave at  $\omega_1$ , as a function of the single photon detuning  $\Delta_1$  for various values of  $I/I_{\text{sat}}$ .

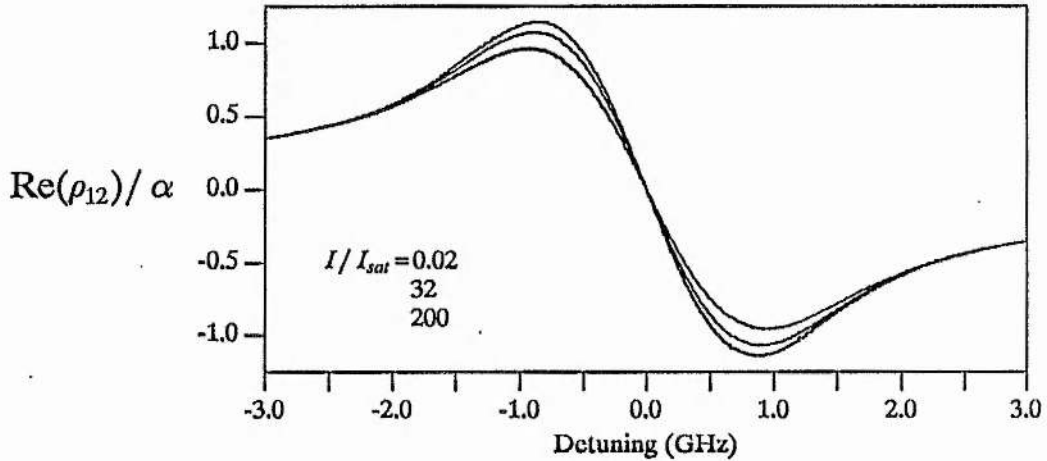


Figure 2.7 : Refractive index change experienced by an optical wave interacting with a two-level atom and increasing optical saturation.  $\Gamma=0.02$  GHz.

As expected, the maximum and minimum of the dispersion are separated by the Doppler width due to the inhomogeneous broadening. There is no apparent hole burning as  $\Delta_1$  is varied because this is the refractive index experienced by the strong pumping wave itself. With increasing optical field strength and higher saturation, the refractive index deviations from unity decrease due to equalisation of population in the upper and lower atomic levels. This occurs much less rapidly with optical field strength than in a homogeneous system because the width of the power broadened hole burnt into the ground state population must rival the Doppler width in an inhomogeneous atomic system in order to saturate the refractive index [80].

(ii) Consider now the three level atom with two applied optical fields but with the intermediate state off resonance ( $\Gamma_2=0.02$ ,  $\Gamma_3=0.05$ ,  $\alpha=0.001$ ,  $\beta=0.001$  and  $\Delta_1=10$ ). This situation is analogous to SHG, or SFM with a non-resonant intermediate state as discussed in Chapter 5. Figure 2.8 shows the upper state population,  $\rho_{13}$  coherence squared and the

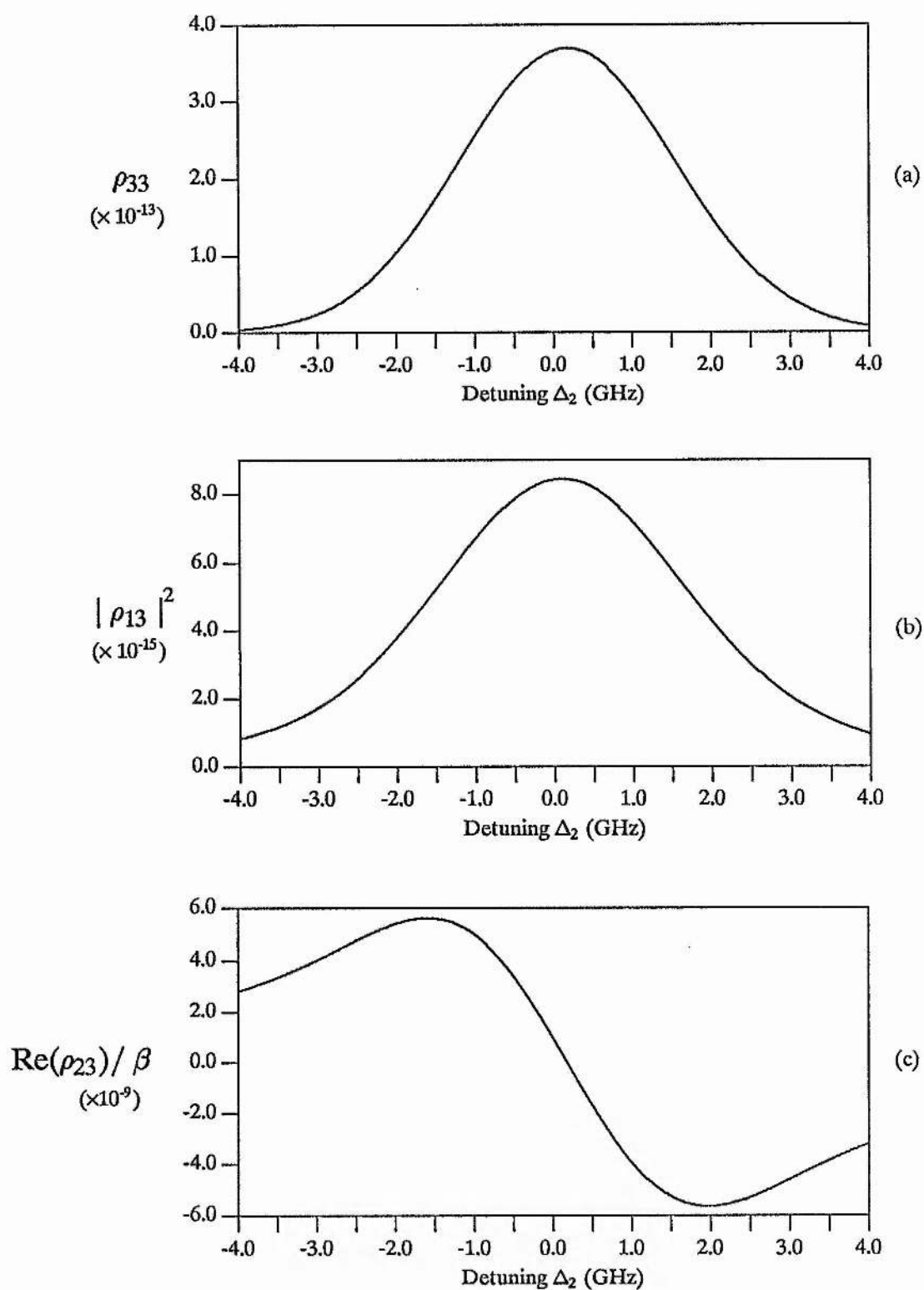


Figure 2.8 : Variation of (a) upper state population, (b) upper-lower state atomic coherence, (c) refractive index at frequency  $\omega_2$  with detuning from two-photon resonance. Intermediate state detuned from resonance by  $\Delta_1 = 10$  GHz.

refractive index experienced by the wave at frequency  $\omega_2$  as a function of detuning from two-photon resonance. The upper state population distribution is Doppler broadened with a width of  $(k_1+k_2)u$ , where  $u$  is the most probable atomic velocity. This is as expected for two-photon excitation with co-propagating beams. The  $\rho_{13}$  coherence also has this width due to all homogeneous atomic velocity groups being equally excited by the two-photon absorption. This agrees with the experimental observations [14]. The refractive index at  $\omega_1$  remains unchanged as  $\omega_2$  is tuned through two-photon resonance but  $\omega_2$  experiences a small but changing refractive index due to the two-photon absorption.

(iii) The intermediate state is now brought into resonance with  $\Delta_1 = 0.25$  GHz ( $< \Delta v_D$ ) and the other parameters unchanged, so that the two weak optical fields couple the Doppler broadened atomic transitions, as in simultaneously resonant SFM. Figure 2.9 shows the calculated population of the upper level. The two-photon spectroscopic lineshape due to  $\rho_{33}$  is now essentially Lorentzian due to the hole burning effect of  $\omega_1$  on the  $|1\rangle \rightarrow |2\rangle$  inhomogeneous velocity distribution and the two-photon resonance appears at  $(k_1+k_2)\Delta_1/k_1$  due to the residual Doppler shift of this selected velocity group. The width of the two-photon resonance is approximately equal to the natural linewidth  $\Delta v = \Delta v_3 + 2.036 \Delta v_2$  since  $\alpha$  and  $\beta$  are chosen to be less than the saturation intensities in this example. There is approximately no change in the ground state population or refractive index at  $\omega_1$  when  $\omega_1 + \omega_2$  is two-photon resonant because the optical fields are weak. Figure 2.9 also shows the refractive index for  $\omega_2$  and the coherence term  $|\rho_{12}|^2$ . The refractive index changes for  $\omega_2$  are appreciable and now have a Lorentzian width to reflect the population distribution in the intermediate and final states.

The upper-lower state coherence retains a Doppler broadened width but now has an apparent hole at the frequency of the excited homogeneous velocity group. Although the physical mechanism for this behaviour is not clear at present, it is only apparent for no saturation on the lower  $|1\rangle \rightarrow |2\rangle$  transition. When  $I/I_{\text{sat}} > 1/3$ , the spectral shape of the  $|\rho_{13}|^2$  coherence becomes essentially Lorentzian due to the dominant contribution from the hole burnt homogeneous atomic group. This is seen in the following example.

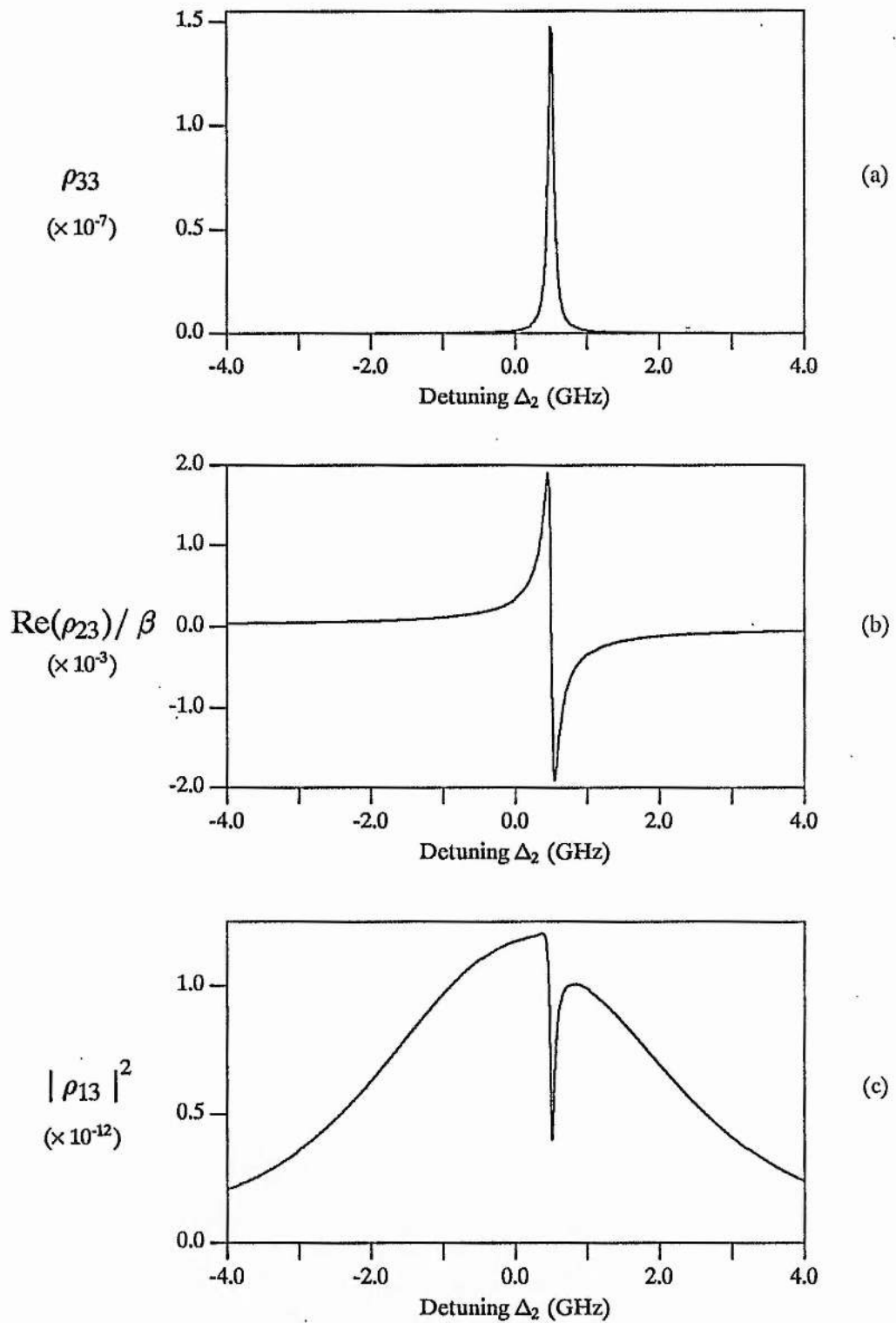


Figure 2.9 : Variation of (a) upper state population, (b)  $n(\omega_2)$  and (c) upper-lower state atomic coherence with detuning from two-photon resonance. Intermediate state detuned from resonance by  $\Delta_1 = 0.25$  GHz and optical field strengths  $\ll$  saturation intensities.

(iv) With  $\alpha$  increased to 0.0224, several times the saturation intensity ( $\sim 10$ ), the quantities of interest are shown again in Figure 2.10. The upper state population  $\rho_{33}$  is again Lorentzian due to velocity selective excitation but is power broadened by the strong laser field at frequency  $\omega_1$ . Although the change in the ground state population  $\rho_{11}$  is extremely small ( $\sim 5 \times 10^{-4} \%$ ), there is a movement of population due to two-photon resonance and the refractive index for  $\omega_1$  subsequently varies as shown in Figure 2.10 (b). The refractive index variations for frequency  $\omega_2$  are now larger due to a greater excited population in the intermediate state by the stronger optical field at  $\omega_1$ . The maxima and minima of the refractive index changes are again separated by the full width of the power broadened Lorentzian population distribution. The coherence term  $|\rho_{13}|^2$  is now Lorentzian in shape and is centred at the frequency for exact two-photon resonance for the excited homogeneous velocity group.

(v) Consider now  $\beta$  increased ( $\beta=0.028$ ) to become  $\sim 5$  times the single photon saturation intensity in addition to  $\alpha = 10 I_{\text{sat}}$ . This is the condition which was most typical for the SFM experiments discussed in Chapter 6. The magnitude of  $\rho_{33}$  is increased due to the additional strong field at frequency  $\omega_2$  and there is further power broadening. A distinct Lorentzian change in the ground state population is now evident due to the coupling of the three atomic levels by the two strong optical fields and movement of population up the ladder system. The refractive index changes for  $\omega_1$  are increased by this population redistribution on two-photon resonance and are of a more complex form due to the different power broadened widths of the  $\rho_{11}$  and  $\rho_{22}$  population changes. The refractive index for  $\omega_2$  is of a similar form to the previous example but its magnitude is decreased due to the greater saturation by the optical field at  $\omega_2$ . The spectral shape of the  $|\rho_{13}|^2$  coherence is again a power broadened Lorentzian and the magnitude of  $\rho_{13}$  rivals that of the atomic population  $\rho_{33}$ .

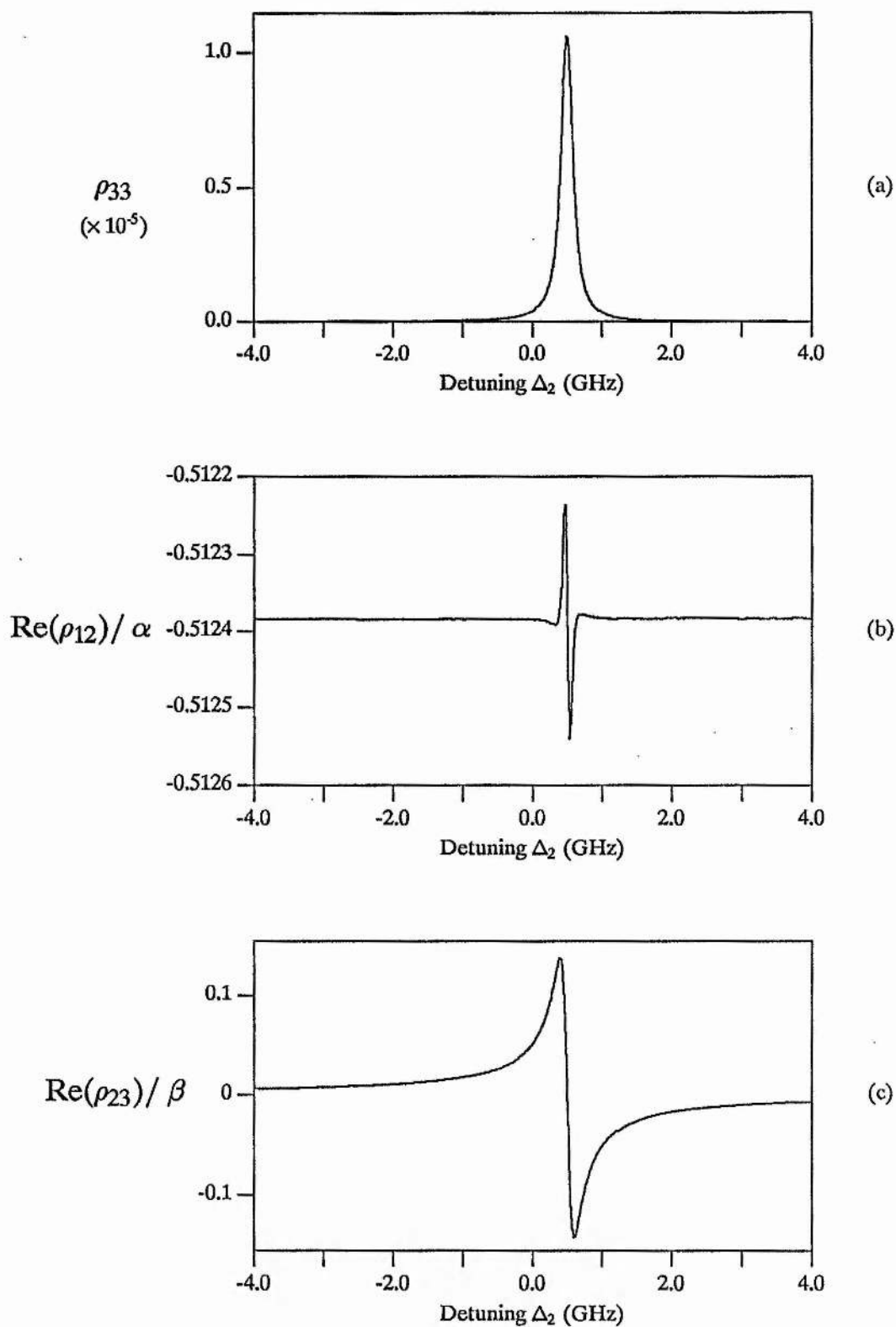
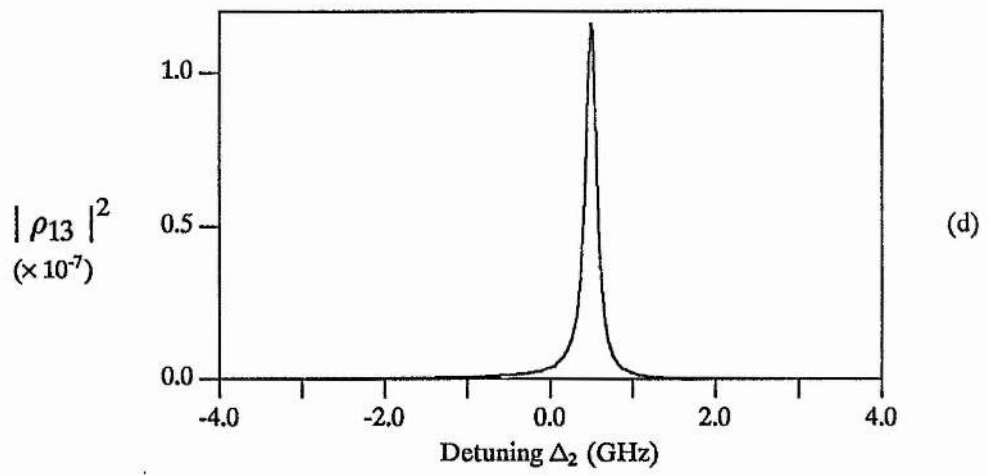


Figure 2.10 : Variation of (a) upper state population, (b)  $n(\omega_1)$ , (c)  $n(\omega_2)$  and (d) upper-lower state atomic coherence with detuning from two-photon resonance. Intermediate state detuned from resonance by  $\Delta_1 = 0.25$  GHz,  $\alpha = 10 I_{\text{sat}}$  and  $\beta \ll I_{\text{sat}}$ .



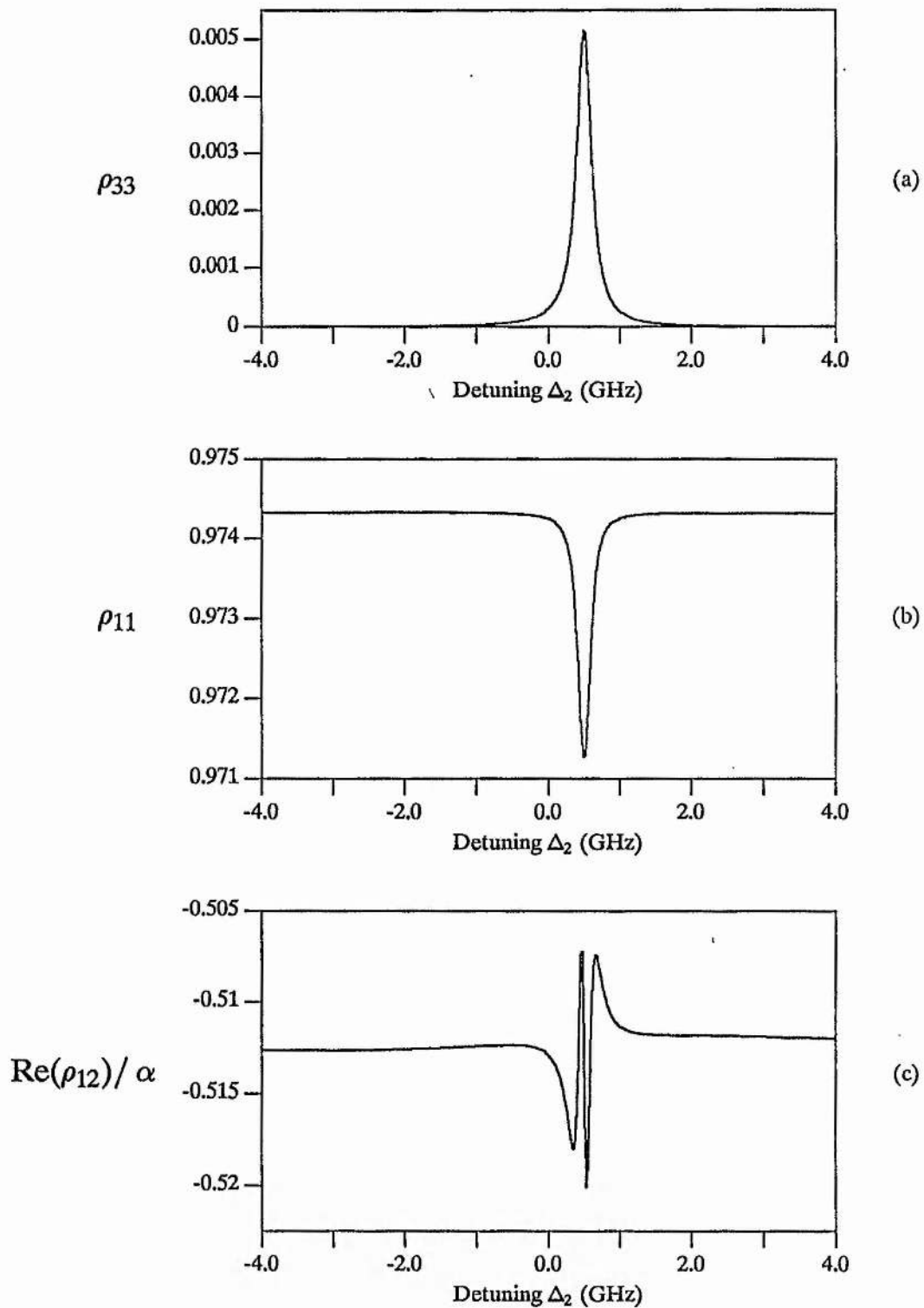
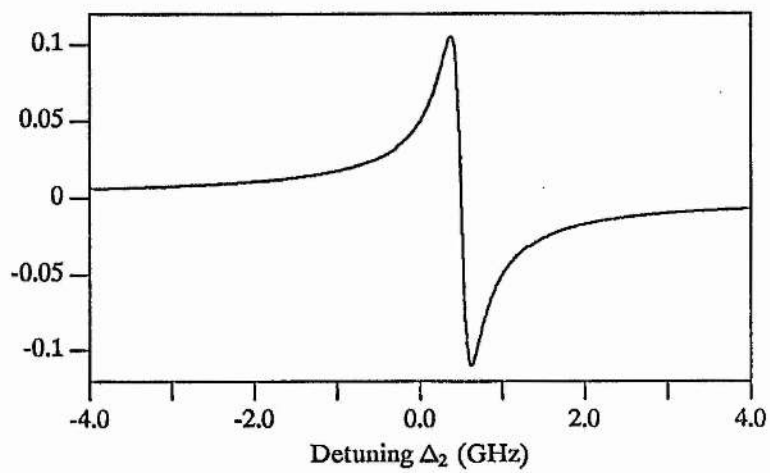


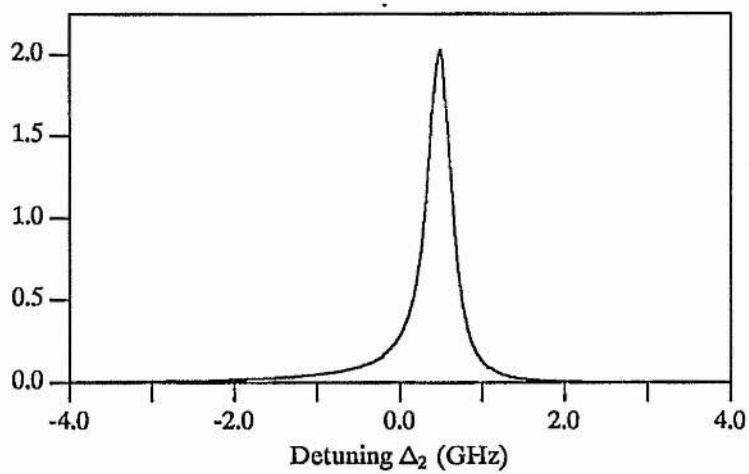
Figure 2.11 : Variation of (a) upper state population, (b) ground state population, (c)  $n(\omega_1)$ , (d)  $n(\omega_2)$  and (e) upper-lower state coherence, with detuning from two-photon resonance. Intermediate state detuned from resonance by  $\Delta_1 = 0.25$  GHz,  $\alpha = 10 I_{\text{sat}}$  and  $\beta = 5 I_{\text{sat}}$ .

$\text{Re}(\rho_{23})/\beta$



(d)

$|\rho_{13}|^2$   
( $\times 10^{-5}$ )



(c)

The phase matching implications for simultaneously resonant SFM can be seen by considering example (v) which is typical of the experimental results presented in Chapter 6. The phase mismatch is approximately given by

$$\Delta k \sim 2\pi \left( -\frac{\Delta n(\omega_1)}{\lambda_1} - \frac{\Delta n(\omega_2)}{\lambda_2} \right) = \Delta k_1 + \Delta k_2 \quad (2.3.28)$$

where  $\Delta n(\omega_1) \propto \text{Re } \rho_{12} / \alpha$  and  $\Delta n(\omega_2) \propto \text{Re } \rho_{23} / \beta$ . For collinear plane waves, the dependence of the SFM power on the phase mismatch is

$$P(\omega_1 + \omega_2) \propto \frac{\ell^2 \sin^2(\Delta k \ell / 2)}{(\Delta k \ell / 2)^2} \quad (2.3.29)$$

Assuming that  $\Delta k_1 \ell / 2 \sim 3$  for the given value of  $\text{Re } \rho_{12} / \alpha$  when  $\omega_1 + \omega_2$  is not two-photon resonant the additional phase mismatch due to  $\Delta k_2$  and further  $\Delta k_1$  alters the generated SFM power as the frequency  $\omega_2$  is tuned through two-photon resonance. This is shown in Figure 2.12 where the driving coherence term for the sum frequency wave  $|\rho_{13}|^2$  is modulated as a function of frequency due to the frequency dependent refractive index variations.

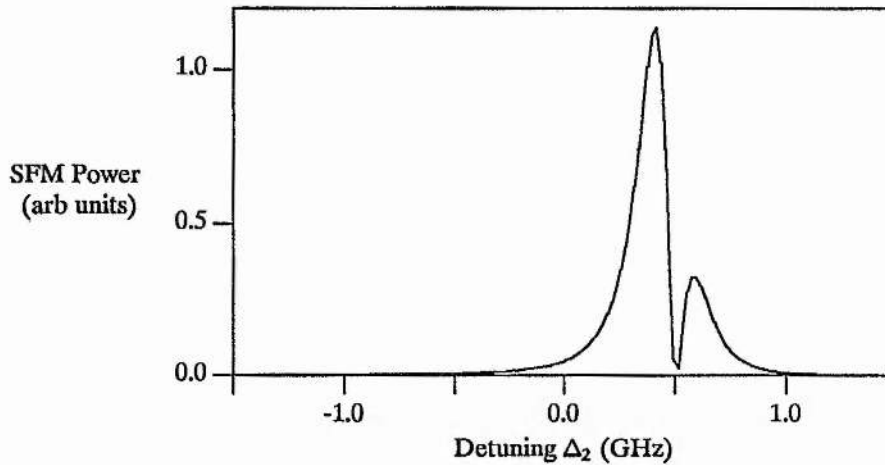


Figure 2.12 : Calculated SFM power as a function of detuning from two-photon resonance with phase mismatching effects accounted for across the line profile.

The dip in the SFM power due to phase mismatching occurs on the low frequency side of the Lorentzian  $|\rho_{13}|^2$  line profile. A similar calculation with  $\Delta_1 = -0.25$  GHz shows that the dip in SFM power occurs on the high frequency side as shown in Figure 2.13.

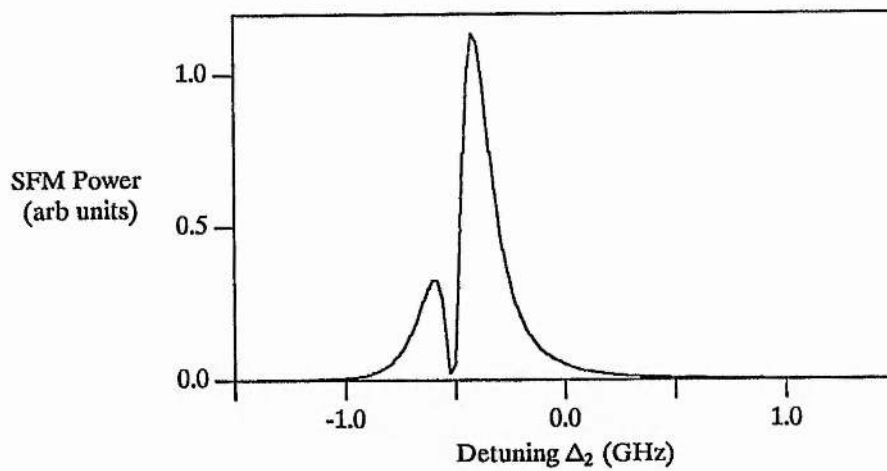


Figure 2.13 : Calculated SFM power with phase mismatching for  $\Delta_1 = -0.25$  GHz.

These phase-matching variations in generated SFM power due to refractive index changes in the simple three level atom model are shown in Chapter 6 to be applicable to the experimental results for simultaneous single and two-photon resonant, magnetic field induced SFM in sodium vapour.

# **CHAPTER 3**

## **EXPERIMENTAL APPARATUS**

## Chapter 3

### EXPERIMENTAL APPARATUS

This chapter describes the apparatus used for the experimental nonlinear optical studies discussed in this thesis. Some of the apparatus was common to all of the experiments. Where particular equipment was used for specific experiments, it is identified by its allocation to the chapter subject: IV - saturation spectroscopy, V - sum frequency mixing, VI - simultaneously resonant SFM, VII - optical pumping.

#### 3.1 DYE LASER SYSTEMS

A total of four continuous wave (cw) dye laser systems were used for the experiments and each is briefly described below. The dye lasers were pumped by a single argon ion laser (Spectra Physics 171-07 or 2030-20) operating at  $\sim 4\text{W}$  @ 514.5 nm to pump a single dye laser or at  $\sim 10\text{W}$  @ 514.5 nm ( $15\text{W}$  @ all lines) to simultaneously pump two dye lasers. When pumping more than one dye laser, the argon ion output beam was split in two by a combination of a dual wavelength half-wave plate and a polarising beamsplitter cube (Newport). This allowed the power ratio in the two pump beams to be varied by rotating the half-wave plate.

##### *3.1.1 Spectra Physics 380D dye laser*

The Spectra Physics 380D was a cw, frequency stabilised, single-mode ring dye laser which produced several hundred milliwatts of tunable, scannable, narrow linewidth laser radiation. This laser is described in detail by the manufacturer's literature [81], Kane [82] and Sinclair [14]. A schematic diagram of the ring dye laser cavity is shown in Figure 3.1.

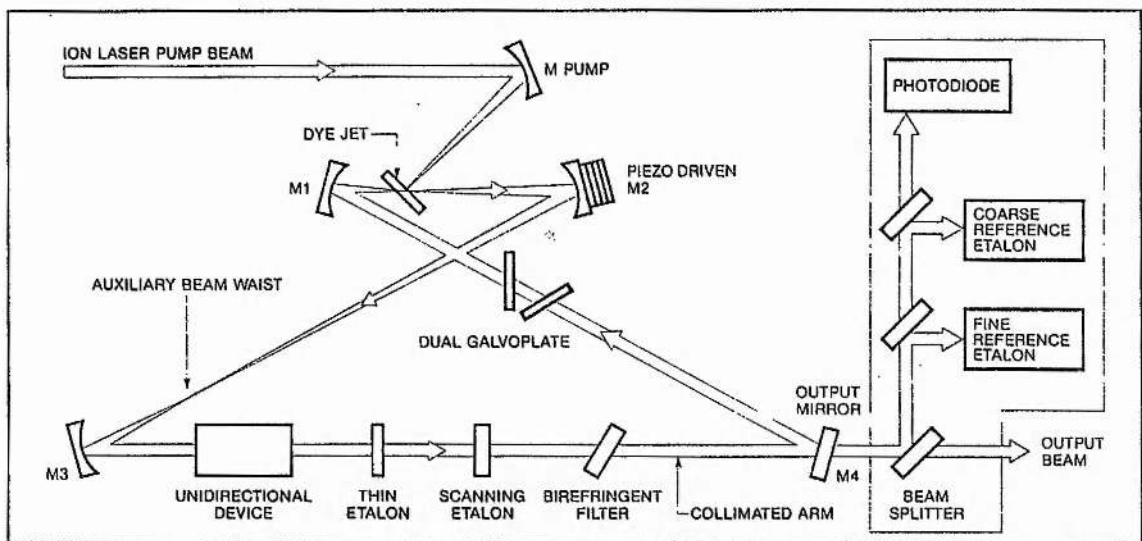


Figure 3.1 : Schematic diagram of the Spectra Physics 380D laser cavity (from the manufacturer's handbook).

The active medium of the dye laser was a thin, free flowing, high pressure jet of rhodamine 6G dye dissolved in an ethylene glycol solvent. The four laser cavity mirrors formed a figure of eight ring configuration with the light being constrained to travel around this ring in one direction only by a polarisation selective unidirectional device. This travelling wave arrangement prevented spatial hole burning of the gain and encouraged single-mode operation of the laser. A three plate birefringent filter and thick air-spaced Fabry-Perot etalon locked to the laser mode frequency were used to achieve single-mode frequency selection and allowed the laser to be tuned. The 380D dye laser was electronically scanned up to 30 GHz by rotating the Brewster angled rhombs on galvanometers to change the optical length of the laser cavity. A Brewster angled quartz astigmatism compensator was used to correct for the off-axis angles of the laser beam on the cavity mirrors.

In addition, the passive laser linewidth of  $\sim 20$  MHz was reduced to  $\sim 500$  kHz rms by actively stabilising the laser cavity. A small fraction of the output laser beam was split off to a combination of two external confocal interferometers (Spectra Physics 488), one of free spectral range (FSR) = 500 MHz which was temperature stabilised and one of FSR = 10 GHz. By monitoring the laser intensity and the interferometer central fringe with photodiodes, a laser frequency variation was converted to a normalised intensity variation and this was used as a discriminant by the laser servo system electronics. The low frequency error correction signals

were fed back to the laser cavity to rotate the Brewster angled quartz rhombs and the high frequency variations were corrected by moving the mirror M2 on a piezoceramic with a bandwidth of  $\sim 10$  kHz.

Using rhodamine 6G as a laser dye gave a tuning range from  $\sim 565 - 625$  nm with a maximum output power of  $\sim 600$  mW. This laser served as the scannable source of laser radiation in all of the experiments.

### 3.1.2 Spectra Physics 380A dye laser (V)

This laser was the unstabilised version of the 380D ring dye laser with the cavity and intracavity elements being identical to the 380D except that mirror M2 was fixed and not mounted on a piezoceramic. The linewidth of the 380A ring dye laser is  $\sim 20$  MHz ( $5$  MHz  $< 1$  s). Rhodamine 6G was again used as the laser dye.

### 3.1.3 Coherent 699-21 dye laser (VI)

The 699-21 was the tunable, scannable, frequency stabilised single-mode ring dye laser commercially produced by Coherent Radiation Ltd [83]. The principle of operation of this laser was the same as for the Spectra Physics 380D with a few minor differences. The laser cavity is schematically shown in Figure 3.2 and was in a vertical plane as opposed to the horizontal plane of the 380D.

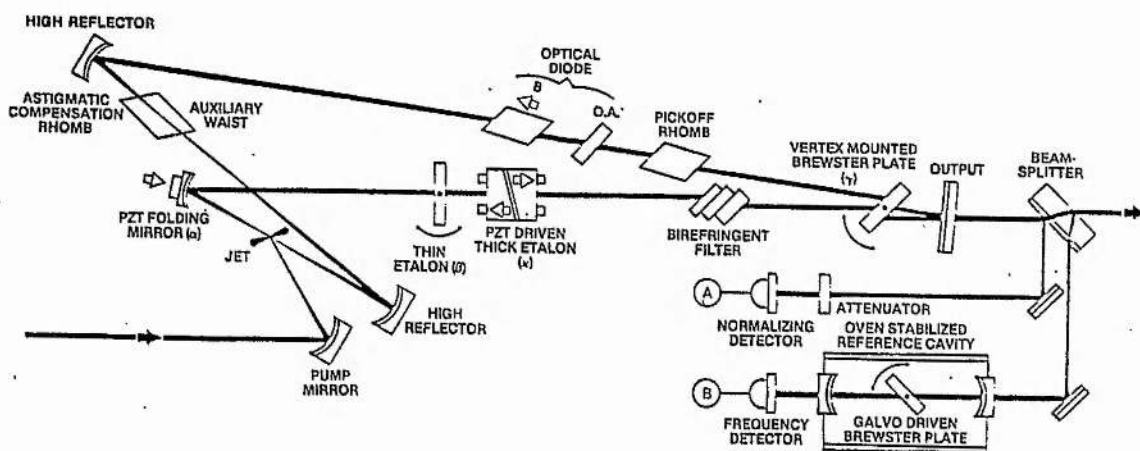


Figure 3.2 : Schematic diagram of the Coherent CR 699-21 laser cavity (from the manufacturer's handbook).

All of the optic mounts were mounted on a 1" diameter Invar bar which gave excellent long term stability of the laser cavity. Again, an external interferometer was used to stabilise the laser linewidth to  $\approx 1$  MHz. The laser additionally required an intracavity thin etalon to select single-mode operation and the unidirectional device ("optical diode") is Brewster angled rather than near normal incidence as in the 380D. The pumping threshold of this laser was found to be higher than the 380D and typically 6W @ 514.5 nm pump power was required, as opposed to 4W for the 380D, to generate the equivalent output power with rhodamine 6G dye.

### 3.1.4 *Standing-wave dye laser (V, VII)*

The standing-wave dye laser was a simple three mirror cavity design which was constructed in the Department of Physics and Astronomy, University of St. Andrews. The laser cavity is schematically shown in Figure 3.3.

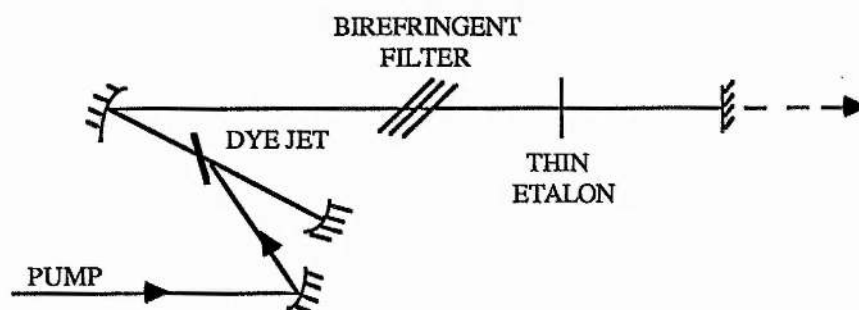


Figure 3.3 : Schematic diagram of the home-built standing wave laser cavity.

The cavity plane was vertical with a horizontal dye jet (Rhodamine 6G) to match the vertical polarisation of the argon ion pump beam. The folded cavity was used to correct the intracavity beam astigmatism introduced by the Brewster angled dye jet [84]. Frequency selective elements were introduced into the laser cavity according to the required linewidth but the laser always operated on multi-longitudinal modes in a standing wave.

This laser was operated in two configurations:

(i) two or three plate intracavity birefringent filter to reduce the linewidth to  $\sim 27$  GHz and  $\sim 17$  GHz respectively (V),

(ii) single plate birefringent filter and solid thin etalon (FSR = 500 GHz) to give a measured linewidth  $< 5$  GHz (VII).

In this latter configuration for the optical pumping experiments, the laser frequency was locked onto the sodium  $D_1$  or  $D_2$  resonance transitions by an optogalvanic servo system. A schematic diagram of the complete servo system is shown in Figure 3.4.

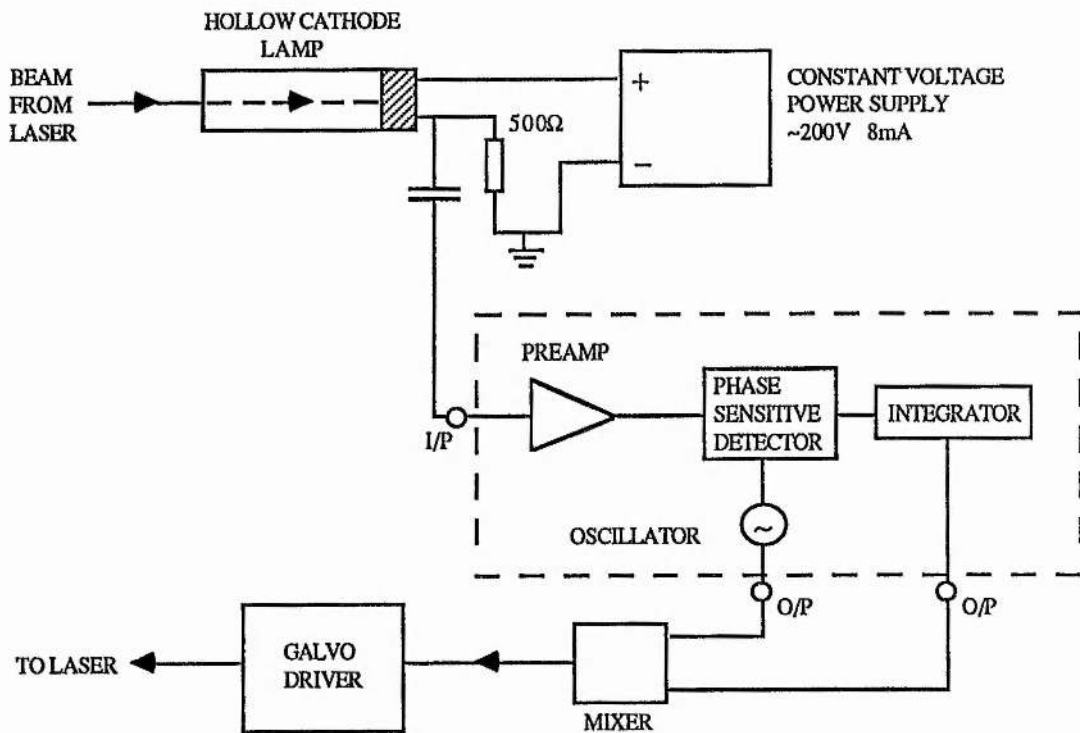


Figure 3.4 : Schematic diagram of the optogalvanic servo system used to lock the standing wave dye laser onto a sodium resonance.

The optogalvanic signal from the sodium hollow cathode lamp provided the discriminant for the laser servo electronic system [82]. When the laser was tuned onto a sodium resonance line, the excitation of atoms in the hollow cathode discharge by the laser light reduced the required discharge voltage through increased ionisation. This change was detected by supplying the lamp from a constant voltage power supply and measuring the

voltage change across an external ballast resistor. A phase sensitive section of the servo system was used to actively modulate the thin etalon tilt on a galvanometer and detect the optogalvanic signal at the modulation frequency to lock the laser on the centre of the Doppler broadened sodium resonance line. The integrator section of the servo system removed the long term drift in the laser frequency.

## 3.2 MONITORING AND DETECTION DEVICES

### 3.2.1 *Laser Parameters*

The wavelength of the single-mode ring dye lasers was measured to a precision of 1 part in  $10^6$  by an in-house built Kowalski-style travelling wavemeter [82]. The beam from a calibrated frequency stabilised Helium-Neon laser and a fraction of the unknown wavelength dye laser beam were overlapped and passed in opposite directions around a Michelson interferometer. The optical path of one arm of the interferometer was mechanically scanned and the generated interference fringes from the He-Ne and the dye laser beam were counted electronically. A simple electronic ratio technique allowed the wavelength of the dye laser to be directly displayed in approximately 10s.

Single-mode operation of each of the ring dye lasers was verified with a piezo-scanned confocal Fabry-Perot interferometer with a FSR  $\sim 1.5$  GHz. This interferometer was also used as a relative frequency marker to measure the detuning of the CR 699-21 dye laser from a sodium 3S-3P D line transition (VI).

The absolute frequencies of the 380D and 699-21 dye lasers were measured with an iodine cell and a sodium cell respectively (VI).

The reflectivity of mirror M3 in the 380D laser cavity was not 100% and the few milliwatts of emitted laser power was passed through a quartz cell containing iodine vapour at room temperature. The induced molecular fluorescence was detected perpendicular to the laser beam by an RCA 931B photomultiplier tube. Scanning the 380D laser produced a fluorescence spectrum which could be compared to a calibrated atlas of the  $I_2$  absorption spectrum obtained by Fourier Transform Spectroscopy [85]. The absolute laser frequency could be measured to an accuracy of 1 part in  $10^8$ .

To obtain an absolute frequency calibration of the 699-21 laser at the sodium 3S-3P

transition frequencies, a quartz sodium cell was constructed. The 100 mm long and 15 mm diameter cell body had optical quality quartz windows (Jencons Scientific Ltd) and a side arm into which pure sodium metal was diffused after evacuation and bake out of the cell. The cell body and the sidearm had independent heating elements made from nichrome ribbon non-inductively wound on glass formers. The entire cell was enclosed in a stainless steel box and insulated with mineral wool. The cell body was heated via a 240V AC mains variac with the output voltage stepped down by a 240:30 1A transformer. The sidearm was heated by a Digitron 3800K temperature controller whose variable output voltage was stepped down by a 240:15 15A transformer. The temperature controller held the sidearm temperature constant to a few degrees Kelvin. The cell body was heated to  $\sim 30^\circ\text{C}$  higher than the typical measured sidearm temperature of  $150^\circ\text{C}$  to prevent condensation of sodium on the cell windows. Both temperatures were measured with 1.5 mm diameter type K thermocouples.

This cell was used in a saturated absorption set up as shown in Figure 3.5 to provide Doppler free spectra of the Na D line transitions and a calibration of the 699-21 laser frequency to a few tens of MHz.

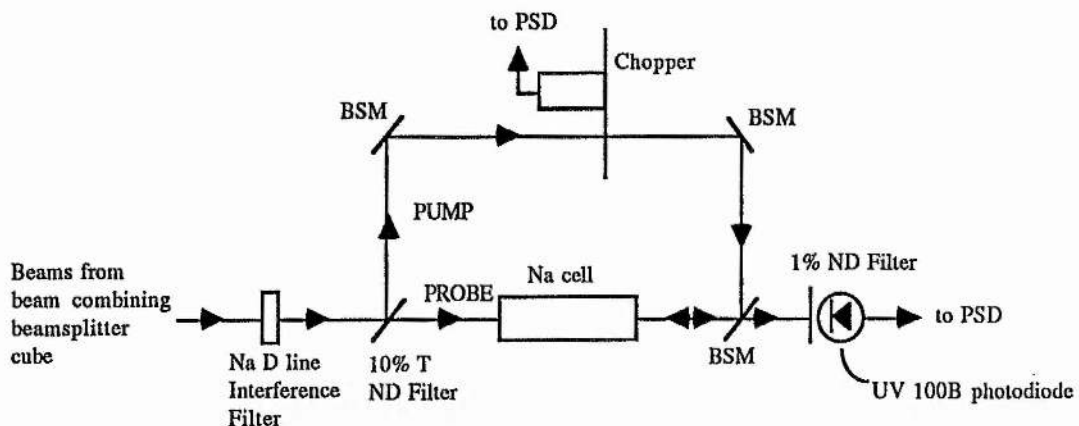


Figure 3.5 : Schematic diagram of the saturated absorption spectroscopy set up used to calibrate the 699-21 laser frequency.

The sodium D line interference filter (Ealing Electro-Optics) removed the unwanted laser beam at the 3P-4D sodium transition wavelength of 568 nm which was present due to the combining of  $\omega_1$  and  $\omega_2$  on the beamsplitter cube for the SFM experiments. An ND filter in front of the photodiode prevented saturation of the photodiode signal. The  $3S_{1/2} (F=1) \rightarrow 3P,$

$3S_{1/2} (F=2) \rightarrow 3P$  and the frequency midway between them (crossover resonance in the saturation spectrum - see Chapter 4) could easily be resolved and the frequency of the 699-21 laser was tuned relative to these known frequencies.

The electronic scans of the 380D dye laser were calibrated by measuring the fringe spacing of a low finesse, temperature stabilised, FSR = 250 MHz confocal Fabry-Perot etalon.

### 3.2.2 *Signal detection apparatus*

Various photomultiplier tubes were used to detect the laser radiation at visible and ultraviolet wavelengths. A Hamamatsu R166UH high gain solar blind photomultiplier tube was used for measurement of the generated sum frequency power at 289 nm (V, VI) and for the collisional induced fluorescence from the Na 5P-3S transition at 285 nm (VI §6.4.3). The cascade 4P-3S fluorescence at 330 nm from two-photon excitation was detected with a 1P28 photomultiplier tube. Both of these tubes were used in conjunction with two Corning 9863 ultraviolet transmitting filters to discriminate against the visible fundamental laser beams. For some experiments (VI) a Monospek 1000 1m double Czerny monochromator was used for wavelength selection before the emitted radiation was detected at the output slits by a photomultiplier tube. The monochromator was used with the slits fully open so that it acted as a ~2.5 nm (FWHM) filter. A calibrated UV 100B photodiode was used to measure the power of the high efficiency SFM beam (VI, §6.8).

Generally, a lock-in, phase sensitive detector was used to improve the signal to noise ratio at low signal levels. One of the fundamental laser beams was chopped by a mechanical chopper at a frequency of ~2 kHz and a Brookdeal 401 or EG&G 5209 lock-in detector was used. The output signal from the detector was sent to a chart recorder or a computerised data recording system [86].

## 3.3 METAL VAPOUR

Sodium vapour, used as the nonlinear atomic medium for magnetic field induced SFM, was produced in heat-pipe ovens. Heat pipe ovens [87] are devices for producing uniform densities of metal vapours and their general construction is schematically shown in Figure 3.6.

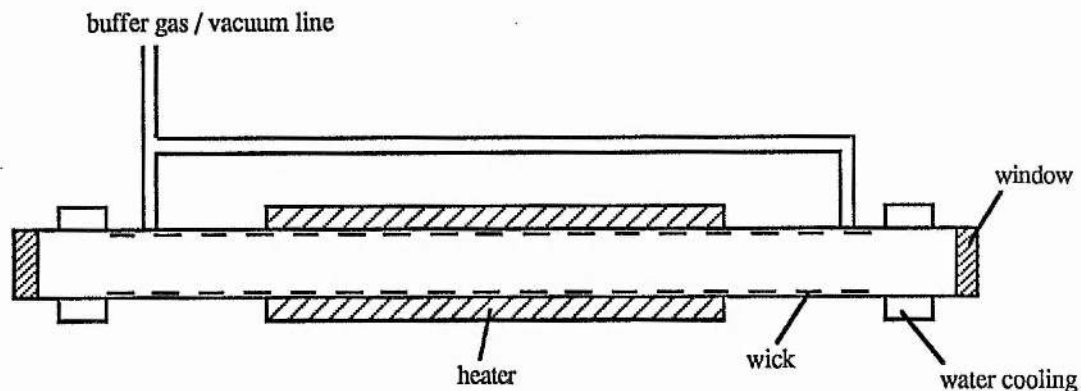


Figure 3.6 : Schematic diagram of a heat-pipe oven.

The oven was made from a material such as stainless steel which did not chemically react with the atomic vapour. The main oven body contained a supply of the alkali metal and had a fine stainless steel mesh lining which acted as a wick. Ultraviolet transmitting optical windows were mounted on water cooled flanges which protected the sealing O-rings against thermal damage. The central section of the oven was heated by an electrical heating cord (Electrothermal) which was driven by a temperature controller (FGH Controls Ltd., Type 5900-K-2-0-240 Vigilant with TRZ-10-240 triac power controller). The heat-pipe oven temperature was measured with a type K thermocouple (Comark) mounted in the wall of the oven. The actual sodium vapour temperature was experimentally found to be  $\sim 30 - 40^{\circ}\text{C}$  less than the measured temperature on the thermocouple due to temperature gradients in the walls of the heat-pipe oven. A vacuum/gas handling system was connected so that the oven could be evacuated or buffer gas added.

In principle, the heat-pipe oven operated by heating an alkali metal (or other metal) to produce a vapour pressure which equaled the pressure of the added inert buffer gas. When this was achieved, the buffer gas was forced to the water cooled ends of the oven where it acted as a cold barrier to protect the oven windows against metal vapour contamination. The generated metal vapour condensed on the wick at the water cooled flanges and returned to the heated centre of the oven by capillary action. This cyclic action of metal vapour produced a highly uniform zone of metal vapour density.

In practice, the heat-pipe ovens used in this study were relatively short in length and the

buffer gas pressure was made greater than the sodium vapour pressure at the working temperatures to restrict the mean free path of the sodium atoms and prevent contamination and damage of the oven windows. However, this still produced a relatively uniform metal vapour zone [14].

The construction and design of the heat-pipe ovens used in this study is detailed in reference 14. The oven illustrated in Figure 4.3.4 of reference 14 was mainly used for this SFM study. A new short heat-pipe oven, of a similar design to the one illustrated in Figure 4.3.3 (a) of reference 14, was constructed to restrict the length of the sodium vapour zone to the length of the electromagnet poles. This prevented large linear absorption of the single photon resonant laser beam in "dead" regions of the sodium vapour zone which were not subject to the transverse magnetic field.

A different type of sodium oven was designed and constructed for the experiments to attempt to induce the  $\chi^{(2)}$  nonlinearity in the atomic vapour by optical pumping (VII) since the sodium vapour was additionally required to be transversely illuminated. A schematic diagram of the Na oven/cell design is shown in Figure 3.7.

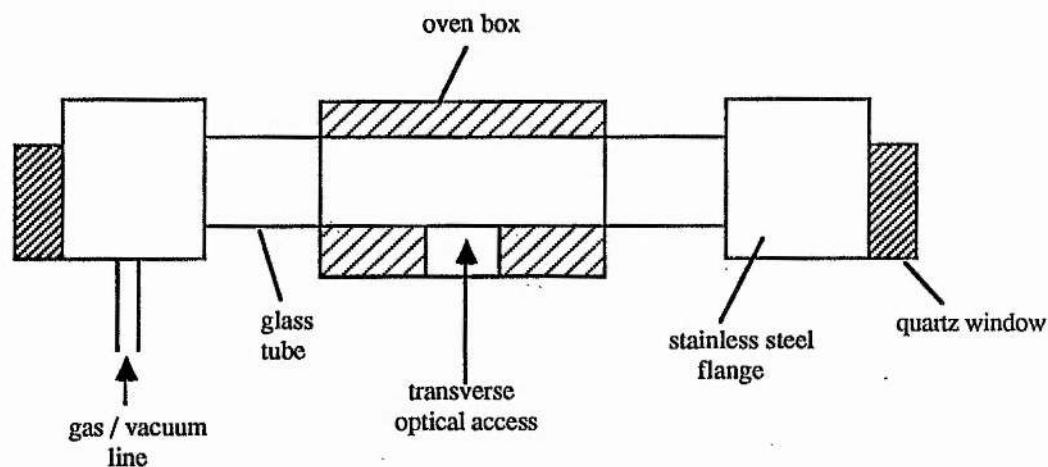


Figure 3.7 : Schematic diagram of the sodium cell used for the optical pumping experiments described in Chapter VII.

The main cell body was constructed from a 1" diameter soda glass tube which was

chemically lined with an alkali vapour resistant barium borate coating (Glassbulbs). Most ordinary glasses such as Pyrex suffer damage from high temperature alkali metal vapours and become opaque. Owing to the fragile nature of the transparent resistant coating, the soda glass was difficult to work without damaging the coating and so air cooled stainless steel flanges mounted with O-rings were used to hold the quartz cell windows. The windows were displaced off-centre so that the longitudinal laser beam could pass close to the cell wall where the transverse laser beam entered the cell. Water cooling of the windows was not required since this cell was generally operated with a high pressure of buffer gas and this prevented sodium contamination of the windows. A gas/vacuum handling line was connected to one of the stainless steel flanges to allow gas to be added and the cell pumped out. The centre section of the cell was heated by an oven which was composed of Eureka wire non-inductively wound on a T shaped glass former which allowed transverse access to the wall of the cell. A type K thermocouple was used to measure the cell temperature and was connected to a Digitron 3800K temperature controller with the output voltage stepped down by a 240:15 15A transformer.

At an absolute temperature  $T$ , the sodium density  $N$  was given by [11]

$$N(\text{m}^{-3}) = \frac{9.66084 \times 10^{24}}{T} \exp[-12423.3/T + 17.3914] \quad (3.1)$$

and the vapour pressure of the sodium vapour was

$$P(\text{mbar}) = NT \times 1.38 \times 10^{-25} \quad (3.2)$$

The vapour also contained a proportion of sodium dimer molecules  $\text{Na}_2$ , with the percentage of dimers present in the atomic vapour at a given temperature being  $\sim 1\%$  [88].

### 3.4 TRANSVERSE MAGNETIC FIELD

A large Newport type A electromagnet was used to produce the symmetry breaking transverse magnetic field. A power supply for this magnet was designed and constructed. The 10 cm diameter plane pole pieces were machined at the faces to produce a rectangular section of length  $\sim 10$  cm and width  $\sim 2.5$  cm to tailor the magnetic field more closely to the laser beam. The pole pieces were separated by  $\sim 9$  cm and could produce magnetic fields of  $\sim 4$

kG (0.4T) with a magnet current of  $\sim 12$  A. The strength of the magnetic field was calibrated with a Hall probe (Scientifica and Cook).

### 3.5 OPTICS

Three main types of optical components were used to control the polarisation of the laser beams: Glan Taylor linear polarisers, a zero order quarter wave plate for  $\lambda = 590$  nm (VII) and Soleil-Babinet compensators as variable wave plates.

A non-polarisation sensitive beamsplitter cube (Melles Griot 03 BSC 009) was used to collinearly combine the two fundamental beams for the SFM experiments. To achieve higher input powers for SFM, this could be replaced by a knife edge mirror for one of the beams with a resultant slight non-collinearity in the overlap of the two fundamental beams.

A dichroic mirror was often placed at the output end of the sodium heat-pipe oven to separate most of the fundamental visible laser radiation from the generated ultraviolet beam. The reflectivity of this mirror was  $\sim 99\%$  at 590 nm and the transmission  $\sim 70\%$  at 289 nm, the wavelength of the sum frequency beam.

## **CHAPTER 4**

**MEASUREMENT OF THE ZEEMAN SPLITTING  
OF THE SODIUM 3S and 3P ATOMIC STATES  
BY SATURATED ABSORPTION SPECTROSCOPY**

## Chapter 4

### MEASUREMENT OF THE ZEEMAN SPLITTING OF THE SODIUM 3S and 3P ATOMIC STATES BY SATURATED ABSORPTION SPECTROSCOPY

Magnetic field induced second harmonic generation (SHG) [14] and sum frequency mixing (SFM) (Chapter 5) in sodium vapour use the sodium 3P atomic states as nonresonant intermediate states for two-photon absorption. The relatively small laser detuning from the 3S-3P dipole transition provides some single photon resonant enhancement for the nonlinear optical processes. In these cases, the laser detuning is always much greater than the Doppler width or the magnetic splitting of the 3S-3P D line transitions and the perturbing effect of the transverse magnetic field on the energy of the sodium 3P states can be neglected. However, when the SFM nonlinear process is "two-step" with simultaneous single and two-photon resonant enhancement (Chapter 6), then the magnetic splittings of the sodium D line transitions become relevant and the laser detuning from each individual hyperfine transition frequency is required.

It was desirable to have an in situ experimental method of measuring the frequency splittings of the various D line hyperfine transitions with an applied magnetic field. These could then be compared with the theoretical Zeeman splittings to calibrate the magnetic field and obtain laser detuning measurements for the SFM nonlinear optical process. The Zeeman energy splittings of the sodium  $3S_{1/2}$  and 4D atomic states can be measured by Doppler-free two-photon absorption [89, 90]. A relatively simple experimental technique of obtaining high-resolution, Doppler-free spectra of the sodium 3S-3P single photon transitions is to use saturated absorption spectroscopy.

A few investigations have previously been carried out to examine the Zeeman splitting of the sodium D lines with a Doppler-free laser spectroscopic method. The magnetic splitting and line intensities of the  $3S_{1/2}$ - $3P_{1/2}$  ( $D_1$ ) [91] and  $3S_{1/2}$ - $3P_{3/2}$  ( $D_2$ ) [92] sodium transitions have been studied by Windholz and Musso. They used laser induced fluorescence in an atomic beam to obtain Doppler-free spectra up to magnetic field strengths of  $\sim 300$  G. The line intensity of a given D line hyperfine transition varied with magnetic field strength because of

the change in coupling of the nuclear and electronic angular momenta. The experimental line intensities and frequency splittings agreed well with their developed theoretical calculations. Polarisation spectroscopy has also been used to study Zeeman splittings of the sodium  $D_1$  line [93]. A heterodyning technique produced high resolution experimental spectra which agreed favourably with theory. However, interpretation of the Zeeman spectrum was not straightforward due to the many additional cross-over resonances and comparison between theory and experiment would have been impossible without prior knowledge of the hyperfine structure and g-factors of the atomic states.

Although, as shown later in this chapter, the use of saturated absorption (or saturation) spectroscopy in determining Zeeman structure is also limited by cross-over resonances, it is believed that no previous study has used this laser spectroscopic technique for measuring magnetic field splittings of the sodium  $D_1$  and  $D_2$  resonance lines.

## 4.1 SATURATED ABSORPTION SPECTROSCOPY

### 4.1.1 *Basic Principles of Saturation Spectroscopy*

The resonant interaction of a strong light field with an inhomogeneously broadened atomic transition can produce a velocity selective modification to the level populations in the ground and excited state. Consider the two level atom shown in Figure 4.1 which is interacting with a strong narrow linewidth laser field at frequency  $\omega$ .

When the detuning  $\Delta$  of the laser field from the atomic transition is less than the Doppler width  $\Delta v_D$  then the effect of the strong field is to selectively excite a homogenous velocity group from the ground state. The Doppler width of the transition is

$$\Delta v_D \text{ (HWHM)} = v_{ab} \sqrt{\frac{2k_B T}{Mc^2} \ln 2} \quad (4.1.1)$$

where  $M$  is the mass of the atom,  $k_B$  is Boltzmann's constant and  $T$  is the absolute temperature of the atomic vapour. The component of velocity along the laser beam direction brings a group of atoms exactly into resonance with the laser field by the Doppler effect. A so-called Bennett hole is burnt into the broad inhomogeneous ground state population distribution and a narrow homogeneous velocity group populates the excited state. The change to the population

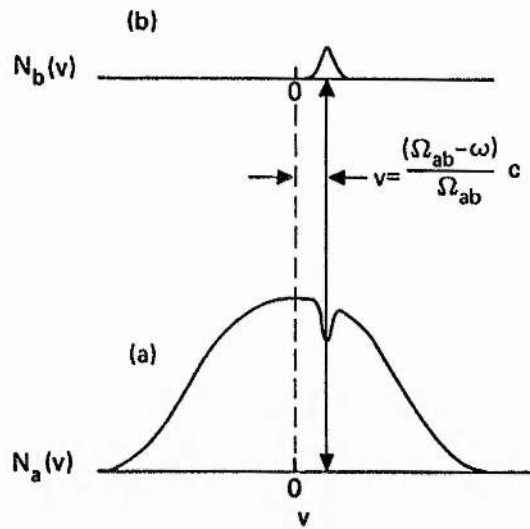


Figure 4.1 : Simple two level atom with resonant frequency  $\Omega_{ab}$  interacting with an intense light field and the inhomogeneous level populations as functions of atomic velocity (from [95]).

distributions by the intense pump laser field is probed by measuring the absorption of a weak counter-propagating laser beam of the same frequency as the pump beam. The intensity of the probe beam is weak so that it does not also perturb the atomic populations. Both waves are usually obtained from the same laser source.

When the laser frequency is scanned across the inhomogeneous atomic transition, the pump and probe beams will interact with equal magnitude velocity groups but opposite in direction due to the beams being counter-propagating. Both waves will only interact with the same homogeneous velocity group when the zero velocity component is excited. The probe wave then experiences less absorption from the ground state due to the hole burning effect of the pump field and the decrease in probe absorption can be detected. This is usually done by modulating the pump beam and detecting the probe absorption change at the modulation frequency with a phase-sensitive detector.

The change (or saturation) in the absorption of the probe wave occurs at the zero velocity frequency of the atomic transition, i.e. the natural atomic frequency, and over a small frequency range due to the narrow homogeneous width of the burnt hole by the pump field. This is the basic principle of saturation spectroscopy to obtain high resolution Doppler-free spectra of atomic transition frequencies.

In the absence of the saturating pump field, the absorption of the probe wave  $\omega_p$  in the inhomogeneously broadened two level atomic medium is given by

$$\alpha_o(\omega_p) = \sqrt{\frac{M}{2k_B T}} \frac{\sigma_o \Delta N_o}{\sqrt{\pi}} \int_{-\infty}^{\infty} \frac{\gamma^2 e^{-Mv^2/2k_B T}}{(\delta - kv)^2 + \gamma^2} dv \quad (4.1.2)$$

where  $\sigma_o$  is the peak atomic absorption cross-section,  $\Delta N_o$  is the thermal population difference between the ground and excited state,  $\delta = \omega_p - \omega_{21}$ ,  $\gamma$  is the inverse of the excited state decay time and the normalised Maxwell distribution of atomic velocities has been used. The line shape of  $\alpha_o(\omega_p)$  is the convolution of a Lorentzian with a Gaussian lineshape and is named a Voigt profile. With a resonant saturating field at frequency  $\omega_s$ , the absorption coefficient for the probe wave becomes

$$\alpha(\omega_p, \omega_s) = \sqrt{\frac{M}{2k_B T}} \frac{\sigma_o}{\sqrt{\pi}} \int_{-\infty}^{\infty} \left[ 1 - \frac{G\gamma^2}{(\omega_{21} - \omega_s - k_s v)^2 + [\gamma(1+G)]^2} \right] \frac{\gamma^2}{(\delta - k_p v)^2 + \gamma^2} \exp(-Mv^2/2k_B T) dv \quad (4.1.3)$$

This is again a Voigt profile but now a "hole" has been created in the absorption of the probe wave at the frequency of the pump wave. The power broadened width (HWHM) of the burnt hole is  $\gamma(1+G)^{1/2}$  where  $G$  is the saturation parameter

$$G = I_s / I_{sat} \quad (4.1.4)$$

$I_{sat}$  is the saturation intensity ( $Wm^{-2}$ ) of the atomic transition and is defined as the pump laser intensity required to make the probe absorption coefficient one half of the unsaturated value  $\alpha_o$ .

For a simple two-level atomic transition and only spontaneous decay from the excited state

$$I_{sat} = \frac{nc \epsilon_0}{2} \frac{\hbar^2}{|\mu_{21}|^2} \gamma^2 \quad (4.1.5)$$

where  $|\mu_{21}|$  is the dipole matrix element for the transition (see also § 6.5.1).

More detailed descriptions of saturation spectroscopy and of the interaction of resonant light fields with atomic transitions, including coherence effects and other subtleties, can be found in references 7, 49, 94, 95, 96 and 97.

#### 4.1.2 Line Broadening Mechanisms

Several factors can contribute to the measured homogeneous linewidth of the saturated absorption spectrum [148]. The relative magnitudes of these contributions is important when using this nonlinear spectroscopic technique to study closely spaced transition frequencies which are expected for the Zeeman structure of the sodium 3S-3P resonances. If the experimental linewidth is large compared to the magnetic splitting then the different Zeeman hyperfine transitions may not be resolved.

(a) **Natural broadening** - If spontaneous emission from the excited state is the only decay process in the two level atomic system, then the measured saturated absorption linewidth  $\gamma$  (HWHM) is equal to the inverse of the lifetime  $\tau$  of the excited state.

$$\Delta\omega \text{ (HWHM)} = \gamma = 1/\tau \quad (4.1.6)$$

For sodium, the lifetime of the 3P states is 16ns and this gives a natural linewidth  $\Gamma$  ( $= \gamma/2\pi$ ) = 10 MHz (HWHM).

(b) **Power broadening** - The linewidth of the burnt hole in the ground state population distribution depends upon the intensity of the pump field as shown in equation (4.1.3). This is due to induced stimulated emission and absorption by the pump field decreasing the effective lifetime of the excited state. The increase in linewidth is  $(1+G)^{1/2}$  times the homogeneous linewidth due to natural decay and collisions. (See also § 6.5.1)

$$\Delta\omega = \Delta\omega_h (1+G)^{1/2} \quad (4.1.7)$$

The saturation intensity for sodium 3S-3P transitions is  $\sim 6.4 \text{ mW cm}^{-2}$  therefore the pump beam intensity should be comparable to or a few times this value to avoid serious power broadening.

(c) **Transit-time broadening** - Although the lifetime of the ground state of the two

level atomic system is approximated to be infinite, there is a finite interaction time of an atom with the pump and probe fields due to the thermal motion of the atom through the laser beam. This interaction time  $T$  introduces transit-time broadening with a linewidth contribution (HWHM) of  $\sim 2.79/T$ . The motion of an atom with velocity  $v$  through a laser beam of diameter  $d$  gives the broadening as

$$\Delta\omega \text{ (HWHM)} = 2.79 \frac{v}{d} \quad (4.1.8)$$

An average thermal velocity of  $\sim 500 \text{ ms}^{-1}$  and a laser beam diameter of  $\sim 1 \text{ mm}$  gives a broadening of  $\sim 220 \text{ kHz}$ .

(d) **Spherical wavefronts** - The wavefront curvature of a Gaussian laser beam restricts the effective transit time and can broaden the saturated absorption linewidth.

The linewidth contribution is

$$\Delta\omega \text{ (HWHM)} \approx \pi \sqrt{2 \ln 2} \ vw / R\lambda \quad (4.1.9)$$

where  $v$  is the velocity of the atom through the laser beam of width  $w$ , wavefront radius of curvature  $R$  and wavelength  $\lambda$ . In order that the curvature of the wave surface does not much broaden the homogeneous linewidth  $R \gg \pi w^2/\lambda$ , eg. for  $w = 1 \text{ mm}$ ,  $\lambda = 600 \text{ nm} \Rightarrow R \gg 5 \text{ m}$ . In general, a very flat wave surface should be used for very high resolution spectroscopy but with the above values and  $v \sim 500 \text{ ms}^{-1}$ , the broadening is only  $\sim 100 \text{ kHz}$ .

(e) **Residual Doppler broadening** - If the counter-propagating pump and probe beams are not collinear but cross at a small angle  $\theta$ , there is a residual Doppler broadening due to slightly different velocity groups being probed and pumped. The linewidth contribution is

$$\Delta\omega \text{ (HWHM)} \approx 0.6 \theta \Delta\omega_D \quad (4.1.10)$$

where  $\Delta\omega_D$  (HWHM) is the Doppler width given in equation (4.1.1). The sodium 3S-3P Doppler width (FWHM), at normal sodium vapour temperatures, is  $\sim 1.5 \text{ GHz}$ , which requires the crossing angle to be  $\theta \leq 11 \text{ mrad}$  in order for natural broadening to still limit the saturated absorption linewidth.

(f) **Pressure broadening** - The presence of an inert buffer gas with the atomic system

under study can increase the saturated absorption linewidth through non-radiative decay processes (see also § 6.4). This gives an additional increase in the homogeneous linewidth of

$$\Delta\nu (\text{HWHM}) = \beta P \quad (4.1.11)$$

where  $\beta$  (MHz/mbar) is the pressure broadening coefficient and  $P$  (mbar) is the perturber gas pressure. Typical values of  $\beta \sim 25$  MHz/mbar but if the buffer gas pressure is low then pressure broadening can be neglected. Sodium atom collisions are also rare at low atomic densities and can be neglected.

#### 4.1.3 Crossover Resonances

The ideal two level atomic system discussed so far is not often appropriate to real experimental situations. Usually other degenerate or non-degenerate energy levels lie within the same Doppler width and these produce additional resonance effects in the saturated absorption spectrum. Consider the two common cases of:

- (i) Two transitions sharing a common ground state level.

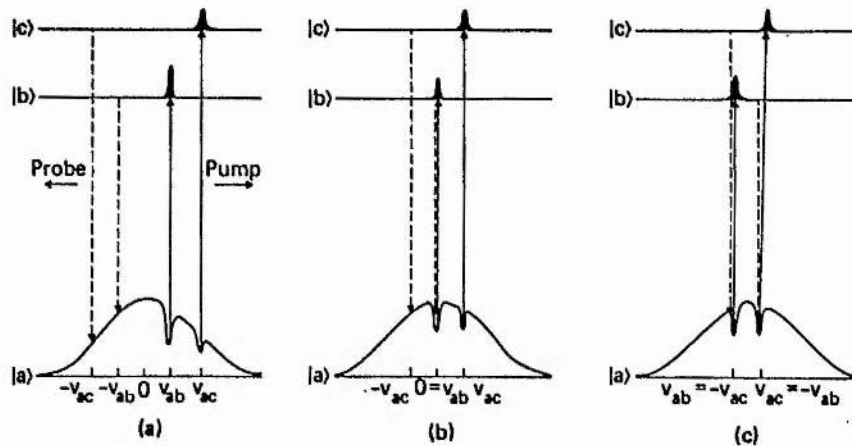


Figure 4.2 : Schematic three level atom interacting with a pump and probe field (from [95]).

The pump field creates two homogeneous holes in the ground state population distribution at velocities  $v_{ab}$  and  $v_{ac}$  due to the  $|a\rangle \rightarrow |b\rangle$  and  $|a\rangle \rightarrow |c\rangle$  transitions

respectively. When  $\omega = \omega_{ab}$  or  $\omega = \omega_{ac}$ , the pump and probe waves interact with the same  $v = 0$  velocity group and the normal saturated decrease in the probe beam absorption occurs. However, when  $\omega_s$  is tuned halfway between  $\omega_{ab}$  and  $\omega_{ac}$ , the probe wave connected with the  $\omega_{ab}$  transition interacts with the hole produced by the pump wave at the  $\omega_{ac}$  transition frequency and vice versa. This produces an apparent resonant decrease in the probe absorption and gives rise to a crossover resonance.

(ii) Two transitions sharing a common excited state.

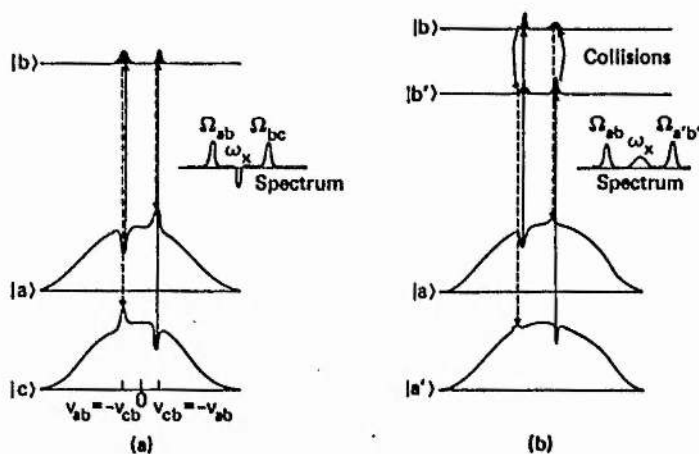


Figure 4.3 : Schematic three level atom with two ground states interacting with a pump and probe field of frequency  $\omega$  (from [95]).

Velocity selective optical pumping produces a crossover resonance when atoms in the excited state  $|b\rangle$  can relax to either of the ground state levels  $|a\rangle$  and  $|c\rangle$ . As shown in Figure 4.3 (a), a pumped homogeneous group of atoms relaxing back to the initially pumped ground state can be excited again by the strong laser field but atoms decaying into the other ground state level can be removed only by the weak probe beam and by slow relaxation processes. If collisions are weak then this optical pumping process remains velocity selective.

As the frequency  $\omega$  is tuned across the inhomogeneous profile, there appears to be a resonant increase in probe absorption when  $\omega$  is halfway between the  $|a\rangle \rightarrow |b\rangle$  and  $|c\rangle \rightarrow |b\rangle$  transition frequencies due to the velocity selective optical pumping.

Other cross-over resonances can also occur when different transitions apparently have no common levels as shown in Figure 4.3 (b). Collisional transfer of population between two radiating unconnected atomic levels which retains the velocity selective nature of the process can mix the saturation behaviour of the probe absorption due to the different atomic transitions. Four level cross-over resonances can occur [98], e.g. if the level  $|a\rangle$  in Figure 4.3 (a) is also connected to an excited state  $|d\rangle$ , then the velocity selective optical pumping on the  $|c\rangle \rightarrow |b\rangle$  transition can produce a saturated absorption cross-over resonance for the probe wave on the  $|a\rangle \rightarrow |d\rangle$  atomic transition.

The appearance of cross-over resonances complicates the saturated absorption spectrum and makes interpretation difficult in the absence of some prior knowledge of the actual atomic transition frequencies. The crossover signals can be suppressed by modulating the ground state populations (at a different modulation frequency from the original saturating beam) with a second saturating laser beam tuned to the centre of one of the atomic transitions [99]. This ensures that the saturated absorption signal only originates from the  $v = 0$  atomic homogeneous group by detecting the phase sensitive signal at the sum of the two modulation frequencies.

#### 4.1.4 *Optical Pumping*

If the atomic system under study has two ground states both radiatively coupled to an excited state, as shown in Figure 4.3 (a), then optical pumping in the ground state can change the effective saturation intensity. The effect of optical pumping in saturated absorption spectroscopy has been studied in atomic barium [100]. Optical pumping removes population from the ground state level in resonance with the pump laser field and transfers it to the other relatively long lived ground state level. This makes it easier to saturate the absorption from the pumped ground state and hence the required saturation intensity is decreased by a factor of  $\sim 2\tau/T$  where  $\tau$  is the radiative lifetime of the upper excited state and  $T$  is the shortest relaxation time for the optical pumping (eg. due to the finite transit-time of an atom through the laser beam or collisions with the cell walls). Typically  $\tau \sim 10$  ns and  $T \sim 1$   $\mu$ s, so the reduction in saturation intensity is  $\sim 100$  times. Velocity selective optical pumping (VSOP) is a Doppler-free spectroscopic technique which measures the absorption or polarisation of a probe beam due to

the selection of a homogeneous velocity group by single-mode laser optical pumping [101]. Saturation of the atomic resonance line under study is not required with this method and therefore no power broadening is present to increase the linewidth [102, 103].

#### 4.1.5 Velocity Changing Collisions

Since saturation spectroscopy is a velocity selective nonlinear spectroscopic technique, any perturbation of the atomic system which changes the atomic velocity can have serious implications for the saturated absorption spectrum. Velocity changing collisions (vcc), due to elastic collisions between the atom under study and inert buffer gas atoms, change the velocity but not the atomic state of the active atom. With an applied resonant saturating field, vcc's change the velocity of the nonresonant homogeneous velocity groups so that they can also be excited by the laser field. As shown in Figure 4.4, this fills in the burnt hole in the ground state population distribution at the saturating field frequency and results in excitation of atoms across the whole inhomogeneous Doppler width. The effect of vcc and phase-changing collisions on the saturated absorption lineshape has been studied in the time-delayed mode by Ducloy and Feld [103a,103b].

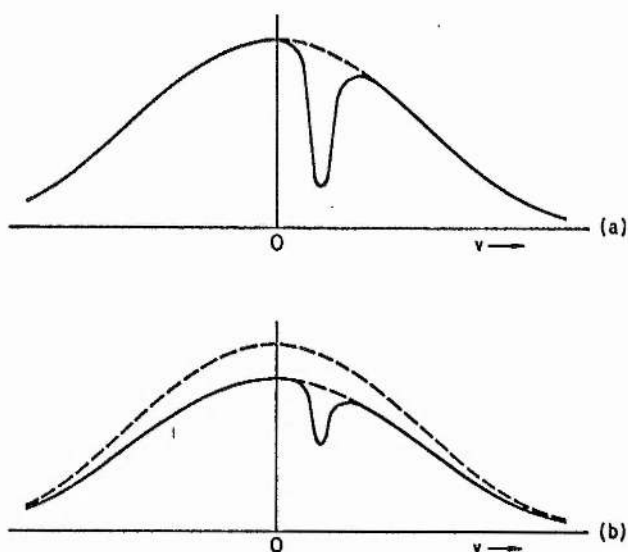


Figure 4.4 : Hole burning in the ground state velocity distribution:  
(a) no vcc, (b) in the presence of vcc. (from [96])

The vcc tend to only thermalise the ground state population distribution since this state

is long lived compared to the excited state.

In the presence of vcc, the saturated absorption spectrum is changed from being a narrow Lorentzian line on zero background (due to phase sensitive detection) to a residual narrow resonance on a broad thermal distribution [104]. Similar broadening effects due to vcc are seen in VSOP [105, 106]. The increase in the measured saturation spectrum linewidth due to vcc was seen in the first pulsed saturated absorption study in sodium [107]. Increasing the time delay between the pump and probe pulses in the presence of ~3 torr of Ar buffer gas showed complete thermalisation of the velocity selected groups in ~150 ns.

A simple rate equation description of a two level atomic system gives the time dependent variation of a given velocity group due to vcc as [105]

$$\left. \frac{dn_i(v)}{dt} \right|_{\text{vcc}} = \Gamma_v [f(v) N_i - n_i(v)] \quad (4.1.12)$$

where  $\Gamma_v$  is the vcc rate,  $f(v)$  is the normalised Maxwell thermal velocity distribution function and  $N_i$  is the total population density of the ground state. A more complete collisional model of the effect of vcc on the saturated absorption lineshape gives [104]

$$I(\Delta) \propto \left[ \frac{1}{2} \frac{\gamma^2}{\gamma^2 + \Delta^2} + \sqrt{\Pi} \frac{\gamma}{ku} \sum_{n=1}^{\infty} \left( \frac{\Gamma_{\text{vcc}}}{\Gamma_t} \right)^n \frac{1}{(1 - \alpha^{2n})^{\frac{1}{2}}} \right. \\ \left. \exp \left( - \frac{\Delta^2}{k^2 u^2} \frac{1 + \alpha^n}{1 - \alpha^n} \right) \right] \exp \left( - \frac{\Delta^2}{k^2 u^2} \right) \quad (4.1.13)$$

where  $\Delta = \omega_{21} - \omega$  is the laser detuning from the atomic resonance,  $\gamma$  (HWHM) is the linewidth of the narrow saturated absorption resonance and  $u$  is the most probable speed of the equilibrium velocity distribution ( $= (2k_B T/M)^{\frac{1}{2}}$ ). The parameter  $\alpha$  is related to the strength of a hard-sphere collision and can be calculated as a function of the perturber/active atom mass ratio [108]. The total decay rate  $\Gamma_t$  is the sum of the excited state decay rate  $\Gamma$  ( $= 1/\tau$ ) and the vcc rate  $\Gamma_{\text{vcc}}$ . This lineshape has a simple interpretation. The first term is due to atoms undergoing no vcc during their interaction with the light fields and is a Lorentzian with a narrow homogeneous linewidth. The second term is due to atoms which have undergone

partial thermalisation due to vcc giving a broad inhomogeneous Gaussian contribution to the overall lineshape. The width of this vcc contribution (FWHM) is  $\Delta v_{\text{Doppler}}/\sqrt{2}$ .

For a continuous-wave (cw) excitation scheme for saturation spectroscopy, the broadening effects of the vcc will dominate over the homogeneous saturation since the interaction time of the atoms with the laser fields (transit-time) is generally much greater than the velocity thermalisation time due to vcc.

#### 4.2 EXPERIMENTAL ZEEMAN SPLITTINGS MEASURED BY SATURATION SPECTROSCOPY

Preliminary experimental measurements of the Zeeman splitting of the sodium 3S-3P transitions by saturation spectroscopy were made with the classic Hänsch-Borde arrangement schematically shown in Figure 4.5.

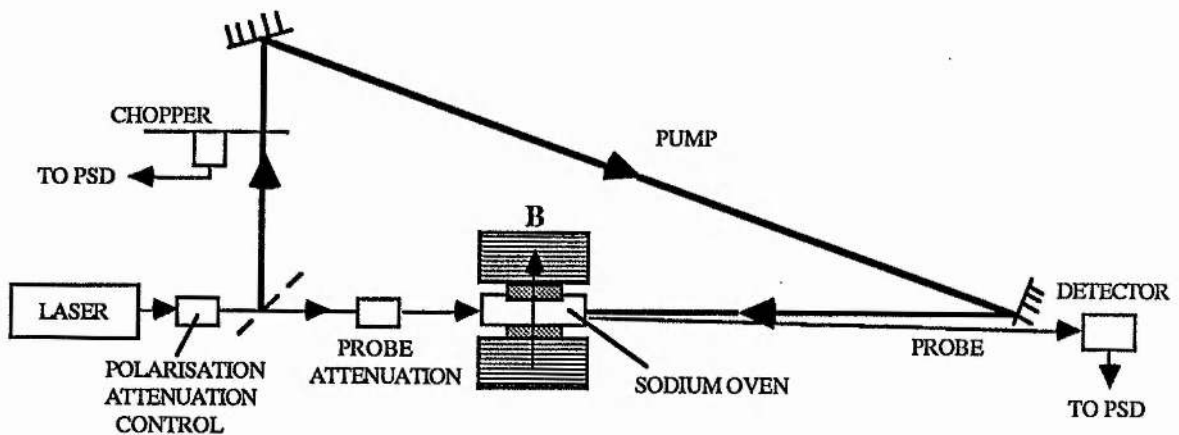


Figure 4.5 : Schematic diagram of the experimental apparatus used for saturation spectroscopy.

The pump and probe beams are both derived from the same single-mode laser source and counterpropagate in the sodium heat-pipe oven at a small angle. The pump beam is modulated with a mechanical chopper and the probe absorption signal at the modulation frequency is processed by a phase-sensitive lock-in detector.

Figure 4.6 shows the experimental saturated absorption spectrum for the sodium  $D_2$  line ( $3S_{1/2} - 3P_{3/2}$ ) obtained with a very small transverse magnetic field ( $\sim 40$  G) and the laser linear polarisation perpendicular to the magnetic field direction ( $\Delta M_F = \pm 1$  excitation).

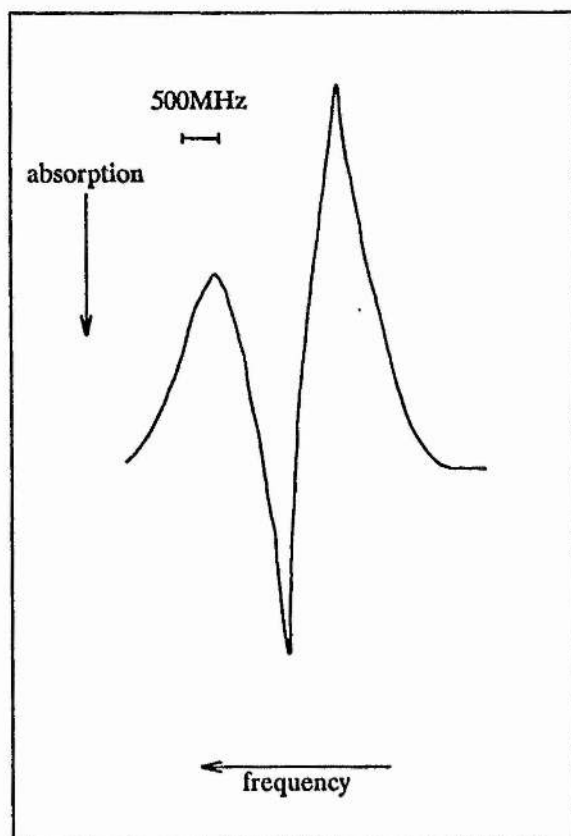


Figure 4.6 : Experimental saturated absorption spectrum for the sodium  $D_2$  transition with  $B \approx 40$  G,  $T \sim 100^\circ\text{C}$ .

In spite of the slight Zeeman splitting and power broadening, the spectrum obviously does not just consist of narrow ( $\sim$  few tens of MHz) Lorentzian lineshapes as would be expected by phase sensitive detection with no vcc (see energy level structure for Na in Chapter 2). The dominating component is a broad ( $\sim 1$  GHz) inhomogeneous line associated with each ground state hyperfine level due to vcc. Although no buffer gas was added to the sodium oven for this experiment, there is sufficient outgassing and leaks in the oven to raise the background gas pressure for vcc to take place. At these low Na densities there are very little vcc's between the sodium atoms themselves [107]. The linewidth of the broad pedestal indicates that nearly complete velocity thermalisation has been achieved by vcc ( $\Delta v_D/\sqrt{2} = 1.03$  GHz  $\approx$  measured linewidth).

The optical pumping crossover resonance at a frequency midway between the  $F=1$  and

F=2 ground state transition frequencies is well shown as the increase in probe absorption.

To attempt to reduce the sensitivity of the saturated absorption signal to the broadening effects of vcc's, the experiment was adapted to a novel quasi-pulsed arrangement. If the optical pumping rate to produce saturation is made greater than the vcc rate due to buffer gas collisions, then by switching on the pump light faster than  $1/\Gamma_{\text{vcc}}$ , the saturated absorption signal at the start of the pump light pulse should be relatively free of vcc effects. Saturation spectroscopy using pulsed lasers is free of vcc effects when there is no delay between the pump and probe pulses due to this difference in saturating and vcc rates.

For the cw pump beam considered here a relatively fast switch on/off time ( $<1 \mu\text{s}$ ) was achieved by using two  $\times 20$  microscope objectives to focus and recollimate the pumping beam through the chopper blade. A R212 photomultiplier tube biased with a  $50 \Omega$  resistor and a  $\sim 14$  dB high speed amplifier (NE5539 built on a Radiospares RS435-664) was used as a sensitive submicrosecond response time detector for the probe beam signal. To selectively examine the saturated absorption signal at various parts of the  $\sim 500 \mu\text{s}$  long pump pulse, a Brookdeal boxcar system was used. This was synchronised to the chopped pump beam by sampling a small part of the pump beam with a BPX65 photodiode (risetime  $\sim 1$  ns) biased with a  $50 \Omega$  resistor. This reduced the pulse to pulse jitter which occurred when the boxcar was triggered from the electronic signal generated by the mechanical chopper.

Even with a probe beam power of only  $\sim 20 \mu\text{W}$ , the signal from the photomultiplier tube tended to be saturated when the pump beam was on with a DC level of  $\sim -1.5$  V and an AC saturated absorption signal of  $\sim 50$  mV. However, saturating the photomultiplier tube produced an apparent peak on the leading edge of the modulated saturated absorption signal when the laser was tuned onto a hyperfine transition (see Figure 4.7) and measuring this part of the signal enhanced the peaks of the saturation spectrum. The large peak indicated that the pump beam may have been significantly changing the absorption for the probe beam and allowing much more light onto the photomultiplier tube. This effect of the peak seemed to be purely an experimental manifestation. The magnitude of the peak was critically dependent on the position of the probe beam on the photomultiplier photocathode. Side-on tubes such as the R212 are noted for their non-uniform spatial performance [109].



Figures 4.8(a) and 4.8(b) show the experimental saturation spectra for a low value of magnetic field ( $\sim 40$  G) and two different linear polarisations of the light relative to the magnetic field direction to excite  $\Delta M_F = 0$  and  $\Delta M_F = \pm 1$  hyperfine transitions.

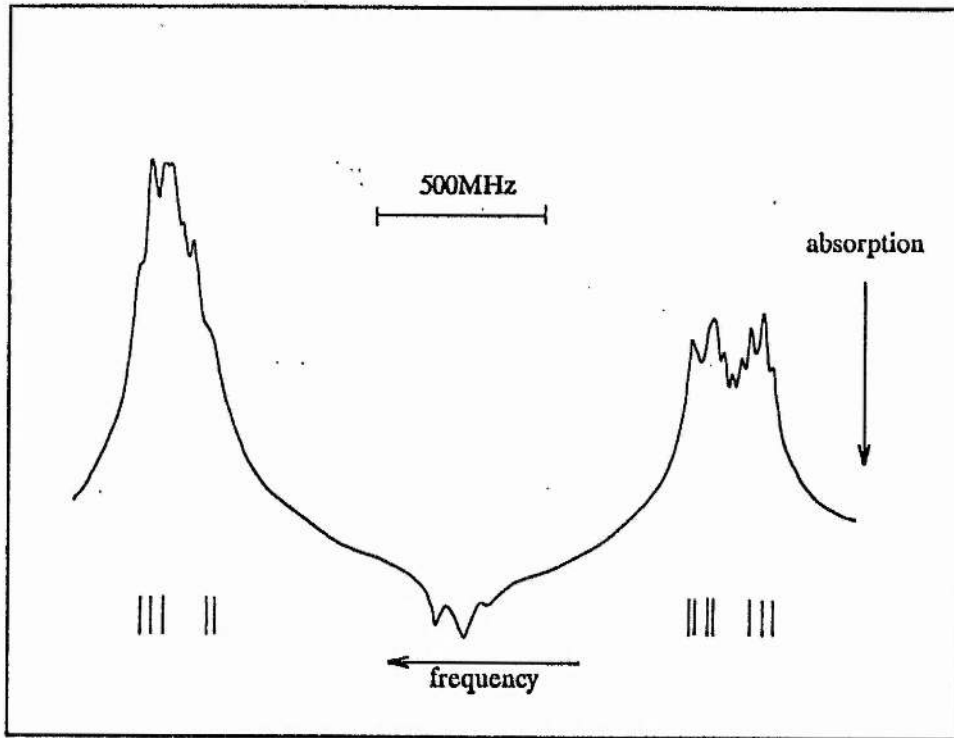


Figure 4.8 (a): Experimental saturation spectrum for Na  $D_1$  line and theoretical hyperfine splittings.  
 $B \approx 40$  G

$\Delta M_F = 0$   
 Boxcar gate width  $\sim 2 \mu\text{s}$   
 $T \sim 120^\circ\text{C}$

Comparing this spectrum to Figure 4.6 shows the great benefit in using this new adapted spectroscopic technique. The individual hyperfine transitions are fairly well resolved and the broad pedestal due to vcc is reduced. The optical pumping crossover resonances at a frequency halfway between the  $F=1$  and  $F=2$  ground states are well resolved but note the additional crossover resonances within

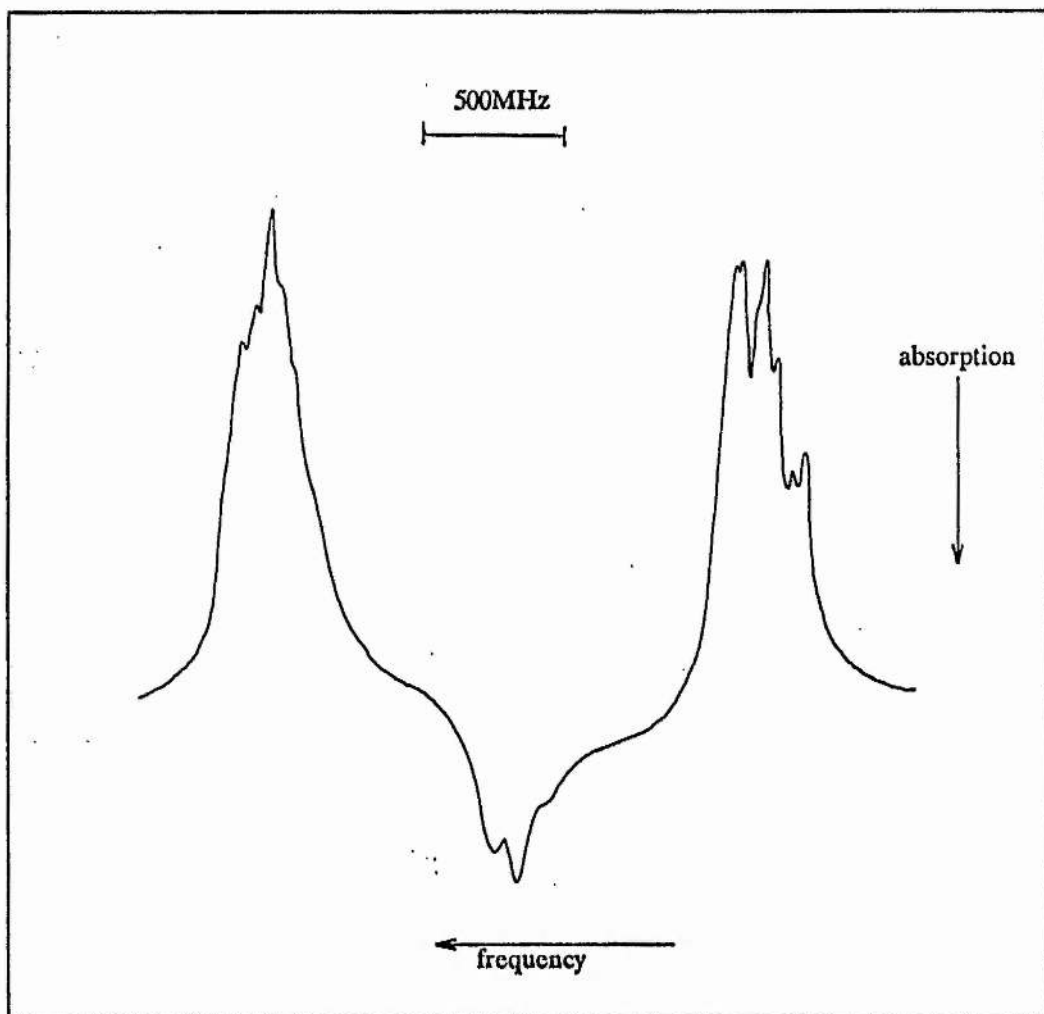


Figure 4.8(b) : Experimental saturation spectrum for Na  $D_1$  line.  
 $B \approx 40$  G

$\Delta M_F \pm 1$   
 Boxcar gate width  $\sim 2 \mu\text{s}$   
 $T \sim 120^\circ\text{C}$

each group of hyperfine transitions originating from the  $F=1$  and  $F=2$  ground states. These crossover resonances are due to three and four level effects as previously discussed. The appearance of these resonances complicates the Zeeman spectrum, especially at higher values of magnetic field where the hyperfine transition frequency splittings are larger. This leads to a difficulty in interpreting the saturated absorption spectrum as with polarisation spectroscopy and is a limitation of this spectroscopic technique. Some comparison of the measured Zeeman/Paschen-Back/Back-Goudsmit hyperfine transition frequency splittings could be made

though to verify that the previous calibration of the magnetic field strength with a Hall probe was reasonably accurate.

The experimental advantage of measuring the saturated absorption signal at the start of the pump light pulse where the large peak was evident and vcc broadening effects should have been reduced is shown in Figures 4.9 (a) and (b) where the boxcar gate is set at two different parts of the chopped pump pulse (saturated photomultiplier tube).

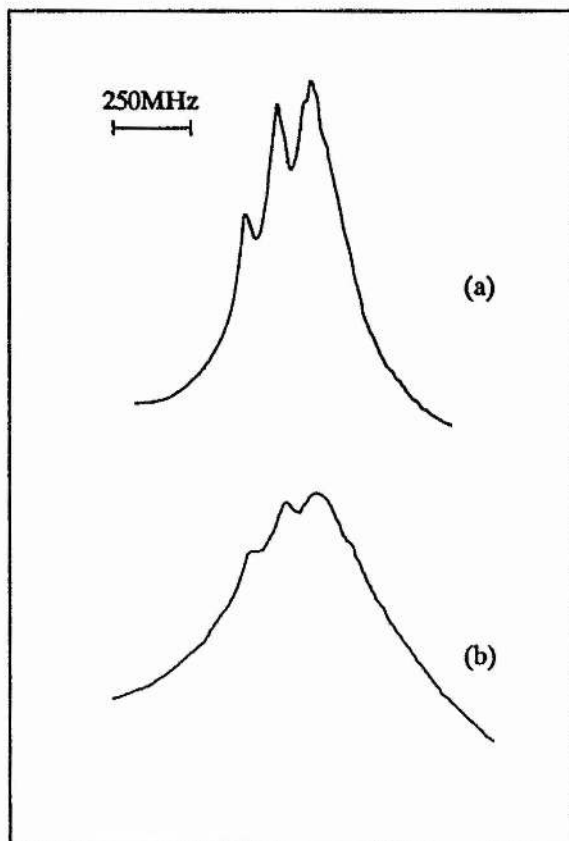


Figure 4.9 : Experimental saturation spectra for the  $3S_{1/2} (F=1) \rightarrow 3P_{1/2}$  transition.

- (a) Boxcar gate on start of pump pulse
  - (b) Boxcar gate delayed  $\sim 6 \mu\text{s}$  from start of pump pulse
- $T \sim 120^\circ\text{C}$   
 $B \sim 100 \text{ G } (\Delta M = \pm 1)$   
Boxcar gate width  $\sim 2 \mu\text{s}$

The saturated absorption signal with the delayed gate time shows increased broadening and less distinct narrow resonances which may have been due to vcc having had time to deplete and redistribute the burnt homogeneous hole across the inhomogeneous velocity distribution.

By using the boxcar system to scan the gate across the whole of the chopped light pulse, a complete picture of the saturated absorption pulse with the photomultiplier tube unsaturated could be obtained and the different excitation and relaxation time constants were measured upon changing the laser detuning and buffer gas pressure. Figure 4.10 (a) and (b) shows the saturated absorption pulse with no buffer gas added to the sodium heat-pipe oven and tuned exactly on and well off a Zeeman hyperfine transition respectively. The measured pumping time constant for the signal when the laser is tuned onto a Zeeman transition is  $\tau_{\text{pump}} \sim 8 \mu\text{s}$ . When the laser is tuned off resonance so that the saturated absorption signal is due to vcc, the overall change in probe absorption is reduced and the estimated vcc time constant  $\tau_{\text{vcc}} \sim 40 \mu\text{s}$ . In both cases, when the pump light is switched off, the saturation signal decreases exponentially due to relaxation of the optical pumping. The measured relaxation time for no added buffer gas is  $\tau_{\text{relax}} \sim 62 \mu\text{s}$ .

When buffer gas is deliberately added to the heat-pipe oven there are three main effects. The first is that no narrow Doppler-free peaks can now be resolved due to the rapid thermalisation of the homogeneous saturation by the increased number of buffer gas atoms and collisional broadening. The time constant for vcc is also reduced, as expected, and decreases with increasing buffer gas pressure. Thirdly, the relaxation time constant  $\tau_{\text{relax}}$  was measured to increase with increasing buffer gas pressure suggesting that the relaxation of the optical pumping was due to a transit time effect. Increasing the buffer gas pressure slows the diffusion of the pumped atoms from the probe-beam region and leads to less rapid relaxation (see Chapter 7). The saturated absorption pulses for two different buffer gas pressures and the laser tuned off resonance so that the signal was due to vcc are shown in Figure 4.11 (a) and (b).

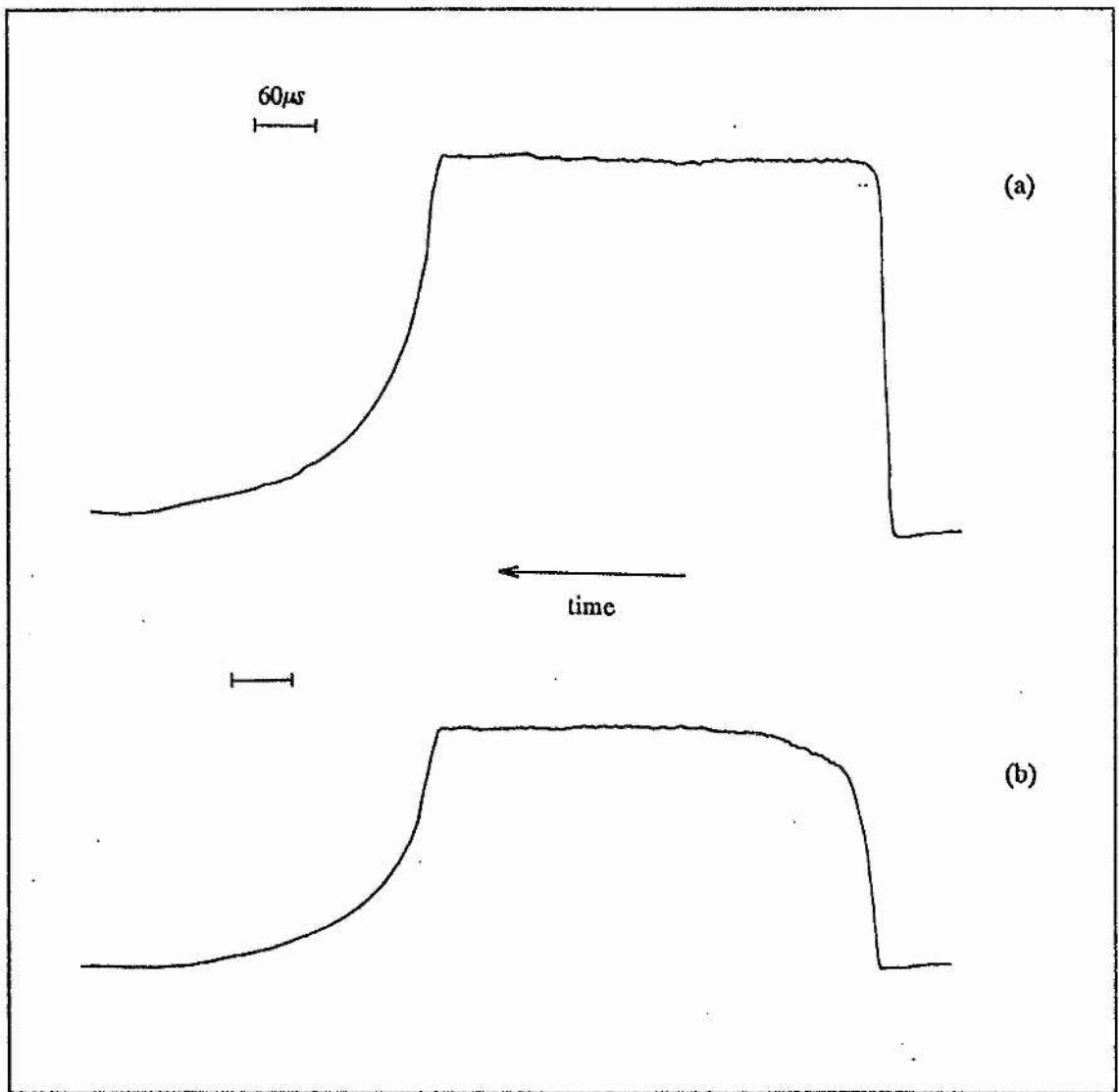


Figure 4.10: Chopped saturated absorption signal with no added buffer gas (Na  $D_1$  line).

- (a) Laser tuned on a hyperfine resonance
- (b) Laser tuned off resonance
- $T \sim 120^\circ\text{C}$
- $B \sim 40 \text{ G}$  ( $\Delta M = \pm 1$ )

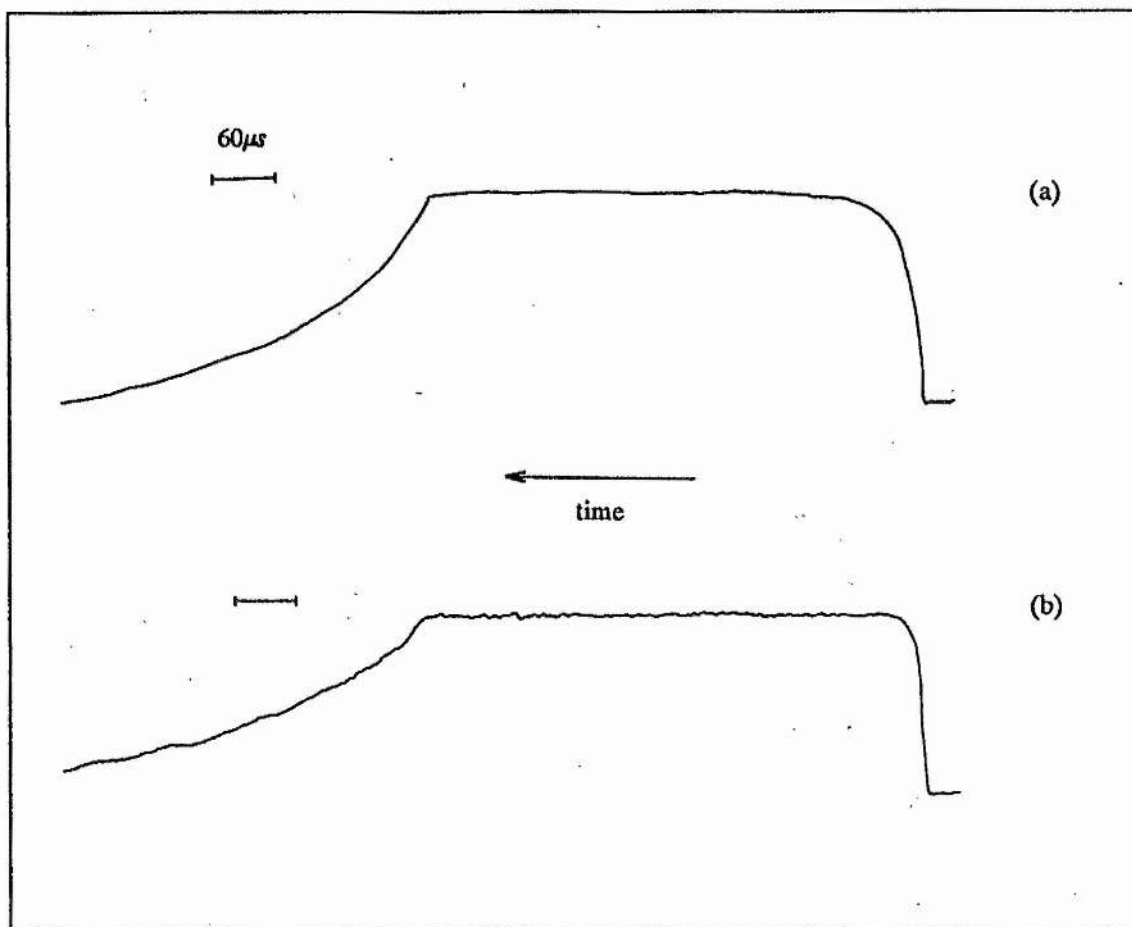


Figure 4.11 : Chopped saturated absorption signal with buffer gas added to sodium oven. Laser tuned off resonance on Na  $D_1$  line.  
 $T \sim 120^\circ\text{C}$   $B \sim 40 \text{ G}$  ( $\Delta M = \pm 1$ )

- (a)  $\sim 1.5 \text{ mbar of He}$   
 $\tau_{\text{vcc}} \sim 25 \mu\text{s}$        $\tau_{\text{relax}} \sim 160 \mu\text{s}$
- (b)  $\sim 10 \text{ mbar of He}$   
 $\tau_{\text{vcc}} \sim 7 \mu\text{s}$        $\tau_{\text{relax}} \sim 175 \mu\text{s}$

# CHAPTER 5

MAGNETIC FIELD INDUCED  $\chi^{(2)}$   
SUM FREQUENCY MIXING

## Chapter 5

### MAGNETIC FIELD INDUCED $\chi^{(2)}$ SUM FREQUENCY MIXING

With the application of a transverse magnetic field to an atomic vapour, the induced  $\chi^{(2)}$  nonlinearity is not restricted to allow only second harmonic generation (SHG) to become possible. Other nonlinear three-wave mixing processes such as sum-frequency mixing (SFM), difference frequency mixing (DFM) and parametric amplification are also permissible. As reviewed in Chapter 1, the first two of these nonlinear effects have been demonstrated in atomic vapours under the symmetry breaking action of transverse electric or magnetic fields. These investigators all used large bandwidth pulsed lasers to verify bulk and certain microscopic properties of the nonlinear optical effects with low resolution.

This is the first reported investigation of a continuous-wave (cw), three-wave SFM process using a transverse DC magnetic field to induce the  $\chi^{(2)}$  nonlinearity. High resolution studies were carried out using two single mode lasers to examine the microscopic behaviour of SFM. Bulk effects of the nonlinear medium were studied by the phase matching behaviour of SFM under cw excitation.

SFM can be regarded as a non-degenerate case of SHG where the two fundamental interacting photons have different energies. The SFM nonlinear optical process must satisfy the law of conservation of energy  $\omega_1 + \omega_2 = \omega_3$  and of momentum  $\mathbf{k}_3 = \mathbf{k}_1 + \mathbf{k}_2$ . With an atomic vapour as a nonlinear medium,  $\omega_1$ ,  $\omega_2$  and  $\omega_3$  are often chosen to be close to natural atomic resonant frequencies to give resonant enhancement of the nonlinear optical process [37]. The other oscillating nonlinear polarisations at  $2\omega_1$ ,  $2\omega_2$  and  $\omega_1 - \omega_2$  are usually far from atomic resonances and are neglected.

The SFM experiments reported here used the same sodium 3S-4D two-photon transitions for resonant enhancement of the sum frequency  $\omega_3 (= \omega_1 + \omega_2)$  as were used in SHG for resonant enhancement of the second harmonic frequency [43]. For SHG, the single

photon detuning  $\Delta_1$  was  $\sim 300 \text{ cm}^{-1}$  but with SFM additional single photon resonant enhancement was obtained by tuning  $\omega_1$  closer to the 3S-3P D line transitions. The frequency  $\omega_2$  was varied to retain on-resonance two-photon resonant enhancement. The single photon detuning was kept larger than the Na 3S-3P transition Doppler width so that no population was excited into the intermediate state for this particular case. A schematic diagram of the sodium energy levels involved in the magnetic field induced SFM nonlinear optical process and the interacting frequencies was given in Figure 1.4

## 5.1 SFM : MICROSCOPIC EFFECTS

As might be anticipated, the microscopic behaviour of magnetic field induced SFM was found to be the same as for SHG in sodium vapour. This was due to the use of the same resonant 3S-4D two-photon transitions in both processes and the SFM single photon detuning greater than the D line Doppler width.

### 5.1.1 *Combination of $\omega_1$ and $\omega_2$ for SFM*

The wavelengths  $\lambda_1$  and  $\lambda_2$  of the two fundamental laser beams were each varied over  $\sim 15 \text{ nm}$  from the SHG wavelength of  $578.7 \text{ nm}$ . Coherent SFM signals at  $289.4 \text{ nm}$  were detected for each particular value of  $\lambda_1$  and  $\lambda_2$  provided that  $\omega_1 + \omega_2 = \omega_{3S-4D}$  and the transverse magnetic field was non-zero. This tuning range was limited by the gain curve of the rhodamine 6G dye lasers. The wavelengths  $\lambda_1 = 589.0 \text{ nm}$  and  $\lambda_1 = 589.6 \text{ nm}$  were excluded from the combination of  $\lambda_1$  and  $\lambda_2$  since these wavelengths correspond to direct excitation of the  $D_2$  and  $D_1$  sodium transitions respectively.

### 5.1.2 *Magnetic Field Strength*

The SFM power variation with the strength of the transverse magnetic field was measured with  $\lambda_1 = 591.55 \text{ nm}$  (polarisation perpendicular to the magnetic field direction) and  $\lambda_2 = 566.458 \text{ nm}$  (polarisation parallel to the magnetic field direction). One beam at wavelength  $\lambda_1$  came from the cw standing wave dye laser with the linewidth narrowed to

~27 GHz with a two-plate intracavity birefringent filter. The second beam at  $\lambda_2$  came from the Spectra-Physics 380D single-mode ring dye laser.

For low magnetic field strengths ( $\leq 500$  G), the SFM power increased proportionally with the square of the magnetic field as shown in Figure 5.1. For higher magnetic field strengths, the total SFM power saturated due to the Zeeman splitting in the 3S and 4D sodium states exceeding the two-photon Doppler width. This is clearly evident in Figure 5.2 where because the resolution limiting linewidth of  $\omega_1$  was much larger than the Zeeman splitting, no line profile structure was resolved and the total SFM power was measured.

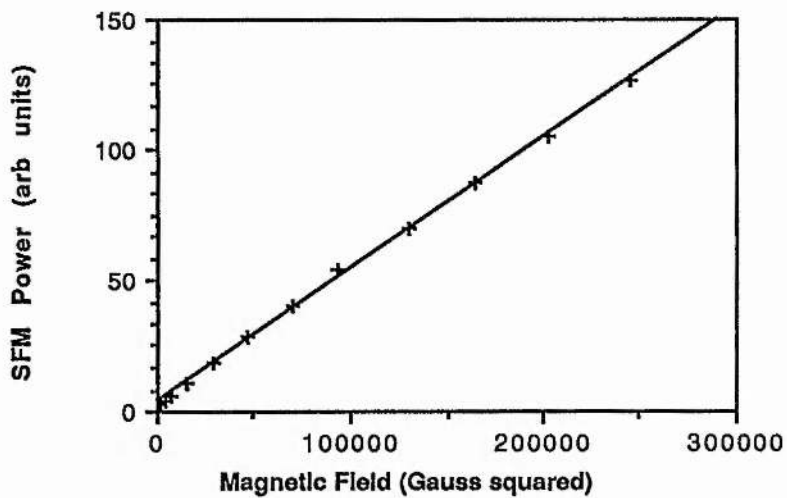


Figure 5.1 : Experimental results of SFM power against the square of the magnetic field strength for low fields ( $\leq 500$  G).

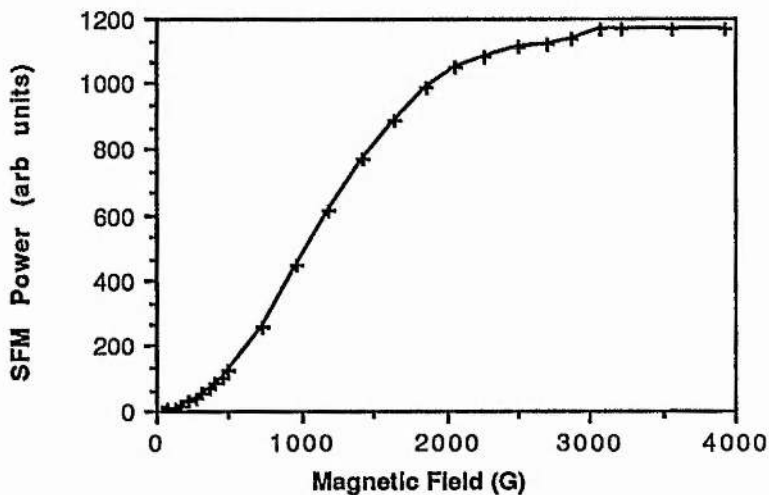


Figure 5.2 : Experimental results of SFM power against magnetic field strength.

### 5.1.3 Laser Intensity

For SHG, the intensity of the second harmonic wave depended upon the square of the intensity of the fundamental beam. For SFM the situation is different because a photon must be simultaneously absorbed from each beam separately. The SFM power depends upon the product of the laser powers at the two individual frequencies. Figure 5.3 shows the experimental variation of the SFM power against the power of the beam at  $\omega_1$  and  $\omega_2$ . As expected, in each case the dependence is linear rather than quadratic.

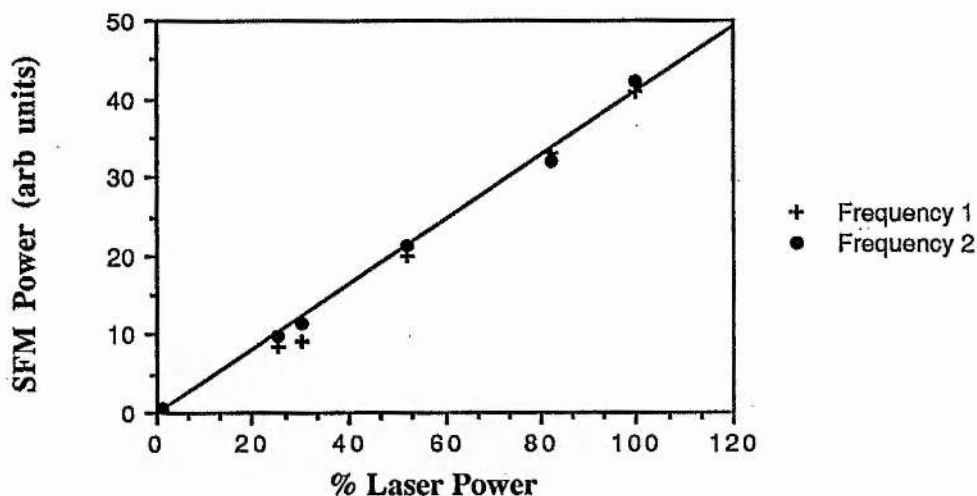


Figure 5.3 : Experimental results of SFM power against  $P(\omega_1)$  and  $P(\omega_2)$ .  
 $\lambda_1 = 590.658$  nm (polarisation  $\perp$  to B)  
 $\lambda_2 = 567.282$  nm (polarisation  $\perp$  to B)  
B  $\sim 1500$  G T  $\sim 270^\circ\text{C}$

### 5.1.4 Excitation of Quadrupole Moments

For linearly polarised fundamental laser beams, the  $Q_{xy}$  quadrupole moment is driven by  $\Delta m = \pm 2$  quadrupole transitions and the component of laser polarisation perpendicular to the magnetic field direction. The  $Q_{zy}$  quadrupole moment is driven by  $\Delta m = \pm 1$  quadrupole transitions and the product of the components of laser polarisation perpendicular and parallel to the magnetic field direction [43]. Since only one fundamental beam was required for SHG, only the quadrupole moment  $Q_{xy}$  could solely be excited (with the polarisation of the beam at right angles to the magnetic field direction). The quadrupole moment  $Q_{zy}$  was driven by rotating the incident laser beam polarisation angle from  $90^\circ$  to the magnetic field direction but

the  $Q_{xy}$  moment was necessarily also excited. The contributions to the second harmonic power from these two sources were separated by the different polarisation states of the second harmonic wave emitted from each quadrupole moment.

Using two incident laser beams for SFM offers the flexibility of exciting either only  $Q_{xy}$  or only  $Q_{zy}$  or both  $Q_{xy}$  and  $Q_{zy}$ . The quadrupole moment that is driven depends upon the relative polarisations of the two interacting fundamental beams. This was clearly shown by the line profiles obtained with two single-mode fundamental laser beams in a strong magnetic field. There are shown in Figure 5.4.

In a high strength magnetic field, the  $\Delta m = \pm 1$  and  $\Delta m = \pm 2$  transitions are well split in frequency and can be separately resolved even with Doppler broadening. Figures 5.4 (a) and (b) show that SFM can excite the quadrupole moments separately by choosing the correct relative laser polarisations for the two incident beams. The magnitude of the SFM intensity for orthogonal laser polarisations is  $\sim 3$  times that for parallel polarisations due to the smaller Zeeman shifting of the  $\Delta m = \pm 1$  over the  $\Delta m = \pm 2$  quadrupole transitions. Note that a similar line profile to Figure 5.4 (b) could be obtained by interchanging the laser polarisation directions at  $\lambda_1$  and  $\lambda_2$ . With the laser polarisations at an angle of  $45^\circ$  to the magnetic field direction, both  $Q_{xy}$  and  $Q_{zy}$  quadrupole moments were driven as shown in Figure 5.4 (c). The total line profile is a sum of the contributions from each quadrupole moment and is similar to the line profiles obtained for SHG with a  $45^\circ$  angled fundamental laser beam.

## 5.2 SFM : MACROSCOPIC EFFECTS

Although the microscopic behaviour of the magnetic field induced SFM nonlinear optical process has been shown to be consistent with the SHG study, the phase matching behaviour of the two three-wave mixing processes is different. Phase matching in a nonlinear optical process is a macroscopic effect due to the propagation of the interacting waves in the bulk nonlinear medium.

A coupled plane wave treatment of SFM gives

$$\frac{dE(\omega_3)}{dz} = -i\kappa e^{i\Delta kz} \quad (5.2.1)$$

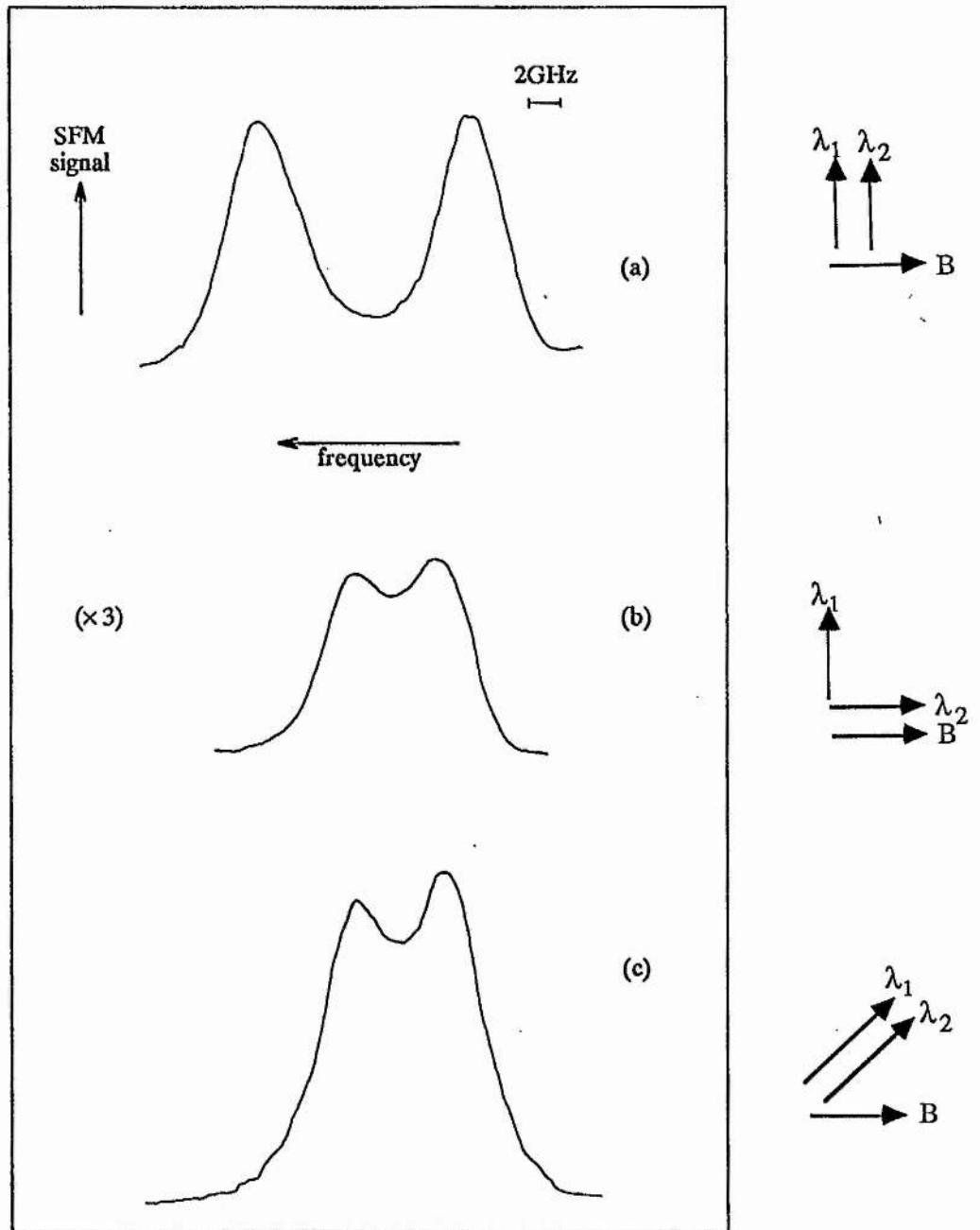


Figure 5.4 : Experimental line profiles for SFM with different incident laser polarisations.

$B \sim 2900 \text{ G}$      $T \sim 240^\circ\text{C}$   
 $\lambda_1 = 588.362 \text{ nm}$  (Spectra-Physics 380A)  
 $\lambda_2 = 569.416 \text{ nm}$  (Spectra-Physics 380D)

where  $\Delta k$  is the phase mismatch between the three waves defined by

$$\Delta k = \underline{k}_3 - \underline{k}_1 - \underline{k}_2. \quad (5.2.2)$$

The magnitude of the wave vectors  $|\underline{k}_i|$  is  $2\pi n_i/\lambda_i$  where  $n_i$  is the refractive index of the nonlinear medium at the wavelength  $\lambda_i$ . Integrating equation (5.2.1) over the length  $\ell$  of the nonlinear medium gives the output intensity of the generated sum frequency wave as

$$I(\omega_3) \propto \ell^2 \frac{\sin^2(\Delta k \ell/2)}{(\Delta k \ell/2)^2}. \quad (5.2.3)$$

The  $\text{sinc}^2(\Delta k \ell/2)$  function describes the phase matching of the nonlinear effect and is a maximum when  $\Delta k = 0$ . In general,  $\Delta k \neq 0$  because the refractive index  $n$  of the nonlinear medium is wavelength dependent and  $n_1 \neq n_2 \neq n_3$ . The refractive index of an atomic vapour at a wavelength  $\lambda$  is found from the Sellmeier equation [4]

$$n(\lambda) - 1 = \frac{N r_e}{2\pi} \sum_{ij} \frac{\alpha_i f_{ij}}{\frac{1}{\lambda_{ij}^2} - \frac{1}{\lambda^2}} \quad (5.2.4)$$

where  $N(\text{m}^{-3})$  is the particle density of the atoms,  $r_e$  ( $2.818 \times 10^{-15}$  m) is the classical electron radius,  $f_{ij}$  is the oscillator strength of the atomic transition at wavelength  $\lambda_{ij}$  and  $\alpha_i$  is the fractional population of the atomic level  $i$ .

The refractive index of an atomic vapour is significant at frequencies far from natural atomic resonant transitions where absorption is negligible because the dispersion associated with the transition decreases less rapidly with frequency than the absorption (see §6.6.3).

For magnetic field induced SHG in sodium vapour the wavelengths of the fundamental and generated waves are fixed at 578.7 nm and 289.4 nm respectively. The refractive index of the atomic vapour at these two wavelengths was calculated by inserting the relevant sodium transition wavelengths and oscillator strengths [110] into the Sellmeier equation. This gives a fixed positive value of  $\Delta k'$  ( $=\Delta k/N$ ) of  $8.97 \times 10^{-20} \text{ m}^2$ . However, for magnetic field induced SFM, the two fundamental wavelengths  $\lambda_1$  and  $\lambda_2$  can be varied and this gives the possibility of  $\Delta k'$  taking a range of positive and negative values. Thus the dependence of the SFM power with sodium density is changed depending on the sign and magnitude of  $\Delta k$ . The SFM nonlinear optical process may be optimally phase matched by controlling the phase

mismatch with the wavelengths  $\lambda_1$  and  $\lambda_2$  and the focusing of the laser beams into the sodium heat-pipe oven. Different phase matching techniques also become possible and these are reviewed in the next section.

### 5.2.1 *Phase-matching Techniques for Nonlinear Optical Processes in Atomic Vapours*

Several schemes for phase-matching nonlinear optical processes in atomic vapours have been achieved and most of these are comprehensively reviewed in reference 4. Five of these phase-matching techniques are briefly described here with consideration of their possible use in phase-matching magnetic field induced SFM.

(a) **Anomalous Dispersion** - This technique utilises the linear dispersion of the nonlinear atomic medium to achieve phase-matching of collinear nonlinear optical processes. Since the magnitudes of the wavevectors of the interacting waves are dependent upon the refractive index of the atomic nonlinear medium, if the interacting frequencies are chosen to lie on either side of a natural strong atomic resonance with anomalous dispersion then the wavevector contributions can be balanced to give the nominal phase-matching condition of  $\Delta k = 0$ .

The first proposal of this method for phase-matching in a gaseous nonlinear medium was by Armstrong et al [13]. This technique was demonstrated by Bjorklund et al [111] to essentially perfectly phase-match a two-photon resonant four-wave mixing nonlinear optical process in sodium vapour. Their collinear  $\chi^{(3)}$  mixing process was shown to be tunable and could be phase-matched from the far infrared to the vacuum ultraviolet regions of the spectrum. Significantly enhanced production of coherent VUV radiation was subsequently achieved with this phase-matched mixing process in Sr vapour [112]. Enhancement of the nonlinearity and phase-matching via anomalous dispersion allowed production of cw VUV radiation at 170 nm [113].

This technique of phase-matching using anomalous dispersion is the most suitable for magnetic field induced SFM. It has the advantage that the frequencies of the two fundamental waves can be chosen to be close to and on either side of the two strong D line resonances in

sodium at 589.0 nm ( $D_2$ ) and 589.6 nm ( $D_1$ ). Phase-matching by this method is also insensitive to the spatial distribution of the nonlinear atomic medium. This would have been advantageous if the sodium oven had been operated in a true heat-pipe mode with an active region of pure sodium vapour. Figure 5.5 shows the calculated value of  $\Delta k'$  versus  $\lambda_{1,2}$  using equations (5.2.2) and (5.2.4) for SFM on the Na 3S-4D two-photon transition.

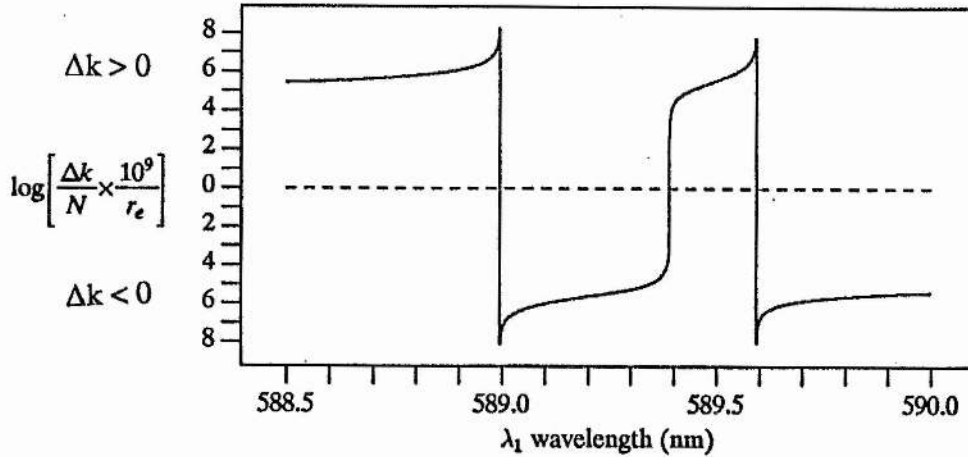


Figure 5.5 : Calculated value of the phase mismatch for SFM, normalised by the sodium particle density.

Note that there is a cancellation point between the two D line resonances where  $\Delta k = 0$  due to a refractive index greater than 1 for  $\lambda_1$  and less than 1 for  $\lambda_2$ . The importance of this particular value of  $\lambda_1$  and  $\lambda_2$  is that the magnetic field induced SFM effect can be nominally phase-matched at all sodium particle densities  $N$ , with the SFM power increasing as  $N^2$ .

With plane wave input beams at  $\lambda_1$  and  $\lambda_2$ , the peaks of the phase match oscillations will occur at sodium densities  $N_i$  determined by

$$N_i = \frac{(2i-1)\pi}{|\Delta k'| \ell} \quad (5.2.5)$$

where  $i = 1, 2, 3, 4, \dots$ . When  $|\Delta k'|$  becomes larger near the  $D_1$  and  $D_2$  sodium resonance lines, the oscillations of SFM power with  $N$  start to occur at lower sodium densities. This is only true when a plane wave approximation is made. With focused input beams, not

only the magnitude but the sign of  $\Delta k$  becomes important (see §5.2.2).

(b) **Buffer Gas** - The addition of an inert buffer gas to the active nonlinear atomic medium to achieve phase-matching was first proposed by Harris and Miles [114] for third harmonic generation in an alkali metal vapour. This was experimentally demonstrated for the frequency tripling of 1.064  $\mu\text{m}$  radiation in rubidium vapour phase-matched with xenon [115].

The principle of phase matching a nonlinear optical process by means of a buffer gas is to use the dispersion of the gas to cancel the phase mismatch produced by the atomic vapour alone. The overall refractive index of the mixture of gases is then the same at all the interacting wavelengths.

The inert gases have their main absorption resonances in the deep UV region of the spectrum and show normal dispersion for larger wavelengths. By adding a sufficient pressure of buffer gas, the overall refractive index of the mixture of gas and atomic vapour can be controlled to make  $\Delta k = 0$  and nominal phase-matching takes place. This method of phase-matching is only valid when  $\Delta k$  is originally negative because the dispersion of the inert gas is always greater than unity at the wavelengths of interest in SFM.

The use of this buffer gas phase-matching technique is widely practiced [116; 117, 11] and other similar methods involving metal vapour mixtures have been reported [118]. The main problem with phase-matching with this technique is due to non-uniform mixing of the gas and atomic vapour [119]. With two metal vapours it is difficult to separately control the vapour pressures in the same heat-pipe oven [118].

The ratio of buffer gas atoms to metal vapour atoms to create phase-matching is dependent upon the magnitude of  $\Delta k$  due to the nonlinear medium but is typically in excess of 100. An order of magnitude calculation is presented here for phase-matching magnetic field induced SFM by this technique with Ar buffer gas. Consider  $\lambda_1 = 591.000 \text{ nm}$  and  $\lambda_2 =$

566.967 nm so that the phase mismatch due to the sodium vapour is  $\Delta k' = -2.537 \times 10^{-19} \text{ m}^2$  and is negative. The dispersion of the argon buffer gas was calculated at the three wavelengths of interest to give  $\Delta k'_{\text{Ar}} = 1.281 \times 10^{-23} \text{ m}^2$  [120]. Therefore the required ratio of argon gas atoms to sodium atoms is  $\sim 19800$ . For a sodium temperature of  $300^\circ\text{C}$ , the sodium particle density is  $2.31 \times 10^{20} \text{ m}^{-3}$ . The required argon particle density is then  $\sim 4.475 \times 10^{24} \text{ m}^{-3}$  or equivalently a pressure of  $\sim 188$  mbar.

However, the magnetic field induced SFM process is a resonant nonlinear effect unlike the nonresonant third harmonic studies. Addition of high pressures of buffer gas to the sodium vapour causes collisional dephasing of the 3S-4D coherence and decreases the generated SFM power [44]. If the collisional dephasing decreases the SFM power by less than the increase due to achieving phase-matching then the addition of high pressures of buffer gas may be beneficial to the SFM nonlinear effect.

Using the above figures and a vapour zone length of 10 cm gives the phase-match  $\text{sinc}^2$  ( $\Delta k \ell / 2$ ) value of  $5.13 \times 10^{-3}$ . Achieving nominal phase-matching ( $\Delta k = 0$ ) with 188 mbar of Ar gives an increase in the  $\text{sinc}^2$  ( $\Delta k \ell / 2$ ) term of  $\sim 195$  times. The expected theoretical decrease in SFM power due to collisional dephasing of 188 mbar of Ar is  $\sim 10$  times less for a magnetic field of  $\sim 2750$  G and  $\sim 40$  times less for a magnetic field of  $\sim 200$  G [14]. So, adding the buffer gas to achieve phase-matching may actually increase the generated SFM power by several times. This was not experimentally verified in this particular study.

The dispersion of the Ar buffer gas may also explain why the experimentally observed decrease in SHG power with buffer gas pressure was more rapid than expected theoretically [44]. The further increase in phase mismatch due to the argon gas would also decrease the SHG power in addition to the collisional dephasing. Calculating the expected decrease in SHG power by phase-matching due to Argon dispersion at a pressure of 234 mbar gives an additional decrease of  $\sim 20$  times which is almost exactly the decrease measured experimentally.

(c) **Noncollinear Beam Geometry** - The phase mismatch  $\Delta k$  given in equation (5.2.2) is a vectorial difference of  $\underline{k}_3$  and  $\underline{k}_{1,2}$  and so nominal phase matching can be achieved when  $\Delta k < 0$  for collinear beams by arranging the fundamental beams to be non-collinear as shown in Figure 5.6.

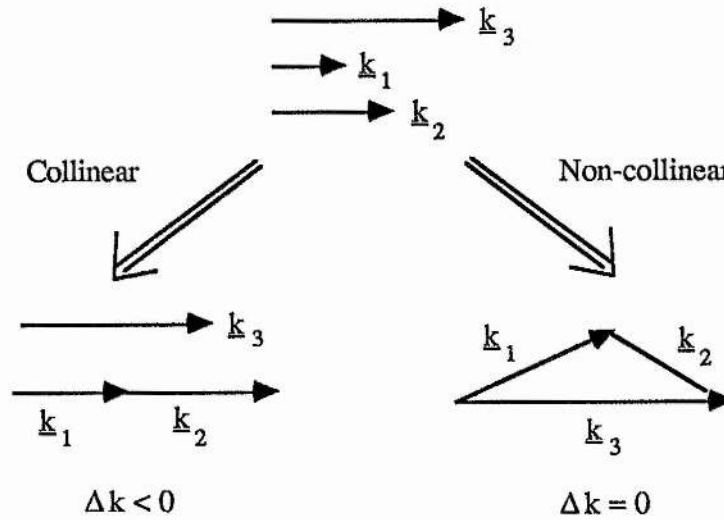


Figure 5.6 : Schematic diagram of non-collinear beam geometry to achieve phase matching.

Bethune et al [32] used this method of phase-matching in their study of quadrupole SFM in atomic sodium vapour. The non-collinear fundamental beams were also required to induce the  $\chi^{(2)}$  nonlinearity in the isotropic atomic vapour [33]. The angle  $\theta$  between  $\underline{k}_1$  and  $\underline{k}_2$  to give nominal phase matching  $\Delta k = 0$  for plane waves is given by

$$\theta^2 = 2 \left[ \left(1 + \lambda_2/\lambda_1\right) \Delta n(\lambda_1) + \left(1 + \lambda_1/\lambda_2\right) \Delta n(\lambda_2) \right] \quad (5.2.6)$$

where  $n(\lambda_i) = 1 + \Delta n(\lambda_i)$  is the refractive index of the vapour. This equation is valid provided that  $\Delta n(\lambda_1) > 0$ ,  $|\Delta n(\lambda_1)| > \lambda_1/\lambda_2 |\Delta n(\lambda_2)|$  and  $\theta \ll 1$ . The required angle  $\theta$ , when the single photon detuning in the SFM experiment is  $\sim 20 \text{ cm}^{-1}$ , is a few tens of milliradians. The necessary phase-match angle increases as the square root of the sodium density  $N$ .

With a non-collinear beam geometry, the effective interaction length for the nonlinear optical process is reduced. For nominal phase-matching, the generated sum frequency power

$P(\omega_3) \propto N^2 L^2$  where  $L$  is the interaction length. If the average radial spot size of the fundamental beams is  $w_0$ , then the effective interaction length for beams crossed at an angle  $\theta$  is  $L \sim 2w_0/\theta$ . Consider two input beams crossed at 40 mrad and with a spot size of  $\sim 100 \mu\text{m}$ . For a wave-length of 590 nm, the collinear phase matched interaction length is  $\sim 10$  cm due to the confocal parameter  $kw_0^2$  of the beams. The corresponding crossed beam effective interaction length is  $\sim 4$  mm which implies a reduction in SFM power of  $\sim 625$  times over the phase-matched collinear beam case.

For magnetic field induced SFM it is desirable to have collinear waves for maximum interaction length and to phase match with the anomalous dispersion method rather than this non-collinear beam technique. Also, under low magnetic fields, destructive interference between the non-collinear and magnetic field induced  $\chi^{(2)}$  nonlinearity has been observed [37]. To avoid these effects, the magnetic field induced SFM nonlinear optical process was only studied in a collinear beam geometry.

(d) **Periodic Phase-Matching** - In a nonlinear medium with a finite phase mismatch  $\Delta k$ , the coherence length  $\ell_c$  is defined as

$$\ell_c = \frac{\Pi}{|\Delta k|} \quad (5.2.7)$$

ie. the distance of propagation over which the phase of the generated sum frequency wave has changed by  $\Pi$  radians. The amplitude of the generated wave changes with propagation distance  $z$  according to

$$E_3 \propto \frac{1 - e^{i \Delta k z}}{i \Delta k} \quad (5.2.8)$$

When the wave propagates from a position  $z_0$  to  $z_0 + \ell_c$ , the phase of the sum frequency wave has changed by  $\Pi$  radians and constructive interference occurs so that maximum net sum frequency power is generated. Similarly, destructive interference occurs when  $z = 2\ell_c$  and no net sum frequency power is produced. In general, if the length of the nonlinear medium  $\ell$  is an odd multiple of  $\ell_c$  then net nonlinear optical output power is generated and if  $\ell$  is an even multiple of  $\ell_c$ , no net generation is achieved. However, if the  $\chi^{(2)}$  nonlinearity is induced by a

static transverse field then reversing the polarity of the static field after a distance  $\lambda_c$  is equivalent to an additional phase change of  $\Pi$  radians. This phase change cancels the phase shift due to the phase velocity mismatch  $\Delta k$  and the resultant sum frequency wave from each section of the nonlinear medium is in phase and constructively interferes. This allows continual net generation of the sum frequency wave with propagation of the waves in the nonlinear medium.

This periodic phase-matching method has been used by Shelton and Buckingham [121] to phase-match electric field induced SHG in gases. They used an array of pin electrodes of fixed separation with the electric field polarity reversed on alternate electrodes. When the pressure of the various gases used as nonlinear media was varied, the value of  $\Delta k$  could be optimised for the SHG process to become periodically phase-matched for the particular electrode spacing. This technique was found to be useful in determining the refractive indices of gases from the phase-matching behaviour of periodic electric field induced SHG [122].

A disadvantage of the periodic phase-matching technique is that it is restricted to one particular value of  $\Delta k$  only, if the electrode geometry is fixed. Changing the electrode geometry presents problems due to the electric fields becoming non-uniform when the electrodes are closely spaced.

Magnetic field induced SFM could in principle be similarly phase-matched by a periodic array of magnetic poles. However in practice the spacing of the magnetic poles would typically be a few millimetres which would be difficult to achieve experimentally. Again, the fixed magnetic pole geometry would only allow phase-matching for one particular set of experimental parameters.

(e) **Intensity Dependent Refractive Index** - A phase-matching technique of limited applicability has been demonstrated which utilises the nonlinear refractive index  $n_2$ , where  $n = n_0 + n_2 I$ , induced by a high intensity beam in an atomic vapour. Li et al [123] showed that third harmonic generation (THG) in barium vapour was periodic in input power due to the intensity dependent refractive index contribution cancelling the phase mismatch produced by the linear refractive index  $n_0$ . A very high input power was required (866 MW) to induce a

large enough non-resonant  $n_2$  to counteract the dispersion due to  $n_0$ .

For experimental cw magnetic field induced SFM, the incident laser powers are low and the frequencies are far enough from natural sodium resonant transitions to make this phase-matching method impractical.

### 5.2.2 Focusing Effects

The plane wave approximation used in equations (5.2.1) and (5.2.3) is no longer valid when a correct treatment of focused, Gaussian profile input laser beams is considered [124, 46]. When a Gaussian beam is focused, it undergoes a smaller phase shift when the wave travels through a focus than a plane waves does in propagating over the same distance. For no absorption, the electric field of the focused fundamental wave can be described by

$$\underline{E}(x,y,z,t) = \frac{E_0 e^{i(kz - \omega t)}}{(1 + i\tau)} e^{[-(x^2 + y^2)/w_0^2 (1 + i\tau)]} \quad (5.2.9)$$

where  $\tau = 2(z-f)/b$  is a normalised propagation distance of the wave from the focus at  $z=f$ . The variable  $b$  is the confocal parameter of the beam and is equal to  $kw_0^2$  where  $k$  is the wavevector and  $w_0$  is the minimum beam radius. Calculating the generation of the nonlinear wave due to this fundamental wave by the formal theory is involved but shows that the sum frequency (or second harmonic) power is dependent upon

$$P_3 \propto P_1 P_2 \ell h(\sigma, \xi, \mu) \quad (5.2.10)$$

for no linear absorption and no double refraction which is the case for a non-single-photon-resonant SFM process in an atomic vapour.  $P_1$  and  $P_2$  are the powers of the two incident beams,  $\ell$  is the interaction length and  $h(\sigma, \xi, \mu)$  is the function described below which contains all of the dependence of  $P_3$  on the phase mismatch ( $\sigma = \frac{1}{2}\Delta kb$ ), the strength of focusing ( $\xi = \ell/b$ ) and the focal position in the nonlinear medium ( $\mu = (\ell - 2f)/\ell$ ).

The function  $h(\sigma, \xi, \mu)$  is given by

$$h(\sigma, \xi, \mu) = \frac{\pi^2}{\xi} |H(\sigma, \xi, \mu)|^2 \quad (5.2.11)$$

where  $H(\sigma, \xi, \mu)$  is the integral function

$$H(\sigma, \xi, \mu) = \frac{1}{2\pi} \int_{-\xi(1-\mu)}^{\xi(1+\mu)} \frac{e^{i\sigma\tau}}{(1+i\tau)} d\tau. \quad (5.2.12)$$

The main difference between focused and plane wave phase-matching is that the behaviour of the function  $h$  becomes asymmetric with respect to the sign of  $\Delta k$  when  $\xi \geq 1$ , ie. when the length of the nonlinear medium is greater than or approximately equal to the confocal parameters of the fundamental beams. As shown in Figure 5.5, the anomalous dispersion of the sodium D lines allows different signs and magnitudes of  $\Delta k$  to be selected for magnetic field induced SFM according to the chosen values of the two input laser frequencies.

The maximum value of  $h(\sigma, \xi, \mu)$  occurs with  $\xi = 2.84$  and is no longer at the nominal phase-matching condition of  $\Delta k = 0$  but with  $\Delta k$  slightly less than zero. This is due to the converging and diverging parts of the focused Gaussian beams being able to satisfy a non-collinear phase-matching condition, similar to that discussed in §5.2.1 (c) and Figure 5.6. The variation of  $h$  with  $\xi$  is shown in Figure 5.7 for various values of parameter  $B$ . This parameter  $B$  is proportional to the beam walk-off angle in the nonlinear medium and is always equal to zero for an atomic vapour.

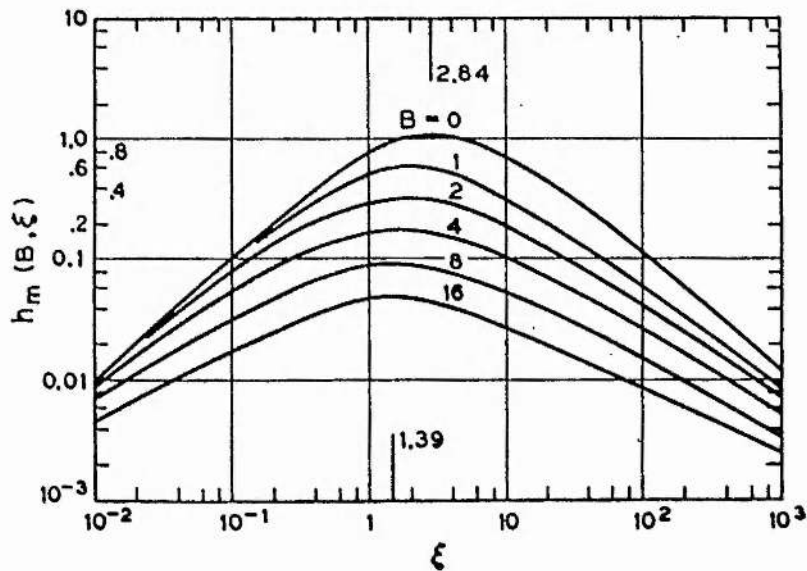


Figure 5.8 : Function  $h$  for optimum phase-matching as a function of  $\xi = \ell/b$  for several values of double-refraction parameter  $B$  (from [46]).

The function  $|H(\sigma, \xi, \mu)|^2$  has a single main maximum value which defines a unique optimum phase mismatch  $\Delta k_m$  and corresponding parameter  $\sigma_m = \frac{1}{2} \Delta k_m b$ . The optimum phase-matching parameter  $\sigma_m$  as a function of  $\xi$  is shown in Figure 5.8. The function  $|H|^2$  displays oscillatory behaviour for increasing values of  $|\Delta k|$  and has zeros determined by the same coherence length as in equation (5.2.7).

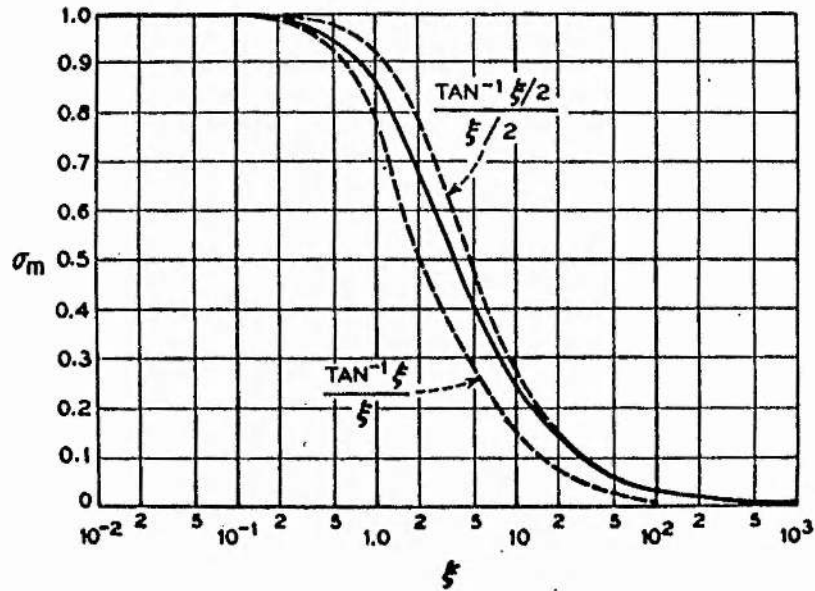


Figure 5.8 : Optimum phase-matching parameter  $\sigma_m(\xi)$  (from [46]).

The position of the beam focus in the nonlinear medium is important in the consideration of SFM and SHG. Kleinman and Miller [125] have shown theoretically and experimentally that when  $\Delta k$  takes on its optimum value for phase-matching  $\Delta k_m$ , focusing the fundamental beams in the centre of the nonlinear medium produces the greatest sum frequency (second harmonic) output power.

When  $\Delta k < 0$  and is not optimised, the generated second harmonic power becomes oscillatory with the position of the focus along the length of the nonlinear medium. Focusing the input beams just inside the front or rear regions of the nonlinear medium produces the largest second harmonic powers. When  $\Delta k > 0$  and is not optimised, the maximum generated second harmonic power again corresponds to focusing near the interfaces of the nonlinear

medium but no oscillatory power variation is seen with moving the focal position of the beam in the nonlinear medium.

It is interesting to note that for an infinite nonlinear medium the integral function  $H$  can be evaluated analytically and shows that net sum frequency (second harmonic) generation does occur for the nominal phase-matching condition  $\Delta k = 0$ , unlike the case of third harmonic generation where the net generation of power is zero in an infinite nonlinear medium at  $\Delta k = 0$  [126].

### 5.2.3 *Experimental Results for SFM Phase-matching*

The phase-matching behaviour for cw magnetic field induced SFM was examined as a function of sodium particle density  $N$  for various combinations of  $\lambda_1$  and  $\lambda_2$ .

The fundamental laser beam at wavelength  $\lambda_1$  came from the standing wave dye laser with a three plate birefringent filter as an intracavity frequency selective element to reduce the linewidth to  $\sim 17$ GHz. The beam at wavelength  $\lambda_2$  was supplied by the frequency stabilised, single-mode Spectra-Physics 380D ring dye laser. The combined beams at  $\lambda_1$  and  $\lambda_2$  were focused into the centre of the sodium heat-pipe oven. The sum frequency signal was recorded with decreasing  $N$  as the sodium heat-pipe oven cooled from a high temperature.

The theoretical phase-matching behaviour of SFM with Na particle density at the laser wavelengths of interest was calculated by using a computer model to evaluate  $\Delta k$  and then numerically integrating the function  $H(\sigma, \xi, \mu)$  to give values of  $|H|^2$ . The numerical methods to do this were based on the information supplied in references [124] and [46].

The theoretical difference between plane wave and focused beam phase-matching behaviour is well illustrated in Figure 5.9 This shows the calculated variation of second harmonic power ( $|H|^2$ ) versus sodium vapour temperature for two values of  $\xi$ :  $\xi = 1$  corresponding to a focused input beam and  $\xi = 0.1$  which approximates to a plane wave input beam.

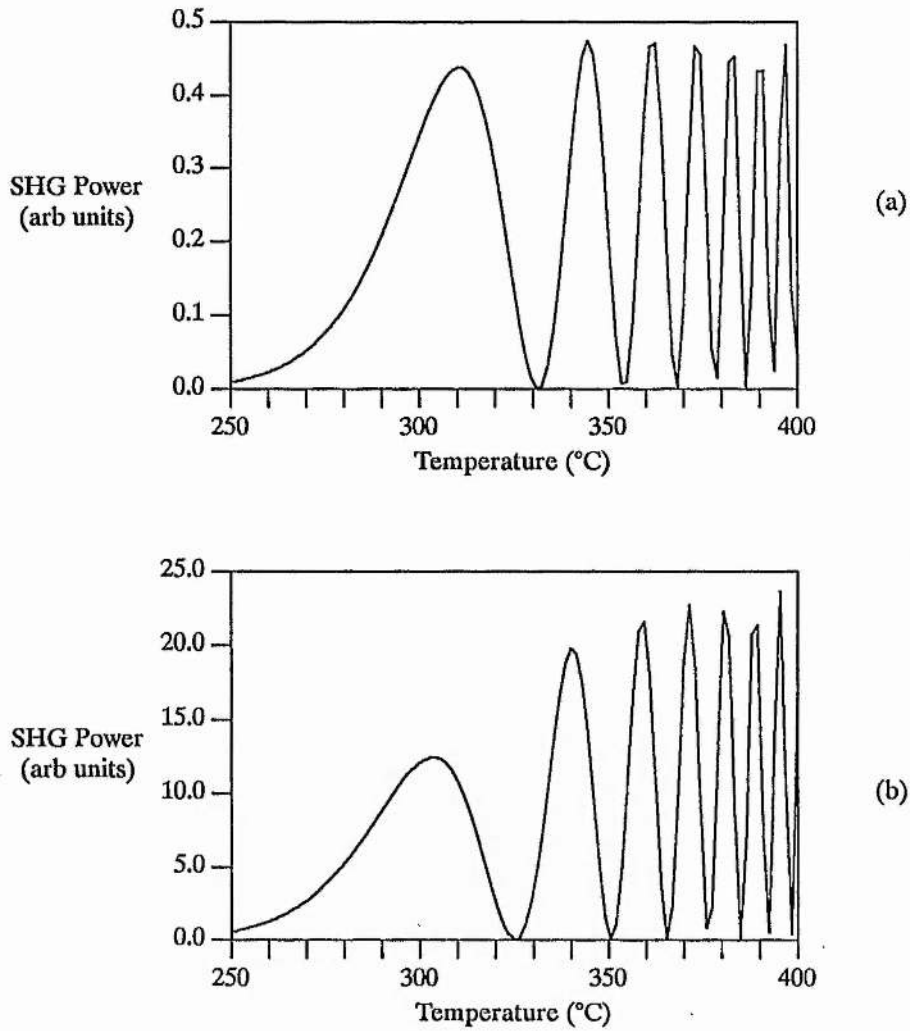


Figure 5.9 : Calculated variation in SHG power with sodium vapour temperature.

- (a)  $\xi = 0.1$  - Plane wave  
 (b)  $\xi = 1$  - Focused

Beams focused in centre of nonlinear medium.

For focused SHG, the heights of the peaks of the phase-match oscillations increase with particle density and the whole oscillatory behaviour shifts to lower sodium vapour temperatures.

For an approximate calibration of the heat-pipe oven temperature, cooling rate and Na

density, the focused SHG phase-matching behaviour was recorded experimentally using only the ring dye laser at  $\lambda = 578.7$  nm. This was compared with the theoretical calculation for SHG with a focused beam and the confocal parameter equal to the vapour zone length (beam focused into heat-pipe oven with a 20 cm focal length lens to  $\sim 100$   $\mu\text{m}$  spot size  $\Rightarrow b \sim 10$  cm). Figure 5.10 shows the experimental results normalised to the theoretical calculation (for the first phase-match peak).

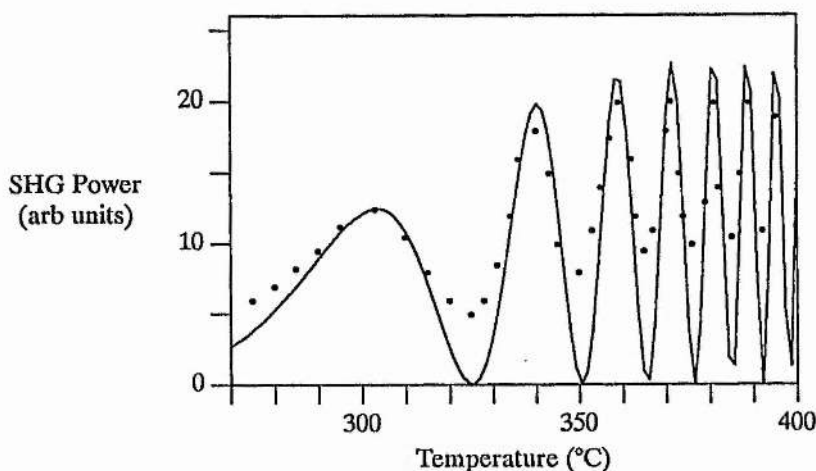


Figure 5.10 : Experimental (points) and theoretical (line) variation of SHG power with Na vapour temperature.

$B \sim 1$  kG  
 Laser polarisation  $\perp$  to magnetic field  
 $f = 20$  cm focusing lens

The theoretical calculation and the experimental results agree well. These results showed that the actual sodium vapour temperature was  $\sim 30^\circ\text{C}$  less than measured on the temperature controller which was reasonable. The heat-pipe oven appeared to cool fairly linearly from the set temperature of  $430^\circ\text{C}$  at about  $\sim 0.13^\circ\text{C s}^{-1}$ . For other set temperatures, the measured cooling rates varied and were not always linear, probably due to the cooling water flow rate and temperature. The maxima and minima in the experimental SHG power variations were less than expected theoretically due to non-uniform temperature distributions in the sodium vapour during the cooling time. When the temperature of the sodium vapour was varied slowly and allowed to reach thermal equilibrium, the minima in the phase-matching behaviour were more pronounced.

To illustrate the asymmetry of the SFM phase-matching behaviour with the sign of  $\Delta k$  for focused beams, the cases (i)  $\Delta k > 0$ , (ii)  $\Delta k = 0$  and (iii)  $\Delta k < 0$  are now considered.

(i)  $\Delta k > 0$

The variation of the SFM power with increasing sodium particle density with a positive phase mismatch  $\Delta k$  is similar to that for SHG (where  $\Delta k$  is also positive). The phase-matching behaviour shows oscillations in the SFM power of comparable magnitude, the number of which depends on the value of  $|\Delta k|$ . If  $|\Delta k|$  is large then the coherence length is short and the first phase-match peak occurs at a low sodium density. This is followed by many other peaks as the length of the nonlinear medium rapidly becomes multiples of the short coherence length with increasing  $N$ . Figure 5.11 shows the theoretical and calculated focused phase-match behaviour for three different combinations of  $\lambda_1$  and  $\lambda_2$  giving  $\Delta k > 0$ .

The first phase match peak for (b) occurs at a lower sodium vapour temperature than for (a) due to the larger magnitude of  $\Delta k'$  for (b) compared to (a). Figure 5.11 (c) shows an example of the positive phase mismatch region when  $\lambda_1$  is situated between the two Na D line resonances.

Overall, the agreement of the experimental results with the theoretical calculations was fair. The experimental points were standardised to the sodium temperatures assuming that the theoretical variation of the SFM power with  $N$  was more accurate than the known experimental sodium vapour temperatures. The experimental results may have also been slightly displaced from the theoretical prediction due to the dispersion of the buffer gas (see §5.2.3 (iii)). The overall temperature behaviour between theory and experiment was consistent between the three results in Figure 5.11. Experimental SFM variations were again less than theory because of the non-uniform temperatures of the sodium vapour. The decrease in the height of the phase-match oscillations at higher temperatures may have been due to the linear absorption of the fundamental or sum frequency beams by sodium atoms or dimers.

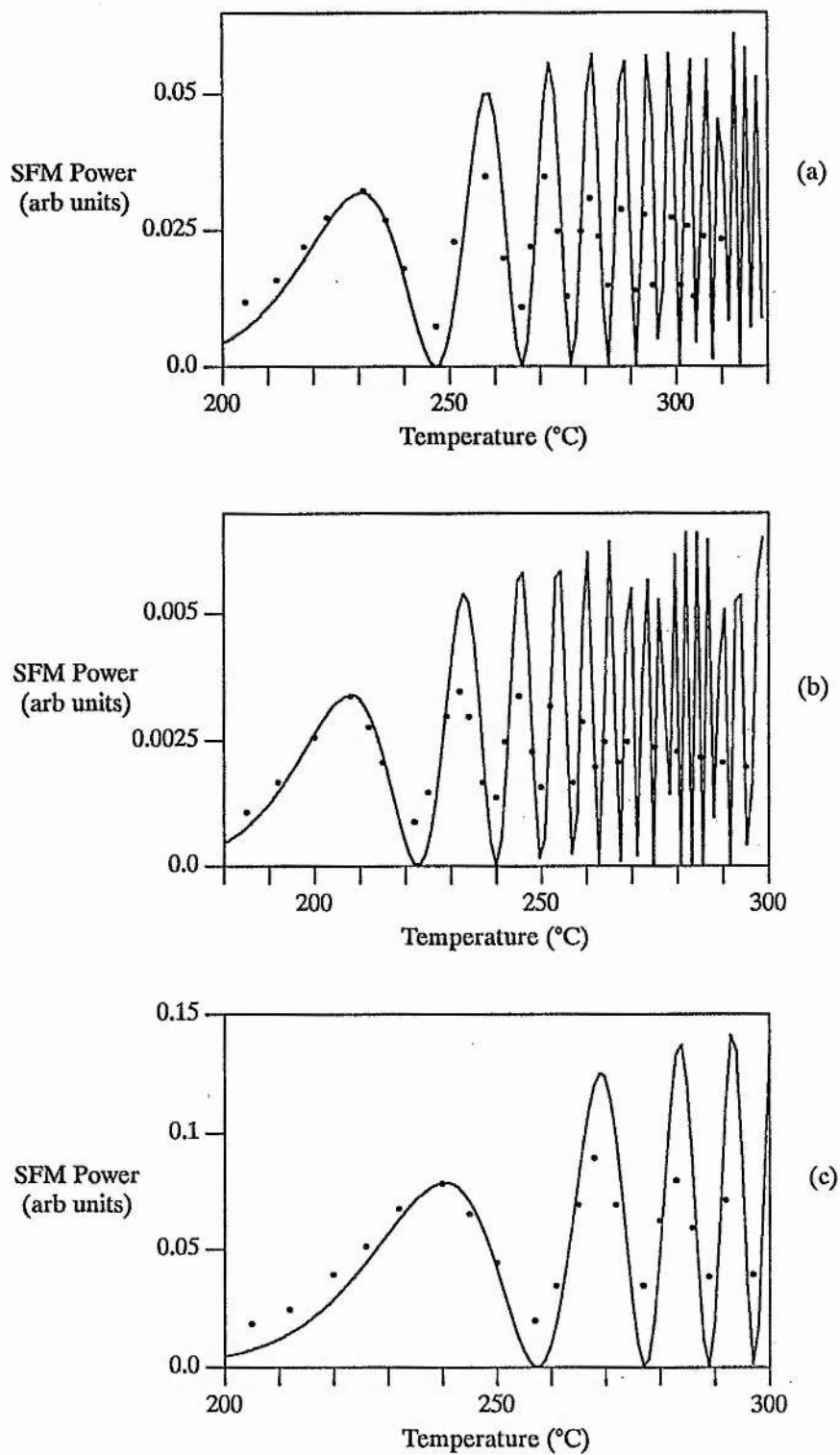


Figure 5.11 : Experimental (points) and theoretical (line) variation in SFM power with Na density.

$\xi = 1$

(a)  $\lambda_1 = 588.790$      $\lambda_2 = 569.016$

(b)  $\lambda_1 = 588.933$      $\lambda_2 = 568.882$

(c)  $\lambda_1 = 589.500$      $\lambda_2 = 568.354$

(ii)  $\Delta k \approx 0$

When the wavelengths of the two input beams for SFM are tuned to  $\lambda_1 \sim 589.390$  nm and  $\lambda_2 \sim 568.456$  nm, the magnitude of  $\Delta k' \approx 0$  due to the equal but opposite contributions from  $\Delta n(\lambda_1)/\lambda_1$  and  $\Delta n(\lambda_2)/\lambda_2$ . This is the cancellation point between the two sodium D line resonances as shown in Figure 5.5.

The importance of this particular laser tuning is that  $\Delta k' \approx 0$  is independent of the sodium particle density and arises solely from the detuning denominator in the Sellmeier equation (5.2.4), so that when phase-matched the SFM power should continue to increase as  $N^2$ . The optimum value of  $\Delta k'$  to give maximum SFM power for any focusing requirements can be selected by careful tuning of  $\lambda_1$  and  $\lambda_2$  close to the above wavelengths. This offers the unique possibility of retaining proper optimised phase-matching of the SFM nonlinear optical process at all sodium densities.

Continual increase in SFM power generation with increasing Na density was seen experimentally up to a maximum temperature of  $\sim 400^\circ\text{C}$  which was limited by the heating cord on the heat-pipe oven. Figure 5.12 shows the theoretical and normalised experimental results for tuning  $\lambda_1, \lambda_2$  close to the  $\Delta k \approx 0$  point.

Note that the applied magnetic field required here to induce a large SFM signal was only a few 10's of Gauss because the nonlinear process was phase-matched at the high sodium densities.

In principle, the SFM power should continue to increase proportionally with  $N^2$  at higher sodium densities providing that the absorption of the interacting frequencies by the increasing population of sodium dimers is low.

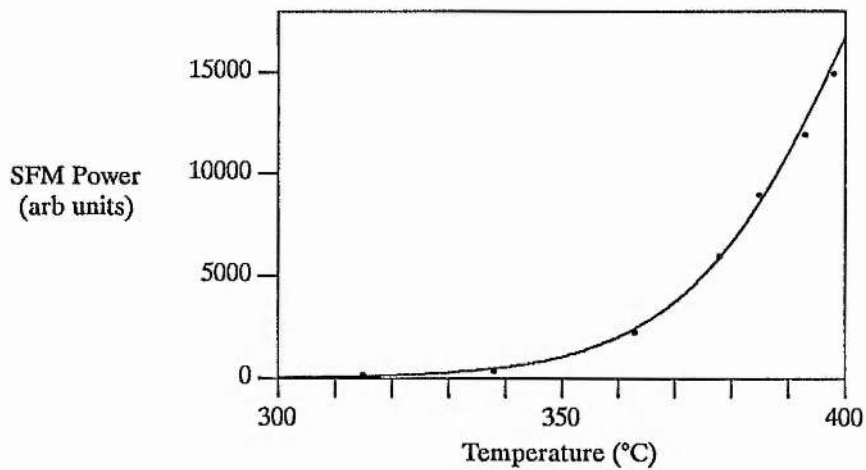


Figure 5.12 : Experimental (points) and theoretical (line) variations in SFM power with Na vapour temperature.

$\lambda_1 \sim 589.388$  nm (polarisation  $\perp$  to B)  
 $\lambda_2 \sim 568.458$  nm (polarisation  $\parallel$  to B)  
 $B \sim 40$  G  
 $\xi \approx 1$

(iii)  $\Delta k < 0$

As shown in Figure 5.5, the  $\lambda_1$  wavelength regions for which  $\Delta k < 0$  are  $589.0 \text{ nm} < \lambda_1 < 589.4 \text{ nm}$  and  $\lambda_1 > 589.6 \text{ nm}$ . The theoretical focusing asymmetry of the SFM phase-matching when  $\Delta k' > 0$  and  $\Delta k' < 0$  is shown in Figure 5.13 for equal but opposite values of  $\Delta k'$ . When  $\Delta k < 0$  there is one large peak in the SFM power at the optimum value of  $\sigma$  given in Figure 5.7 which is several times the magnitude of the  $\Delta k > 0$  oscillations.

Much smaller amplitude phase-match oscillations occur with decreasing  $\Delta k$ .

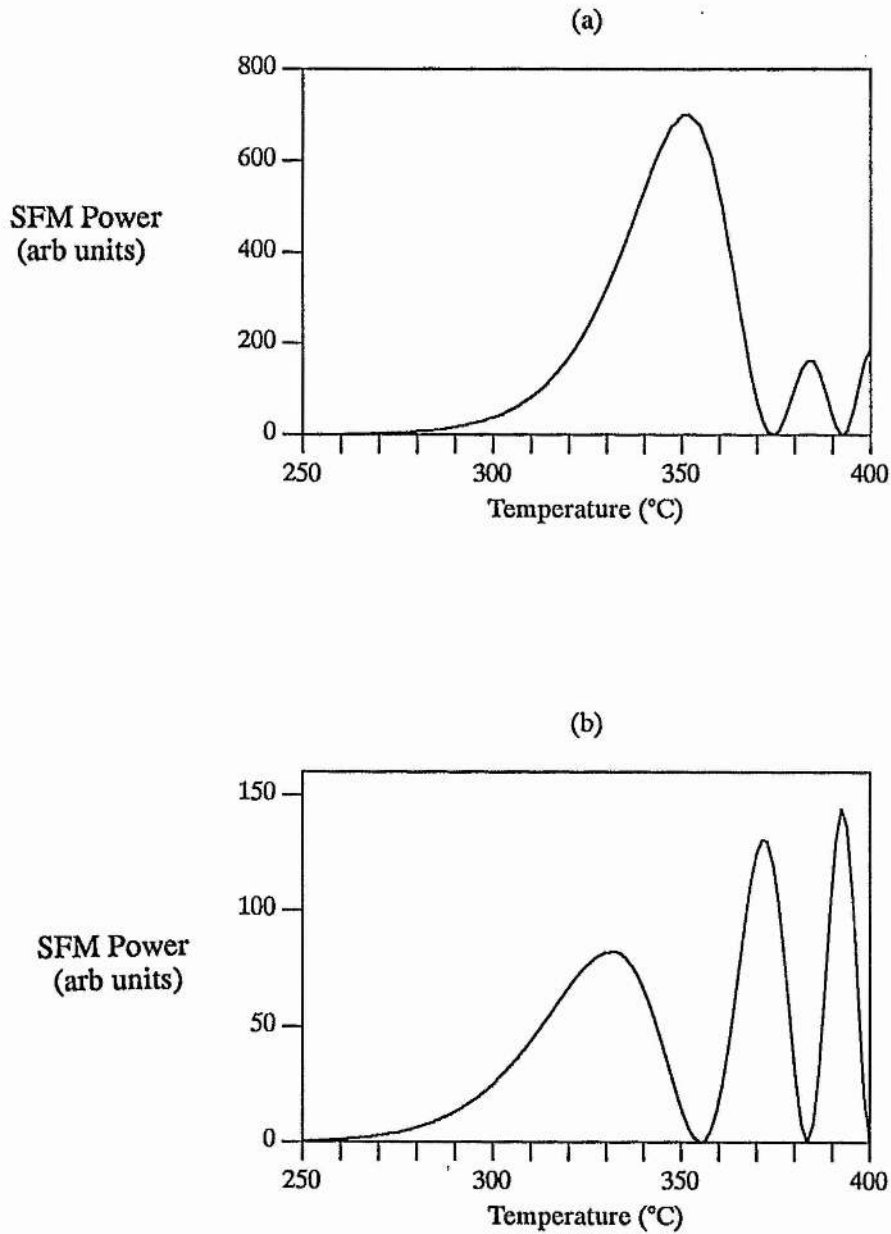


Figure 5.13 : Theoretical variation in SFM power with increasing Na vapour temperature for equal but opposite values of phase mismatch  $\Delta k$ .

- (a)  $\Delta k > 0$   
 (b)  $\Delta k < 0$   
 $\xi = 1.0$

The experimental magnetic field induced SFM phase-matching behaviour for  $\Delta k < 0$  showed similar qualitative features with the focusing theory but did not fit quantitatively as the

experimental results did for  $\Delta k > 0$ . Upon increasing the sodium particle density with a negative value of  $\Delta k$ , the SFM power displayed one large peak value of  $\sim 5$ - $10$  times the magnitude of the  $\Delta k > 0$  signal. Slight but not obvious oscillations in SFM power were seen for higher particle densities. A typical theoretical and experimental result for  $\Delta k < 0$  is shown in Figure 5.14.

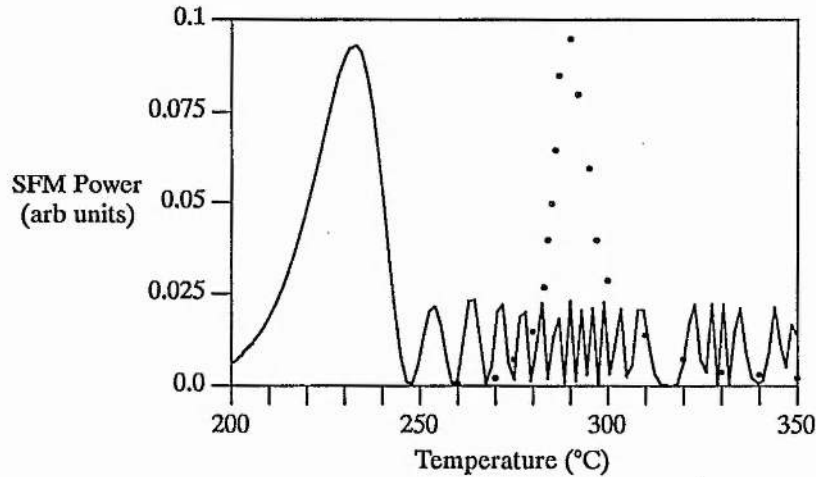


Figure 5.14 : Experimental (points) and theoretical (line) variations in SFM power with Na vapour temperature.

$$\lambda_1 \approx 589.090 \text{ nm}$$

$$\lambda_2 \approx 568.736 \text{ nm}$$

$$B \approx 750 \text{ G}$$

$$\xi \approx 1$$

The large peak in SFM power occurred experimentally at much higher Na densities than expected theoretically. Two possible explanations for the quantitative difference are considered below:

(a) **Buffer gas dispersion** - As discussed in section 5.2.1 (b), the normal dispersion of an inert buffer gas can change the overall refractive indices which the interacting waves experience in the nonlinear medium. When  $\Delta k < 0$ , this effect due to the buffer gas can reduce  $|\Delta k|$  and the SFM phase-matching behaviour should be shifted to higher sodium vapour

temperatures.

Consider the example of  $\lambda_1 = 589.718$  nm,  $\lambda_2 = 568.152$  nm and typically  $\sim 4.5$  mbar of Ar buffer gas added to the sodium heat-pipe oven. The calculated phase mismatch due to the buffer gas is  $\Delta k_{\text{Ar}} = 1.4 \text{ m}^{-1}$  and due to the sodium is  $\Delta k/N = -1.693 \times 10^{-18} \text{ m}^2$ . The theoretical peak SFM power is at  $N = 2.56 \times 10^{19} \text{ m}^{-3}$  ( $245^\circ\text{C}$ ) which gives  $\Delta k = -43.3 \text{ m}^{-1}$ . Therefore, the dispersion of the argon gas is too small to compensate the wavevector mismatch due to the sodium vapour.

(b) **Non-collinear beams** - When  $\Delta k < 0$ , a non-collinear beam geometry can achieve phase-matching as shown in section 5.2.1 (c) and this may have caused the difference between theory and experiment.

If the input beams were completely collinear and were focused into the centre of the oven to a spot size  $\omega_0$  of  $\sim 100 \mu\text{m}$  then the natural diffraction angle  $\theta (= \lambda/\pi\omega_0)$  is  $\sim 2$  mrad which is too small for non-collinear beam phase matching to take place within the diverging beams at the experimental sodium particle densities. However, a calculation of the necessary beam intersection angle to produce phase-matching at the peak of the experimental SFM power gives the required angle of  $\sim 14$  mrad. This angle corresponds to a misalignment of the two incident laser beams at the focusing lens of less than 1.5 mm which is within the accuracy that the beams could be experimentally overlapped. When the beam positions were not changed, the calculated beam intersection angle at the Na density corresponding to peak SFM power for different wavelengths  $\lambda_1$  and  $\lambda_2$  was consistent. This suggests that a slight experimental non-collinearity of the laser beams was responsible for the difference between the expected theoretical and experimentally observed phase-matching behaviour of the magnetic field induced SFM.

When the confocal parameters of the fundamental laser beams were made larger ( $\sim 5$  times) than the interaction length for the SFM nonlinear effect, the  $\Delta k < 0$  SFM phase-matching behaviour became oscillatory similar to that for  $\Delta k > 0$ . This was because the

incident waves behaved more as plane waves and the focusing effects were reduced. Figure 5.15 shows an example of the theoretical and normalised experimental SFM phase-matching behaviour for  $\Delta k < 0$  and  $\xi > 1$ .

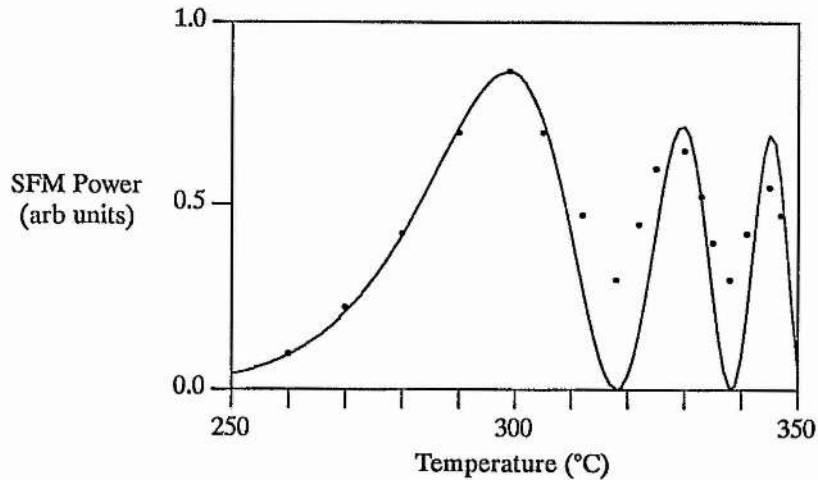


Figure 5.15 : Experimental (points) and theoretical (line) SFM power variation with Na vapour temperature for  $\Delta k < 0$  and  $\xi = 5$ .

$\lambda_1 \sim 592.006$  nm (polarisation  $\perp$  to B)  
 $\lambda_2 \sim 566.044$  nm (polarisation  $\parallel$  to B)  
 $B \sim 775$  G

The experimental sodium vapour temperatures corresponding to the peaks and troughs of the phase-match oscillations agree well with the theory. The maximum and minimum experimental SFM power variations are again probably less than the theoretical prediction due to non-uniform vapour temperatures and the effects of dimer absorption. The laser beams were easier to collinearly align with a longer focal length lens and so any non-collinear beam phase-matching effects were likely to be reduced.

# CHAPTER 6

SUM FREQUENCY MIXING WITH A RESONANT OR  
NEAR-RESONANT INTERMEDIATE STATE

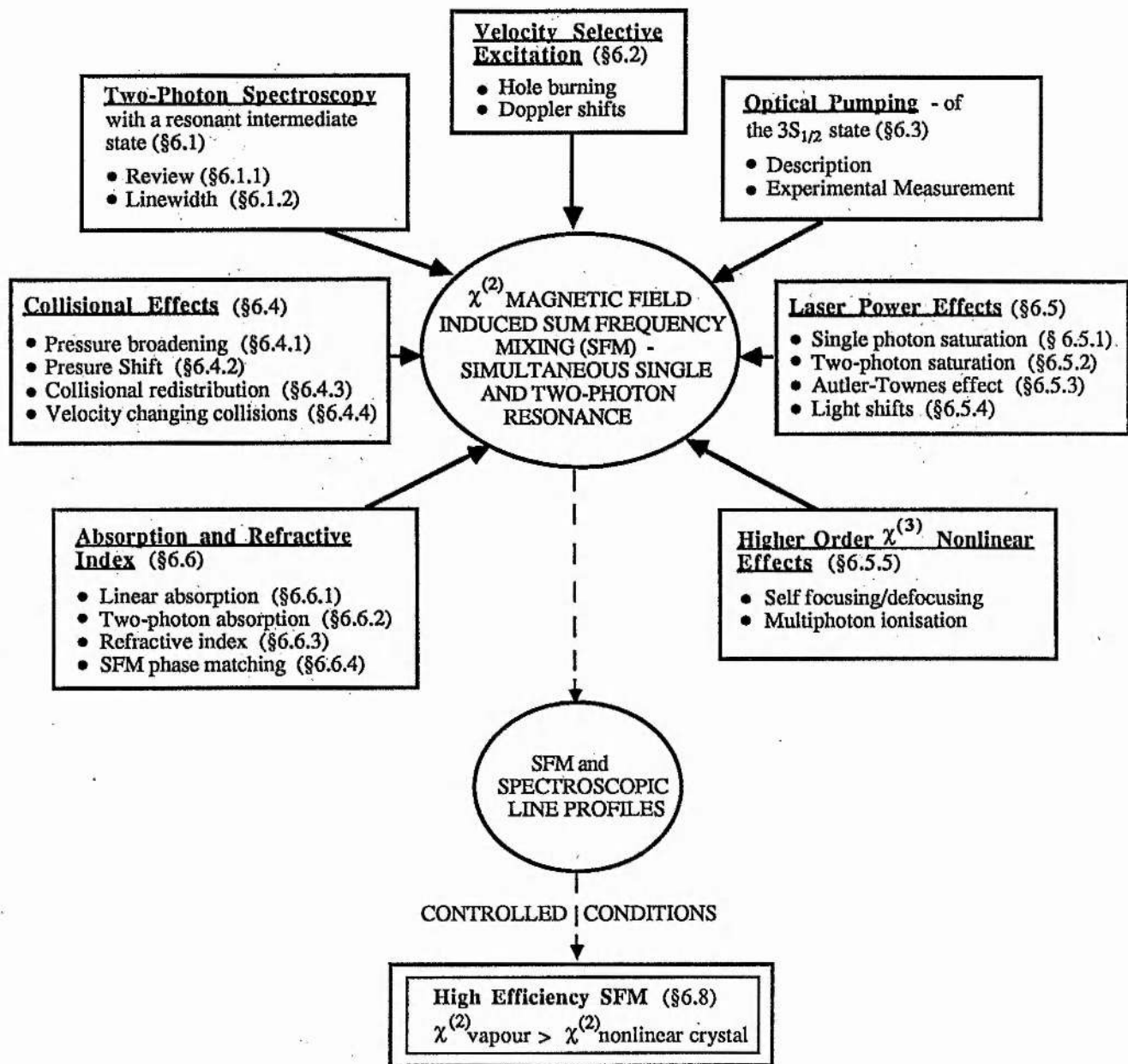
## Chapter 6

### SUM FREQUENCY MIXING WITH A RESONANT OR NEAR-RESONANT INTERMEDIATE STATE

In this chapter, the  $\chi^{(2)}$  nonlinear process of cw, magnetic field induced sum frequency mixing (SFM) is considered with the two incident laser fields simultaneously on resonance with the single and two-photon atomic transitions. This tuning of the laser frequencies was chosen to greatly enhance the two-photon excitation rate and was used to generate much higher SFM powers, so that the  $\chi^{(2)}$  nonlinearity of the atomic sodium nonlinear medium became effectively larger than that of a good nonlinear crystal.

As discussed in Chapter 2, the previous studies of coupled three level Doppler broadened atomic systems have been mainly concerned with spectroscopy of atomic energy levels via atomic populations. Here, the efficient generation of coherent radiation at new frequencies and a study of its properties is the main objective, although the two studies are connected. The additional use of on-resonance single photon atomic transitions for magnetic field induced SFM introduces many new considerations into the nonlinear optical process. These are outlined in the plan of this chapter (which is shown on page 108 ), briefly discussed below and described in detail in the following sections.

Tuning the first laser frequency  $\nu_1$  within the Doppler width of the single photon  $3S_{1/2}$  -  $3P$  sodium transitions greatly increases the probability of two-photon absorption through increased single photon resonant enhancement . Since the two incident narrow linewidth laser fields are now resonant with the two Doppler broadened dipole transitions, step-wise excitation through an intermediate state population becomes allowed in addition to coherent two-photon excitation. These processes become velocity selective due to the hole burning effect of the laser fields in the inhomogeneous atomic population distributions, similar to that discussed for saturated absorption spectroscopy in Chapter 4. The different Doppler shifts of the velocity selected homogeneous atomic groups, selected by  $\nu_1$  on the lower dipole transition, changes the apparent frequency of the further single and two-photon transitions due to the second laser



field at frequency  $\nu_2$ . The coherent SFM nonlinear optical process becomes dependent upon these effects, which have previously been studied in two-photon spectroscopy of the sodium 3S - 4D two-photon transition.

The  $3S_{1/2}$  ground state of sodium contains non-degenerate hyperfine structure and so significant optical pumping of the  $3S_{1/2}$  state by the laser field  $\nu_1$  on resonance with the excited 3P states can occur. The ground state population changes the refractive index and absorption cross-sections of the atomic nonlinear medium as do the created populations in the excited atomic states by the laser excitation. When the laser fields are strong to induce a large nonlinear effect and are simultaneously on resonance with the single and two-photon transitions, saturation of both these atomic transitions occurs and there is significant population movement through the excited sodium states. Higher order  $\chi^{(3)}$  nonlinear effects can be induced by the strong laser fields near resonance.

The study of the SFM process was carried out in a gas cell with added buffer gas and so collisions of the buffer gas atoms with the active sodium atoms led to eg. collisional broadening of the homogeneous linewidth and non-radiative transitions to other nearby atomic levels.

This is believed to be the first ever study of a three-wave mixing nonlinear optical process with two-photon excitation and a resonant intermediate state.

## 6.1 TWO-PHOTON SPECTROSCOPY

Magnetic field induced SFM under simultaneous single and two-photon resonant enhancement is intimately related to the consideration of two-photon absorption with a resonant intermediate state since each process involves a similar excitation scheme.

### 6.1.1 *Single and Two-Photon Resonant Enhancement*

The process of two-photon absorption with equal frequency photons is well understood and has been reviewed many times, see for example [67,95,127]. However, the case where the two photons involved have different frequencies is interesting since new features can be

seen. The study of unequal frequency two-photon excitation was pioneered by Bjorkholm and Liao who experimentally demonstrated and theoretically studied the effects of single and two-photon resonant enhancement from the viewpoint of two-photon spectroscopy.

The calculated absorption cross-section of an atom for light at frequency  $\nu_2$  induced by light at frequency  $\nu_1$ , ie. the induced absorption cross-section for two-photon transitions from ground state  $|g\rangle$  to excited state  $|f\rangle$  via intermediate states  $|i\rangle$  is [47]

$$\sigma(\nu_2) = 1.15 \times 10^{-34} \left| \sum_i \langle f | z | i \rangle \langle i | z | g \rangle \right. \\ \left. [1/(E_i - h\nu_1) + 1/(E_i - h\nu_2)]^2 \nu_2 \rho(\nu_1 + \nu_2) I_1 \right. \text{cm}^2 \quad (6.1.1)$$

where  $I_1$  ( $\text{W cm}^{-2}$ ) is the intensity of the beam at frequency  $\nu_1$  and  $\rho(\nu_1 + \nu_2)$  is the normalised line shape function for the transition. When values for the dipole matrix elements relevant to atomic sodium are calculated and with an intermediate state detuning  $h\Delta \equiv E_{3p} - h\nu_1$  of  $\sim 0.1 \text{ cm}^{-1}$ , the induced cross-section for  $\nu_2$  is  $\sim 5 \times 10^{-14} I_1 \text{ cm}^2$  which is easily made comparable to the strong sodium 3S-3P single photon absorption cross-section of  $\sim 3 \times 10^{-10} \text{ cm}^2$  ( $= \lambda^2/4\pi$ ).

Using two tunable, single-mode, cw dye lasers and counterpropagating beams to reduce Doppler broadening, Bjorkholm and Liao could easily identify the four separate 3S-4D two-photon transitions in sodium [55]. By measuring the strength of the emitted 4P-3S fluorescence signal, the strength of the two-photon absorption cross-section was shown to be enhanced by over 7 orders of magnitude when the frequency of one beam approximately corresponded to that of the 3S-3P single photon transitions. Their results are reproduced in Figure 6.1.

For the on resonance study, the line strength was  $6 \times 10^9$  larger than that for excitation with equal frequency photons [48].

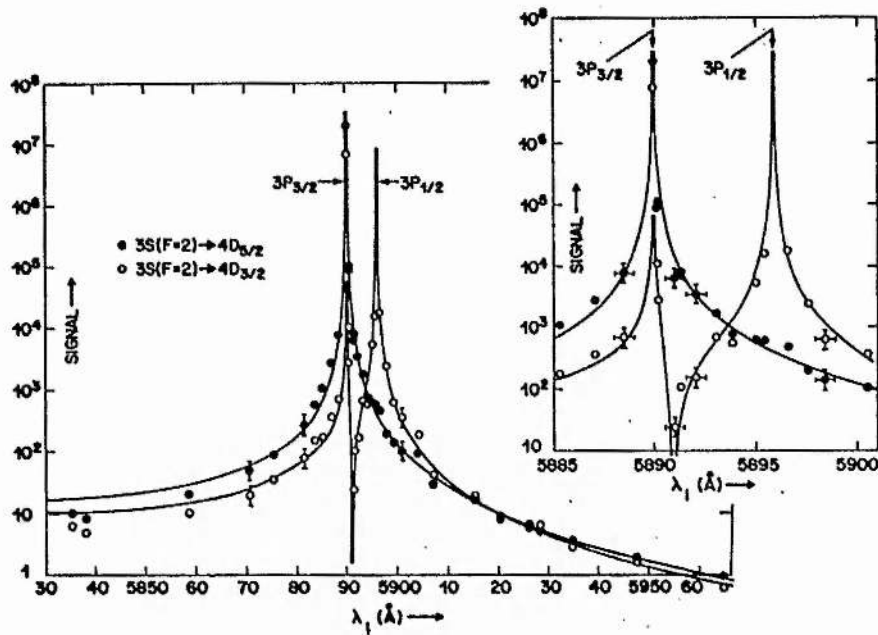


Figure 6.1 : Normalised two-photon transition rates as a function of  $\lambda_1$ . Points are experimental and curves are theoretical (from [47]).

The resonant enhancement curves show destructive interference effects in the absorption when a route to a single final atomic state can pass through two intermediate states with antiphase contributions (minimum at 589.1 nm on the  $3S (F=2) \rightarrow 4D_{3/2}$  transition via the  $3P_{1/2}$  and  $3P_{3/2}$  intermediate states). Since the  $3P_{1/2} \rightarrow 4D_{5/2}$  single photon dipole transition is forbidden, the  $3S (F=2) \rightarrow 4D_{5/2}$  two-photon transition only shows one resonant enhancement peak at the  $3S \rightarrow 3P_{3/2}$  wavelength. Note that the laser powers were attenuated so that saturation effects could be neglected.

Unlike the case of equal frequency, counterpropagating two-photon spectroscopy where all of the atoms contribute to the signal through equal cancellation of the Doppler shifts for all velocity groups, the use of unequal frequencies leads to a reduction in the number of excited atoms. Consider the atom shown in Figure 6.2 subjected to oppositely propagating light beams of frequency  $\nu_1$  and  $\nu_2$ .

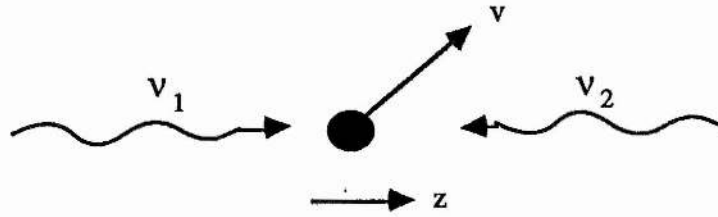


Figure 6.2 : Schematic diagram of an atom with velocity component  $v_z$  interacting with two light waves of frequency  $\nu_1$  and  $\nu_2$ .

In the rest frame of the atom, the incident waves are Doppler shifted to

$$\nu_1' = \nu_1 \left(1 - \frac{v_z}{c}\right) \quad \text{and} \quad \nu_2' = \nu_2 \left(1 + \frac{v_z}{c}\right)$$

so that the apparent sum frequency is

$$\nu(v_z) = \nu_1' + \nu_2' = \nu_1 + \nu_2 + \frac{v_z}{c} (\nu_2 - \nu_1). \quad (6.1.2)$$

Thus the sum frequency becomes velocity dependent when  $\nu_1 \neq \nu_2$  and only those atoms for which  $\nu(v_z)$  lies within the homogeneous linewidth of the two-photon transition  $\nu_0$  can be excited.

At the peak of the two-photon absorption line, the fraction of atoms  $\eta$  in the Doppler broadened line which can simultaneously interact with the light is [128]

$$\eta = \sqrt{\pi} y e^{-y^2} \operatorname{erfc}(y). \quad (6.1.3)$$

The parameter  $y$  is defined as

$$y = \sqrt{\ln 2} \frac{\nu_0}{|\nu_2 - \nu_1|} \frac{\Delta\nu_h}{\Delta\nu_D} \quad (6.1.4)$$

where  $\Delta\nu_h$  is the two-photon homogeneous linewidth (FWHM) and  $\Delta\nu_D$  is the Doppler width (FWHM). The function  $\operatorname{erfc}(z)$  is the error function for a complex argument [129]

$$\operatorname{erfc}(z) = \operatorname{erfc}(a + iy) = \frac{1}{\pi} \int_{-\infty}^{\infty} \frac{[y + i(a-x)] e^{-x^2}}{y^2 + (a-x)^2} dx. \quad (6.1.5)$$

Figure 6.3 shows the variation of  $\eta$  with  $y^{-1}$  and also of the linewidth of the two-photon

transition  $\delta\nu$  (FWHM), normalised to the homogeneous linewidth  $\Delta\nu_h$ .

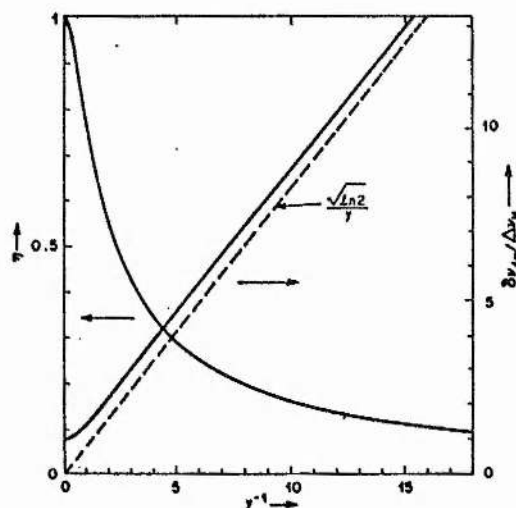


Figure 6.3 : Curves of the atomic efficiency  $\eta$  and normalised linewidth  $\delta\nu/\Delta\nu_h$  as functions of  $y^{-1}$  (from [128]).

As expected, when  $y^{-1} \ll 1$  the linewidth  $\delta\nu$  is equal to the homogeneous linewidth  $\Delta\nu_h$  and for  $y^{-1} \gg 1$ ,  $\delta\nu$  equals the residual Doppler broadening  $\Delta\nu_D |(\nu_2 - \nu_1)| / \nu_0$ .

Thus in spite of the fraction of atoms excited when  $\nu_2$  is in resonance with the 3S-3P transition only being  $\eta < 0.1$ , the resonant enhancement due to the single photon transition more than compensates for the reduction in the number of interacting atoms and produces the large signal strengths.

### 6.1.2 On Resonance Excitation

In the previous section, the description of two-photon absorption was valid for  $\Delta > \Delta\nu_D$ , ie. an intermediate state detuning outside the single-photon Doppler width. Bjorkholm and Liao subsequently carried out a detailed study of the two-photon absorption line shape and strength for detunings  $\Delta \leq \Delta\nu_D$  [48]. In general, under these detuning conditions, the absorption line is composed of two types of line shape:

(a) A Voigt profile (a Gaussian convoluted with a Lorentzian) with a Doppler broadened linewidth (FWHM) of

$$\approx \left| (v_1 + \epsilon v_2) / v_{fg} \right| \Delta v_{fg} \approx \left| (v_1 + \epsilon v_2) / v_{ig} \right| \Delta v_{ig} \quad (6.1.6)$$

when the linewidth is large compared to the homogeneous linewidth of the final state. The widths  $\Delta v_{fg}$  and  $\Delta v_{ig}$  are the Doppler widths of the two-photon transition and the intermediate to ground state single photon transition respectively. The parameter  $\epsilon$  equals +1 for copropagating beams and -1 for counterpropagating beams. This line shape is the one described in section 6.1.1 and displays full or residual Doppler broadening.

(b) A Lorentzian line of linewidth (FWHM)

$$\Delta v_f + \left| (v_1 + \epsilon v_2) / v_{ig} \right| \Delta v_i \quad (6.1.7)$$

where  $\Delta v_f$  and  $\Delta v_i$  are the homogeneous linewidths of the final and intermediate states respectively. This line is truly Doppler-free and occurs as a result of velocity selective excitation on the  $|g\rangle \rightarrow |i\rangle$  transition.

The relative magnitudes of the two lineshape components (a) and (b) deviate as  $v_1$  approaches the 3S-3P transition frequency. As shown in Figure 6.4, the Doppler-free Lorentzian line dominates over the residual Doppler broadening when  $v_1$  is tuned within the Doppler width of the D line transition. Note that the signal strength scale was chosen so that unity corresponds to the signal strength for equal frequency two-photon excitation.

## 6.2 VELOCITY SELECTIVE EXCITATION

A qualitative understanding of how velocity selective excitation occurs on resonance is obtained by considering a simple hole-burning argument. This is exactly the same situation as applies to saturation spectroscopy but now the probe frequency is in general different from that of the pump and probes the upper state pumped level population. Narrow linewidth light  $\Delta v_L < \Delta v_h$  interacting with the two lower levels of a three level cascade system with a detuning  $\Delta < \Delta v_D$  selectively excites a particular group of atoms whose velocities are such that  $|v_{ig} - (1 + v/c)v_1| \ll \Delta v_i$ , ie. the homogeneous velocity group which is Doppler shifted to be exactly resonant with the light at fixed frequency  $v_1$ .

Upon tuning  $v_2$ , a homogeneous velocity group is produced in the final state which

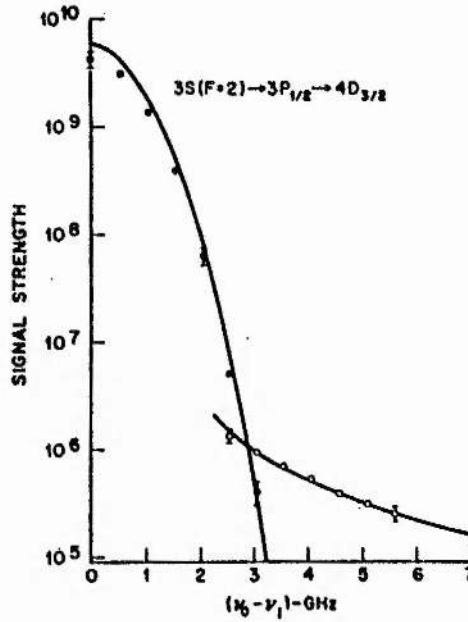


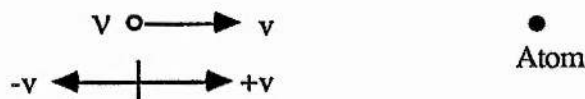
Figure 6.4 : Experimentally measured and theoretically calculated peak heights of the two-photon signal as a function of the detuning  $\nu_{3S-3P} - \nu_1$  for oppositely propagating beams. Solid circles correspond to the Doppler-free on-resonance line and open circles to the Doppler-broadened off-resonance line (from [48]).

reflects the intermediate state population. The fluorescence signal due to the upper state population is Doppler-free and the linewidth is determined by (6.1.7). The absolute frequency of  $\nu_2$  at resonance depends upon the velocity of the packet which is excited into the intermediate state due to the Doppler shift of the two-photon frequency.

### Doppler Shifts

The Doppler shifts of the incident light and the atomic resonant frequencies are defined as follows. Two frames of reference are considered:

**Stationary atom** - the atom (observer) is regarded at rest and the incident light is Doppler shifted



$$v_{\text{atom}} = v \frac{1}{(1 - v/c)} \approx v \left(1 + \frac{v}{c}\right) \quad (v \ll c) \quad (6.2.1)$$

**Moving atom** - atom (source) is regarded in motion with velocity  $v$  and the atomic transition frequencies are Doppler shifted. Light (observer) is at a fixed frequency  $v$ .



$$v_{\text{observed}} = v_{\text{ig}} (1 - v/c) \quad (6.2.2)$$

These definitions are chosen for the sign of  $v$  so that a positive single photon detuning  $\Delta = v_{\text{ig}} - v$  selects a positive velocity group  $+v = 2\pi \Delta / k$ .

Energy level structure in the ground, intermediate or final states of the atom complicates the observed two-photon spectrum due to different Doppler shifts of the various levels. If the ground state has non-degenerate energy levels then a different velocity group is selected by a beam at fixed frequency  $\nu_1$  for each possible ground-to-intermediate-state transition. The Doppler shifts of the different velocity groups causes a ground-state splitting of  $\delta\nu_g$  to appear as a splitting of  $(\nu_2/\nu_1) \delta\nu_g$  in the two-photon spectrum. Similarly, intermediate-state structure gives rise to a splitting in the spectrum of  $\delta\nu_i (\nu_1 + \epsilon\nu_2) / \nu_1$ . Final-state splittings depend upon which velocity group is excited and will be  $\delta\nu_f (1 - v/c)$ .

If counterpropagating beams are used for the excitation ( $\epsilon = -1$ ) and  $\nu_1 \approx \nu_2$  then the intermediate-state structure is barely resolved. The splitting is much larger if copropagating

beams excite the two-photon resonance ( $\epsilon = +1$ ) and the two-photon spectrum then yields Doppler-free information about the intermediate-state level structure in contrast to the off-resonant case.

The coherence between the ground and upper states  $\rho_{fg}$  which is responsible for SFM is inversely proportional to the laser detunings from single and two-photon resonance. In general, for fixed values of  $\Delta$  and  $\delta$ , three types of velocity group contribute to SFM as shown in Figure 6.5

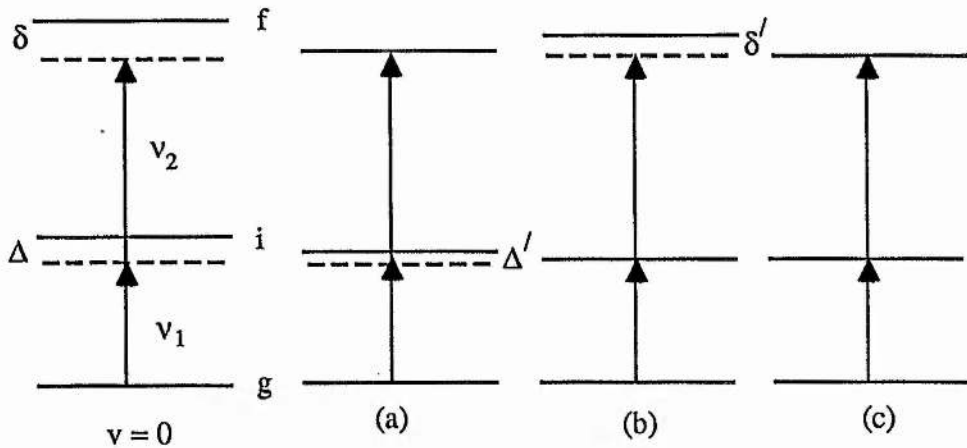


Figure 6.5 : Schematic diagram of 3 level atom at rest with single photon detuning  $\Delta$  and two-photon detuning  $\delta$ .

- (a) Two-photon but not single photon resonant.
- (b) Single photon but not two-photon resonant.
- (c) Single and two-photon resonant.

Case (a) is similar to that for the SHG experiment except that since  $\Delta < \Delta v_D$ , the excitation is of a homogeneous velocity group rather than being velocity independent.

Case (b) can be regarded as the opposite of (a) where the single photon transition on resonance provides the main resonant enhancement for the nonlinear optical effect. Note that for this detuning condition, the sum frequency is tunable upon tuning  $v_2$ .

Case (c) produces the largest resonant enhancement where the light fields are both single and two-photon resonant. This case corresponds to particular values of  $\Delta$  and  $\delta$  only. It can be shown by calculating Doppler shifts that

$$(a) \delta' = 0 \Rightarrow \Delta = \frac{v_{21} \delta}{(v_{21} + v_{32} + \delta)} \quad (6.2.3)$$

$$(b) \Delta' = 0 \Rightarrow \delta = \Delta \left[ 1 + \frac{v_{32}}{(v_{21} + \Delta)} \right] \quad (6.2.4)$$

are the conditions for simultaneous single and two-photon resonance.

Another feature of velocity selective excitation is that the apparent frequency of the SFM wave as seen by the other atoms depends upon whether the selected velocity group is moving in the same or opposite direction to the wave vectors of the incident light waves.

Generation of the sum frequency wave can occur in one direction only, namely the direction of propagation of the two incident waves, so a selected velocity group travelling in this direction will emit a blue-shifted sum frequency wave whilst a velocity group travelling in an opposite direction to the incident beams will emit a red-shifted sum frequency wave.

### 6.3 OPTICAL PUMPING

Due to the hyperfine structure of the ground state of sodium and the use of on-resonance single photon transitions in resonant SFM, hyperfine optical pumping becomes possible by a frequency selective depopulation of the ground state [50]. This is shown in Figure 6.6 where population is preferentially accumulated in the  $F=1$  sublevels due to strong light excitation from the  $F=2$  ground states. The mechanism for populating the  $F=1$  levels is spontaneous emission.

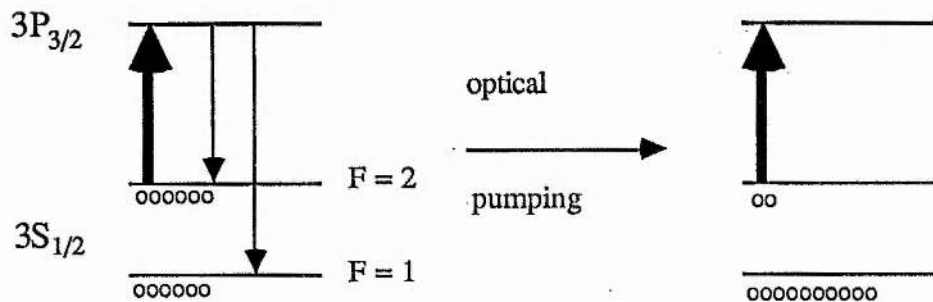


Figure 6.6 : Simple schematic diagram of frequency selective optical pumping of Na.

In spite of the excitation being primarily velocity selective, the presence of collisions due to buffer gas atoms destroys any velocity selective optical pumping (VSOP) due to thermalisation by velocity changing collisions (vcc) [130] (see also Chapter 4). The vcc also aid optical pumping across the whole Doppler width of the transition [105, 106]. Inelastic collisions may equalise the hyperfine state populations if the pressure of the buffer gas is too high but the presence of buffer gas can also aid optical pumping by restricting diffusion of the pumped atoms (see Chapter 7).

Movement of population in the ground state of the atom has serious implications for the resonant SFM nonlinear optical process. The first main effect is loss of population on the favoured on-resonance single photon excitation route. If optical pumping is 100% efficient then all of the ground-state population is transferred to a ground state level with which the incident light is relatively weakly interacting. This causes a depletion of the nonlinear mixing process. The second main effect on SFM through the change in ground state population by optical pumping is the corresponding changes in refractive index of the atomic vapour. The refractive index associated with the 3S-3P D line resonance transitions reflects the population distribution in the ground-state hyperfine sublevels and the excited 3P states (see § 6.6). Large changes in refractive index for the wave at frequency  $\nu_1$  are produced by the optical pumping effect and phase matching of the SFM nonlinear optical process is modified to reduce the generation efficiency of the sum-frequency wave.

The magnitude of the movement of ground-state population through optical pumping was measured with the schematic experimental arrangement shown in Figure 6.7.

The two cw frequency stabilised, single-mode ring dye lasers were used as the pump and the probe beams and each laser was tuned to the  $3S_{1/2} - 3P_{3/2}$   $D_2$  Na transition. Both beams were unfocused with beam diameters of  $\sim 4$  mm and crossed at a small angle in the sodium oven. The pump beam power was  $\sim 60$  mW (typical for a SFM experiment) with the probe beam attenuated to  $< 0.5$  mW. The temperature of the sodium oven was set to give  $> 50\%$  linear absorption for the chopped probe beam without the pump beam being present.

The results obtained with an applied magnetic field of  $\sim 40$  G and both laser

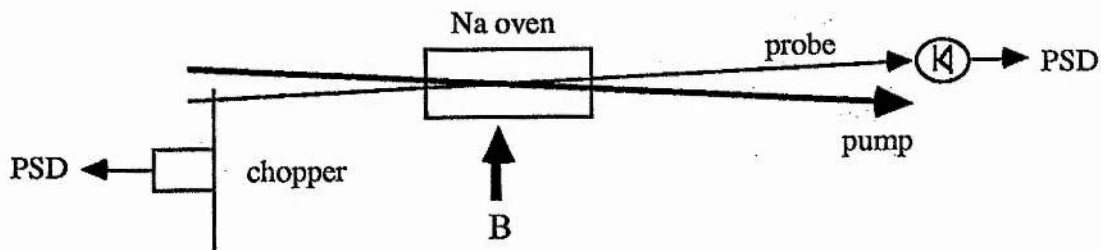


Figure 6.7 : Schematic diagram of the experiment to measure the degree of optical pumping.

polarisations perpendicular to the B field are shown in Figure 6.8. They clearly show the effects of optical pumping on the absorption of the probe beam upon fixed tuning of the pump beam to the  $3S (F=1) \rightarrow 3P_{3/2}$ ,  $3S (F=2) \rightarrow 3P_{3/2}$  transitions and midway between them. The frequency of the pump beam was measured from the saturated absorption spectrum of the  $3S \rightarrow 3P_{3/2}$  transitions and the crossover resonance midway between these transitions (see § 4.1.3) in the reference Na cell.

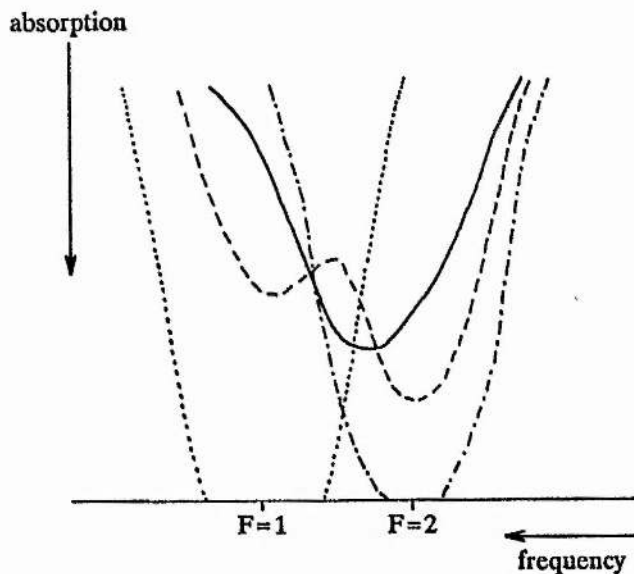


Figure 6.8 : Absorption of the probe beam for

- probe only
- - - - - pump tuned midway between F=1 and F=2
- · · · · pump tuned to F=1
- · - · - pump tuned to F=2

Tuning the pump beam to the  $3S (F=1) \rightarrow 3P_{3/2}$  transition obviously greatly increases the population in the  $F=2$  ground-state sublevels and vice versa showing that strong optical pumping is taking place. Complete absorption of the probe beam is achieved with the pump beam tuned exactly onto the  $F=1, 2$  resonances. Note the relatively narrow width of the localised decrease in probe absorption with the pump laser tuned to the crossover resonance showing that complete velocity thermalisation has not taken place. However, most of the Doppler width is optically pumped.

Evidence of optical pumping was also seen at higher values of the applied transverse magnetic field, and this was again dependent upon the detuning of the pumping light.

## 6.4 COLLISIONAL EFFECTS

### 6.4.1 *Pressure Broadening*

The collisions of buffer gas atoms with excited atomic energy states of sodium causes the lifetime of these states to be reduced due to the phase of the atomic wavefunction being perturbed and collision-induced transitions to other atomic levels. This is a homogeneous broadening mechanism which can be described by

$$\Delta v_h (\text{HWHM}) = \Delta v_N (\text{HWHM}) + \beta P. \quad (6.4.1)$$

$\Delta v_N$  is the natural linewidth equal to  $1/2 \pi \tau_s$  where  $\tau_s$  is the spontaneous emission lifetime of the atomic state. The pressure broadening coefficient is  $\beta$  (MHz/mbar) and  $P$  (mbar) is the pressure of the perturbing buffer gas. The pressure broadening coefficient is dependent upon the temperature of the vapour.

$$\beta_1 = \beta_2 \sqrt{\frac{T_2}{T_1}} \frac{\sigma_1}{\sigma_2} \quad (6.4.2)$$

where  $\sigma_n$  is the sodium-buffer gas collision cross-section at an absolute temperature  $T_n$  [131]. The values of  $\sigma_n$  are approximated to be independent of temperature so that it is possible to convert measured values of  $\beta$  at one temperature to the required temperature conditions.

The pressure broadened linewidth of the sodium  $3S-4D$  transition has been measured by Doppler-free two-photon absorption [132, 14], free induction decay of the coherently excited  $4D$  state [133], tri-level echoes [131] and Doppler limited two-photon absorption [134].

A measurement of the pressure broadening of the sodium D lines,  $3S_{1/2} - 3P_{1/2}$  ( $D_1$ ) and  $3S_{1/2} - 3P_{3/2}$  ( $D_2$ ), has been made by an absorption technique [135]. The broadening of the sodium diffuse series 3P-4D transitions by noble gas collisions was measured by emission from a high intensity sodium discharge [136].

Table 1 summarises the data in the literature and a calculated value of the equivalent pressure broadening coefficient.

Transition	Buffer gas	Tabulated Value	Temperature (K)	$\beta_T$ (MHz/mbar)
3S - 4D	Ar	$9.6 \pm 1.0 \times 10^{-9} \text{ rad s}^{-1} (\text{atom cm}^{-3})^{-1}$	563	20
	He	$7.7 \pm 0.9 \times 10^{-9} \text{ rad s}^{-1} (\text{atom cm}^{-3})^{-1}$	563	16
$3S_{1/2} - 3P_{1/2}$	Ar	$\frac{1}{2}(2.94 \pm 0.2) \times 10^{20} \text{ cm}^{-1} (\text{atom cm}^{-3})^{-1}$	460	7
	He	$\frac{1}{2}(2.02 \pm 0.1) \times 10^{20} \text{ cm}^{-1} (\text{atom cm}^{-3})^{-1}$	460	5
$3S_{1/2} - 3P_{3/2}$	Ar	$\frac{1}{2}(2.41 \pm 0.2) \times 10^{20} \text{ cm}^{-1} (\text{atom cm}^{-3})^{-1}$	460	6
	He	$\frac{1}{2}(2.32 \pm 0.2) \times 10^{20} \text{ cm}^{-1} (\text{atom cm}^{-3})^{-1}$	460	6
$3P_{1/2} - 4D_{3/2}$	Ar	$4.3 \pm 0.3 \times 10^{-20} \text{ cm}^2 (\text{atom cm}^{-3})$	500	19
	He	$3.6 \pm 0.2 \times 10^{-20} \text{ cm}^2 (\text{atom cm}^{-3})$	500	16

Table 1 : Experimental pressure broadening data for sodium transitions.

Helium and argon were used as the buffer gases in the SFM experiments at pressures of  $\sim 1$  mbar ( $25^\circ\text{C}$ ) and at working temperatures of  $\sim 120^\circ\text{C}$ . The lifetime of the 4D state of Na against spontaneous emission is  $\sim 52$  ns [137, 138] and of the 3P state is  $\sim 16$  ns [110] giving  $\Delta\nu_N$  (3S-4D)  $\sim 3$  MHz and  $\Delta\nu_N$  (3S-3P)  $\sim 10$  MHz. Therefore, the calculated experimental collision-broadened homogeneous linewidths are:

$$\begin{aligned} \text{Ar} - \Delta\nu_h(3\text{S}-4\text{D}) &\sim 35 \text{ MHz (HWHM)} \\ \Delta\nu_h(3\text{S}-3\text{P}_{1/2}) &\sim 18 \text{ MHz} \\ \Delta\nu_h(3\text{S}-3\text{P}_{3/2}) &\sim 17 \text{ MHz} \end{aligned}$$

$$\begin{aligned} \text{He} - \Delta\nu_h(3\text{S}-4\text{D}) &\sim 29 \text{ MHz (HWHM)} \\ \Delta\nu_h(3\text{S}-3\text{P}_{1/2}) &\sim 16 \text{ MHz} \\ \Delta\nu_h(3\text{S}-3\text{P}_{3/2}) &\sim 17 \text{ MHz} \end{aligned}$$

These traditional measured line broadening values ignore the velocity selective aspect of the

two-photon excitation process on resonance. A recent detailed study by O'Callaghan and Gallagher using the same on-resonance unequal photon excitation scheme as discussed in this chapter showed that the broadening coefficients are velocity dependent as would be expected [139]. Higher velocity atoms selected by larger 3S-3P detunings produce larger widths and broadening rates, eg. for the  $3S_{1/2} - 3P_{1/2} - 4D$  two-photon route, the 4D pressure broadening coefficients (FWHM) at single photon 3S-3P detunings of  $\Delta = 0.0$  GHz,  $-1.5$  GHz are 80 MHz/Torr and 104 MHz/Torr respectively. The theory for the two-photon line shape including effects due to coherent excitation, incoherent excitation (due to dephasing collisions), interference between coherent and incoherent excitation and velocity changing collisions gave good agreement with the measured lineshapes [140].

#### 6.4.2 Pressure Shifts

During a collision with a perturbing buffer gas atom the energy levels of the sodium atom are shifted due to the interaction. The magnitude of the shift is less than the pressure broadening and can be positive or negative in frequency depending upon the colliding atoms. Table 2 summarises the data in the literature for sodium transition pressure shifts [132, 135, 136].

Transition	Buffer gas	Tabulated shift	Temperature (K)	Shift (MHz/mbar)
3S - 4D	Ar	$-5.9 \pm 0.8 \times 10^{-9} \text{ rad s}^{-1} (\text{atom cm}^3)^{-1}$	563	-12
	He	$1.7 \pm 0.4 \times 10^{-9} \text{ rad s}^{-1} (\text{atom cm}^3)^{-1}$	563	+3.5
$3S_{1/2} - 3P_{1/2}$	Ar	$-0.754 \pm 0.02 \times 10^{20} \text{ cm}^{-1} (\text{atom cm}^{-3})^{-1}$	460	-3.5
	He	$-0.002 \pm 0.03 \times 10^{20} \text{ cm}^{-1} (\text{atom cm}^{-3})^{-1}$	460	-0.01
$3S_{1/2} - 3P_{3/2}$	Ar	$-0.805 \pm 0.04 \times 10^{20} \text{ cm}^{-1} (\text{atom cm}^{-3})^{-1}$	460	-4
	He	$-0.037 \pm 0.035 \times 10^{20} \text{ cm}^{-1} (\text{atom cm}^{-3})^{-1}$	460	-0.2
$3P_{1/2} - 4D$	Ar	$-2.6 \pm 0.3 \times 10^{-20} \text{ cm}^2 (\text{atom cm}^{-3})$	500	-11
	He	$0.4 \pm 0.3 \times 10^{-20} \text{ cm}^2 (\text{atom cm}^{-3})$	500	+2
$3P_{3/2} - 4D$	Ar	$-3.0 \pm 0.3 \times 10^{-20} \text{ cm}^2 (\text{atom cm}^{-3})$	500	-13
	He	$0.6 \pm 0.3 \times 10^{-20} \text{ cm}^2 (\text{atom cm}^{-3})$	500	+3

Table 2 : Experimental pressure shift data for sodium transitions.

Since all of these energy level shifts are less than the SFM experimental pressure broadened homogeneous linewidths, the shift will be neglected.

#### 6.4.3 Collisional Redistribution

Population changes occur within a set of atomic sublevels because of collisions. Nonradiative transitions between fine, hyperfine and magnetic energy levels are induced by buffer gas collisions where the energy lost or gained in the atomic energy levels is balanced by the kinetic energy of the colliding atoms.

The fine state mixing between the  $4D_{3/2}$  and  $4D_{5/2}$  levels of sodium has been studied by equal frequency two-photon absorption [141, 142]. The cross-sections  $\sigma(5/2 \rightarrow 3/2)$  and  $\sigma(3/2 \rightarrow 5/2)$  were measured experimentally by preferentially exciting to one of the 4D levels and examining the collision induced fluorescence from the other. The population of each 4D sublevel becomes equal with a relatively low pressure of buffer gas ( $\sim 1$  mbar). Population changes between the  $3P_{1/2}$  and  $3P_{3/2}$  fine-structure levels of sodium have been examined in a similar way but with unequal frequency on-resonance two-photon excitation [143, 144, 139, 140]. Experimental results showed that the fine-structure state changes appear to happen with little or no change in velocity of the sodium atom since the lineshape remains sub-Doppler [145]. Non-radiative transitions between the Zeeman-split magnetic energy levels of a given S, P or D state also occur due to inert gas collisions. The mixing between the Zeeman substates in the 3P states of sodium has been studied in very high magnetic fields [146]. In the SFM case, the collision induced mixing depends upon which velocity selected Zeeman levels are excited and would be difficult to interpret because of the large number of closely spaced levels involved, each with different Doppler shifts.

Inelastic collisions transfer population from the optically excited levels and populate nearby levels [147]. This collisional process is parasitic to the SFM nonlinear optical effect since population is lost from the coherently excited routes. Of particular relevance to on-resonance SFM is that strong fluorescence with a wavelength of  $\sim 285$  nm was detected in addition to the normal 330 nm fluorescence from the sodium 4P states. This was attributed to a

collision induced transfer of a component of the large excited 4D population to the higher lying 5P states (energy separation  $\sim 493 \text{ cm}^{-1} \approx 1.8 k_B T$  at 393 K) and subsequent 5P-3S fluorescence at 285.5 nm. The 5P signal closely followed the 4P fluorescence signal upon tuning  $\nu_2$  through the 4D states and was also present when no transverse magnetic field was applied. The proximity of the 285 nm fluorescence to the 289 nm coherent SFM emission necessitated the experimental use of a monochromator based detection system to distinguish between these two wavelengths.

#### 6.4.4 *Velocity Changing Collisions*

In contrast to state changing collisions and collisional redistribution, velocity changing collisions (VCCs) modify the initial narrow homogeneous hole which is burnt into the ground state velocity distribution and cause the excited distribution to broaden and shift to equilibrium (see also § 4.1.5). Non-degenerate two-photon spectroscopy has been used to examine the complex contribution of these type of collisions to the two-photon spectrum [145]. In general, the vcc only act on the 3S ground state sublevels because the lifetime of the 3P states is very short and so the 3P steady state velocity distribution shows a "persistence of velocity". Typical vcc cross-sections are  $\sim 40 \text{ \AA}^2$  but depend on the type of buffer gas. Since on-resonance SFM is velocity selective, vcc's will also effect this nonlinear optical process in a similar manner.

#### 6.5 LASER POWER EFFECTS

In general, nonlinear optical effects require high laser powers to induce the nonlinear polarisations because the higher order susceptibilities are weak. For simultaneous single and two-photon resonant magnetic field induced SFM, the two-photon and single photon transitions are strongly driven by the light fields, leading to saturation and higher order nonlinear effects.

### 6.5.1 Single Photon Saturation

Under weak excitation with low strength optical electric fields ( $E_{\text{light}} \ll E_{\text{atom}}$ ), the interaction of light with a two level atomic dipole transition is dominated by the rapid decay rate  $\gamma$  from the upper level by spontaneous emission and the ground state population remains unperturbed. With higher light intensity, the rate of excitation from the ground state by the light can be made equal to that of excited state decay and the transition becomes saturated (see also § 4.1.5). The strength of interaction of the light field with the atom can be described by the Rabi frequency  $\Omega$  which is given by

$$\Omega \text{ (rad s}^{-1}\text{)} = \frac{\mu_{12} \cdot \underline{E}}{\hbar} \quad (6.5.1)$$

where  $\mu_{12}$  is the dipole matrix element between the ground state and upper state and  $\underline{E}$  ( $\text{Vm}^{-1}$ ) is the electric field of the light. Light intensity and equivalent electric field are defined by

$$I \text{ (Wm}^{-2}\text{)} = \frac{n c \epsilon_0}{2} |E|^2. \quad (6.5.2)$$

The saturation intensity for a simple two level atomic system, ie. in the absence of optical pumping or branching effects, is [148, 95]

$$I_{\text{sat}} \text{ (Wm}^{-2}\text{)} = \frac{n c \epsilon_0}{2} \frac{\hbar^2}{|\mu_{12}|^2} \frac{\gamma}{\tau} \quad (6.5.3)$$

where  $\gamma$  is the transverse relaxation rate of the transition equal to  $\frac{1}{2}(\gamma_1 + \gamma_2)$  and  $\tau$  is the longitudinal relaxation time of the atomic populations.

The dipole matrix element  $\mu_{12}$  is found directly from the spontaneous emission coefficient  $A_{21}$  for the transition [149].

$$|\mu_{21}|^2 = \frac{3\pi\epsilon_0\hbar c^3}{\omega_{21}^3} A_{21}. \quad (6.5.4)$$

When  $I = I_{\text{sat}}$ , the absorption coefficient of the ground state is reduced to one half of its unsaturated value. As  $I \rightarrow \infty$ , the absorption coefficient  $\alpha \rightarrow 0$  and the populations of the ground and excited atomic states are equalised. Saturation broadens the homogeneous

linewidth of the transition due to the large number of induced transitions by the optical field [148].

$$\Delta\nu'_{21} = \Delta\nu_{21} (1 + I/I_{\text{sat}})^{\frac{1}{2}} \quad (6.5.5)$$

This is called saturation or power broadening.

The A coefficient for the 3S-3P transition of sodium is  $0.629 \times 10^8 \text{ s}^{-1}$  [110] which implies an average dipole moment of  $\sim 2.14 \times 10^{-29} \text{ Cm}$ . The 16 ns lifetime of the P state gives  $\Delta\nu_{21} = 10 \text{ MHz}$  if spontaneous emission is the only decay process. The average saturation intensity is  $\sim 6.4 \text{ mW cm}^{-2}$  for the collision-free D line resonances. Each 3S-3P hyperfine transition actually has its own dipole matrix element and individual saturation intensity [74]. In the presence of collisions, the lifetime of the P state is reduced as discussed in §6.4.1 and the saturation intensity will be a factor of  $(\Delta\nu_{\text{collision}} / \Delta\nu_{\text{spontaneous}})^2$  times the natural saturation intensity of  $6.4 \text{ mW cm}^{-2}$ .

The 3P-4D saturation intensity is more complicated to calculate since the 4D level can decay to other levels and these additional decay channels decrease the longitudinal relaxation time. When the lifetimes of the upper and lower states are  $T_2$  and  $T_1$  respectively and the rate of direct relaxation from  $|2\rangle \rightarrow |1\rangle$  is  $A_{21}$ ,  $I_{\text{sat}}$  becomes [95]

$$I_{\text{sat}} = \frac{n(\omega)c\epsilon_0}{2} \frac{\hbar^2}{|\mu_{12}|^2} \frac{\gamma}{(T_1 + T_2 - A_{21} T_1 T_2)} \quad (6.5.6)$$

The coefficient  $A(4D-3P)$  is  $0.131 \times 10^8 \text{ s}^{-1}$  and  $A(4D-4P)$  is  $0.067 \times 10^8 \text{ s}^{-1}$  [110] giving a total 4D state lifetime of 50.5 ns ( $\Delta\nu_{\text{spont}} \sim 3.2 \text{ MHz}$ ). The average dipole moment for the 3P-4D transition, as found from equation (6.5.4) is  $\sim 9.25 \times 10^{-30} \text{ Cm}$ . For decay through spontaneous emission only, the saturation intensity is  $\sim 13 \text{ mW cm}^{-2}$ . The collision broadened case requires explicit values of  $T_1$ ,  $T_2$  and  $\gamma$  to be inserted into (6.5.6) to calculate the new saturation intensity.

### 6.5.2 Two-Photon Saturation

The equivalent Rabi frequency for a two-photon transition is [33]

$$\Omega_{TP}^2 = \left| \sum_i \frac{\langle f | \mu | i \rangle \langle i | \mu | g \rangle E_1 E_2}{\hbar^2 (\omega_i - \omega_1 - i \gamma_{ig})} \right|^2 \quad (6.5.7)$$

and saturation of the two-photon absorption occurs when the two-photon absorption rate

$$W_{TP} = 2 \Omega_{TP}^2 \frac{\gamma_{fg}}{[(\omega_{fg} - \omega_1 - \omega_2)^2 + \gamma_{fg}^2]} \quad (6.5.8)$$

equals the longitudinal relaxation time of the upper state  $|f\rangle$  [150,151]. The limiting effect of two-photon saturation on non-resonant non-collinear SFM in Na vapour has been considered by Bethune et al [33]. For a 3S-3P detuning of  $41.2 \text{ cm}^{-1}$ , the generated SFM power became nonlinear in the product of the two beam powers at  $\sim 10^9 \text{ W}^2 \text{ cm}^{-4}$ .

For the simultaneous single and two-photon resonant magnetic field induced SFM process, an approximate order of magnitude calculation of  $I_1 I_2$  required for saturation with  $\omega_i - \omega_1 = 0$ ,  $\omega_{fg} - \omega_1 - \omega_2 = 0$ ,  $\gamma_{3S-3P} \sim 2\pi \times 18 \text{ MHz}$ ,  $\gamma_{3S-4D} \sim 2\pi \times 35 \text{ MHz}$  (both collision broadened - see § 6.4.1) based on the above detuning and laser powers gives  $I_1 I_2 \sim 500 \text{ W}^2 \text{ cm}^{-4}$ . This value is not strictly valid since the perturbative approximations assumed in deriving  $\Omega_{TP}$  and  $W_{TP}$  only apply when  $\Delta = \nu_1 - \nu_{ig} \gg \Delta\nu_{ig}, \Delta\nu_{fi}, \nu_{fg} - \nu_1 - \nu_2$  [127]. These conditions obviously do not apply for on-resonance single and two-photon excitation for SFM and so the product of laser intensities required for saturation of the two-photon absorption becomes more complicated.

Two-photon saturation changes the level populations of the ground state  $|g\rangle$  and final state  $|f\rangle$  and in single photon saturation. The  $|f\rangle \rightarrow |g\rangle$  transition linewidth is also broadened by

$$\Delta\nu'_{fg} = \Delta\nu_{fg} (1 + \Omega_{TP}^2 / \Omega_{TP \text{ sat}}^2)^{\frac{1}{2}} \quad (6.5.9)$$

### 6.5.3 Autler-Townes Effect

The strong interaction of light with the lower two levels  $|g\rangle$  and  $|i\rangle$  of a cascade three level atomic system modifies the absorption profile of a beam coupling the intermediate state

$|i\rangle$  to the final state  $|f\rangle$  [73]. Two resonances appear, split from the unperturbed transition frequency, separated by  $(\Delta^2 + 4\Omega^2)^{\frac{1}{2}}$  where  $\Delta = \omega_{gi} - \omega_l$  and  $\Omega$  is the Rabi frequency for the  $|g\rangle \rightarrow |i\rangle$  transition. This effect, first observed by Autler and Townes in microwave spectroscopy [152], is due to the strong coupling between the quantum atom and quantum light field. The coupled atom-wave system creates new eigenstates which have modified resonant features. The optical equivalent of the Autler-Townes effect (also called dynamic Stark effect, linear AC Stark effect, AC Stark splitting) has been distinctly observed in two-photon spectroscopy [153, 154, 155, 156] and cross-saturated absorption [157, 158] for moderate light intensities.

This splitting is not observed in the SFM nonlinear optical process, even though the optical fields are strong, because the conditions for observing the effect require counterpropagating beams and  $v_{if} < v_{ig}$  [159] neither of which is satisfied.

#### 6.5.4 Light Shifts

Atomic energy levels can be shifted in energy as a result of interaction with strong light fields. These level shifts are known as "light shifts" or as the "AC Stark effect" [160, 161]. Perturbation theory gives the frequency shift of an atomic level  $|g\rangle$  as ( $\Omega^2 \ll \Delta^2$ )

$$\delta v_g = \frac{1}{4} \sum_i \left[ \frac{|\mu_{ig} E|^2}{\hbar^2 (\omega_{ig} - \omega)} + \frac{|\mu_{ig} E|^2}{\hbar^2 (\omega_{ig} + \omega)} \right] \quad (6.5.10)$$

At higher laser intensities, the shift is [162]

$$\delta v_g = \frac{\Delta v}{2} \left[ \left( 1 + \sum_i \frac{|\mu_{ig} E|^2}{\hbar^2 \Delta v^2} \right) - 1 \right] \quad (6.5.11)$$

where  $\hbar \Delta v = E_{ig} - \hbar \omega$ .

The energy level shifts are due to virtual transitions caused by non-resonant light. Two-photon absorption processes generally involve such transitions and light shifts are therefore intrinsic to two-photon processes. The AC Stark effect can also be regarded as a frequency averaged normal Stark effect on an atomic level. As the frequency of the light  $\omega \rightarrow 0$ , the shift becomes the same as that due to a DC electric field.

Liao and Bjorkholm [161,162] have directly observed these shifts and intensity-dependent asymmetric line broadening on the 3S-4D two-photon transition in Na using unequal frequency, high-resolution two-photon spectroscopy. The measurements agreed well with the theory for  $|\Delta\nu| > 4$  GHz and the level shifts were shown not to arise because of either single or two-photon saturation. However for  $|\Delta\nu| < 4$  GHz, as is considered in this chapter, the perturbation theory was shown to break down and the shifts no longer became linearly dependent on light intensity.

The magnitude of any light shifts for the on-resonance SFM experiment is difficult to estimate. Velocity groups exactly resonant with the single and two-photon transitions which produce the dominant SFM effect should have very small shifts but other velocity groups with different Doppler shifts which contribute to the Doppler broadened background may have their energy levels shifted considerably by the strong light. The large number of involved atomic levels and inhomogeneous broadening also complicates the light shift effect.

### 6.5.5 Higher Order Nonlinear Effects

Moderate to high laser powers at frequencies close or on atomic resonances induce higher order nonlinear effects than the  $\chi^{(2)}$  responsible for SFM. These may limit the SFM conversion efficiency. Of the range of possible  $\chi^{(3)}$  effects possible, only two are considered further here, namely self-focusing and three-photon ionisation, since they do not require phase matching to be satisfied.

The phenomena of self-focusing/defocusing has been observed many times in atomic vapours under near resonant light excitation [163, 164] and is considered as a limiting factor in nonlinear optical mixing processes [33,11]. Self-focusing is due to saturation of the anomalous dispersion of a dipole transition which induces an intensity dependent component in the refractive index of the vapour. The refractive index  $n$  is then

$$n = n_0 + \Delta n |E|^2 \quad (6.5.12)$$

where  $\Delta n |E|^2$  is the optical field induced refractive index change. The Gaussian intensity distribution of an incident laser beam causes the atomic vapour to act as a lenslike medium, with the beam being focused on the high frequency side of the transition and defocused on the

low frequency side. Steady-state cw self-focusing has been observed on the 3S-3P transition in sodium [163]. Moderate powers of  $\sim 10^7 \text{ W cm}^{-2}$  at detunings of  $\sim 1\text{-}2 \text{ GHz}$  from the  $3S_{1/2}\text{-}3P_{3/2}$  transition produced strong focusing and defocusing effects. Self-trapping of the light was produced when self-focusing balanced the natural diffraction of the beam to produce a constant diameter filament in the vapour. Higher order beam filamentation, complex spatial patterns and beam breakup occurred with higher input powers or tuning closer to resonance. Exactly on resonance there is no nonlinear refraction component but spatial modifications of the beam profile can be produced by nonlinear absorption [165]. Weaker intensity outer portions of the beam are stripped away by the absorption and subsequent diffraction of the modified beam shape produces a non-Gaussian output.

For the SFM and spectroscopic line profiles obtained in § 6.7, the input laser beams were unfocused giving a power density of only  $\sim 1 \text{ W cm}^{-2}$  and the sodium density was kept low at  $\sim 10^{11} \text{ cm}^{-3}$  so that the self-focusing/defocusing effects were negligible. With the laser beams deliberately focused into the oven (§ 6.8) to increase the SFM conversion efficiency, strong focusing and defocusing of the beam at frequency  $\nu_1$  close to the 3S-3P sodium transition was observed at certain tuning of  $\nu_1$ . The light intensity and sodium density each had to be increased by  $\sim 100$  times to observe this intensity dependent refractive index effect. The limitation of self-focusing on the SFM conversion efficiency was not examined experimentally.

A sodium atom excited to the 4D state by on-resonance two-photon absorption is completely ionised by subsequent absorption of a photon from either beam at  $\nu_1$  (3S-3P) and  $\nu_2$  (3P-4D). The ionisation level for sodium is 5.139 eV so  $\nu_1 + \nu_2 + \nu_1$  generates a 1.25 eV photoelectron and  $\nu_1 + \nu_2 + \nu_2$  generates a 1.33 eV photoelectron. The cross-section for this three-photon ionisation process is expected to be very large since it is also single and two-photon resonantly enhanced [166]. Multiphoton ionisation limits the SFM process by absorption of the incident light and reduction of the ground state population which can change the phase matching. Emitted photoelectrons broaden and shift atomic energy levels by the Stark effect and reduce the resonant enhancement of the SFM process.

Bethune et al [33] measured a fractional ionisation of  $\sim 1\%$  when  $I_1 = I_2 =$

0.5 MW cm<sup>-2</sup>,  $\omega_{3S-4D} - \omega_1 - \omega_2 = 0$  and  $\omega_{3S-3P} - \omega_1 = 10$  cm<sup>-1</sup>. The ionisation cross-section for an atom in the 4D state is  $\sigma_i \sim 10^{-18}$  cm<sup>2</sup> [167]. With incident intensity values of  $\sim 1$  W cm<sup>-2</sup> for cw SFM, this gives an ionisation rate of  $\sim 3$  s<sup>-1</sup> which is very small compared to the other decay rates due to spontaneous emission and collisions.

## 6.6 ABSORPTION AND REFRACTIVE INDEX

### 6.6.1 *Linear Single-Photon Absorption*

Single-photon on-resonance resonant enhancement of SFM introduces linear absorption of the beams at the dipole transition frequencies. The intensity of the incident light is reduced exponentially with distance according to Beer's absorption law

$$I_v(z) = I_v(0) e^{-\alpha_v z} \quad (6.6.1)$$

The optical depth of the atomic vapour is described by  $\alpha_v L$ , where  $L$  is the length of interaction. If  $\alpha_v L \ll 1$  then the vapour is "optically thin" whereas if  $\alpha_v L \gg 1$ , the vapour is "optically thick".

The absorption coefficient  $\alpha_v$  can be described in terms of  $\chi''$ , the imaginary component of the linear electric susceptibility  $\chi = \chi' + i\chi''$ .

$$\alpha_v = k\chi''(\nu) \quad (6.6.2)$$

where  $k = 2\pi/\lambda$ .  $\chi''(\nu)$  for a single, homogeneously broadened Lorentzian transition is given by [168]

$$\chi''(\nu) = \frac{N e^2}{16\pi^2 m \epsilon_0} \frac{\Delta\nu}{\nu_0} \frac{1}{(\nu - \nu_0)^2 + (\Delta\nu/2)^2} \quad (6.6.3)$$

where  $N$  is the density of atoms in the absorbing state,  $\nu_0$  is the frequency of the dipole transition and  $\Delta\nu$  is the FWHM linewidth of the transition. A normalised graph of  $\chi''(\nu)$  is shown in Figure 6.9.

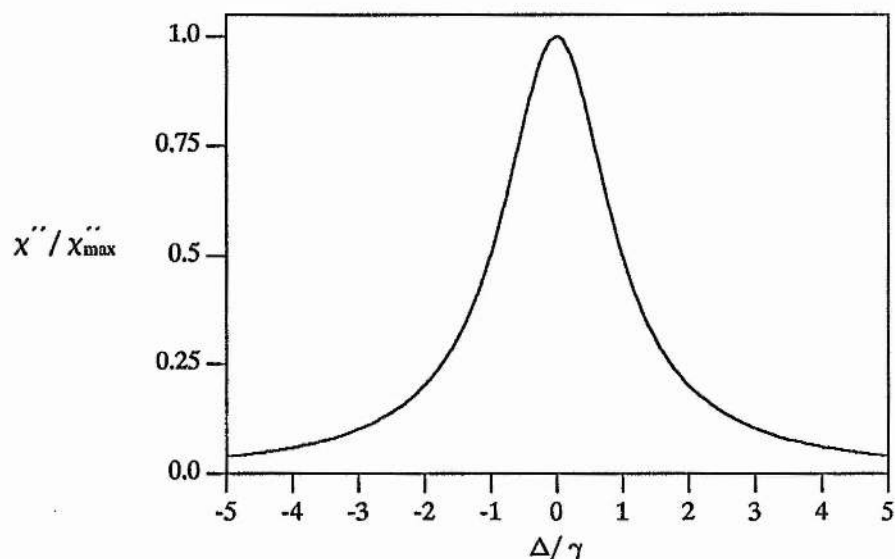


Figure 6.9 : Plot of normalised  $\chi''(\nu)$ , the imaginary component of the electronic susceptibility (absorption).

The total absorption coefficient for the 3S-3P and 3P-4D transitions requires the contributions from the several separate fine/hyperfine transitions to be taken into account. These frequencies are non-degenerate due to the coupling energies and the splittings due to the applied magnetic field. The contributions are weighted by the population in each substate  $N_i$  and the oscillator strength  $f_{ij}$  for each particular transition frequency  $\nu_{ij}$ . The thermal motion of the atoms is also included in the Doppler shifts of the transition frequencies. Thus,  $\alpha_\nu$  becomes

$$\begin{aligned} \alpha_\nu &= k \sum_{ij} \int_{\text{DOPPLER}} \chi''(\nu_{ij}) \\ &= k \left( \frac{e^2}{16\pi^2 m \epsilon_0} \right) \sum_{ij} \int_{-\infty}^{\infty} \frac{\Delta \nu_{ij}}{(\nu_{ij} - k\nu)} \frac{N_i f_{ij}}{(\nu - k\nu - \nu_{ij})^2 + (\Delta \nu_{ij} / 2)^2} f(\nu) d\nu \end{aligned} \quad (6.6.4)$$

where  $f(\nu)$  is the normalised Maxwell velocity distribution

$$f(v) = \left( \frac{M}{2\pi k_B T} \right)^{\frac{1}{2}} \exp \left[ - \frac{Mv^2}{2k_B T} \right] \quad (6.6.5)$$

This produces a Doppler-broadened absorption line shape for the dipole transitions.

Linear absorption of the incident light reduces the SFM conversion process as the intensity of the beam(s) decreases with propagation distance through the nonlinear medium. Saturation of the 3S-3P transition reduces the linear absorption for  $\nu_1$  but will increase absorption for  $\nu_2$  at the 3P-4D transition due to the excited population in the 3P states. The effective interaction length  $L$  for nonlinear optical conversion is dependent upon the optical thickness of the sodium vapour. For an optically thin vapour the physical size of the sodium oven and magnet pole pieces determines  $L$ . When the density of the vapour is increased so that it becomes optically thick, none of the beam at frequency  $\nu_1$  may be transmitted through the sodium oven, due to complete absorption in a distance  $L'$  much less than  $L$ . The effective interaction length for the nonlinear effect then becomes  $L'$  and the generated SFM is reduced. The intensity of the generated sum frequency is proportional to  $N^2$  and  $L^2$  in the absence of phase matching effects. Since  $L \propto 1/\alpha_\nu$  and  $\alpha_\nu \propto N$ , the reduction of SFM through linear absorption should be compensated for by the corresponding increase in particle density. In practice, phase matching requirements limit the generation efficiency at higher densities [33] and this simple relationship is no longer valid.

### 6.6.2 Two-Photon Absorption

As shown in (6.1.1), light at frequency  $\nu_1$  induces an absorption resonance at frequency  $\nu_2 = \nu_{\text{two-photon}} - \nu_1$ . If the intensity of the fields is high or if the induced absorption is close to a natural atomic transition frequency, linear absorption of the beam at frequency  $\nu_2$  can be strong enough to directly measure the resonant behaviour as  $\nu_1 + \nu_2 \rightarrow \nu_{\text{two-photon}}$  [7,169,170]. When  $\nu_1$  and  $\nu_2$  are tuned within the Doppler widths of the single photon transitions as for simultaneous on-resonance SFM, it is difficult to separate the absorption of the beams at frequencies  $\nu_1$  and  $\nu_2$  due to two-photon transitions via atomic coherences and two-step single photon transitions via atomic populations.

### 6.6.3 Refractive Index

The Kramers-Kronig relationships show that dispersion is associated with absorption. The refractive index connected with an absorption resonance is found from the real part of the linear electric susceptibility  $\chi'$  and is given by

$$n = (1 + \chi'(\nu) / 2). \quad (6.6.6)$$

The ratio of  $\chi'/\chi''$  is fixed for the particular case of a Lorentzian lineshape and is

$$\frac{\chi'(\nu)}{\chi''(\nu)} = \frac{2(\nu_0 - \nu)}{\Delta\nu} \quad (6.6.7)$$

so that  $\chi'$  can easily be found once the absorption  $\chi''$  is determined (or vice versa) as

$$\chi'(\nu) = \frac{Ne^2}{8\pi^2 m\epsilon_0} \frac{1}{\nu_0} \frac{(\nu_0 - \nu)}{(\nu - \nu_0)^2 + (\Delta\nu/2)^2}. \quad (6.6.8)$$

A graph of  $\chi'(\nu)/\chi''(\nu)_{\max}$  is shown in Figure 6.10. Notice that the refractive index is significant at frequencies where the absorption is negligible and is responsible for the off-resonant phase matching of SHG and SFM as discussed in Chapter 5.

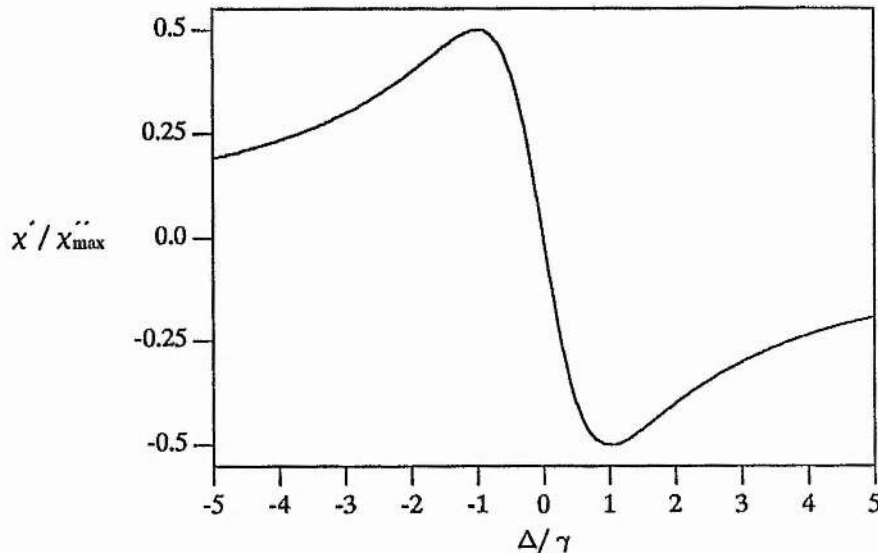


Figure 6.10 : Plot of normalised  $\chi'(\nu)$ , the real component of the electronic susceptibility (refractive index).

Doppler broadening is again described in terms of a shift of the resonant frequency  $\nu_0$

of the atom and is weighted with the Maxwell velocity distribution as in (6.6.4). This produces a broadened dispersion line shape similar to Figure 2.7 with the maximum and minimum refractive index values being separated by  $\Delta\nu_D$ , the FWHM Doppler width .

Two-photon dispersion can also contribute to the refractive index due to an induced absorption resonance as discussed in § 2.3.4 and § 6.6.2. This has previously been observed with the intermediate state off resonance by the rotation of the polarisation of a beam at frequency  $\nu_1 \sim 3S_{1/2}-3P$  in sodium by a strong beam at a frequency  $\nu_2$  such that  $\nu_1+\nu_2 \sim 3S_{1/2}-5S_{1/2}$  two-photon resonance [171]. Single and two photon resonant enhancement was used to obtain large rotation angles ( $\sim 90^\circ$ ) for limited strong laser beam power of  $\sim 1.5 \text{ MW cm}^{-2}$ .

The frequency dependent refractive index of the 3S-3P transition is complicated near resonance due to the large number of atomic hyperfine resonances with an applied transverse magnetic field B. The refractive index experienced by a wave at a fixed frequency  $\nu$  changes with the Zeeman shifting of the atomic frequencies and with the relative polarisation of the incident beam to the magnetic field direction. However, the presence of several closely spaced transition frequencies leads to cancellation of refractive index contributions as illustrated in Figure 6.11. This cancellation effect is utilised in § 6.8 to achieve higher efficiency SFM.

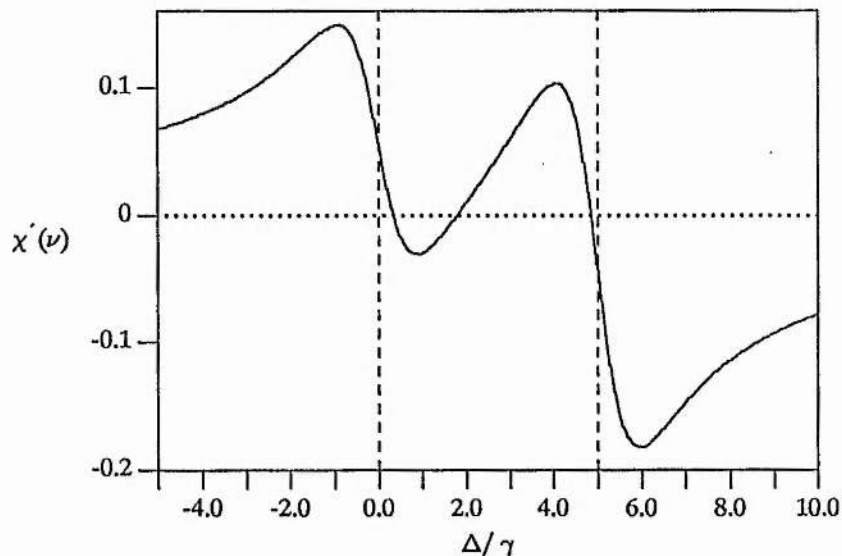


Figure 6.11 : Graph of refractive index contributions for two closely spaced oscillators at  $\Delta/\gamma=0$  and  $\Delta/\gamma=5$  with relative strengths 1:2, showing cancellation effects.

The exact form of the final refractive index profile depends on the relative oscillator strengths of the nondegenerate transitions and Doppler broadening will tend to smooth out the extreme variations of refractive index.

Optical pumping can produce large changes in the population of the ground state sublevels (see § 6.3). This produces a corresponding change in the refractive index profile. Consider Figure 6.11, as population is pumped from  $\nu_0 = 0 \rightarrow \nu_0' = 5$ , the refractive index component associated with  $\nu_0' = 5$  increases and that for  $\nu_0 = 0$  decreases which significantly modifies the total shape of the dispersion curve at a fixed frequency.

The refractive index for the second wave at the 3P-4D transition frequency has in general two components for on-resonance SFM excitation. The first is an off-resonant contribution due to the strong 3S-3P dipole transition which is independent of any population movement in the ground state since the wavelength of the second wave is over 20 nm from the D line wavelengths.

The second contribution is due to the homogeneous excitation of population into the 3P state by the on-resonance laser excitation at the 3S-3P D line transition frequency, which was discussed in Chapter 2. The resonant Sellmeier equation

$$\delta\eta(\nu) = \frac{N\Gamma_e c^2}{2\pi} \sum_{ij} \frac{\alpha_i f_{ij} (\nu_{ij}^2 - \nu^2)}{(\nu_{ij}^2 - \nu^2)^2 + \Gamma_{ij}^2 \nu^2} \quad (6.6.9)$$

can be used to estimate the required population in the intermediate level for the on and off resonant refractive index contributions for  $\nu_2$  to be equal. The maximum value of the on-resonance contribution occurs at  $\nu^2 = \nu_{ij}^2 - \Gamma_{ij} \nu_{ij}$ . Using  $f_{3S-3P} = 0.982$ ,  $f_{3P-4D} = 0.106$ ,  $\nu_{3S-3P} = c/589.3 \text{ nm}$ ,  $\nu_{3P-4D} = c/568.55 \text{ nm}$ ,  $\Gamma_{3P} = 18 \text{ MHz}$  and  $\Gamma_{4D} = 35 \text{ MHz}$  this gives a value for the necessary percentage population in the 3P states as  $\sim 0.1\%$  of the ground state population. For a burnt hole width of  $2 \times 18 \text{ MHz}$  at line centre this corresponds to excitation of  $\sim 5\%$  of the velocity group, i.e.  $\sim 1/5$  of the saturation intensity, which is easily achieved. Thus, the on-resonance refractive index component dominates over the

off-resonance component for a small population in the 3P states and near resonant excitation at the 3P-4D atomic frequency, which agrees with the theoretical three-level model in Chapter 2. At exact line centre of the 3P-4D transition, there is no contribution from the on-resonance refractive index and only the off-resonant component remains.

The resonant behaviour of the Sellmeier equation (6.6.9) is very large at  $\nu \sim \nu_{ij}$  and compensates for the reduction in particle density  $N$ . As an order of magnitude calculation,  $\delta\eta$  ( $c/578.734$  nm) at  $300^\circ\text{C}$  for SHG is equal to  $\delta\eta$  ( $\nu - \nu_{ij}$ ) at  $\sim 120^\circ\text{C}$  for  $\nu - \nu_{ij} \approx 700$  MHz which is about half the Doppler width away from resonance.

#### 6.6.4 *Phase Matching*

As was shown in the theoretical analysis in Chapter 2, the phase matching of the on-resonance SFM nonlinear optical process is critically dependent upon the refractive index experienced by the two fundamental optical waves. For on-resonance SFM, the bulk effect of phase matching can never be ignored, even for low sodium particle densities, because of the simultaneous near or on resonant nature of the nonlinear optical process.

The phase matching behaviour is much more complicated for on-resonance SFM since the refractive index experienced by the wave at  $\nu_2$  will be changing rapidly with frequency due to the contribution of the velocity selected group. As has been shown in § 2.3.4, the strong two-photon coupling also leads to a significant change in the refractive index for  $\nu_1$  when two-photon resonance is achieved.

## 6.7 EXPERIMENTAL RESULTS FOR ON-RESONANCE SUM FREQUENCY MIXING

### 6.7.1 *Two-Photon Spectroscopy with a Resonant Intermediate State*

Two-photon spectroscopy in a two-step on-resonance configuration was carried out to determine experimental parameters under the same conditions as for sum-frequency mixing rather than for measuring absolute atomic level energy splittings. The theoretical background to interpret these experimental spectroscopic results, including velocity-selective excitation, saturation, collisional effects and optical pumping, has been given in §6.1, 6.2, 6.3, 6.4 and 6.5.

To obtain the line profiles,  $\nu_1$  (tuned onto the sodium  $D_1$  or  $D_2$  lines) was held at a fixed detuning relative to the sodium hyperfine structure measured by saturation spectroscopy in the sodium reference cell and the second laser frequency  $\nu_2$  was tuned through the enhancing 4D states.

The population of the sodium 4D states under on-resonance two-photon excitation was monitored via the cascade 330 nm fluorescence from the 4P states to the ground state. Figure 6.12 shows the experimental 330 nm line profile for counterpropagating beams at the  $3S_{1/2} - 3P_{3/2}$  ( $D_2$  line) and  $3P_{3/2} - 4D$  frequencies.

As expected, the four transitions have Doppler-free linewidths and correspond to the two-photon transitions (from right to left):

1.  $3S_{1/2}(F=2) \rightarrow 4D_{5/2}$
2.  $3S_{1/2}(F=2) \rightarrow 4D_{3/2}$
3.  $3S_{1/2}(F=1) \rightarrow 4D_{5/2}$
4.  $3S_{1/2}(F=1) \rightarrow 4D_{3/2}$

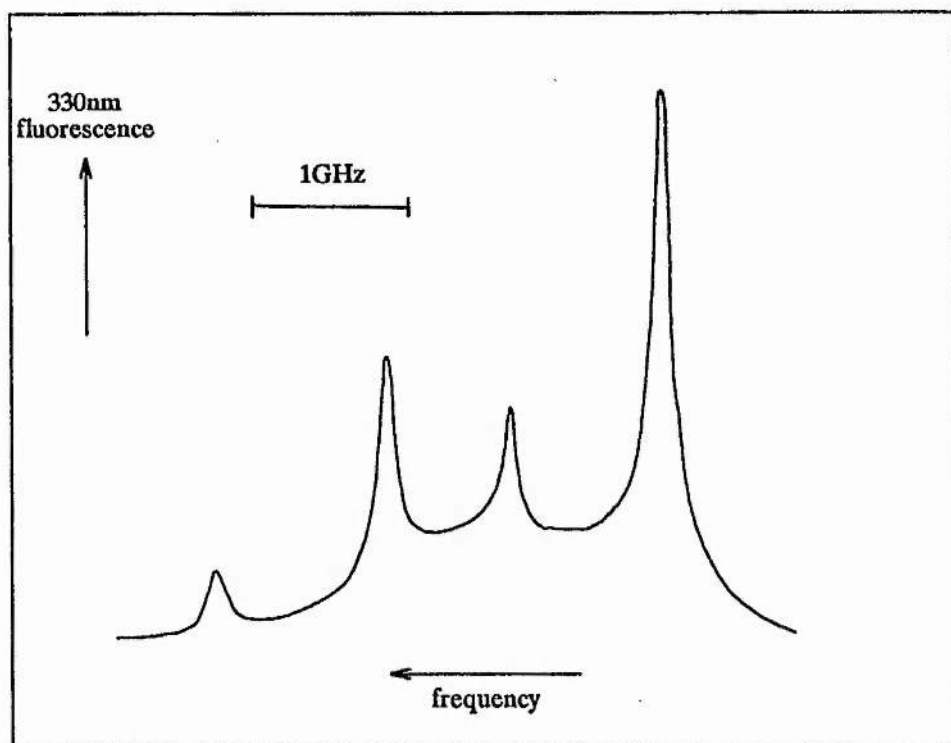


Figure 6.12: Experimental two-photon spectrum at 330 nm for counterpropagating beams.  
 1 mbar Ar buffer gas  $T \sim 120^\circ\text{C}$   
 $B \sim 0 \text{ G}$   
 $\nu_1$  tuned midway between the  $3S_{1/2} (F=1) \rightarrow 3P_{3/2}$   
 and  $3S_{1/2} (F=2) \rightarrow 3P_{3/2}$  transition frequencies  
 (ie. crossover resonance in saturation absorption spectrum)  
 $I_1 \sim 460 \text{ mW cm}^{-2}$  (polarisation  $\parallel$  to B)  
 $I_2 \sim 860 \text{ mW cm}^{-2}$  (polarisation  $\perp$  to B)

The measured and theoretical line splittings are shown in Table 3 and are in good agreement. The average measured linewidth (HWHM) of the components is  $\Delta\nu \sim 91 \pm 15$  MHz which is equal to the estimated theoretical linewidth of  $\sim 91$  MHz including collisional and power broadening of the single and two-photon transitions and the hyperfine structure of the  $3P_{3/2}$  state.

<u>Measured Splitting (MHz)</u>		<u>Theoretical Splitting (MHz)</u>
1. → 3.	1833 ± 15	1772 x 1.0355 = 1835
2. → 4.	1841 ± 15	" " = 1835
1. → 2.	1023 ± 15	1028
3. → 4.	1041 ± 15	1028

Table 3 : Measured and theoretical frequency splittings of the sodium 3S-4D two-photon transitions in zero magnetic field.

Counter and copropagating beam two-photon line spectra were obtained simultaneously by allowing an on axis back reflection from the window of the sodium heat-pipe oven to overlap with the co-propagating beams. Figure 6.13 shows an example of the lineshape for  $\nu_1$  tuned ~ 1.5 GHz below the  $3S_{1/2} (F=2) \rightarrow 3P_{3/2}$  transition.

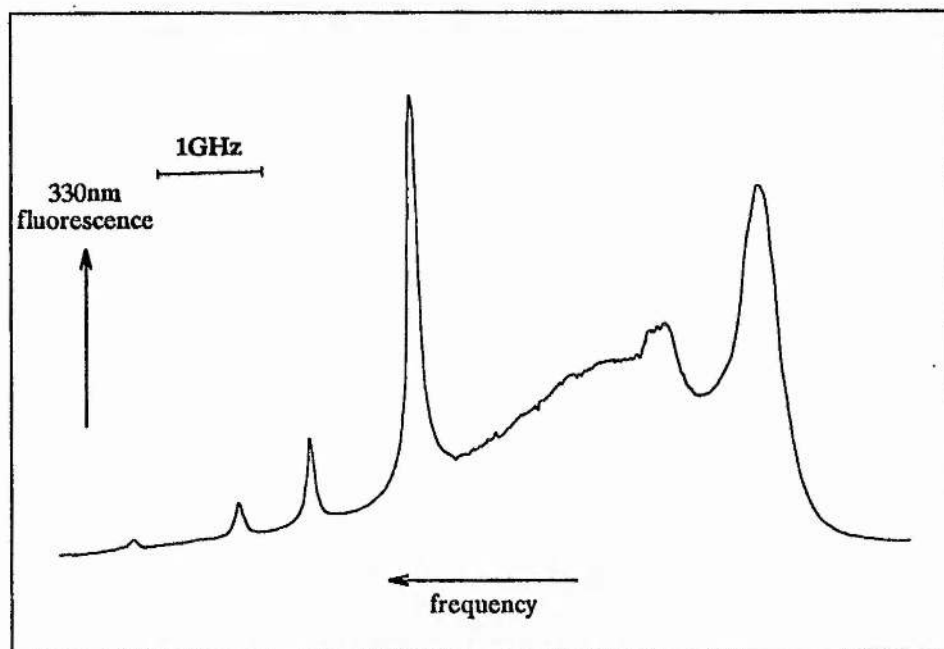


Figure 6.13 : Experimental two-photon spectrum at 330 nm for co- and counterpropagating beams -  $D_2$  line.

1 mbar He buffer gas     $T \sim 120^\circ\text{C}$   
 $B \sim 0 \text{ G}$   
 $\nu_1$  tuned ~ 1.5 GHz below the  $3S_{1/2} (F=2) \rightarrow 3P_{3/2}$   
transition frequency  
 $\nu_1$  (polarisation  $\parallel$  to B)  
 $\nu_2$  (polarisation  $\perp$  to B)

The four narrow counterpropagating Doppler-free peaks are the same as in Figure 6.12. The two broader Doppler-free peaks superimposed on the Doppler broadened background are the copropagating beam Lorentzian line shapes. These two peaks corresponding to the  $4D_{3/2}$  and  $4D_{5/2}$  states arise from the  $F=2$  ground state sublevel only since the single photon detuning of  $\nu_1$  from the  $F=1$  hyperfine level is outside the Doppler width for the  $3S_{1/2}$  ( $F=1$ )  $\rightarrow$   $3P_{3/2}$  transition. The measured linewidth of the largest co-propagating peak is  $\Delta\nu$  (HWHM)  $\sim 220 \pm 15$  MHz. The theoretical collisionally broadened linewidth for no saturation  $\Delta\nu$  (HWHM)  $\sim 160$  MHz (see §6.1.2, §6.4.1), allowing for the unresolved individual  $F=1, 2$  and  $3$  hyperfine components in the  $3P_{3/2}$  state. The additional experimental broadening was probably due to single and two-photon saturation but the laser powers were not known for this particular spectrum.

Figure 6.14 shows a similar spectrum to Figure 6.13 but with the  $3S_{1/2} \rightarrow 3P_{1/2}$  (D1 line) transition used for single photon resonant enhancement. The two narrow resonances on the left are due to counterpropagating beam two-photon on-resonance excitation. Only two peaks are observed and these are due to the  $4D_{3/2}$  state only because the  $3P_{1/2} \rightarrow 4D_{5/2}$  dipole transition is forbidden. The two broader resonances on the right are copropagating beam two-photon transitions. The frequency splitting of these peaks is  $375 \pm 15$  MHz. This is in good agreement with the theoretical velocity selected splitting of 387 MHz, equal to  $2.0375$  ( $= (\nu_1 + \nu_2) / \nu_1$ ) times the 190 MHz hyperfine splitting of the  $3P_{1/2}$  state (see §6.2). Again, the linewidths of all the peaks are due mainly to collisional and power broadening.

The four copropagating two-photon transitions for single photon enhancement on the  $3S_{1/2} \rightarrow 3P_{1/2}$  transition are shown in Figure 6.15. Two groups of transitions due to both the  $F=1$  and  $F=2$  hyperfine ground states are now evident, each composed of two further peaks due to the  $F=1$  and  $F=2$  hyperfine levels of the  $3P_{1/2}$  state. The measured splittings agree well with theory and the linewidths are power and collisionally broadened as before. Note that the low and high frequency peaks

are now associated with the  $F=1$  and  $F=2$  ground states respectively because the beams are co-propagating.

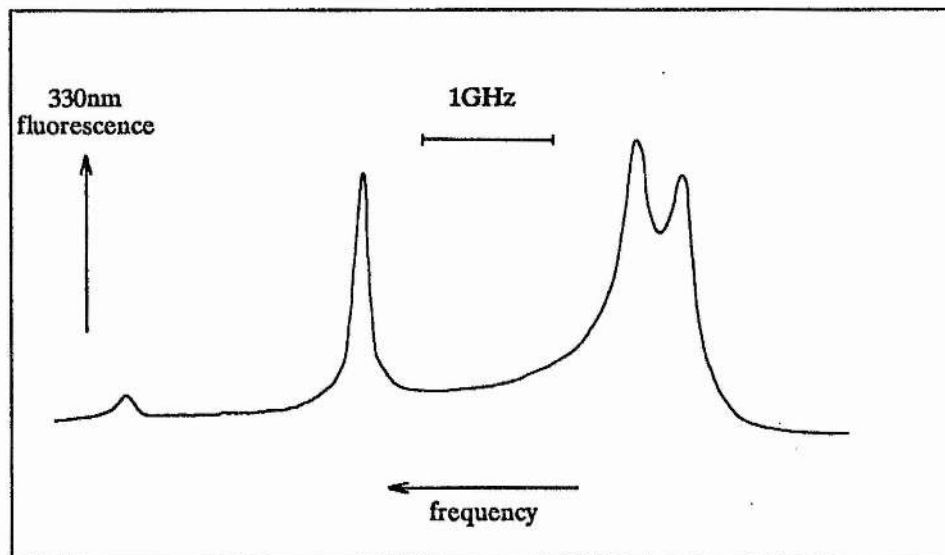


Figure 6.14 : Experimental two-photon spectrum at 330 nm for co- and counterpropagating beams -  $D_1$  line.

$B \sim 0$  G       $T \sim 120^\circ\text{C}$   
1 mbar He buffer gas  
 $\nu_1$  tuned  $\sim 1$  GHz below the  $3S_{1/2}$  ( $F=2$ )  $\rightarrow$   $3P_{3/2}$   
transition frequency  
 $\nu_1$  (polarisation  $\parallel$  to B)  
 $\nu_2$  (polarisation  $\perp$  to B)

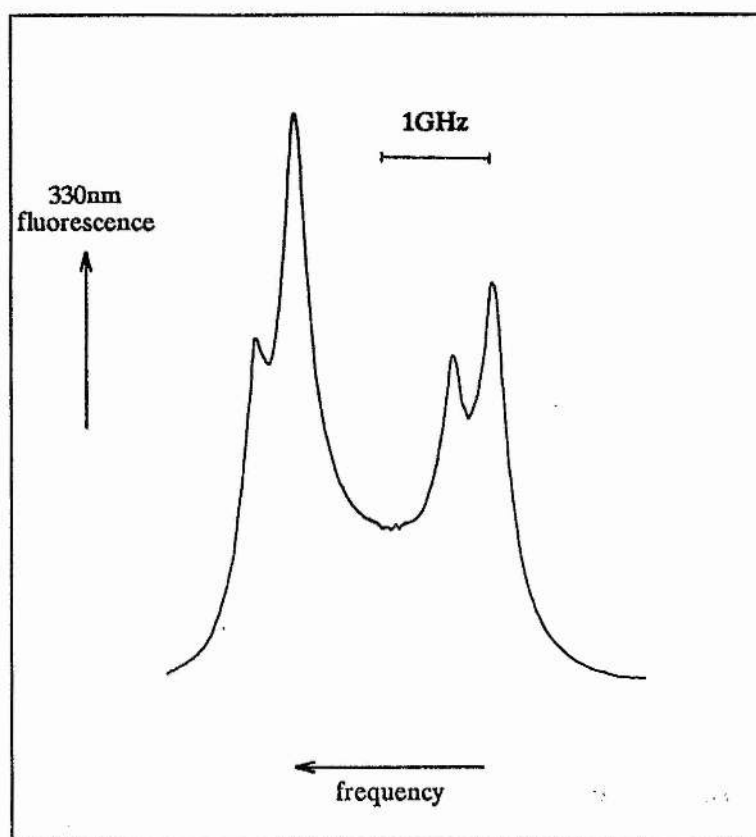


Figure 6.15 : Experimental two-photon spectrum at 330 nm for copropagating beams -  $D_1$  line.

$B \sim 0$  G                       $T \sim 120^\circ\text{C}$   
 1 mbar Ar buffer gas  
 $\nu_1$  tuned midway between the  $3S_{1/2}$  ( $F=1$ )  $\rightarrow$   $3P_{3/2}$   
 and  $3S_{1/2}$  ( $F=2$ )  $\rightarrow$   $3P_{3/2}$  transition frequencies  
 (ie. crossover in saturation spectrum)  
 $I_1 \sim 400$  mW cm $^{-2}$  (polarisation  $\perp$  to B)  
 $I_2 \sim 800$  mW cm $^{-2}$  (polarisation  $\perp$  to B)

Frequency selective optical pumping on the 3S-3P single photon transition (§6.3) was found to modify the measured line intensities in the two-photon spectrum. An example is shown in Figure 6.16 for simultaneous co- and counterpropagating beam two-photon excitation. The laser frequency at  $\nu_1$  was tuned exactly on resonance with the  $3S_{1/2}$  ( $F=1$ )  $\rightarrow$   $3P_{3/2}$  transition which resulted in optical pumping of atoms into the  $F=2$  hyperfine ground state sublevel. However, the co-propagating two-photon resonances originating in the  $F=1$  ground state sublevel are still more intense than those associated with the  $F=2$  hyperfine state, because

the optical pumping is not 100% efficient and a larger homogeneous population still remains at the laser frequency.

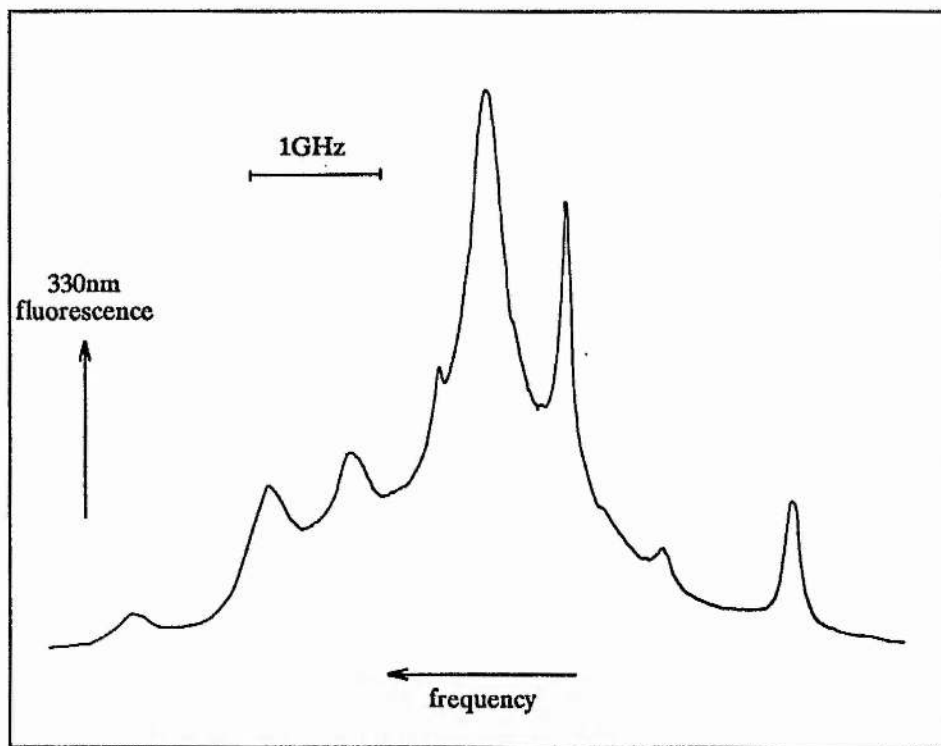


Figure 6.16: Experimental two-photon spectrum displaying effect of frequency selective optical pumping. Co- and counterpropagating beams -  $D_2$  line.

$B \sim 0$  G                       $T \sim 120^\circ\text{C}$   
 1 mbar He buffer gas  
 $\nu_1$  tuned onto the  $3S_{1/2}$  ( $F=1$ )  $\rightarrow$   $3P_{3/2}$   
 transition frequency  
 $\nu_1$  (polarisation  $\parallel$  to B)  
 $\nu_2$  (polarisation  $\perp$  to B)

The large 4P fluorescence signals at very low sodium atomic densities ( $\sim 10^{11}$   $\text{cm}^{-3}$ ) verified that the magnitude of the two-photon absorption was greatly increased due to on or near single photon resonant enhancement as discussed in §6.1.1. The measured frequency splittings of the two-photon transitions agreed well with the theoretical values, subject to the residual Doppler shifts due to velocity selective excitation. The spectroscopic linewidths were collisionally and power broadened due to saturation with large laser powers on resonance and

the presence of buffer gas in the heat-pipe oven. Optical pumping increased and decreased the apparent strength of the two-photon transitions due to created population imbalances in the  $3S_{1/2}$  ground state hyperfine levels.

### 6.7.2 SFM Line Profiles

The sum frequency emission and the spontaneous fluorescence line profiles were recorded under the same experimental conditions for comparison. The SFM profile at 289 nm displays the coherent behaviour of the 3S-4D quadrupole and the fluorescence at 330 nm is proportional to the populations in the  $4D_{3/2}$  and  $4D_{5/2}$  atomic energy states due to two-photon and stepwise excitation.

The large increase in two-photon absorption cross-section due to simultaneous single and two-photon resonant enhancement also produced a much larger SFM nonlinear optical effect. Typical sodium densities used for the SFM experiments were  $\sim 10^4$  less than used for SHG which would imply a decrease in the nonlinear SFM of  $\sim 10^8$ . The measured SFM signals were comparable or greater than those obtained for SHG even at these very low sodium densities due to the extra resonant enhancement.

For SHG in sodium vapour, the experimental Doppler line profiles for the 330 nm fluorescence and the 289 nm second harmonic frequency closely follow each other, subject to the quadrupole selection rules for SHG over two-photon excitation [43]. Generally, for on-resonance SFM, the line profiles for coherent SFM and the 330 nm fluorescence differed from each other considerably. This was due to the quadrupole selection rules again but mainly due to the phase matching of the SFM nonlinear effect which cannot be neglected near resonance. As an illustrative example, consider the relatively simple case of SFM at a very low value of transverse magnetic field strength as shown in Figure 6.17.

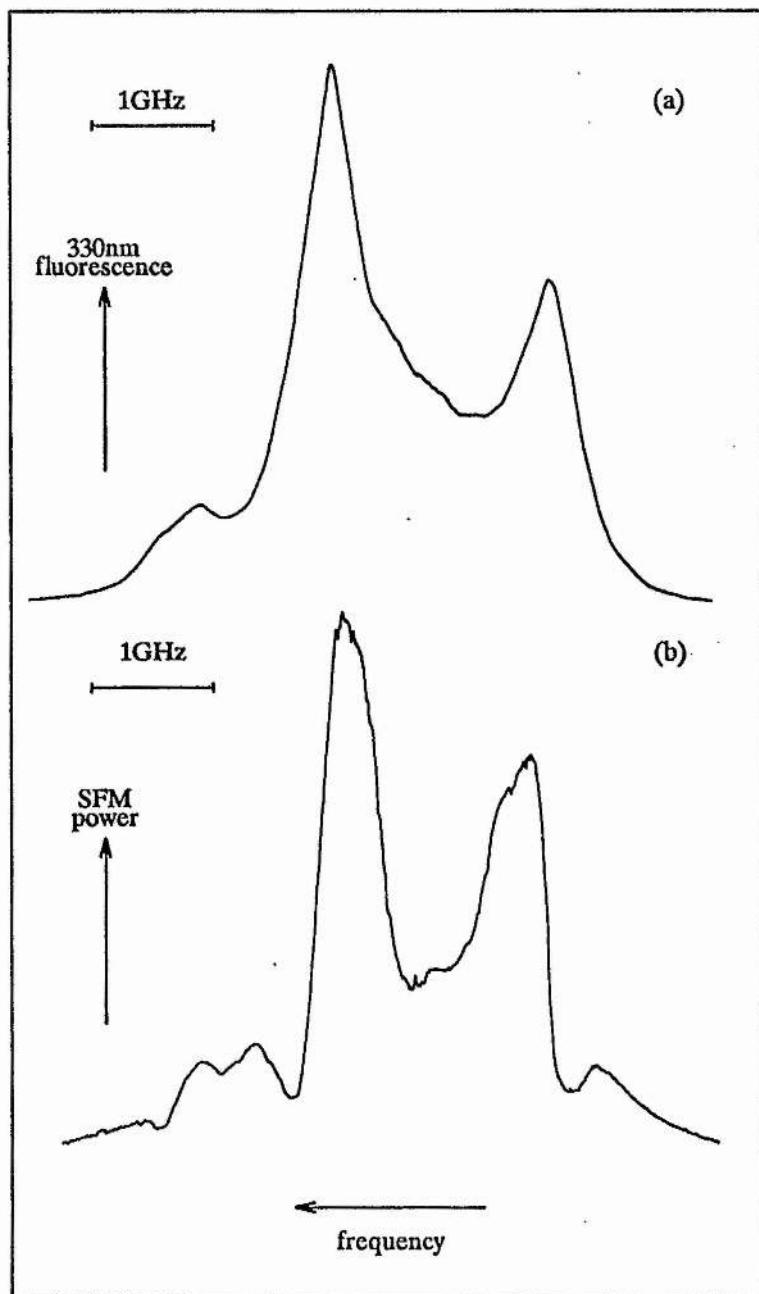


Figure 6.17 : Experimental line profiles for (a) 330 nm fluorescence and (b) 289 nm SFM.

$B = 40 \text{ G}$

$T \sim 120^\circ\text{C}$

1 mbar He buffer gas

$\nu_1$  tuned midway between the zero magnetic field

$3S_{1/2} (F=1) \rightarrow 3P_{3/2}$  and  $3S_{1/2} (F=2) \rightarrow 3P_{3/2}$

transition frequencies (ie. crossover resonance in saturation spectrum)

$I_1 \sim 240 \text{ mW cm}^{-2}$  (polarisation  $\perp$  to  $B$ )

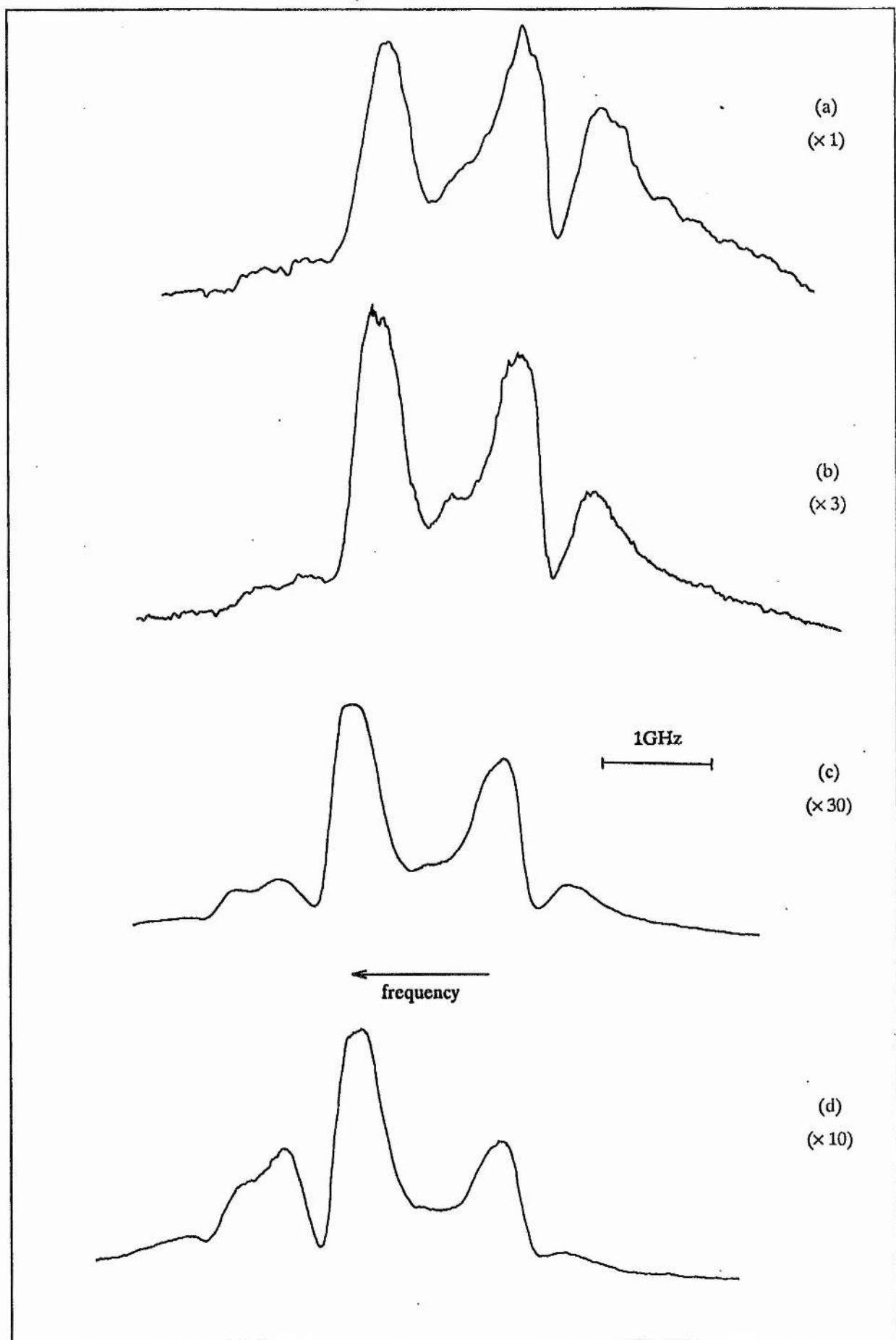
$I_2 \sim 875 \text{ mW cm}^{-2}$  (polarisation  $\perp$  to  $B$ )

The upper line profile is the 4D population for copropagating beams with a very low value of transverse magnetic field. In such a field, the Zeeman splitting of the S and D sodium states is much smaller than the fine or hyperfine interaction energies, so the line profile is similar to that for zero applied magnetic field. There are four main velocity selected homogeneous groups (one unresolved) corresponding to the two-photon transitions (right to left) :  $3S_{1/2} (F=1) \rightarrow 4D_{5/2}$ ,  $3S_{1/2} (F=1) \rightarrow 4D_{3/2}$ ,  $3S_{1/2} (F=1) \rightarrow 4D_{5/2}$  and  $3S_{1/2} (F=2) \rightarrow 4D_{3/2}$ . The homogeneous linewidth of the groups is broadened due to the small Zeeman splitting, collisions and laser powers above saturation intensities. Note that the line intensities of the two-photon transitions involving the  $4D_{3/2}$  and  $4D_{5/2}$  are not in the ratio of their statistical weights  $(5/2 : 3/2) = (3 : 2)$ . This is probably due to the  $4D_{3/2}$  state having an additional dipole allowed relaxation channel to the  $3P_{1/2}$  state which the  $4D_{5/2}$  state does not.

The 289 nm coherent SFM line profile shows that the nonlinear optical process also occurs preferentially for the velocity selected groups but the line shape is different to that for the two-photon excitation. This is due to the dependence of SFM on phase matching.

By tuning the laser frequency  $\nu_1$  to various frequencies across the inhomogeneous  $3S_{1/2} - 3P_{3/2} D_2$  line transition, homogeneous atomic groups are selected with different velocities. If the SFM line profile variations had been caused by microscopic rather than a macroscopic effect, the SFM line shape would then remain the same for different  $\nu_1$  frequencies, subject to an overall scaling produced by optical pumping in the  $3S_{1/2}$  ground state. Figure 6.18 shows the experimental SFM line profiles obtained for different fixed frequencies of  $\nu_1$  around the sodium  $D_2$  line and the marked changes in the SFM line profile depending upon the  $\nu_1$  frequency.

Any microscopic interference on the two-photon absorption route would be expected to also modify the 330 nm line profile, which did not show this behaviour. An analysis of the quadrupole selection rules for the coherent transitions within a selected velocity group did not give an interference effect which was sub-homogeneous linewidth in width.



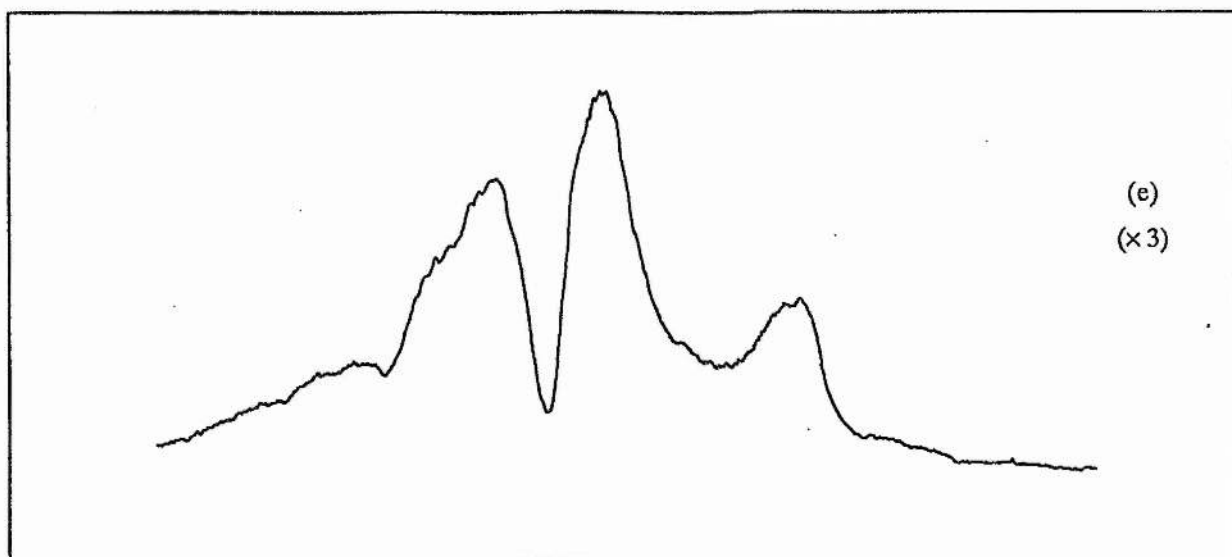


Figure 6.18 : SFM line profiles for  $\nu_1$  frequencies of

- (a)  $3S_{1/2} (F=1) \rightarrow 3P_{3/2}$
- (b)  $3S_{1/2} (F=1) \rightarrow 3P_{3/2} - 0.25 \text{ GHz}$
- (c) midway between (a) and (e)  
(ie. crossover resonance on  $3S_{1/2} \rightarrow 3P_{3/2}$  transition in saturation spectrum)
- (d)  $3S_{1/2} (F=2) \rightarrow 3P_{3/2} + 0.25 \text{ GHz}$
- (e)  $3S_{1/2} (F=2) \rightarrow 3P_{3/2}$

$B = 40 \text{ G}$     $T \sim 120^\circ\text{C}$     $\nu_1$  (polarisation  $\perp$  to  $B$ )  
 $1 \text{ mbar Ar buffer gas}$     $\nu_2$  (polarisation  $\perp$  to  $B$ )

The behaviour of the SFM line profiles with  $\nu_1$  detuning was consistent with the expected refractive index and phase-matching variations. With  $\nu_1$  centred between the two  $3S_{1/2}$  hyperfine ground states (c), the optical pumping is minimised and the largest SFM power is produced. The line profile shows asymmetric dips in the SFM power at each of the velocity selected homogeneous atomic groups which do not occur for the atomic populations. These are due to the homogeneous refractive index changes for  $\nu_2$  which were discussed in the three level model in Chapter 2 and shown in Figures 2.12 and 2.13. The background phase-mismatch  $\Delta k$  value for this profile, which is mainly due to the refractive index experienced by  $\nu_1$  on the  $3S \rightarrow 3P$  dipole transition, is not zero because the different oscillator strengths of the  $F=1$  and  $F=2$  ground states offset the zero dispersion frequency from this midpoint tuning of  $\nu_1$ . When  $\nu_1$  is removed from the midpoint frequency, there is significant optical pumping to one or other of the hyperfine ground states. This induced population change increases or decreases the background refractive index for  $\nu_1$  and hence  $|\Delta k|$  increases to reduce the overall SFM power further by additional phase mismatching. The homogeneous phase matching variations due to  $\nu_2$  are greater for the ground state sublevel which has a larger velocity selected population excited into the  $3P$  state, which in turn produces a larger refractive index change for  $\nu_2$ . In spite of the optical pumping, the larger homogeneous refractive index change occurs for velocity groups associated with the ground state hyperfine level which is depleted by the field at  $\nu_1$ . This occurs because the optical pumping is less than 97% efficient and there is still a larger homogenous population for the low velocity group which is resonant with the laser frequency  $\nu_1$  than for the high velocity group associated with the pumped ground state sublevel, which is also resonant with the field at  $\nu_1$ .

The magnitude of the phase match oscillations on the SFM line profile increased with increasing sodium vapour density, due to larger atomic populations creating greater refractive index changes in the nonlinear medium. An example of this is shown in Figure 6.19 for a particular frequency range of a SFM line profile.

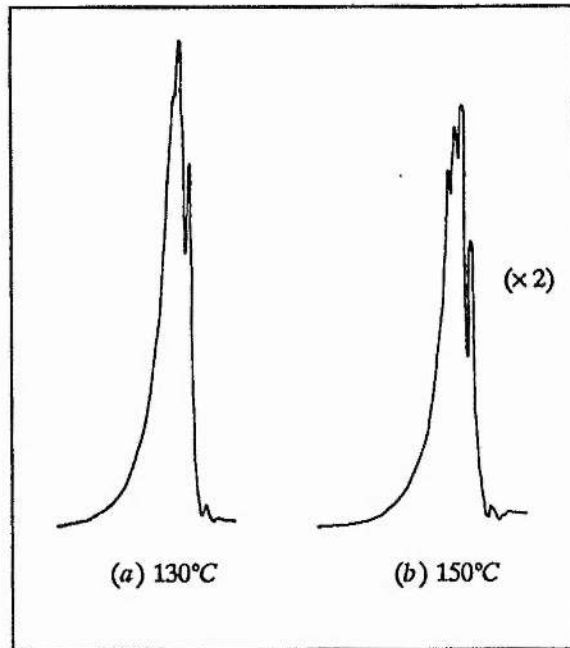


Figure 6.19: Larger phase match variations on SFM line profile for increasing sodium vapour temperatures.  
 $B = 1500\text{G}$   
 Laser polarisation  $\perp$  to  $B$ .

**Optical Pumping** - Generally much larger SFM signals were recorded with the frequency of  $\nu_1$  adjusted to minimise optical pumping. This avoided large changes in refractive index for the wave at frequency  $\nu_1$ .

**Buffer Gas** - Larger pressures of buffer gas ( $\sim 10$  mbar) in the sodium heat-pipe oven reduced the overall SFM signal, probably through collisional dephasing, and Doppler-free features were no longer resolved due to the large collisional broadening of the homogeneous linewidth.

**Magnetic Field** - No on-resonance SFM signal was obtained when the magnetic field was set to zero, confirming that the  $\chi^{(2)}$  nonlinear process relied on the symmetry breaking action of the transverse magnetic field. With higher magnetic fields than a few 10's of Gauss, the SFM line profiles became much more complicated and difficult to fully interpret. Consider the fluorescence and SFM line profiles shown in Figure 6.20 as an (untypical) example.

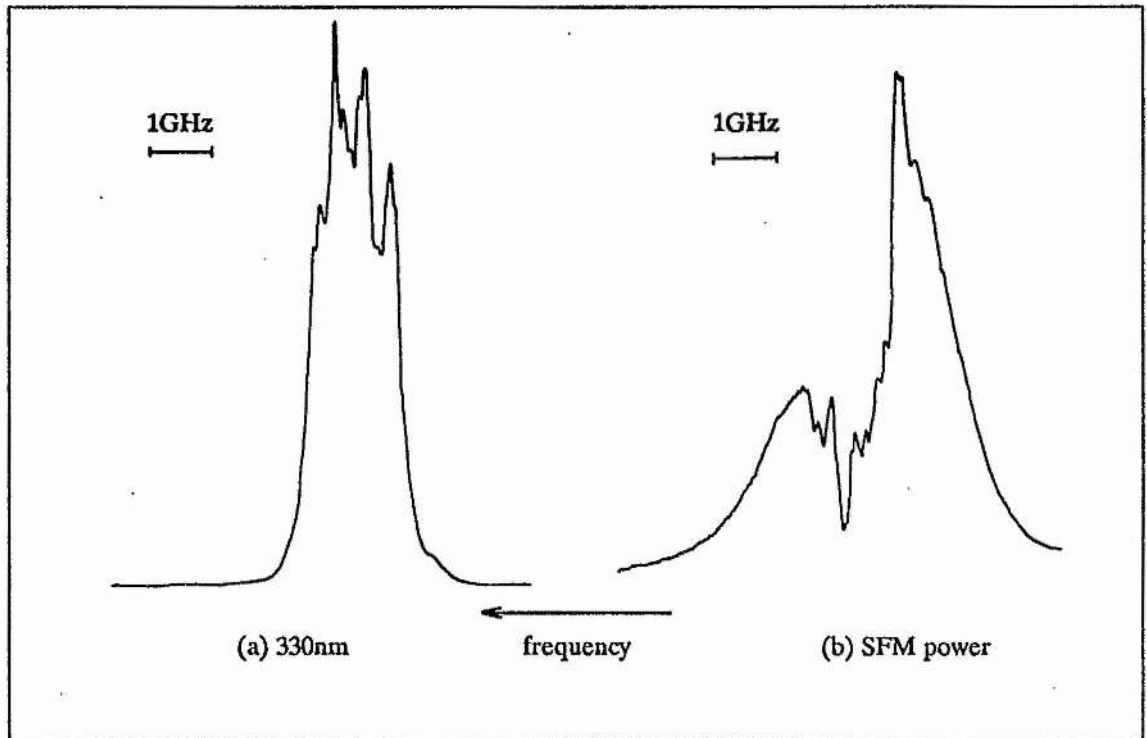
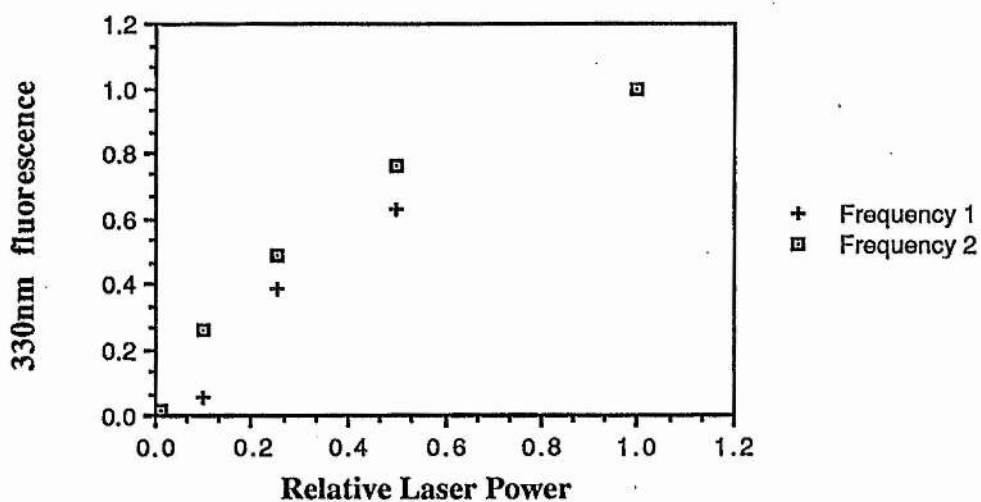


Figure 6.20 : Experimental line profiles for (a) 330 nm fluorescence and (b) 289 nm SFM for a transverse magnetic field strength of  $B \sim 500$  G.

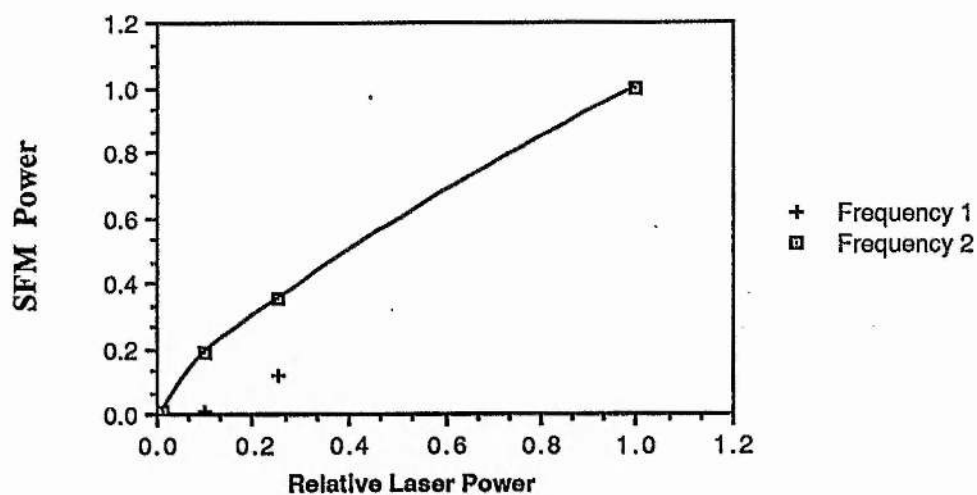
1 mbar Ar buffer gas     $T \sim 120^\circ\text{C}$   
 $\nu_1$  tuned midway between the  $3S_{1/2} (F=1) \rightarrow 3P_{3/2}$   
and  $3S_{1/2} (F=2) \rightarrow 3P_{3/2}$  transition frequencies  
(ie. crossover resonance in saturation absorption spectrum)  
 $\nu_1$  (polarisation  $\perp$  to B)  
 $\nu_2$  (polarisation  $\perp$  to B)

Note that there is significant SFM generation where there is little 4D state population. This was due to only single photon enhanced velocity groups contributing to SFM as shown in Figure 6.5 (b) which do not significantly populate the 4D state. The Doppler-free 330 nm peaks correspond to both single and two-photon resonant enhancement, with the 289 nm SFM line profile becoming complicated due to the on-resonance refractive index effects causing phase mismatching.

**Laser Powers** - The dependence of the magnitude of the 330 nm fluorescence signal and the 289 nm coherent SFM on laser power is shown in Figure 6.21. The plotted values are averaged peak values for the  $3S_{1/2} (F=1) \rightarrow 4D_{5/2}$  and  $3S_{1/2} (F=2) \rightarrow 4D_{5/2}$  two-photon transition signals against normalised laser power. Calibrated neutral density filters were inserted into each beam separately to attenuate the incident light.



(a)



(b)

Figure 6.21 : Dependence of (a) 330 nm fluorescence and (b) 289 SFM on laser powers.

$B = 40 \text{ G}$        $T \sim 120^\circ\text{C}$  (330)  $\sim 140^\circ\text{C}$  (289)  
 2 mbar Ar buffer gas  
 $\nu_1$  tuned midway between the  $3S_{1/2} (F=1) \rightarrow 3P_{3/2}$   
 and  $3S_{1/2} (F=2) \rightarrow 3P_{3/2}$  transition frequencies  
 (ie. crossover resonance in saturation absorption spectrum)  
 $I_1 \sim 440 \text{ mW cm}^{-2}$  (polarisation  $\perp$  to B)  
 $I_2 \sim 640 \text{ mW cm}^{-2}$  (polarisation  $\perp$  to B)

The extremely nonlinear dependence of the 330 nm and 289 nm on the product of the laser powers showed that saturation effects due to the single-photon and two-photon transitions were present. The rapid reduction of SFM with power at  $\nu_1$  was probably due to increased linear absorption at lower powers and decreasing interaction length.

The overall line profiles appeared to change very little in shape upon independently varying the powers of the beams at  $\nu_1$  and  $\nu_2$  although for very weak laser powers, the signal to noise ratio was poor and line features were less distinct. When the incident beams were focused into the sodium heat-pipe oven to increase the power density, the 330 nm line profile became distorted and the 289 nm profile became broadened due to power broadening of the homogeneous groups and greater "only single-photon enhanced" SFM.

## 6.8 SUM FREQUENCY MIXING WITH IMPROVED CONVERSION EFFICIENCY

The conversion efficiency of the SFM nonlinear optical process under the experimental conditions in §6.7 was very low, in spite of the single and two-photon resonant enhancement. This was due to the very low sodium density of  $\sim 10^{11} \text{ cm}^{-3}$  and the low powers of the unfocused incident beams from the cw dye lasers. However, the conversion efficiency could be increased to make the nonlinearity of the atomic vapour comparable to that of a typical, good nonlinear crystal even though a weak quadrupole moment was utilised in the SFM process. To achieve this, four parameters were varied: the intensity of the incident light beams, the atomic sodium density, the magnetic field strength and the laser detunings relative to the  $3S_{1/2} - 3P_{3/2}$  and  $3P_{3/2} - 4D$  transitions.

The intensity of the incident light was increased by focusing both fundamental beams collinearly into the sodium heat-pipe oven with a 20 cm focal length lens to a spot diameter of  $\sim 200 \mu\text{m}$ . This increased the intensity of each beam by  $\sim 400$  times and gave a confocal parameter for the Gaussian beams approximately equal to the length of the oven.

The temperature of the sodium oven was increased to  $\sim 240\text{-}250^\circ\text{C}$  which gave a corresponding particle density increase of  $\sim 1.2\text{-}2 \times 10^3$ . For all other parameters being fixed, this should have given an increase in SFM power of  $\sim 10^6$ . However as the sodium temperature was raised to this value, the single photon absorption of the beam at frequency  $\nu_1$  became extremely high near resonance and all of the beam was absorbed in the first few millimetres of the oven which greatly decreased the effective interaction length.

The strength of the transverse magnetic field was increased to  $\sim 4 \text{ kG}$  ( $0.4\text{T}$ ) which had two beneficial effects. The first was that with the  $\Delta m = \pm 1$   $3S_{1/2} \rightarrow 3P_{3/2}$  transition frequencies symmetrically split by several Doppler widths at this large magnetic field, the residual linear absorption at the midpoint frequency between the transitions was greatly reduced. A fraction of the beam at frequency  $\nu_1$  was transmitted over  $\sim 8 \text{ GHz}$  around the midpoint frequency for a 10 cm oven length and  $\sim 4 \text{ kG}$  magnetic field at a sodium density of  $\sim 2.5 \times 10^{13} \text{ cm}^{-3}$ . At the peak of the transmission, the linear absorption coefficient was estimated to be  $\alpha \sim 0.22 \text{ cm}^{-1}$ . The second effect due to the magnetic field was that the

refractive index contributions due to the  $\Delta m = \pm 1 3S_{1/2} \rightarrow 3P_{3/2}$  transitions had cancellations near the midpoint frequency, as discussed in § 6.6.3. This gave the possibility of phase matching the SFM nonlinear process at these high sodium densities. A disadvantage of the large magnetic field was that the single photon detuning at the midpoint frequency was increased due to the large Zeeman splitting and the SFM process became "off-resonant". (cf. Chapter 5)

With the experimental parameters  $N \sim 2 \times 10^{13} \text{ cm}^{-3}$ ,  $B \sim 4 \text{ kG}$ ,  $P(\nu_1) \sim 170 \text{ mW}$  (polarisation  $\perp$  to  $B$ ),  $P(\nu_2) \sim 210 \text{ mW}$  (polarisation  $\perp$  to  $B$ ),  $\Delta_1 \sim$ midpoint frequency (= crossover resonance frequency of Na  $D_2$  transition in reference cell) and a  $f = 20 \text{ cm}$  lens focusing the (nearly) collinear beams into the heat-pipe oven, a SFM power of  $4.6 \mu\text{W}$  at  $289 \text{ nm}$  was measured with a calibrated UV - 100B photodiode. This amount of UV power induced fluorescence on a white card which was easily visible to the unaided eye. Plate 1 shows the SFM beam emerging from the heat-pipe oven as a well defined blue/white spot on the card.



Plate 1 : Photograph of high efficiency SFM. The generated UV beam created a blue/white spot on the card.

Compare this generated UV power by SFM in the sodium vapour to SHG in a bulk nonlinear material such as a crystal of ammonium dihydrogen arsenate (ADA). For intracavity SHG with a 15 mm long crystal of ADA, 16 W of fundamental single- mode power produced 13 mW of second harmonic power [82]. For an equivalent input power of  $(170 \times 210)^{\frac{1}{2}}$  mW = 189 mW and a single pass through the crystal, the generated second harmonic power would be  $\sim 2 \mu\text{W}$  which is less than half of that generated by SFM in the sodium vapour.

For fixed  $\nu_1$ , tuning  $\nu_2$  produced two Doppler broadened peaks (FWHM  $\sim 4.5$  GHz) separated by  $\sim 25$  GHz which corresponded to the two groups of  $\Delta m = \pm 2$  quadrupole transitions responsible for the SFM emission. However, for fixed  $\nu_2$ , tuning  $\nu_1$  by only  $\sim 200$  MHz completely eliminated the SFM signal which was indicative of a critical frequency dependent phase matching condition being achieved on the lower single photon D line transition. In general, for a fixed value of  $\nu_2$ , the maximum SFM signal depended upon tuning  $\nu_1$  over this range relative to the crossover frequency in the Na reference cell and varying the magnetic field strength by a few hundred Gauss.

Increasing the sodium density further decreased the SFM power, probably due to increased linear single photon absorption or phase mismatching. It was unlikely that the two-photon transition was saturated under these conditions due to the larger single photon detuning and higher power input beams might produce greater SFM beam powers.

# **CHAPTER 7**

$\chi^{(2)}$  **NONLINEARITY INDUCED IN AN ATOMIC  
VAPOUR BY OPTICAL PUMPING**

## Chapter 7

### $\chi^{(2)}$ NONLINEARITY INDUCED IN AN ATOMIC VAPOUR BY OPTICAL PUMPING

As previously discussed in Chapter 1, three-wave nonlinear optical processes with a collinear geometry are not possible in an isotropic medium, such as an atomic vapour. Previous methods to break the symmetry of a vapour and permit  $\chi^{(2)}$  nonlinear optical effects have used transverse dc magnetic or electric fields to couple atomic level wavefunctions and impose a transverse quantisation axis in the atomic medium. Collinear sum frequency mixing (SFM), second harmonic generation (SHG) and difference frequency mixing (DFM) have all now been demonstrated in atomic vapours using these symmetry breaking techniques.

Another possible method of inducing the  $\chi^{(2)}$  nonlinearity in an atomic medium which has previously been suggested [12] but not previously studied is to create a transversal background polarisation of the atoms. A spin polarisation of this type can be formed by using a resonant light beam to optically pump the ground state atomic population into a coherent superposition of orientation substates. A polarisation which is transverse to the fundamental beams for the three-wave mixing process is required so that photon angular momentum is conserved in the nonlinear optical process.

This chapter concerns the experimental investigation of inducing SHG in sodium vapour with the  $\chi^{(2)}$  nonlinearity in the atomic medium created by the novel technique of optical pumping.

#### 7.1 PRINCIPLES OF OPTICAL PUMPING

Optical pumping, which was first proposed by Kastler in the 1950s [172, 173], is a technique of using resonant light to create a non-thermal population distribution among the energy sub-levels of an atomic ground state. The normal Boltzmann thermal distribution of population in degenerate or non-degenerate ground state levels can be completely modified

under the action of a polarised or frequency selective resonant light field.

Optical pumping has now grown into a large subject area of physics in its own right. Much of the understanding of the optical pumping process was obtained with incoherent light sources before tunable lasers opened the field to many different types of atoms, molecules and solids. The use of lasers as well controlled pump sources for optical pumping has led to many detailed studies of the process in atomic beams [75, 174, 175, 176, 177, 178] and preparation of true two-level atoms [179, 180]. However, this chapter concentrates on the particular study of optical pumping in a gas cell which could be suitable as a nonlinear medium for SHG. Excellent and comprehensive review articles on the general subject of optical pumping, including coherence effects, magnetic resonance and the spectroscopy of hyperfine ground state atomic levels, can be found in references 50, 181, 182, 149, 183.

Consider the simple illustrative example of optical pumping shown in Figure 7.1 where right circularly polarised ( $\sigma^+$ ) resonant light is incident on a two-level atom with a degenerate  $S_{1/2}$  ground state and  $P_{1/2}$  first excited state.

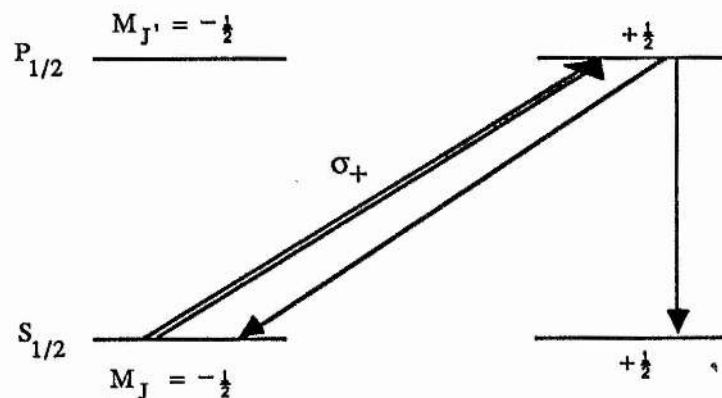


Figure 7.1 : Schematic diagram of a two-level atom interacting with a resonant, circularly polarised light field.

The absorption of a resonant  $\sigma^+$  light beam must occur with the atomic selection rule  $\Delta m_J = +1$  to accommodate the angular momentum of the photons in this pumping beam. Absorption of the light is only allowed from the  $m_J = -\frac{1}{2}$  sublevel of the  $S_{1/2}$  ground state to

the  $m_J = +\frac{1}{2}$   $P_{1/2}$  excited state. The excited population in the  $P_{1/2}$  state can decay through spontaneous emission to either of the degenerate ground state levels and so a component of the excited population collects in the  $m_J = +\frac{1}{2}$  sublevel. In the absence of other relaxation mechanisms, eventually all of the atomic population will be "optically pumped" into this nonabsorbing  $m_J = +\frac{1}{2}$  ground state sublevel and the atom will become transparent to the pumping resonant light beam. The optical pumping process has created a net magnetisation (polarisation or orientation) of the atom since only the spin-up orientation level is now occupied. Changing the pumping light to  $\sigma^-$  polarisation would create the reverse atomic orientation.

The degree of achievable atomic orientation in a gas cell depends upon the balance of the rate of induced optical transitions by the resonant light and the relaxation rate of the pumped energy level. A simple rate equation model of the optical pumping process gives the change in population of the  $S_{1/2}$   $m_J = -\frac{1}{2}$  level in Figure 7.1 as

$$\frac{dn_s(-\frac{1}{2})}{dt} = -\frac{\sigma_a I}{\hbar\omega} n_s(-\frac{1}{2}) + (n_s(+\frac{1}{2}) - n_s(-\frac{1}{2})) / 2T_1 \quad (7.1.1)$$

where  $n_i$  is the population of level  $i$ ,  $I$  is the pumping light intensity,  $\omega$  is the frequency of the light field,  $T_1$  is the spin relaxation time between the S state sublevels and  $\sigma_a$  is the absorption cross-section. This rate equation is valid when there is no spin exchange mechanism between the excited state sublevels. In the steady state, the ratio of population in the two ground state sublevels is

$$\frac{n_s(-\frac{1}{2})}{n_s(+\frac{1}{2})} = \frac{1}{1 + 2T_1 R} \quad (7.1.2)$$

where  $R$  is the pumping rate ( $= \sigma_a I / \hbar\omega$ ). The atomic polarisation (or orientation) induced by optical pumping is defined as

$$P = \frac{n_s(+\frac{1}{2}) - n_s(-\frac{1}{2})}{n_s(+\frac{1}{2}) + n_s(-\frac{1}{2})} \quad (7.1.3)$$

When the pumping rate  $R$  is much greater than the spin relaxation rate  $\Gamma = 1/T_1$ , which is

typical under laser optical pumping, a large fraction of the atoms are pumped into the non-absorbing sublevel and the polarisation  $P \approx 1$ . Even if the pumping rate is relatively small, say under excitation with a discharge lamp, then a large spin polarisation can still be produced by ensuring a very slow spin relaxation rate.

Franzen and Emslie [184] have analysed the optical pumping rate equations for sodium including the ground state hyperfine structure and have shown that the theoretical steady-state polarisation, for none or complete mixing in the excited state, should exceed 0.9 for pumping with only  $D_1$  resonance radiation. When both of the sodium D lines are used for excitation, the degree of atomic polarisation is small since the  $D_2$  line can always absorb resonance radiation even when the ground state is 100% oriented [185].

One method of analysing the magnitude of the atomic orientation created by optical pumping is to examine the transmission of the pumping light through the sample cell. For  $D_1$  line pumping with  $\sigma+$  polarised light, the ground state population is pumped into a non-absorbing sublevel and therefore the transmission of the light increases with increasing atomic orientation. Alternatively, the emitted fluorescent light from the oriented atomic sample can be used to determine the atomic polarisation since the sample has become non-absorbing and no longer re-radiates fluorescence radiation. The intensity of the fluorescent light directly monitors the population of atoms in the  $m_J = -\frac{1}{2}$  ground state sublevel (Figure 7.1).

### 7.1.1 Pumping Source

Optical pumping experiments were carried out for many years using discharge lamps as the light sources for the optical pumping. These sources provided typical photon fluxes of  $\sim 10^{12}$  photons  $\text{cm}^{-2} \text{s}^{-1}$  in a fixed linewidth of a few GHz determined by Doppler broadening. Using lasers as optical pumping sources can provide fluxes of  $\sim 10^{19}$  photons  $\text{cm}^{-2} \text{s}^{-1}$  in variable linewidths down to a few MHz. The larger light intensity produced by lasers and their tunability makes them superior as optical pumping sources. Multimode [186, 187] or single-mode [105, 106, 188, 189, 190] lasers have been shown to be effective in producing large polarisations in sodium vapour through optical pumping. Multimode lasers typically have a linewidth comparable to the atomic transition Doppler width (1-2 GHz) so that all the atomic

velocity groups are pumped simultaneously. Single-mode laser optical pumping selectively optically pumps a particular homogeneous velocity group from the inhomogeneous velocity distribution [191] but pumping over the whole Doppler width can be achieved by using velocity changing collisions to broaden the velocity distribution of the optical pumping [105]. Some of the detailed aspects of laser optical pumping are reviewed by Cohen-Tannoudji in reference 182.

A multimode laser was chosen as the optical pumping source to experimentally investigate inducing the  $\chi^{(2)}$  nonlinearity in sodium vapour. This dye laser system was described in §3.1.4. The estimated pumping rate using this laser source was  $\sim 3 \times 10^8 \text{ s}^{-1}$  based on an average power of 75 mW focused to  $\sim 0.2 \text{ cm}^2$  over the 1.5 GHz sodium Doppler width.

## 7.2 RELAXATION OF THE ATOMIC ORIENTATION

Even with large pumping rates, the spin relaxation rate of the optically pumped atoms must be relatively small to ensure a large steady-state atomic orientation. In a gas cell, several mechanisms contribute to the relaxation of the atomic populations and these are discussed below.

### 7.2.1 *Relaxation on the Cell Walls*

Collisions of the oriented sodium atoms with the cell walls are effective in destroying the optically pumped polarisation of the atomic ground state. The local magnetic and electric fields of the molecules forming the cell walls act randomly on an oriented atom and consequently the orientation is destroyed. The relaxation time is related to the mean time of flight of a pumped atom between the cell walls

$$\tau = L / v \tag{7.2.1}$$

where  $\tau(\text{s})$  is the relaxation time,  $L(\text{m})$  is a characteristic length of the cell and  $v(\text{ms}^{-1})$  is the mean thermal velocity of the atom. Typically  $\tau \sim 10^{-4} \text{ s}$  at thermal velocities of a few hundred metres per second and for cell dimensions of a few cm.

Relaxation of the atomic orientation at the cell walls can be inhibited by coating the walls with certain hydrocarbon compounds, whose long chain molecules prevent the oriented alkali metal atoms from being affected by the local fields at the cell walls. Coatings on the cell walls can increase the relaxation times by a factor of ~5 [194] but are limited to low temperature cells.

### 7.2.2 Diffusion to the Cell Walls

The addition of buffer gas to the metal vapour sample cell can have a beneficial effect on the optical pumping relaxation time through limiting the mean free path of the pumped atom to less than the physical cell dimensions. This prevents collisions of the oriented atoms with the cell walls and confines the atoms to the pumping region in the cell. The change in optically pumped atomic population due to diffusion can be expressed as

$$\frac{dn}{dt} = D \nabla^2 n \quad (7.2.2)$$

where  $n$  ( $\text{cm}^{-3}$ ) is the population density of the pumped atoms and  $D$  ( $\text{cm}^2 \text{s}^{-1}$ ) is the diffusion constant for the alkali metal atoms in a given buffer gas [50]. The diffusion constant for sodium in helium buffer gas at 1 atmosphere pressure is  $0.92 \text{ cm}^2 \text{ s}^{-1}$  [192]. The diffusion constant  $D'$  at any buffer gas pressure  $P$ (mbar) is given by

$$D' = \frac{10153}{P} D. \quad (7.2.3)$$

For a cylinder of length  $L$  and radius  $a$ , the diffusion time  $T$  is [193]

$$T = \frac{1}{\left[ \left( \frac{\pi}{L} \right)^2 + \left( \frac{2.405}{a} \right)^2 \right] D} \quad (7.2.4)$$

The calculated diffusion time for a cylinder appropriate to the experimental optical pumping cell dimensions and a helium buffer gas pressure of ~1 atm would be ~11 ms. Experimentally, a typical measured spin relaxation rate initially decreases with increasing buffer gas pressure through diffusion effects but the relaxation rate increases at higher buffer gas pressures where spin destroying collisions begin to dominate as a relaxation mechanism [194, 195, 196].

### 7.2.3 Spin Destroying Collisions

If the buffer gas pressure is high, the binary collisions between the optically pumped alkali metal atoms and the buffer gas atoms causes relaxation of the acquired orientation [188]. This relaxation rate can be represented by

$$\Gamma_{\text{coll}} = N_p \sigma(v_r) v_r \quad (7.2.5)$$

where  $N_p$  ( $\text{cm}^{-3}$ ) is the atomic density of the buffer gas at pressure  $p$ ,  $v_r$  ( $\text{cm s}^{-1}$ ) is the mean relative velocity of the colliding atoms and  $\sigma(v_r)$  ( $\text{cm}^2$ ) is the velocity averaged spin-disorienting collision cross-section. Helium was chosen as the buffer gas in the experiments described here since it has the smallest ground state relaxation cross-section for sodium ( $\sigma = 2.2 \times 10^{-26} \text{ cm}^2$  [197]).

Collisions also occur between the oriented atoms and this can result in spin exchange which is very effective in destroying the atomic orientation produced by optical pumping. The spin exchange cross-section  $\sigma_{\text{Na-Na}}$  is  $1.109 \pm 0.005 \times 10^{-14} \text{ cm}^2$  [198] and can become the dominant relaxation mechanism when the density of the alkali metal vapour is high [199]. This sets a limit on the achievable atomic orientation at high alkali vapour densities when the vapour is optically thick.

Spin destroying collisions between the metal vapour atoms have also been shown to contribute to the total relaxation but the associated cross-section is less than for spin exchange [200].

### 7.2.4 Radiation Trapping

Most optical pumping studies have been carried out in optically thin atomic vapours where the effects of the alkali metal vapour density are negligible. However, it was widely experimentally verified that the relaxation time of the optically induced atomic orientation rapidly decreased with increasing metal vapour pressure [194]. One consequence of an optically thick alkali metal sample is radiation trapping of the resonance fluorescence where emitted spontaneous photons are rapidly reabsorbed by other atoms. Trapped light provides a weakly polarised, nearly isotropic background of resonant light which competes with the

optical pumping and degrades the orientation of the atomic ground state.

Tupa et al [201] have calculated the effect of radiation trapping on the polarisation of an optically pumped alkali metal vapour. Their theoretical analysis with a cylindrical geometry showed that  $\sim 90\%$  spin polarisation should be achievable in the steady state with a ground state relaxation time of  $\sim 150 \mu\text{s}$ , a pump power of  $\sim 1 \text{ W}$  over a few GHz and an alkali vapour density of  $\sim 10^{13} \text{ cm}^{-3}$ . Figure 7.2 shows the calculated maximum density of alkali metal vapour which can be optically pumped to 90% polarisation as a function of pump power (linewidth approximately equal to the Doppler width) and the spin relaxation time.

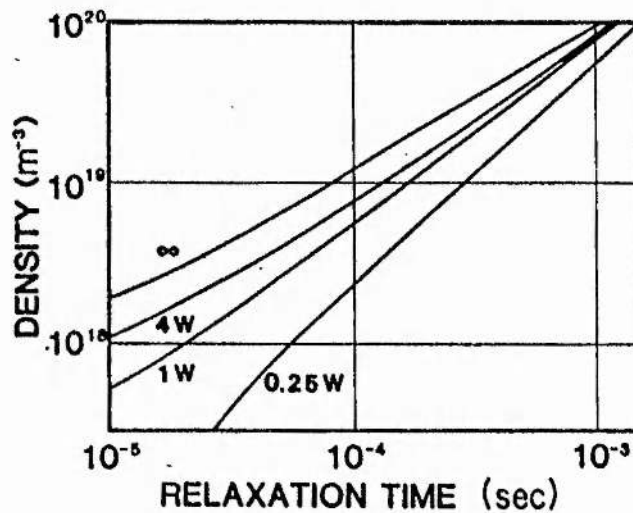


Figure 7.2 : The maximum atomic density which may be optically pumped to a polarisation of 0.9 as a function of ground-state relaxation time  $T_1$  at various incident laser powers (from [201]).

Their calculations are not strictly applicable to experiment since the light intensity was assumed to be constant through the optically pumped sample and the theoretical calculations were not valid at low values of magnetic field where the different atomic transitions lie within the same Doppler width.

Molecular buffer gases such as nitrogen have been shown to be effective in quenching the unpolarised resonance fluorescence ( $\sigma \sim 5 \times 10^{-15} \text{ cm}^2$  for Na in  $\text{N}_2$ ) and preventing radiation trapping. A few mbar of  $\text{N}_2$  is typically used in the buffer gas for this purpose [188, 199, 202].

### 7.3 EFFECT OF OPTICAL PUMPING ON SHG

The effect of the ground state population imbalance created by transverse optical pumping on the SHG nonlinear optical process was predicted using the theoretical model developed by Sinclair [7.39] and reviewed in Chapter 2.

The quadrupole moment which generated the second harmonic wave was

$$Q_{xy} \propto \sum_{\substack{F, M_F \\ J, M_J}} \rho_{SS} (B_2 - B_{-2}) Z [(2\omega - \omega_{ds} + i \gamma_{ds}) / \Omega] \quad (7.3.1)$$

when the laser polarisation was perpendicular to the transverse magnetic field direction. Under normal thermal equilibrium the ground state populations of the hyperfine sublevels were all equal and the  $\rho_{SS}$  density matrix population term could be removed from the summation over  $F$  and  $M_F$  in the  $3S_{1/2}$  sodium ground state. In this case with no applied magnetic field, the  $B_2$  ( $J, M_J, F, M_F$ ) and  $B_{-2}$  ( $J, -M_J, F, -M_F$ ) elements were equal which led to a zero result for the summation in equation (7.3.1). However, in the sodium vapour with transverse optical pumping, the ground state hyperfine populations are significantly changed and the population terms  $\rho_{SS}(F, M_F)$  become hyperfine substate dependent. The  $B_2$  and  $B_{-2}$  factors are now not necessarily cancelled at zero applied magnetic field, due to the different population terms in each ground state hyperfine sublevel, and SHG may become allowed.

The degree of symmetry breaking due to optical pumping is dependent upon the orientation achievable in the sodium vapour. If the induced population imbalance in the ground state is small then the associated SHG nonlinear optical process will be reduced due to the remaining cancellation effects of the atomic two-photon absorption routes. In effect, the influence of optical pumping on SHG at a microscopic level is to select only one particular route among the atomic levels for two-photon absorption and parametric emission.

A quantitative calculation of the influence of optical pumping on SHG due to the induced ground state population imbalance was carried out by adapting the existing computer model of magnetic field induced SHG. The model was changed to assign a population factor to each ground state hyperfine sublevel so that the effect of optical pumping could be included. Figure 7.3 shows a theoretical SHG line profile with the maximum atomic orientation under  $D_1$

$\sigma^+$  optical pumping, ie. all of the ground state population is the ground state  $F = 2, M_F = +2$  sublevel.

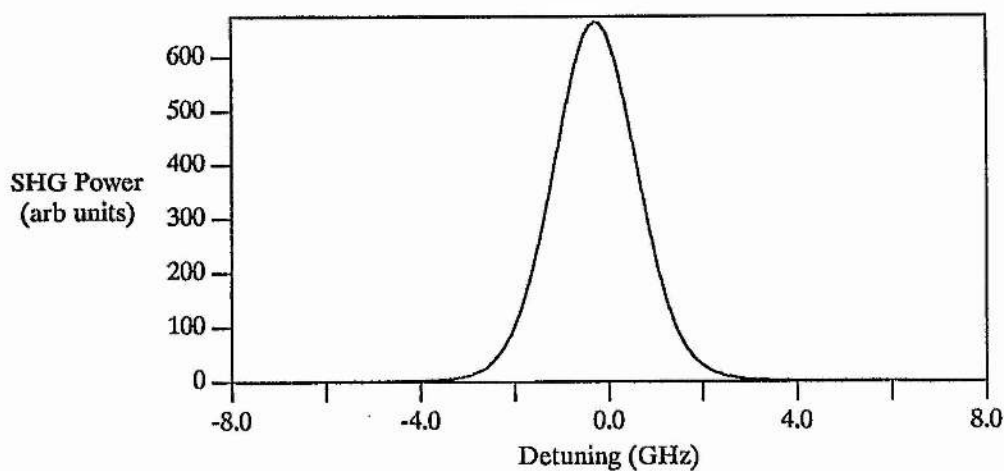


Figure 7.3 : Theoretical SHG line profile with zero applied magnetic field and complete atomic orientation by optical pumping.

The predicted maximum SHG power is equivalent to that generated with a transverse magnetic field strength of  $\sim 245$  G with no optical pumping. Complete orientation with  $\sigma^-$  optical pumping produces a similar SHG line profile with the same maximum SHG power. These theoretical SHG line profiles assumed that the collisional dephasing rate of the Na S-D coherence was small compared to the Doppler width. In practice, the moderate to high buffer gas pressure required for diffusional containment of the optically pumped atoms reduced the SHG power through increased collisional relaxation (see later). The calculated variation of peak SHG power with degree of optical pumping is shown in Figure 7.4. As expected, maximum SHG power occurs for complete polarisation and is zero under normal thermal equilibrium.

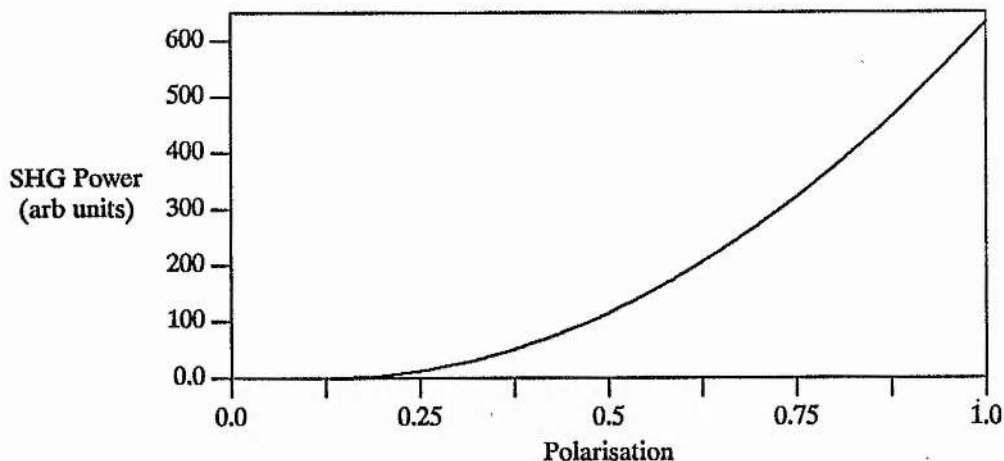


Figure 7.4 : Theoretical variation of peak SHG power with atomic polarisation.

#### 7.4 EXPERIMENTAL RESULTS AND CONCLUSIONS

The experimental apparatus used to investigate the effects of optical pumping on SHG has been described in Chapter 3. Figure 7.5 shows the schematic experimental layout which was developed to maximise the possibility of observing a  $\chi^{(2)}$  nonlinear effect due to optical pumping.

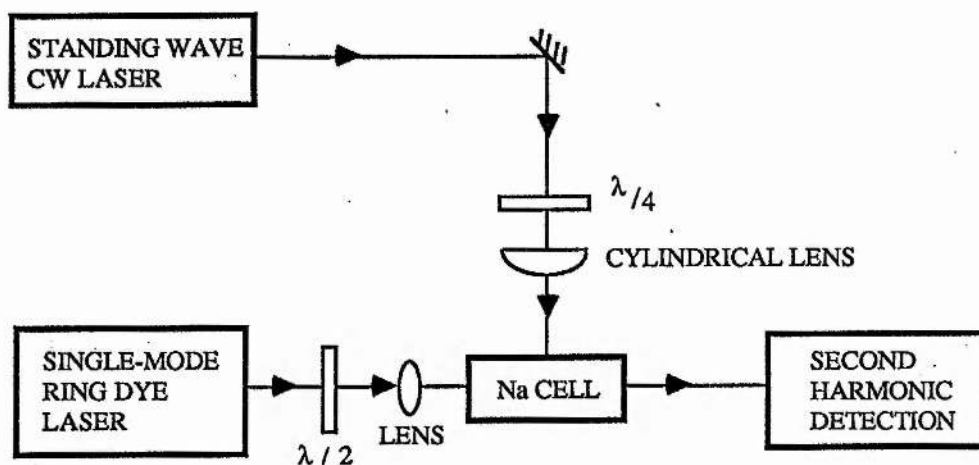


Figure 7.5 : Schematic experimental set-up for examining SHG induced by optical pumping.

The cylindrical lens loosely focused the circularly polarised optical pumping beam into the Na cell to form a pumped region which was  $\sim 1$  cm in length along the cell. A 10 cm focal length

lens was used to focus the fundamental beam for SHG into the cell to ensure that the confocal parameter approximately matched the length of the optically pumped region. The beams could be accurately overlapped by using pinholes to define the beam geometry.

Although the theoretical analysis has shown that optical pumping can possibly induce a significant  $\chi^{(2)}$  nonlinearity to allow SHG, the required experimental conditions for each optical process proved to be stringent and in opposition.

(i) *Sodium vapour density* :- For magnetic field induced SHG, the minimum sodium vapour density at which the second harmonic signal could be recorded with a reasonable signal to noise ratio was  $\sim 10^{13} \text{ cm}^{-3}$ . Unfortunately, at these densities the sodium vapour is optically thick to resonance radiation which makes optical pumping extremely difficult. Spin polarisations of  $> 90\%$  have previously been achieved over a length of 4 cm in pure sodium vapour of density  $\sim 2.5 \times 10^{12} \text{ cm}^{-3}$  ( $9 \times 10^{12} \text{ cm}^{-3}$ ) with an applied magnetic field of 1G (750G) [186]. The multimode pump laser power was  $\sim 400 \text{ mW cm}^{-2}$  in a 2.1 GHz linewidth. The spin polarisation decreased rapidly with increasing Na density and was only  $\sim 30\%$  at the minimum required density for SHG of  $\sim 1 \times 10^{13} \text{ cm}^{-3}$ . Similar values of spin polarisations have been produced by single-mode laser optical pumping of optically thick, pure Na vapour samples in high magnetic fields of  $\sim 3.5 \text{ kG}$  [189].

(ii) *Buffer gas pressure* :- The presence of buffer gas in the sodium cell aids the optical pumping process through restricting the diffusion of the oriented atoms as discussed in §7.2.2. Typical experimental parameters used by several investigators have been a few hundred millibars of a buffer gas (eg. He) and a few tens of millibars of  $\text{N}_2$  to prevent radiation trapping [188, 199, 202, 203]. The buffer gas also pressure broadens the atomic absorption line and enhances the optical pumping with a multimode dye laser [187]. The optimum buffer gas pressure for optical pumping in the configuration for inducing SHG was experimentally determined by monitoring the transmission of the optical pumping beam through the Na cell as a function of He buffer gas pressure. High transmission of the  $\text{D}_1$  circularly polarised pump light is an indication of a large atomic orientation [203]. Maximum transmission of the pumping laser beam occurred with a helium pressure of  $\sim 400 \text{ mbar}$  and a  $\text{N}_2$  pressure of  $\sim 15$

mbar at a relatively low sodium vapour density.

The detrimental effect of the high buffer gas pressure on the magnetic field induced SHG nonlinear optical process was also experimentally determined. The SHG power was measured as a function of He pressure with a similar method to the one used by Sinclair and Dunn with Ar buffer gas [44]. The peak second harmonic power was reduced by a factor of  $\sim 100$  at a He pressure of 400 mbar.

At low sodium densities and high buffer gas pressures, the effect of the  $D_1$  line  $\sigma^+$  optical pumping was easily observed by rotating the  $\lambda/4$  plate to change the pumping radiation polarisation from circular to linear. When the pumping beam was  $\sigma^+$  or  $\sigma^-$  polarised the laser beam was easily transmitted through the cell and the transverse fluorescence intensity reduced significantly, indicating that a large hyperfine atomic orientation had been produced in the non-absorbing  $F = 2$ ,  $M_F = +2$  or  $-2$  ground state sublevel. Conversely, for a linear polarised pumping beam, most of the beam was absorbed as was expected. Imposing a weak ( $\sim 10$  G) guide field for the  $\sigma^+$  optical pumping beam showed that the optical pumping was sensitive to the relative magnetic field-pump beam angle. Maximum atomic orientation through optical pumping was observed when the magnetic field and pump beam were parallel. Tuning the pumping laser beam to the sodium  $D_2$  line showed little change in the transmission of fluorescence upon changing the optical pumping beam polarisation since single photon absorption is always allowed for this resonance line, as mentioned previously.

Even though clear signs of optical pumping could be observed, measurement of unambiguous magnetic field induced SHG signals required the experimental sodium density to be significantly increased and the buffer gas pressure to be reduced. For these SHG experimental conditions, no distinctive optical pumping effects were observed as before. It was attempted to find a compromise between the sodium vapour density and the buffer gas pressure such that each of the magnetic field induced SHG and optical pumping processes could be observed simultaneously and their interaction studied. In practice this proved to be difficult to achieve and even with the developed optimised experimental system, no effect of optical pumping on the SHG nonlinear optical process was observed.

It was concluded that the technique of inducing the  $\chi^{(2)}$  nonlinearity for SHG in sodium vapour by transverse optical pumping was not practical due to the presence of high buffer gas pressures, required for efficient multi-mode laser optical pumping, and more critically due to the difficulty in obtaining a large atomic orientation in high sodium vapour densities, required for a large nonlinear optical effect to be observed.

## 7.5 FUTURE WORK

Possible improvements to the experimental study of  $\chi^{(2)}$  nonlinear optical effects induced by optical pumping may be to use second resonance light for the optical pumping [199]. This would require a laser pump source at the sodium 3S-4P transition wavelength of  $\sim 330$  nm. High vapour densities ( $\sim 10^{14}$  cm $^{-3}$ ) have been optically pumped in Cs using this technique but the maximum spin polarisation was only  $\sim 30\%$  and large buffer gas pressures ( $\sim 0.5$  atm) were required.

Optical pumping by two-photon absorption has also been suggested although an observed spin orientation of  $\sim 20\%$  was attributed to an excimer transition between the alkali metal atoms and the high pressure ( $\sim 100$ 's of mbar) buffer gases [204].

The buffer gas pressure could be decreased significantly by using single-mode laser optical pumping with a low pressure buffer gas to induce velocity changing collisions for complete Doppler pumping [105, 106, 190]. However, only optically thin samples have so far been oriented with this optical pumping technique.

It is proposed that the creation of a  $\chi^{(2)}$  nonlinearity in an atomic vapour by optical pumping might readily be studied via three-wave SFM rather than SHG. As has been shown in this thesis, the required atomic densities for observation of the simultaneous single and two-photon resonant SFM nonlinear optical process are orders of magnitude less than for SHG. Complete atomic orientation through optical pumping should be possible at these atomic vapour densities and  $\chi^{(2)}$  nonlinear effects should possibly be observed.

# **CHAPTER 8**

## **SUMMARY AND FUTURE WORK**

## Chapter 8

### SUMMARY AND FUTURE WORK

#### 8.1 SUMMARY

Continuous-wave, collinear, three-wave sum-frequency mixing (SFM) has been demonstrated and studied for the first time in an atomic vapour using a transverse magnetic field to induce the  $\chi^{(2)}$  nonlinearity.

Both the microscopic and macroscopic behaviour of this nonlinear optical process has been shown to be dependent upon the detuning of the fundamental laser frequencies from the single photon atomic dipole transitions, in addition to the detuning from two-photon absorption.

With both fundamental frequencies tuned outside the single photon atomic transition Doppler widths, the microscopic dependence of SFM on magnetic field strength, laser intensity and laser polarisation were shown to be consistent with the model for second harmonic generation (SHG). The macroscopic SFM phase-matching was different from SHG due to the sign and the magnitude of the phase mismatch  $\Delta k$  being dependent upon the choice of the two fundamental frequencies. The variation of SFM power with sodium particle density was asymmetric with respect to the sign of  $\Delta k$  which was due to focusing effects of the input laser beams. The measured SFM phase matching dependence was in reasonable agreement with the existing theory of focusing phase shifts in parametric optical processes.

Simultaneous single and two-photon resonant enhancement of a nonlinear optical mixing effect was examined for the first time. Additional single photon resonant enhancement increased the atomic two-photon absorption cross-section by several orders of magnitude relative to degenerate frequency two-photon excitation. When the single-mode laser frequencies lay within the single photon atomic transition Doppler widths, the SFM nonlinear optical process became velocity selective due to the hole burning and saturation of

homogeneous velocity groups in the inhomogeneous Doppler profile. Sub-Doppler spectral features were observed in the line profiles of the incoherent fluorescence and the coherent SFM due to velocity selection. Considerable differences between the fluorescence and SFM line profiles were attributed to phase matching effects on the SFM caused by frequency dependent variations in the atomic refractive index. Population imbalances induced by frequency selective optical pumping of the atomic ground state were shown to severely affect the SFM process through refractive index changes and consequent phase mismatching. Careful strategies had to be adopted to minimise such an effect.

Large SFM conversion efficiencies were obtained in relatively low density atomic vapours ( $\sim 10^{13} \text{ cm}^{-3}$ ) by utilising control over single and two-photon resonant enhancement and frequency selective phase matching. Under the optimum conditions,  $\sim 5 \mu\text{W}$  of SFM power was generated which corresponded to a conversion efficiency of  $\sim 1.5 \times 10^{-5}$ . This was greater than the estimated single pass SHG conversion efficiency in a good nonlinear crystal such as ADA. This study of single and two-photon resonant enhancement has shown the potential of atomic vapours as useful nonlinear media for producing significant nonlinear optical conversion.

The Zeeman splittings of the sodium 3S-3P hyperfine transition frequencies were measured using the technique of saturation spectroscopy. Under continuous-wave excitation, the saturation spectrum was broadened by velocity changing conditions (vcc) but their influence was reduced by using a novel experimental method. Sampling the saturated absorption signal at the leading edge of the chopped pump beam where the vcc had little time to broaden the narrow saturated velocity distribution provided greater resolution and allowed the numerous Zeeman transitions to be resolved. The interpretation of the spectrum was shown to be complicated due to the many cross-over resonances from the numerous non-degenerate hyperfine energy levels in the ground and excited state. This imposed a limitation on the usefulness of this spectroscopic technique.

The use of transverse optical pumping to induce the  $\chi^{(2)}$  nonlinearity in an atomic vapour was analysed and shown to be a possible, though weak, process. Detection of this

effect in inducing SHG was not experimentally observed due to the necessary conditions of low sodium vapour density and high buffer gas pressure for good optical pumping. These conditions were in conflict with those for SHG in the same atomic medium and a compromise set of experimental conditions was not possible.

## 8.2 FUTURE WORK

The demonstrated high conversion efficiency for magnetic field induced SFM with both single and two-photon resonant enhancement presents many opportunities for future work in this area.

One immediate improvement in the SFM experiment would be to use the sodium 3S-3D two-photon transition as the enhancing atomic route. The 3P-3D dipole matrix element is ~3.5 times larger than the 3P-4D matrix element [11] and the 3S-3D quadrupole matrix element squared is ~6.9 times larger than the 3S-4D quadrupole element squared [171]. For the same total fundamental input power, the anticipated generated UV power would be ~0.42 mW due to larger atomic matrix elements alone. Recent advances in Ti:Al<sub>2</sub>O<sub>3</sub> laser technology has provided a suitable high power source at the Na 3P-3D transition wavelength of ~820 nm. It should be possible to generate several milliwatts of UV SFM power with only ~500 mW in each fundamental beam on the 3S-3P-3D atomic excitation route. Other improvements in conversion efficiency might be realised by increasing the interaction length with a tailored magnetic field or by using a different atomic medium with more favourable transition matrix elements for SFM.

An interesting development in the atomic excitation route would be to excite the quadrupole moment on the second step and have the parametric emission occurring on the dipole transition (see Figure 8.1). Single photon resonant enhancement has previously been used to induce a weak quadrupole-dipole two-photon absorption in sodium vapour [205]. A calculation of the possible excitation route

$$3S_{1/2} - d \rightarrow 3P - q \rightarrow 4P = d \Rightarrow 3S_{1/2}$$

in sodium shows that the atomic parameters predict a similar generated SFM power to the 3S-4D excitation scheme. Again, a Ti:Al<sub>2</sub>O<sub>3</sub> laser would be a suitable source at the 3P-4P

quadrupole transition wavelength of  $\sim 750$  nm.

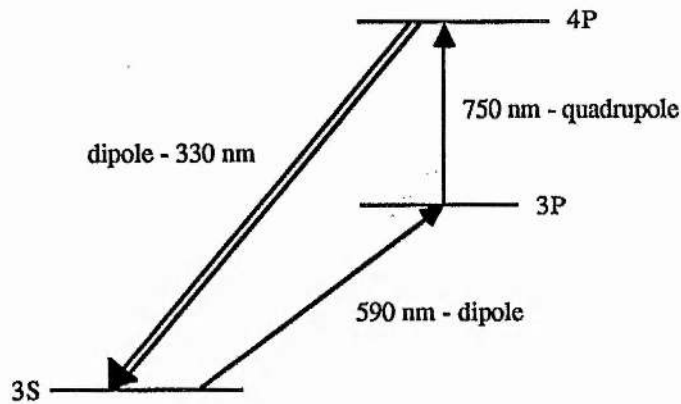


Figure 8.1 : Schematic diagram of a possible SFM excitation route in Na with a quadrupole transition occurring on the second excitation step.

Phase matching of this SFM process may be modified since the parametric emission would occur on a weak but allowed dipole transition which may have a considerable refractive index contribution. The competition between the stimulated emission and the spontaneous fluorescence from the 4P state would be of interest.

An extension of each of these proposed schemes would be to excite high lying Rydberg states of the atomic medium using simultaneous single and two-photon resonance for SFM. Although the quadrupole and dipole transition matrix elements are typically weaker than for low lying states, this method might allow some quasi-tunability of the SFM through the closely spaced, magnetically split levels of the Rydberg states. Obtaining a true tunable SFM nonlinear optical process might be achieved in a suitable molecular nonlinear medium, as suggested by Sinclair [14].

Since the simultaneous single and two-photon excitation scheme for SFM can occur in low atomic densities with good signal to noise ratios, it may be practical to study the microscopic behaviour of the nonlinear optical process in great detail by using an atomic beam as the nonlinear medium. A better insight into the roles of two-photon and stepwise excitation in the mixing process would be obtained without the complications of inhomogeneous broadening and collisions. The 3S-3D route in Na would be a good choice for excitation since

the atom can only decay through spontaneous emission to other levels within the three interacting groups of levels.

Additionally, as mentioned in Chapter 7, it may be possible to study simultaneous single and two-photon resonantly enhanced SFM with the  $\chi^{(2)}$  nonlinearity created in the atomic vapour by transverse optical pumping. The low sodium atomic densities required for efficient optical pumping should also allow reasonable SFM signals to be detected. Again, the observation of an optical pumping effect on  $\chi^{(2)}$  will also depend upon a compromise on buffer gas pressure but this may be reduced through single-mode laser optical pumping as previously discussed in §7.1.1.

## **REFERENCES**

## REFERENCES

1. P. Lorrain and D. Corson, "Electromagnetic Fields and Waves", 2nd Ed. (W.H. Freeman and Co., New York, 1970).
2. A. Yariv, "Quantum Electronics", 3rd Ed. (Wiley, New York, 1989).
3. N. Bloembergen, "Nonlinear Optics", (W.A. Benjamin Inc., New York, 1965).
4. D.C. Hanna, M.A. Yuratich and D. Cotter, "Nonlinear Optics of Free Atoms and Molecules", (Springer-Verlag, Berlin, 1979).
5. T.H. Maiman, Nature 187, 493 (1960).
6. P.A. Franken, A.E. Hill, C.W. Peters and E. Weinreich, Phys. Rev. Lett. 7, 118 (1961).
7. Y.R. Shen, "The Principles of Nonlinear Optics", (Wiley, New York, 1984).
8. "Quantum Electronics : A Treatise - Vol. I Nonlinear Optics, Part A and B", edited by H. Rabin and C.L. Tang, (Academic, New York, 1975).
9. P. Butcher and D. Cotter, "The Elements of Nonlinear Optics", (Cambridge University Press, Cambridge, 1990).
10. W.J. Kozlovsky, C.D. Nabors and R.L. Byer, IEEE J. Quantum Electron. QE-24, 913 (1988).
11. R.B. Miles and S.E. Harris, IEEE J. Quantum Electron. QE-9, 470 (1973).
12. Th. Hänsch and P. Toschek, Z. Physik 236, 373 (1970).
13. J.A. Armstrong, N. Bloembergen, J. Ducuing and P.S. Pershan, Phys. Rev. 127, 1918 (1962).

14. B.D. Sinclair, "Second Harmonic Generation in Sodium Vapour Induced by a Magnetic Field" (Ph.D. thesis, University of St. Andrews, 1987).
15. B.W. Shore and D.H. Menzel, "Principles of Atomic Spectra", (Wiley, New York, 1968).
16. K.J. Kollath and M.C. Standage in "Progress in Atomic Spectroscopy - Part B", edited by W. Hanle and H. Kleinpoppen, (Plenum Press, New York, 1979), p. 955.
17. R.L. Abrams, A. Yariv and P.A. Yeh, IEEE J. Quantum Electron. QE-13, 79 (1977).
18. R.L. Abrams, C.K. Asawa, T.K. Plant and A.E. Popa, IEEE J. Quantum Electron. QE-13, 82 (1977).
19. R.W. Boyd and L.Q. Xiang, IEEE J. Quantum Electron. QE-18, 1242 (1982).
20. D.J. Gauthier, J. Krasinski and R.W. Boyd, Opt. Lett. 8, 211 (1983).
21. R.W. Boyd, D.J. Gauthier, J. Krasinski and M.S. Malcuit, IEEE J. Quantum Electron. QE-20, 1074 (1984).
22. T. Mossberg, A. Flusberg and S.R. Hartmann, Opt. Commun. 25, 121 (1978).
23. J. Okada, Y. Fukuda and M. Matsuoka, J. Phys. Soc. Japan 50, 1301 (1981).
24. J. Bokor, R.R. Freeman, R.L. Panock and J.C. White, Opt. Lett. 6, 182 (1981).
25. V.G. Arkhipkin, N.P. Makarov, A.K. Popov, V.P. Timofeev and V.S. Epstein, Sov. J. Quantum Electron. 11, 656 (1981).
26. R.R. Freeman, R. Panock and J.E. Bjorkholm, IEEE J. Quantum Electron. QE-17, 10 (1981).
27. D.S. Bethune, Phys. Rev. A 23, 3139 (1981).
28. D.S. Bethune, Phys. Rev. A 25, 2845 (E) (1982).

29. S. Dinev, A. de Garia, P. Meystre, R. Salomaa and H. Walther in "Laser Spectroscopy VI", edited by H.P. Weber and W. Luthy, (Springer-Verlag, Berlin, 1983).
30. S.G. Dinev, J. Phys. B : Atom. Molec. Phys. 21, 1111 (1988).
31. S. Dinev, J. Phys. B : Atom. Molec. Phys. 21, 1681 (1988).
32. D.S. Bethune, R.W. Smith and Y.R. Shen, Phys. Rev. Lett. 37, 431 (1976).
33. D.S. Bethune, R.W. Smith and Y.R. Shen, Phys. Rev. A17, 277 (1978).
34. D.S. Bethune, R.W. Smith and Y.R. Shen in "Coherence and Quantum Optics IV", edited by L. Mandel and E. Wolf, (Plenum Press, New York, 1978).
35. A. Flusberg, T. Mossberg and S.R. Hartmann, Phys. Rev. Lett. 38, 59 (1977).
36. M. Matsuoka, H. Nakatsuka, H. Uchiki and M. Mitsunaga, Phys. Rev. Lett. 38, 894 (1977).
37. A. Flusberg, T. Mossberg and S.R. Hartmann, Phys. Rev. Lett. 38, 694 (1977).
38. A. Flusberg, T. Mossberg and S.R. Hartmann in "Coherence and Quantum Optics IV", edited by L. Mandel and E. Wolf, (Plenum Press, New York, 1978).
39. T. Mossberg, A. Flusberg and S.R. Hartmann, Opt. Commun. 25, 121 (1978).
40. H. Uchiki, H. Nakatsuka and M. Matsuoka, Opt. Commun. 30, 345 (1979).
41. H. Uchiki, H. Nakatsuka and M. Matsuoka, J. Phys. Soc. Japan 52, 3010 (1983).
42. M.H. Dunn, Opt. Commun. 45, 346 (1983).
43. B.D. Sinclair and M.H. Dunn, Phys. Rev. A 34, 3989 (1986).
44. B.D. Sinclair and M.H. Dunn, J. Mod. Optics 35, 517 (1988).
45. M. Göppert-Mayer, Ann. der Physik 9, 273 (1931).

46. G.D. Boyd and D.A. Kleinman, J. Appl. Phys. 39, 3597 (1968).
47. J.E. Bjorkholm and P.F. Liao, Phys. Rev. Lett. 33, 128 (1974).
48. J.E. Bjorkholm and P.F. Liao, Phys. Rev. A14, 751 (1976).
49. V.S. Letokov and V.P. Chebotayev, "Nonlinear Laser Spectroscopy", (Springer-Verlag, Berlin 1977).
50. W. Happer, Rev. Mod. Phys. 44, 169 (1972).
51. E. Arimondo, M. Inguscio and P. Violino, Rev. Mod. Phys. 49, 31 (1977) - see this reference for all hyperfine constants for atomic sodium.
52. See eg. G.K. Woodgate, "Elementary Atomic Structure", 2nd Edition (Clarendon Press, Oxford, 1986).
53. G. Breit and I.I. Rabi, Phys. Rev. 38, 2082L (1931).
54. C. Fabre, M. Gross and S. Haroche, Opt. Commun. 13, 393 (1975).
55. T.W. Hansch, K.C. Harvey, G. Meisel and A.L. Schawlow, Opt. Commun. 11, 50 (1974).
56. K. Fredriksson and S. Svanberg, Phys. Lett. 53A, 61 (1975).
57. E.U. Condon and G.H. Shortley, "The Theory of Atomic Spectra", (Cambridge University Press, Cambridge, 1953).
58. I.I. Sobelman, "Springer Series in Chemical Physics Vol. 1 - Atomic Spectra and Radiative Transitions", (Springer-Verlag, Berlin, 1979). See also errata in "Springer Series in Chemical Physics Vol. 7 - Excitation of Atoms and Broadening of Spectral Lines" by I.I. Sobelman, L.A. Vainshtein and E.A. Yukov (Springer-Verlag, Berlin, 1980).
59. B.D. Fried and S.D. Conte, "The Plasma Dispersion Function, The Hilbert Transform of the Gaussian", (Academic Press, New York, 1961).

60. M. Sargent III, M.O. Scully and W.E. Lamb, Jr., "Laser Physics" (Addison -Wesley, Reading, 1977).
61. V.P. Chebotayev in "Topics in Applied Physics Vol. 13 - High Resolution Laser Spectroscopy", edited by K. Shimoda (Springer-Verlag, Berlin, 1976), pp. 207- 251.
62. Th. Hänsch and P. Toschek, Z. Physik 236, 213 (1970).
63. M.S. Feld and A. Javan, Phys. Rev. 177, 540 (1969).
64. H.K. Holt, Phys. Rev. Lett. 19, 1275 (1967).
65. R.G. Brewer and E.L. Hahn, Phys. Rev. A 11, 1641 (1975).
66. R.M. Whitley and C.R. Stroud, Jr., Phys. Rev. A 14, 1498 (1976).
67. N. Bloembergen and M.D. Levenson in "Topics in Applied Physics Vol. 13 - High-Resolution Laser Spectroscopy", edited by K. Shimoda (Springer-Verlag, Berlin, 1976), pp. 315-369
68. R. Salomaa and S. Stenholm, J. Phys. B : Atom. Molec. Phys. 8, 1795 (1975).
69. R. Salomaa and S. Stenholm, J. Phys. B : Atom. Molec. Phys. 9, 1221 (1976).
70. E. Arimondo and G. Orriols, Nuovo Cimento Lett. 17, 333 (1976).
71. H.R. Gray, R.M. Whitley and C.R. Stroud, Jr., Opt. Lett. 3, 218 (1978).
72. G. Janik, W. Nagourney and H. Dehmelt, J. Opt. Soc. Am. B 2, 1251 (1985).
73. P.L. Knight and P.W. Milonni, Phys. Reports 66, 21 (1980).
74. P.M. Farrell, W.R. MacGillivray and M.C. Standage, Phys. Rev. A 37, 4240 (1988).
75. J.J. McClelland and M.H. Kelley, Phys. Rev. A 31, 3704 (1985).
76. C.Y. Fong and Y.R. Shen, J. Opt. Soc. Am. B 3, 649 (1986).

77. P.R. Berman, Phys. Rep. (C) 43, 101 (1978).
78. P.F. Liao and G.C. Bjorklund, Phys. Rev. Lett. 36, 584 (1976).
79. P.F. Liao and G.C. Bjorklund, Phys. Rev. A 15, 2009 (1977).
80. A. Javan and P.L. Kelley, IEEE J. Quantum Electron. QE-2, 470 (1966).
81. Spectra Physics Model 380D Frequency Stabilised Dye Laser Instruction Manual.
82. D.M. Kane, "Atomic Laser Spectroscopy in the UV and Visible" (Ph.D. Thesis, University of St. Andrews, 1983).
83. Coherent Model 699-21 Frequency Stabilised Dye Laser Instruction Manual.
84. H.W. Kogelnik, E.P. Ippen, A. Dienes and C.V. Shank, IEEE J. Quantum Electron. QE-8, 373 (1972).
85. S. Gerstenkorn and P. Luc, "Atlas du spectre d'absorption de la molecule d'iode, 14800 - 20000  $\text{cm}^{-1}$ ", (CNRS, Paris, 1978).
86. A. Poustie, "Computerised Data Recording and Analysis of a High Resolution Spectroscopy Experiment", (Report to Carnegie and Physics Trusts, 1985).
87. C.R. Vidal and J. Cooper, J. Appl. Phys. 40, 3370 (1969).
88. M. Lapp and L.P. Harris, J. Quant. Spectrosc. Radiat. Transfer 6, 169 (1966).
89. F. Biraben, B. Cagnac and G. Grynberg, C.R. Acad. Sci. Paris 279 (ser B), 51 (1975).
90. F. Biraben, B. Cagnac and G. Grynberg, Phys. Lett. 48A, 469 (1974).
91. L. Windholz, Z. Phys. A 322, 203 (1985).
92. L. Windholz and M. Musso, Z. Phys. D 8, 239 (1988).
93. S. Nakayama, G.W. Series and W. Gawlik, Opt. Commun. 34, 382 (1980).

94. W. Demtröder, "Springer Series in Chemical Physics 5 - Laser Spectroscopy, Basic Concepts and Instrumentation", 3rd edition, (Springer-Verlag, Berlin, 1988).
95. M.D. Levenson, "Introduction to Nonlinear Laser Spectroscopy", (Academic Press, New York, 1982).
96. V.S. Letokhov in "Topics in Applied Physics vol. 13 - High-Resolution Laser Spectroscopy", edited by K. Shimoda (Springer-Verlag, Berlin, 1976), pp. 95-171.
97. H. Walther in "Topics in Applied Physics Vol. 2 - Laser Spectroscopy of Atoms and Molecules" edited by H. Walther (Springer-Verlag, Berlin, 1976), pp. 1-24.
98. C.J. Anderson, J.E. Lawler, L.W. Anderson, T.K. Holley and A.R. Filippelli, Phys. Rev. A 17, 2099 (1978).
99. J. Neukammer, H. Rinneberg and Z.X. Zhang, Opt. Commun. 38, 361 (1981).
100. P.G. Pappas, M.M. Burns, D.D. Hinshelwood, M.S. Feld and D.E. Murnick, Phys. Rev. A 21, 1955 (1980).
101. M. Pinard, C.G. Aminoff and F. Laloë, Phys. Rev. A 19, 2366 (1979).
102. Jom Sool Kim, Hong Jin Kong, Sang Soo Lee and Jung Bog Kim, Phys. Rev. A 39, 2236 (1989).
103. S. Nakayama, J. Opt. Soc. Am B. 2, 1431 (1985).
- 103a. M. Ducloy and M.S. Feld in "Laser Spectroscopy III", edited by J.L. Hall and J.L. Carlsten (Springer-Verlag, Berlin, 1977), p.243.
- 103b. M. Ducloy and M.S. Feld, Phys. Rev. A 17, 623 (1978).
104. C. Brechignac, R. Vetter and P.R. Berman, Phys. Rev. A 17, 1609 (1978).
105. P.G. Pappas, R.A. Forber, W.W. Quivers Jr, R.R. Dasari, M.S. Feld and D.E. Murnick, Phys. Rev. Lett. 47, 236 (1981).
106. W.W. Quivers Jr., R.A. Forber, A.P. Ghosh, D.J. Heinzen, G. Shimkaveg, M.A. Attili, C. Stubbins, P.G. Pappas, R.R. Dasari, M.S. Feld, Y. Niv and D.E. Murnick in "Laser Spectroscopy V", edited by A.R.W. McKellar, T. Oka and B.P. Stoicheff (Springer-Verlag, Berlin 1981), pp. 186-196.

107. T.W. Hänsch, I.S. Shahin and A.L. Schawlow, *Phys. Rev. Lett.* 27, 707 (1971).
108. M. Borenstein and W.E. Lamb, *Phys. Rev. A* 5, 1311 (1972).
109. Hamamatsu Photomultiplier Tube Catalogue.
110. W.L. Wiese, M.W. Smith, B.M. Miles, "Atomic Transition Probabilities", Vol. 2, NBS Ref. Data Series - NBS 22 (Washington, 1969).
111. G.C. Bjorklund, J.E. Bjorkholm, P.F. Liao and R.H. Storz, *Appl. Phys. Lett.* 29, 729 (1976).
112. G.C. Bjorklund, J.E. Bjorkholm, R.R. Freeman and P.F. Liao, *Appl. Phys. Lett.* 31, 330 (1977).
113. R.R. Freeman, G.C. Bjorklund, N.P. Economou, P.F. Liao and J.E. Bjorkholm, *Appl. Phys. Lett.* 38, 739 (1978).
114. S.E. Harris and R.B. Miles, *Appl. Phys. Lett.* 19, 385 (1971).
115. J.F. Young, G.C. Bjorklund, A.H. Kung, R.B. Miles and S.E. Harris, *Phys. Rev. Lett.* 27, 1551 (1971).
116. D.M. Bloom, G.W. Bekkers, J.F. Young and S.E. Harris, *Appl. Phys. Lett.* 26, 687 (1975).
117. R.T. Hodgson, P.P. Sorokin and J.J. Wynne, *Phys. Rev. Lett.* 32, 343 (1974).
118. D.M. Bloom, J.F. Young and S.E. Harris, *Appl. Phys. Lett.* 27, 390 (1975).
119. A.H. Kung, J.F. Young and S.E. Harris, *Appl. Phys. Lett.* 28, 239 (erratum) (1976).
120. E.R. Peck and D.J. Fisher, *J. Opt. Soc. Am* 54, 1362 (1964).
121. D.P. Shelton and A.D. Buckingham, *Phys. Rev. A* 26, 2787 (1982).
122. D.P. Shelton and V. Mizrahi, *Phys. Rev. A* 33, 72 (1986).

123. Li Binxue, Huang Yongkai, Li Qun and Liu Yashu, Chinese Physics - Lasers 14, 650 (1987).
124. D.A. Kleinman, A. Ashkin and G.D. Boyd, Phys. Rev. 145, 338 (1966).
125. D.A. Kleinman and R.C. Miller, Phys. Rev. 148, 302 (1966).
126. J.F. Ward and G.H.C. New, Phys. Rev. 185, 57 (1969).
127. G. Grynberg, B. Cagnac and F. Biraben in "Coherent Nonlinear Optics - Recent Advances", edited by M.S. Feld and V.S. Letokhov (Springer-Verlag, Berlin, 1980), pp. 111-164.
128. J.E. Bjorkholm and P.F. Liao, IEEE J. Quantum Electron. QE-10, 906 (1974).
129. W. Gautschi in "Handbook of Mathematical Functions", edited by M. Abramowitz and I.A. Stegun (Washington, NBS, 1965). (See p. 302 for the integral representation of  $\operatorname{Re} \operatorname{erfc}(z)$  and pp. 325-328 for a tabulation of its values.)
130. J.E. Bjorkholm, P.F. Liao and A. Wokaun, Phys. Rev. A26, 2643 (1982).
131. T. Mossberg, A. Flusberg, R. Kachru and S.R. Hartmann, Phys. Rev. Lett. 39, 1523 (1977).
132. F. Biraben, B. Cagnac, E. Giacobiro and G. Grynberg, J. Phys. B : Atom. Molec. Phys., 10, 2369 (1977).
133. P.F. Liao, N.P. Economou and R.R. Freeman, Phys. Rev. Lett. 39, 1473 (1977).
134. D.M. Bruce, M.Y. Mirza and W.W. Duley, Opt. Commun. 27, 76 (1978).
135. D.G. McCartan and J.M. Farr, J. Phys. B : Atom. Molec. Phys. 9, 985 (1976).
136. J.F. Kielkopf and R.B. Knollenberg, Phys. Rev. A12, 559 (1975).
137. F. Karstensen and J. Schramm, Z. Physik 195, 370 (1966).

138. W. Gornik, D. Kaiser, W. Lange, J. Luther, H.-H. Radloff and H.H. Schulz, *Appl. Phys.* 1, 285 (1973).
139. M.J. O'Callaghan and A. Gallagher, *Phys. Rev.* A39, 6190 (1989).
140. M.J. O'Callaghan and J. Cooper, *Phys. Rev.* A39, 6206 (1989).
141. F. Biraben, B. Cagnac and G. Grynberg, *C.R. Acad. Sci. Paris* 280, B235 (1975).
142. F. Biraben, K. Beroff, E. Giacobiro and G. Grynberg, *J. Physique* 39, L-108 (1978).
143. M. O'Callaghan and A. Gallagher in "Electronic and Atomic Collisions" edited by D.L. Huestis and R.P. Saxon (North Holland : Amsterdam) 1985, p. 355.
144. P.F. Liao, J.E. Bjorkholm and P.R. Berman, *Phys. Rev.* A20, 1489 (1979).
145. P.F. Liao, J.E. Bjorkholm and P.R. Berman, *Phys. Rev.* A21, 1927 (1980).
146. J.-C. Gay and W.B. Schneider, *Z. Physik A* 278, 211 (1976).
147. T.F. Gallagher, S.A. Edelstein and R.M. Hill, *Phys. Rev. Lett.* 35, 644 (1975).
148. K. Shimoda in "Topics in Applied Physics vol. 13 - High-Resolution Laser Spectroscopy", edited by K. Shimoda (Springer-Verlag, Berlin, 1976), pp. 11-49.
149. A. Corney, "Atomic and Laser Spectroscopy", (Clarendon Press, Oxford, 1977).
150. C.C. Wang and L.I. Davis, Jr., *Phys. Rev. Lett.* 35, 650 (1975).
151. J.F. Ward and A.V. Smith, *Phys. Rev. Lett.* 35, 653 (1975).
152. S.H. Autler and C.H. Townes, *Phys. Rev.* 100, 703 (1955).
153. H.R. Gray and C.R. Stroud, Jr., *Opt. Commun.* 25, 359 (1978).
154. J.E. Bjorkholm and P.F. Liao, *Opt. Commun.* 21, 132 (1977).

155. J.L. Picqué and J. Pinard, *J. Phys. B : Atom. Molec. Phys.* 9, L77 (1976).
156. C. Delsart and J.-C. Keller, *J. Phys. B : Atom. Molec. Phys.* 9, 2769 (1976).
157. A. Schabert, R. Keil and P.E. Toschek, *Appl. Phys.* 6, 181 (1975).
158. A. Schabert, R. Keil and P.E. Toschek, *Opt. Commun.* 13, 265 (1975).
159. S. Feneuille and M.-G. Schweighofer, *J. Physique* 36, 781 (1975).
160. A.M. Bonch-Bruевич and V.A. Khodovoi, *Usp. Fiz. Nauk* 93, 71 (1967) [*Sov. Phys. Usp.* 10, 637 (1968)].
161. P.F. Liao and J.E. Bjorkholm, *Phys. Rev. Lett.* 34, 1 (1975).
162. P.F. Liao and J.E. Bjorkholm, *Opt. Commun.* 16, 392 (1976).
163. J.E. Bjorkholm and A. Ashkin, *Phys. Rev. Lett.* 32, 129 (1974).
164. D. Grischkowsky, *Phys. Rev. Lett.* 24, 866 (1970).
165. K. Tai, H.M. Gibbs, M.C. Rushford, N. Peyghambarian, J.S. Satchell, M.G. Boshier, R.J. Ballagh, W.J. Sandle, M. Le Berre, E. Ressayre, A. Tallet, J. Teichmann, Y. Claude, F.P. Mattar and P.D. Drummond, *Opt. Lett.* 9, 243 (1984).
166. M.R. Teague and P. Lambropoulos, *J. Phys. B : Atom. Molec. Phys.* 9, 1251 (1976).
167. S.J. Smith and P.B. Hogan in "Laser Spectroscopy IV", edited by H. Walther and K.W. Rothe, (Springer-Verlag, Berlin, 1979), pp. 360-367.
168. A. Yariv, "Optical Electronics", 3rd edition (Holt-Saunders, Tokyo, 1985).
169. J.J. Hopfield, J.M. Worlock and K.J. Park, *Phys. Rev. Lett.* 11, 414 (1963).
170. J.J. Hopfield and J.M. Worlock, *Phys. Rev.* 137, A1455 (1965).
171. C.E. Tull, M. Jackson, R.P. McEachran and M. Cohen, *Can. J. Phys.* 50, 1169 (1972).

172. A. Kastler, J. Phys. Radium 11, 255 (1950).
173. J. Brossel, A. Kastler and J. Winter, J. Phys. Radium 13, 668 (1952).
174. Jack T. Cusma and L.W. Anderson, Phys. Rev. A 28, 1195 (1983).
175. V.I. Balykin, Opt. Commun. 33, 31 (1980).
176. W. Dreves, W. Kamke, W. Broermann and D. Fick, Z. Phys. A 303, 203 (1981).
177. W. Dreves, H. Jänsch, E. Koch and D. Fick, Phys. Rev. Lett. 50, 1759 (1983).
178. A. Fischer and I.V. Hertel, Z. Phys. A 304, 103 (1982).
179. J.A. Abate, Opt. Commun. 10, 269 (1974).
180. M.L. Citron, H.R. Gray, C.W. Gabel and C.R. Stroud, Jr., Phys. Rev. A 16, 1507 (1977).
181. R.A. Bernheim, "Optical Pumping : An Introduction" (W.A. Benjamin, Inc., New York, 1965).
182. C. Cohen-Tannoudji in "Atomic Physics 4", edited by G. ZuPutlitz, E.W. Weber and A. Winnacker (Plenum Press, New York, 1975), p. 589.
183. W. Happer, "Light Propagation and Light Shifts in Optical Pumping Experiments" - Progress in Quantum Electronics Vol. 1 Part 2, edited by J.H. Sanders and K.W.H. Stevens, (Pergamon Press, Oxford, 1970).
184. W. Franzen and A.G. Emslie, Phys. Rev. 108, 1453 (1957).
185. W.B. Hawkins, Phys. Rev. 98, 478 (1955).
186. E.W. Weber and H. Vogt, Phys. Lett. 103A, 327 (1984).
187. G. Alzetta, A. Gozzini, L. Moi and G. Orriols, Nuovo Cimento 36B, 5 (1976).

188. N.D. Bhaskar, M. Hou, M. Ligare, B. Suleman and W. Happer, Phys. Rev. A 22, 2710 (1980).
189. W.D. Cornelius, D.J. Taylor, R.L. York and E.A. Hinds, Phys. Rev. Lett. 49, 870 (1982).
190. R. Walkup, A. Spielfiedel, W.D. Phillis and D.E. Pritchard, Phys. Rev. A 23, 1869 (1981).
191. C.G. Aminoff, Ann. Phys. Fr. 10, 995 (1985).
192. A.T. Ramsey and L.W. Anderson, Nuovo Cimento 32, 1151 (1964).
193. I.M. Sokolov, Opt. Spectrosc. (USSR) 56, 376 (1984).
194. W. Franzen, Phys. Rev. 115, 850 (1959).
195. R.A. Bernheim, J. Chem. Phys. 36, 135 (1962).
196. F. Franz and E. Lüscher, Phys. Rev. 135, A582 (1964).
197. L.W. Anderson and A.T. Ramsey, Phys. Rev. 132, 712 (1963).
198. A. Moretti and F. Strumia, Phys. Rev. 3, 349 (1971).
199. J. Liran, J. Pietras, J. Camparo and W. Happer, Opt. Commun. 31, 169 (1979).
200. N.D. Bhaskar, J. Pietras, J. Camparo, W. Happer and J. Liran, Phys. Rev. Lett. 44, 930 (1980).
201. D. Tupa, L.W. Anderson, D.L. Huber and J.E. Lawler, Phys. Rev. A 33, 1045 (1986).
202. A.C. Tam, J. Appl. Phys. 50, 1171 (1979).
203. N.D. Bhaskar, M. Hou, B. Suleman and W. Happer, Phys. Rev. Lett. 43, 519 (1979).

204. N.H. Tran, N.D. Bhaskar and W. Happer in "Laser Spectroscopy V", edited by A.R.W. McKellar, T. Oka and B.P. Stoicheff (Springer-Verlag, Berlin, 1981), p. 103.
205. P.F. Liao and J.E. Bjorkholm, Phys. Rev. Lett. 36, 1543 (1976).